



TECHNISCHE UNIVERSITÄT WIEN

DISSERTATION

Classical Dynamics of Low Energy Electron-Ion Recombination in Storage Rings

ausgeführt zum Zwecke der Erlangung des akademischen Grades
eines Doktors der technischen Wissenschaften

unter der Leitung von
O.Univ.Prof. Dipl.-Phys. Dr.rer.nat. Joachim Burgdörfer
und
Vertr.Ass. Dipl.-Ing. Dr.techn. Shuhei Yoshida
Institut für Theoretische Physik (E136)

eingereicht an der Technischen Universität Wien
Fakultät für Physik

von
Dipl.-Ing. Maria Hörndl
Matrikelnummer: 9525579
Rienöblgasse 15/12
1040 Wien

Wien, am 5. Juni 2005

Maria Hörndl

Zusammenfassung

Elektron-Ion Rekombination gemessen in Speicherringexperimenten zeigt eine signifikante Erhöhung der Rekombinationsrate für hochgeladene Ionen mit niederenergetischen Elektronen relativ zu den Vorhersagen der Standardtheorie der radiativen Rekombination (RR). Um den fundamentalen Mechanismus dieser Ratenerhöhung zu verstehen, analysieren wir in dieser Arbeit die Rolle der klassischen chaotischen Dynamik in der Anwesenheit von Coulomb- und Magnetfeldern.

Unter Verwendung einer klassischen Monte Carlo Trajektorienmethode untersuchen wir zunächst die chaotische Dynamik eines Elektrons im Ruhesystem des Ions innerhalb der Solenoidregion des Elektronenkühlers. Im gemeinsamen Coulombfeld des Ions und dem homogenen magnetischen Führungsfeld im Kühler werden Elektronen vielfach an einem Ion gestreut, was auf irreguläre Ablenkfunktionen mit fraktaler Struktur wie die später diskutierte Visitsfunktion führt. Demzufolge wird der Nettofluss von Elektronen in die unmittelbare Umgebung eines Ions signifikant verändert verglichen mit dem reinen Coulombfeld, was wiederum die Wahrscheinlichkeit für radiative Rekombination beeinflusst. Wir werden zeigen, dass die chaotische Dynamik abhängig von der Relativgeschwindigkeit zwischen Elektron und Ion entweder auf eine Erhöhung oder auf eine Reduktion der Rekombinationsrate führen kann. Andererseits findet man während der Strahlzusammenführung von Elektronen und Ionen in der toroidförmigen dem Solenoiden vorgelagerten Magnetfeldregion ein transientes elektrisches Feld im Ruhesystem des Ions vor, welches einen zusätzlichen Weg für Übergänge von freien zu gebundenen Elektronen eröffnet. Wir präsentieren Simulationen für die Elektron-Ion Zusammenführung entsprechend der Toroidgeometrie des Testspeicherring Elektronenkühlers. Hohe Rydbergzustände, $n \gtrsim 100$, werden während der Strahlzusammenführung besetzt. Radiativer Zerfall dieser Rydbergzustände innerhalb des Solenoiden kann einen kleinen Bruchteil der gebundenen Elektronen stabilisieren. Wir berechnen die Wahrscheinlichkeit für radiative Stabilization dieser hoch angeregten Zustände in tiefer gebundene im Experiment nachweisbare Elektronen. Hinreichend tief gebundene Elektronen tragen daher, zusätzlich zum RR Kanal, zu der gemessenen Elektron-Ion Rekombinationsrate bei. Die erhaltenen absoluten Überschussraten können in etwa die experimentelle Ratenerhöhung erklären. Auch die Skalierung der Rate mit der Ionenladung und dem magnetischen Führungsfeld stimmt gut mit den Messungen überein.

Eine kurze Analyse eines alternativen theoretischen Ansatzes, bei dem die Erhöhung der Rekombination ebenfalls auf den mechanischen (*d.h.* nicht-radiativen) Einfang während der Strahlzusammenführung zurückgeführt wird, wird präsentiert und konzeptionelle Schwierigkeiten in diesem Model werden diskutiert. Schließlich werden Mehrioneneffekte im Plasma adressiert.

Abstract

Electron-ion recombination observed in storage ring experiments shows a dramatic enhancement of the recombination rate for highly charged ions with low-energy electrons relative to what standard radiative recombination (RR) rates predict. To understand the fundamental mechanism of this enhancement we analyze within this thesis the role of classical chaotic dynamics in the presence of Coulomb and magnetic fields.

Using a classical trajectory Monte Carlo method we first investigate the chaotic dynamics of an electron in the rest frame of the target ion inside the solenoid region of the electron cooler. In the combined Coulomb field of the ion and the homogeneous magnetic guiding field in the cooler electrons are scattered by the ion multiple times involving irregular deflection functions with fractal-like structure such as the visit function to be discussed below. As a result, the net flux of electrons towards the immediate vicinity of the ion is changed significantly compared to the pure Coulomb field, which, in turn, influences the probability for recombination. We will show that the chaotic dynamics can lead to an enhancement or a reduction of the recombination rate depending on the relative velocity between electron and ion. On the other hand, during the merging between electrons and ions in the toroidal-shaped magnetic field section prior to the solenoid a transient motional electric field is present in the rest frame of the ion which opens an additional pathway for free-bound transitions of electrons. We present simulations for the electron-ion merging according to the toroidal geometry of the Test Storage Ring electron cooler. High Rydberg states, $n \gtrsim 100$, are found to be populated during the merging process. Radiative decay of these Rydberg states inside the solenoid can stabilize a small fraction of the bound electrons. We compute the probability for radiative stabilization of these high-lying states to deeper bound electrons observable in the experiment. Thus, sufficiently deeply bound electrons contribute, in addition to the RR channel, to the observed electron-ion recombination rate. The absolute excess recombination rates obtained can approximately account for the experimental enhancement. Also the scaling of the rate with the nuclear charge and the magnetic guiding field is in close agreement with the measurements.

A brief analysis of an alternative theoretical approach, where the enhancement of the recombination is likewise attributed to the mechanical (*i.e.* non-radiative) capture during the merging, is presented and conceptual difficulties within this model are discussed. Finally, effects due to neighboring ions in the plasma are addressed.

Contents

1	Introduction	1
2	Recombination: Theory and Experiment	4
2.1	Experimental Setup: Storage Ring Experiments	4
2.2	Standard Radiative Recombination Theory	9
2.3	Other Recombination Mechanisms	14
2.4	Review of Experimental Results	16
2.5	Alternative Theoretical Proposals	19
3	Chaotic Dynamics in a Magnetic Field	21
3.1	Influence of a Magnetic Field	22
3.2	Electron-Ion Motion: Lab, Center of Mass, and Ionic Rest Frames . .	25
3.3	Classical Chaotic Dynamics	31
3.4	Classical Phase Space Structure: Poincaré Surfaces of Section	36
3.5	Modification of the Recombination Rate	38
3.6	Determination of the Visit Function	39
3.7	The Visit Function: Numerical Results	42
3.8	Weighted Visit Function	46
3.9	Magnetic Field Dependence of the Visit Function	48
3.10	Velocity Projection of Visits	52
3.11	Relative Energy Dependence of the Recombination Rate	54
3.12	Magnetic Field and Charge Dependence of the Recombination Rate .	58
3.13	Temperature Dependence of the Recombination Rate	62
3.14	Parameter Dependences for the Velocity Projection of Visits	63
3.15	Visits in Momentum Space	64
3.16	Formation of Bound States in the Solenoid: Coupling between the Center of Mass and Relative Motions	67
3.17	Summary	68

4	Merging of Electron and Ion Beam	71
4.1	Recombination in Transient Electric Fields	72
4.2	Electron-Ion Merging in the Lab Frame	75
4.3	Transformation to the Rest Frame of the Ion	78
4.4	Electron-Ion Merging in the Rest Frame of the Ion	80
4.5	CTMC Simulation of the Merging	81
4.6	Analysis of Bound-State Distributions	85
4.7	Bound-State Evolution in the Solenoid	88
4.8	Semiclassical Lifetime Estimate	92
4.9	Properties of the Stark Saddle	94
4.10	Evaluation of Radiative Decay Rates	96
4.11	Alternative Approach to Radiative Decay	101
4.12	Magnetic Field and Charge Dependence of the Field-Induced Recombination	104
4.13	Summary	109
4.14	Sum of the Field-Induced Recombination and the Radiative Recombination in the Magnetic Field	110
5	An Alternative Model for the Enhancement	115
5.1	Sudden Turn-On of the Coulomb Field	115
5.2	Test of the Sudden Approximation	117
5.3	Magnetic Field Dependence	118
5.4	Comparison with Realistic Merging Process	119
5.5	Densities and Rydberg States	123
6	Electron Dynamics in Presence of Two Ions	127
7	Summary, Conclusions and Outlook	133
A	Canonical Transformations	136
B	Classical Scaling Invariance	139
C	Symplectic Integration	141
D	Recombination in Momentum Space	146
D.1	Momentum Distributions of Bound and Free Electrons	146
D.2	Perturbative Quantum Mechanical Approach	149
E	Electron-Ion Merging: Lab Frame	156
F	Electron-Ion Merging: Ionic Rest Frame	159

<i>CONTENTS</i>	iii
G Radiative Transition Probabilities	162
H Continuity Across Threshold	164
Bibliography	166
Acknowledgments	172

Chapter 1

Introduction

Electron-ion recombination is a fundamental process of great importance in many areas of basic and applied physics. The cross sections and rate coefficients provide useful information for applications in astrophysics [1] and plasma physics [2] and are also relevant for applications in accelerator physics. For example, the recombination is a significant ion loss mechanism during electron cooling of ions in a storage ring. The basic two- and three-body recombination processes are of very fundamental nature and thus provide an excellent testing ground for collision theory and atomic structure calculations. Low-energy electron-ion recombination also supplies a very promising scheme for the production of antihydrogen by recombination of cold positrons with antiprotons [3, 4]. In this thesis the two-body process of radiative recombination will be investigated.

While a proper theoretical understanding and description of radiative recombination within the framework of quantum electrodynamics (QED) was already provided more than half a century ago by Stobbe [5], Kramers [6] and Bethe and Salpeter [7], it has proven difficult to perform accurate experimental investigations and measurements of rate coefficients due to the smallness of the corresponding cross sections. Only with the recent advent of heavy-ion storage rings for atomic physics such as CRYRING (Sweden), ASTRID (Denmark), TSR and ESR (Germany) the study of the recombination at low temperatures under well-controlled conditions has become possible (see [8, 9, 10, 11, 12] and references therein). In these experiments the incident ion beam is merged with a cold and magnetically guided beam of electrons in the electron cooler. The electrons provide not only the cooling medium for the ion beam, but also supply a very cold target for electron-ion recombination. However, already the first experimental results obtained caused a major surprise since they revealed big deviations from the theoretical predictions: the measured radiative recombination rates show a dramatic enhancement in excess of what is expected from standard two-body radiative recombination theory for the recombination of highly charged ions with electrons at low relative energies (typically $\lesssim 1$

meV). This surprising discrepancy with theory for the supposedly well understood elementary process of radiative recombination has led to intensive investigations both experimentally and theoretically in the past decade. In a series of measurements at different storage rings recombination rates have been explored for bare ions as well as for multielectron ions. The observed enhancement ratios for bare ions, the topic of investigation in this thesis, range from 1.6 for He^{2+} [9] to a factor of 5 for U^{92+} [12]. In addition, the dependence of the enhancement on external parameters such as beam temperatures, electron density and magnetic guiding field has been quantified [10]. Nevertheless, the origin of this discrepancy is still an open question and to contribute to its understanding is the goal of this thesis.

In the experiment the electrons are guided by a longitudinal magnetic field through the cooler. Standard radiative recombination rates according to Refs. [5, 6, 7] are determined at zero magnetic field strength. A quantum mechanical evaluation of the corresponding rate coefficients in the presence of a magnetic field constitutes an exceedingly difficult task, since a full non-perturbative solution for the wavefunction of an electron in combined Coulomb and magnetic fields is not available. Therefore, a quantum mechanical treatment would necessitate a perturbative approach. In this thesis, however, we explore the effect of the magnetic field on the recombination rates via a classical description instead.

We will present a detailed analysis of the classical motion of individual electron-ion pairs in the electron cooler of the storage ring. In the presence of the magnetic guiding field in the cooler the dynamics of an electron in the Coulomb field of the ion is classically chaotic. The chaotic nature of electron trajectories will be investigated for low-lying continuum as well as high-lying bound states. In these regimes a classical description of the electron motion is valid, which has the advantage that the dynamics in the magnetic field can easily be treated non-perturbatively in contrast to a full quantum mechanical treatment. We will thus employ a classical trajectory Monte Carlo (CTMC) method to describe the distribution of electrons in the cooler. The key point is to construct a proper representation of the quantum mechanical cross sections and rate coefficients for radiative recombination in a magnetic field from these CTMC calculations. While the quantum rates are gauge invariant, an approximate classical description to be presented can lead to ambiguities with respect to its formulation in coordinate or momentum space resulting from the freedom of gauge available for the representation of a magnetic field. We will treat direct radiative recombination of an electron into low-lying experimentally observable bound states of the ion. Furthermore, electrons can also be captured non-radiatively by transient electric fields in the toroidal merging region of the electron and ion beams at the entrance into the cooler. We will study the capture of electrons during the merging followed by radiative stabilization in the interaction region inside the solenoid. Classical chaotic motion plays an important role for these recombination processes. We will show that the scattering dynamics in a magnetic field becomes

highly irregular with fractal-like structure involving generalized deflection functions, whereas the chaotic bound-state motion will be mirrored in a statistical distribution of angular momentum states reflecting maximum randomness in the magnetic field. An appropriate incorporation of these chaotic effects into the evaluation of the recombination rates will be discussed and the calculated rate coefficients will be compared with the experimental data.

The thesis is organized as follows. In chapter 2 we take a brief glance at the various recombination experiments and the associated standard radiative recombination theory. In chapter 3 we investigate the classical chaotic scattering dynamics of an electron in the Coulomb field of the target ion and the magnetic field inside the solenoid of the electron cooler, while in chapter 4 we explore the merging of electrons and ions in the toroidal-shaped magnetic field section prior to the solenoid. We calculate radiative recombination rates in chapter 3 and transient electric field-induced recombination during the merging with subsequent radiative stabilization inside the solenoid in chapter 4. Radiative decay of the transiently formed high Rydberg states into sufficiently deeply bound electrons thus contributes, in addition to the radiative recombination channel, to the experimental rate coefficients. The excess recombination rates obtained will be compared with the measurements. Moreover, in chapter 5 a brief analysis of a recently developed alternative model for the rate enhancement [13], which also assigns the enhanced recombination to the beam merging region, is presented. However, in that model recombination is induced only by an instantaneous turn-on of the electron-ion interaction. This oversimplification and other conceptual difficulties are discussed (see also [14, 15, 16]) and compared with the realistic merging process of chapter 4. Chapter 6 addresses the influence of neighboring ions and electrons in the cooler. Finally, in chapter 7 the conclusions of this work are summarized and an outlook to possible future investigations is given.

Parts of this thesis have already been published [14, 17, 18], are in print [19], or submitted for publication [20].

Chapter 2

Recombination: Theory and Experiment

This chapter covers an introduction to the current status of the topic. It contains an overview of recent recombination experiments and measurements, a description of the underlying standard radiative recombination theory including a short discussion of basic recombination mechanisms, the failure of the theory to describe the measurements, and an outline of other theoretical approaches towards an explanation of the rate enhancement.

Atomic units (a.u.) are used throughout this thesis unless otherwise stated. In these units $\hbar = 1$ (Planck's constant), $m_e = 1$ (electron rest mass) and $e = -1$ (charge of the electron). Therefore, $a_B = \hbar^2/(m_e e^2) = 5.29 \times 10^{-11} \text{ m} = 1 \text{ a.u.}$ (Bohr radius), $v = e^2/\hbar = 2.18 \times 10^6 \text{ m/s} = 1 \text{ a.u.}$ (Bohr velocity), $E = m_e e^4/\hbar^2 = 27.2 \text{ eV} = 1 \text{ a.u.}$ (atomic energy), $t = a_B/v = 2.4 \times 10^{-17} \text{ s} = 1 \text{ a.u.}$ (atomic time) and $F = |e|/a_B^2 = 5.14 \times 10^9 \text{ V/cm} = 1 \text{ a.u.}$ (atomic field strength).

2.1 Experimental Setup: Storage Ring Experiments

Recent recombination measurements have been performed either in electron coolers of storage rings (such as [8, 9, 10, 11, 12]) or in single pass electron targets (for example [21, 22]). Here we focus on the experiments at storage ring facilities such as the TSR (Test Storage Ring) at the Max-Planck-Institute for Nuclear Physics in Heidelberg (Germany), the ESR (Experimental Storage Ring) of the Community for Heavy Ion Research (GSI) in Darmstadt (Germany) or the CRYRING facility at the Manne Siegbahn Laboratory in Stockholm (Sweden). In these experiments the electrons required for the recombination are provided by the conventional electron cooling device of the particular storage ring. In the following the most important

properties of these experiments and the performed measurements to obtain typical recombination spectra shall be shortly discussed. Whenever specific numbers are given to identify typical experimental conditions, they refer to the TSR experiment. In this section, as an exception, SI units are frequently used.

A storage ring consists of a few deflecting and focusing units made up by dipole and quadrupole magnets to keep the injected ions circulating in the ring for millions of times. Depending on the ion species lifetimes of up to several minutes can be achieved in the prevailing ultra high vacuum (few 10^{-11} mbar) of the ring. A central element of the storage ring is the electron cooler. It provides a cold beam of electrons which is superimposed on the ion beam over a short distance, for example 1.5 m at the TSR. The purpose of this electron beam is twofold: it cools the circulating ion beam and thus improves its beam quality and it supplies a cold electron target for electron-ion recombination.

The electrons are generated by thermal emission from a hot cathode (with a temperature of typically 1200 - 1400 K), extracted and then further accelerated to energies of few keV. Note that the electron beam is guided by a longitudinal (*i.e.* parallel to its direction of motion) homogeneous magnetic field all along its way through the cooler. The magnetic field avoids a geometric expansion of the electron beam due to its space charge and thus provides for the lateral confinement of the electron gas in the cooler. After emission from the cathode the electrons exhibit an energy distribution determined by the cathode temperature $T_{cathode}$. The corresponding velocity distribution can be characterized by a three-dimensional Maxwell-Boltzmann distribution with temperature $T_{cathode}$. The velocity spread in the longitudinal direction is considerably reduced through the subsequent acceleration of the electrons, whereas the transverse velocity spread remains unaffected.

To decrease also the transverse velocity spread of the electrons and hence the transverse electron temperature the technique of adiabatic magnetic expansion is applied [23, 24, 25]. Accordingly, the electrons are guided through a slowly decreasing longitudinal magnetic field. For the motion of an electron in a constant magnetic field B the quantity E_{\perp}/B (E_{\perp} : transverse energy) is conserved. Furthermore, E_{\perp}/B remains also conserved, if B is changed very slowly, *i.e.* in the adiabatic limit. For a Maxwell-Boltzmann distributed beam of electrons E_{\perp} can be replaced by its average value $\langle E_{\perp} \rangle = kT_{\perp}$. In the experiment the adiabatic expansion is realized by placing the cathode into a solenoid producing a strong magnetic field ($B_{cathode} \approx 1$ T at the TSR) and by installing further solenoids on the way towards the interaction region, which then gradually reduce this strong magnetic field strength to its final value present in the interaction zone ($0.02 \text{ T} \leq B \leq 0.07 \text{ T}$ at the TSR). Thereby, the transverse temperature decreases according to the relation $kT_{\perp} = kT_{cathode}/\zeta$. The ratio $\zeta = B_{cathode}/B$ is the resulting expansion factor. Since the lateral confinement of the electrons in the beam is only imposed by the magnetic field, the beam diameter correspondingly increases with decreasing value of B . At

the TSR, for example, the electron beam exhibits a diameter of merely 9.5 mm at the cathode whereas being expanded to a spatial extent of few cms in the interaction region. The spatial expansion of the beam is due to the conservation of phase space volume, whereupon a decrease in the transverse temperature (or velocity) leads to an increase in the involved transverse coordinate.

Even though this adiabatic expansion is applied (as it is the case at the TSR and the CRYRING electron coolers) the transverse temperature kT_{\perp} of the electron beam in the interaction region is usually still about two orders of magnitude larger than typical longitudinal temperatures kT_{\parallel} . At the TSR temperatures such as $kT_{\perp} = 10$ meV and $kT_{\parallel} = 0.2$ meV are reached. Therefore, the electron velocity distribution is highly anisotropic with $T_{\perp} \gg T_{\parallel}$ given by the product of two Maxwellian distributions

$$f(\vec{v}_e) = f_{MB}(\vec{v}_e) = \frac{m_e}{2\pi kT_{\perp}} e^{-m_e v_{e\perp}^2 / (2kT_{\perp})} \sqrt{\frac{m_e}{2\pi kT_{\parallel}}} e^{-m_e (v_{e\parallel} - \bar{v}_{e\parallel})^2 / (2kT_{\parallel})}, \quad (2.1)$$

where $\bar{v}_{e\parallel}$ represents the mean longitudinal velocity of the electrons. The mean transverse velocity is assumed to be zero.

The electron beam is then merged with the ion beam by a proper bending along a toroidal-shaped magnetic field region. Note that in addition to the longitudinal magnetic guiding field along the curvature of the toroid also a dipole field perpendicular to the toroid bending plane is required to ensure the merging of the electrons within this toroidal plane. For a more detailed discussion of the magnetic field configuration in the toroid region see chapter 4. In the subsequent solenoid the electron and ion beams thus fully overlap with collinear velocities $\vec{v}_e \parallel \vec{v}_{ion}$. In this interaction region (also referred to as cooler region) the cooling and recombination processes take place. Its length l is, in a first approximation, given by the length of the cooling solenoid and typically amounts to 0.5 - 2.5 m depending on the specific electron cooler. For instance, at the TSR $l = 1.5$ m. Having traversed also the demerging toroid the electrons are finally led to the collector via further solenoids. Before arriving at the collector they are retarded and then picked up by a Faraday cup. Note that also the ions experience a small deflection during passage through the toroid magnets. However this deflection is compensated by correction dipoles installed in front of and behind the electron cooler. For a schematic picture of the geometry see Figure 2.1.

The principle of electron cooling was first suggested by Budker [26] at the end of the sixties in order to increase the number of particles being accumulated in a storage ring. Its central idea is to overlap a hot ion beam with a cold beam of electrons both of them having the same average velocity in the laboratory frame. Before cooling, however, the ion beam exhibits much bigger statistical velocity deviations from its mean value than the supplied electron beam. Accordingly, these big ionic velocity

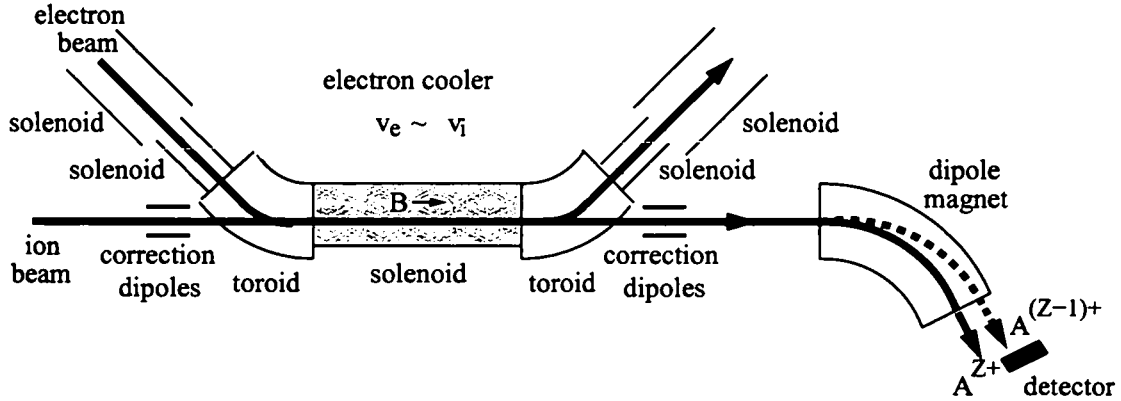


Figure 2.1: Schematic picture of a recombination experiment: the electron and ion beams are merged over a short distance in the electron cooler of the storage ring. The electrons provide not only the cooling medium which can reduce the rest frame kinetic energy of the fast ions but also supply a very cold electron target for electron-ion recombination. In the subsequent dipole magnet the recombined ions are separated from the parent ions due to their lower charge-to-mass ratio. They are absorbed and measured in the recombination detector.

spreads get reduced by Coulomb interactions with the cold electrons: through corresponding collisions faster ions transfer energy and momentum to slower electrons and vice versa. Whereas the ion beam continuously circulates in the storage ring and encounters the electron beam many times, the electron beam is permanently delivered with the same cold temperature from the cathode. In this way the electron beam acts as a cold reservoir for the ion beam, whose temperature decreases and gets adjusted to the electronic beam temperature. Therefore, electron cooling reduces the phase space volume of the "hot" ion beam. It counteracts the heating processes during the circulation given by ion scattering with residual gas particles and intra-beam scattering. Clearly, this cooling mechanism also works for electron and ion beams with initially somewhat different average velocities. Thereby, the average ion beam velocity accommodates to the electronic one. Thus, after cooling the ion beam exhibits the same average velocity and the same temperature as does the electron beam. Theoretically, the process of electron cooling can be described in terms of a binary collision model and an appropriate expression for the cooling force can be derived. Electron cooling is particularly efficient for small differences between \vec{v}_{ion} and \vec{v}_e . Typically, ion currents of several hundred μA get cooled down to a relative momentum uncertainty $\Delta p/p$ smaller than 10^{-4} within few seconds. The ion beam, which can fill up the whole beam pipe after the injection, has then been reduced to a diameter of only 2 – 3 mm.

Electron cooling thus provides a spatially and energetically well defined ion beam, whose interaction with the electron beam in the cooler can be further analyzed. Figure 2.1 shows a sketch of the experimental setup for electron-ion recombination measurements. In the solenoidal interaction region, where the electron and ion beams overlap, free electrons can be captured by the ions. The electrons supply a very cold electron target for electron-ion recombination with transverse temperatures of about $kT_{\perp} \simeq 10$ meV and longitudinal temperatures that are even much lower. The recombined and primary ions leave the electron cooler together and get separated only in the subsequent dipole magnet due to their different charge-to-mass ratios. As a result, the recombined ions (with the smaller charge) experience a smaller deflection in this bending magnet and, hence, leave their revolving orbit in the ring. They are absorbed and counted in a scintillation detector.

The quantity of interest is the recombination rate coefficient α , which constitutes a measure for the probability of the recombination process under investigation. The definition with respect to a velocity averaged product of velocity times cross section will be given in section 2.2. It can be extracted from the so-called reaction rate R ,

$$R = \alpha \frac{\eta I_{ion} l n_e}{v_{ion} q e \gamma^2}, \quad (2.2)$$

where η the efficiency of the detector ($\eta \approx 1$), I_{ion} the ion current, l the nominal length of the interaction region (at the TSR 1.5 m), n_e the electron density (typically several 10^7 cm^{-3}), v_{ion} the ion velocity, q the charge of the ions, e the elementary charge and γ the relativistic Lorentz factor for the transformation between the center of mass and laboratory frames, $\gamma = 1/\sqrt{1 - (v_{ion}/c)^2}$. At the TSR beam velocities of approximately 10 percent of the velocity of light are reached, *i.e.* $\gamma \approx 1$. The ion current (typically few hundred μA) can be expressed in terms of the number of ions N_{ion} circulating in the ring,

$$I_{ion} = q e f N_{ion} = \frac{q e v_{ion} N_{ion}}{U} \quad (2.3)$$

with the revolution frequency f and the ring circumference U (at the TSR $U = 55.4$ m). The rate coefficient thus reads in experimentally accessible quantities

$$\alpha = \frac{R U \gamma^2}{\eta N_{ion} n_e l}. \quad (2.4)$$

Usually, in the experiments entire recombination spectra are recorded, where the recombination rate coefficient Eq. (2.4) is determined as a function of the average relative energy E_{rel} between electrons and ions. For a typical spectrum see Figure 2.8a. Since electron cooling eventually results in an ion beam with the same average velocity as the electron beam, only the rate coefficient at $E_{rel} = 0$ can be

obtained at cooling conditions. To measure also rates for $E_{rel} \neq 0$, the cooler needs to be detuned on purpose, *i.e.* being operated beyond the cooling conditions for a short time interval. In practice, a variation in E_{rel} is accomplished by changing the electron energy, which amounts to altering the cathode voltage at the TSR electron cooler, whereas at the ESR the voltage at drift tubes mounted inside the cooling solenoid is correspondingly changed. After a new value for the electron energy different from the cooling energy has been set, only a short time window of few ms is available for determining the recombination rate. Afterwards, the ionic velocities start to adjust to the new electron velocities as a result of the cooling mechanism. Therefore, measurements at $E_{rel} \neq 0$ have to be performed before the (much heavier and thus more inert) ions can adapt to the new situation in the cooler. In fact, after each measuring time-interval a cooling period is operated in order to guarantee an ion beam of same energy and quality for each measured value of E_{rel} . More details about the experimental setup and the measuring procedure can be found for example in Refs. [27, 28, 29].

2.2 Standard Radiative Recombination Theory

Radiative recombination (RR),

$$e^- + A^{q+} \rightarrow A^{(q-1)+} + h\nu, \quad (2.5)$$

is the process where a free electron (e^-) is captured into a bound state of an ion (A) with initial charge state q . Energy and momentum are conserved by the simultaneous emission of a photon ($h\nu$). A schematic picture of this process, the inverse process of photoionization, is displayed in Figure 2.2. Note that for bare ions $q = Z$, where Z indicates the nuclear charge.

As pointed out in the introduction radiative recombination belongs to the class of elementary QED processes for which accurate calculations can be readily performed. Since in the case of a pure ionic Coulomb field of a bare ion (without a magnetic field considered) the initial and final wavefunctions are known, the cross section for RR is given (in a.u.) by

$$\sigma_{RR}(n, E_e = k^2/2) = \int d\Omega_k \frac{\omega}{2\pi c^3} |\langle u_n | e^{-i\vec{q} \cdot \vec{r}} \hat{e} \cdot \vec{p} | u_k \rangle|^2, \quad (2.6)$$

where u_n is the final hydrogenic bound state with principle quantum number n and u_k the initial hydrogenic continuum state of an electron with wave vector \vec{k} (energy E_e). \vec{p} is the momentum of the electron in the rest frame of the ion. The radiation field has a wave vector \vec{q} , frequency ω ($\omega = E_e + Z^2/(2n^2)$) and a polarization vector \hat{e} . Note that the incoming electron wavefunction u_k is normalized such that

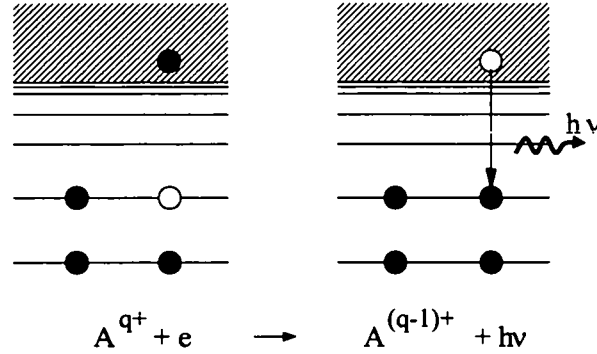


Figure 2.2: Schematic picture of radiative recombination (RR): A free electron is captured into a bound state of the (non-bare) ion with simultaneous emission of a photon.

one electron is incident on a unit area per unit of time. The cross section for RR can be evaluated in closed form for hydrogenic wavefunctions. In the dipole approximation, the transition matrix element becomes proportional to the oscillator strength, $|\langle u_n | \hat{e} \cdot \vec{r} | u_k \rangle|^2$. Bethe and Salpeter [7] (see also Kramers [6]) derived an approximated cross section for RR based on the fact that the oscillator strength crosses the continuum limit smoothly. This parameterization of the RR cross section is convenient compared to the full evaluation of Eq. (2.6). It can be written for bare ions as

$$\sigma_{RR}(n, E_e) = (2.1 \times 10^{-22} \text{cm}^2) \frac{Z^4 E_0^2}{n E_e (Z^2 E_0 + n^2 E_e)}, \quad (2.7)$$

where $E_0 = 13.6 \text{ eV}$ is the Rydberg energy and Z denotes the charge of the bare ion. However, this approximation is only valid in the limit of high quantum numbers $n \gg 1$ and low electron energies $E_e \ll Z^2/n^2 E_0$. To account for deviations from the correct quantum result at low n and high E_e correction factors, the so-called Gaunt factors $G_n(E_e)$, have to be included into the cross section,

$$\sigma_{RR}^{Gaunt}(n, E_e) = (2.1 \times 10^{-22} \text{cm}^2) G_n(E_e) \frac{Z^4 E_0^2}{n E_e (Z^2 E_0 + n^2 E_e)}. \quad (2.8)$$

The use of Gaunt factors is convenient because they are either tabulated [30] or given in a parameterized form [31] in contrast to a full quantum mechanical treatment, which involves the rather tedious evaluation of hydrogenic dipole matrix elements [5].

The total recombination cross section is obtained by summing up the contributions from all possible final states up to a maximum contributing principal quantum

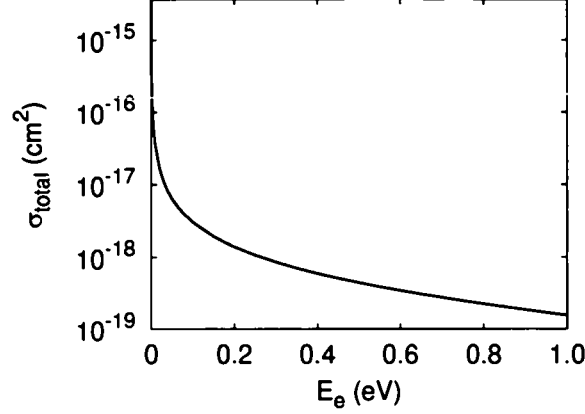


Figure 2.3: The cross section Eqs. (2.8) and (2.9) for radiative recombination of C^{6+} ions and electrons versus the electron energy E_e with $n_r = 30$.

number n_r , *i.e.*

$$\sigma_{total}(E_e) = \sum_{n=1}^{n_r} \sigma_{RR}^{Gaunt}(n, E_e). \quad (2.9)$$

The upper cutoff n_r is determined by field ionization of states caused by motional electric fields in the charge-analyzing dipole magnet downstream from the electron cooler. Hence, electrons recombined into states with $n > n_r$ get reionized again in this bending magnet and therefore do not contribute to the recombination. Figure 2.3 illustrates the RR cross section for C^{6+} ions with electrons.

Eqs. (2.8) and (2.9) represent the recombination cross section for initially bare ions and free electrons. For non-bare ions $\sigma_{total}(E_e)$ must be generalized to

$$\sigma_{total}(E_e) = \sum_{n=n_{min}}^{n_r} (2.1 \times 10^{-22} \text{cm}^2) G_n(E_e) t_n \frac{Z_{eff}^4 E_0^2}{n E_e (Z_{eff}^2 E_0 + n^2 E_e)}. \quad (2.10)$$

Here n_{min} denotes the lowest shell into which electron capture is possible and the quantities t_n are introduced to account for already partially filled shells. $t_n \leq 1$ usually represents the ratio between the number of unoccupied states and all states available for a given n shell (*i.e.* $2n^2$). For non-hydrogenic ions also screening effects through core electrons have to be taken into account. This screening is modeled by replacing the nuclear charge Z by an effective charge Z_{eff} . Based on theoretical or empirical considerations formulae like $Z_{eff} = (Z + q)/2$ (Z is the nuclear charge and q the charge state of the ion) or more complex expressions [32] have been proposed for the effective nuclear charge. However, in this thesis only bare ions will be investigated, where $Z_{eff} = Z = q$.

The experimentally obtained recombination rate is a convolution of the cross section with the velocity distribution $f(\vec{v})$ due to the finite velocity spread of the colliding particles [11, 12, 21, 30],

$$\alpha_{RR} = \langle v\sigma_{total} \rangle = \int \sigma_{total} v f(\vec{v}) d\vec{v}. \quad (2.11)$$

As discussed in section 2.1, in the experiment a homogeneous magnetic field along the direction of the merged beams provides for the lateral confinement of the electron gas in the cooler. The velocity distribution is characterized by two temperatures, T_{\perp} and T_{\parallel} , which correspond to the transverse (v_{\perp}) and the longitudinal (v_{\parallel}) velocity spreads relative to the direction of the magnetic field. The electronic velocity distribution is highly anisotropic with $T_{\perp} \gg T_{\parallel}$ (section 2.1). By comparison, the ionic velocity distribution is negligibly narrow due to the cooling. The ionic velocities after the cooling are precisely defined (with relative velocity uncertainties below 10^{-4}) owing to the much larger ion mass ($m_{ion} \gg m_e$). Accordingly, the distribution function $f(\vec{v})$ is completely dominated by the electron velocity distribution. From Eq. (2.1) $f(\vec{v})$ follows (in a.u.) as

$$f(\vec{v}) = f_{MB}(\vec{v}, v_{rel}) = \frac{1}{2\pi k T_{\perp}} e^{-v_{\perp}^2/(2kT_{\perp})} \sqrt{\frac{1}{2\pi k T_{\parallel}}} e^{-(v_{\parallel} - v_{rel})^2/(2kT_{\parallel})}, \quad (2.12)$$

where v_{rel} is the detuning velocity between the merged ion and electron beams which defines the relative energy, *i.e.* $E_e = v_{rel}^2/2 = E_{rel}$. Note that all velocities refer to the rest frame of the ion. In order to compare experimental results with theoretical ones, both temperatures T_{\perp} and T_{\parallel} are extracted from the analysis of experimental resonance line shapes of dielectronic recombination [33].

In order to apply the standard RR theory within the framework of this thesis the parameterization of [31] for $G_n(E_e)$ has been used. In this form the Gaunt factors read

$$\begin{aligned} G_n(E_e) &= G(n, \eta) = a_0(\eta) + \frac{a_1(\eta)}{n} + \frac{a_2(\eta)}{n^2} \\ a_0(\eta) &= \frac{14.6}{14.7 + \eta^{-1.29}} + \frac{0.0958}{(0.434y + 0.244)^2 + 0.449} \\ a_1(\eta) &= \frac{-0.270}{1 + \eta^{-0.869}} - \frac{0.571}{(0.810 - 0.434y)^2 + 0.200} \\ &\quad + \frac{0.0616}{(0.434y + 0.0476)^2 + 0.400} \\ a_2(\eta) &= \frac{0.307}{3.833 + \eta^{-1.015}} - \frac{0.0311 - 0.0274y}{(0.425 - 0.434y)^4 + 0.151} \\ y &= \ln \eta = \ln \frac{Z}{k_e} = \ln \frac{Z}{\sqrt{2E_e}}. \end{aligned} \quad (2.13)$$

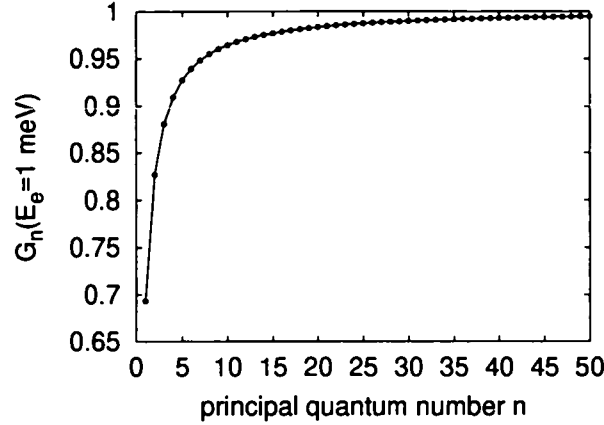


Figure 2.4: Gaunt factors as a function of the principal quantum number n shown for a fixed relative energy of $E_e = 1$ meV. The energy dependence of G_n is very weak at the low energies in the experiments.

Figure 2.4 illustrates the Gaunt factors at an energy of $E_e = 1$ meV for principal quantum numbers up to $n = 50$. The Gaunt factors deviate significantly from one only for the lowest values of n , where the semiclassical approximation of Bethe and Salpeter (Eq. (2.7)) becomes insufficient. Moreover, they depend only weakly on E_e . In fact, for the small collision energies of the recombination experiments the energy dependence of G_n could be approximately neglected.

Finally, Figure 2.5 presents recombination rates evaluated according to the standard RR theory of Eqs. (2.11) and (2.12) for different relative energies E_{rel} between electron and ion beam. If Gaunt factors are not included into the RR cross section the rate coefficients would be somewhat overestimated.

Note that this standard theory does not take into account the magnetic field present in the electron cooler of the experiment properly. Magnetic field effects are considered only indirectly by choosing the anisotropic “thermal” distribution of Eq. (2.12) since the magnetic field restricts the motion of the electrons in transverse direction and hence tends to suppress the relaxation of energy between longitudinal and transverse degrees of freedom through Coulomb interactions. However, the recombination cross sections used to evaluate Eq. (2.11) are extracted from the pure Coulomb problem irrespective of the magnetic field.

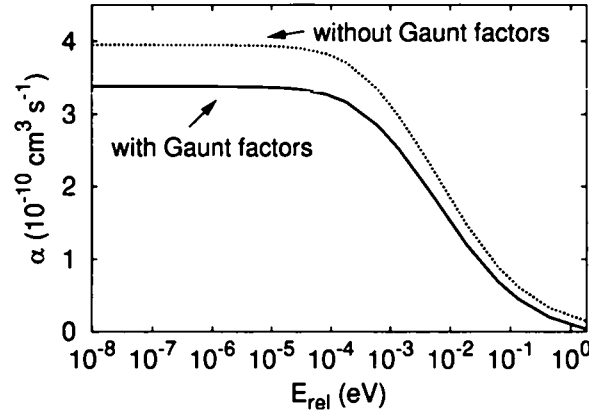


Figure 2.5: Standard radiative recombination theory: rate coefficients are plotted for different relative energies between electrons and ions. Gaunt factors are included into the RR cross section for the solid line, whereas being omitted for the dotted line. Parameters are taken from the TSR experiment [10], where $kT_{\parallel} = 0.2$ meV, $kT_{\perp} = 10$ meV, $Z = 6$ and $n_r = 30$.

2.3 Other Recombination Mechanisms

Free electrons can be captured by ions via several different recombination mechanisms. Radiative recombination (RR) (Eq. (2.5)) is the direct capture of a free electron by an ion A^{q+} where the excess energy and momentum are carried away by the emitted photon. After the capture the electron can be in an excited state and further radiative transitions within the ion will take place until the electron has reached the lowest accessible energy level. RR is a non-resonant process which is possible for any relative energy between electron and ion thus resulting in a continuous contribution of the recombination rate in terms of relative energy. The RR cross section diverges at zero relative energy and continuously decreases towards higher energies (see Figure 2.3).

The electron can also be captured resonantly (inverse Auger process)

$$e^{-} + A^{q+} \rightarrow [A^{(q-1)+}]^{**}, \quad (2.14)$$

where the excess energy is used to excite a core electron within the ion. This so-called dielectronic capture is only possible if the kinetic energy of the projectile electron matches the difference $E_i - E_f$ of the total binding energies of all electrons in the initial and final states of the ion and the ion carries at least one additional electron into the collision. After this capture the ion is in a multiply excited state which can decay in different ways. If the ion stabilizes itself by the emission of photons, such

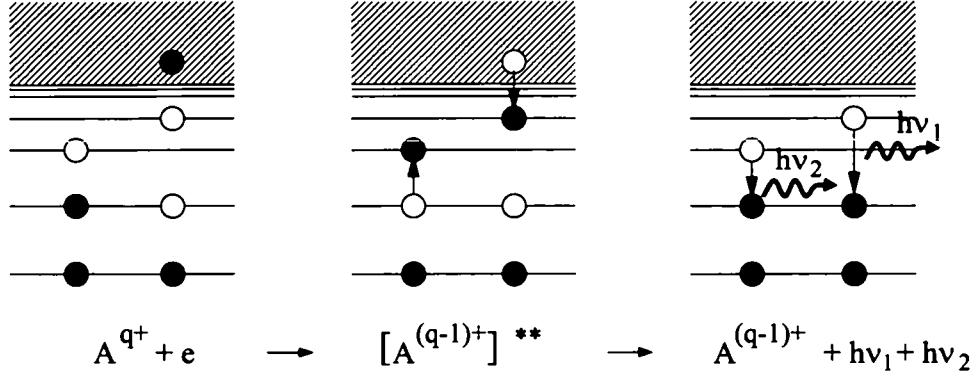


Figure 2.6: Schematic picture of dielectronic recombination (DR): a free electron is captured resonantly accompanied by the excitation of a bound electron in the ion, followed by radiative stabilization through emission of photons.

as

$$[A^{(q-1)+}]^{**} \rightarrow [A^{(q-1)+}]^* + h\nu_1 \rightarrow A^{(q-1)+} + h\nu_1 + h\nu_2, \quad (2.15)$$

while keeping its reduced charge state, the process (Eqs. (2.14) and (2.15)) is called dielectronic recombination (DR). A schematic picture of this two-step process can be found in Figure 2.6. Usually, electron emission

$$[A^{(q-1)+}]^{**} \rightarrow A^{q+} + e^- \quad (2.16)$$

of the intermediate electron-ion complex is much more likely than photoemission. This autoionization process, which is the inverse of dielectronic capture, reduces the ion to its original charge state. Therefore it does not contribute to the measured recombination rate. Experimentally, the process described by Eqs. (2.14) and (2.16) would be observed as resonant elastic or inelastic scattering of the electron on the ion.

Dielectronic capture and thus dielectronic recombination can only occur for non-bare ions. Note that the cross sections for the resonant DR processes exceed those of RR by several orders of magnitude. However, since the discrepancy between theory and experiment found at $E_{rel} \lesssim 1$ meV persists also for bare ions, where contributions from DR can be ruled out, the observed enhancement cannot be explained by the appearance of DR resonances at low relative energies. In order to aim solely at this remaining enhancement and to exclude contributions from DR only bare ions will be investigated throughout this thesis.

Another possible recombination mechanism is three-body recombination (TBR)

$$A^{q+} + e^- + e^- \rightarrow A^{(q-1)+} + e^-, \quad (2.17)$$

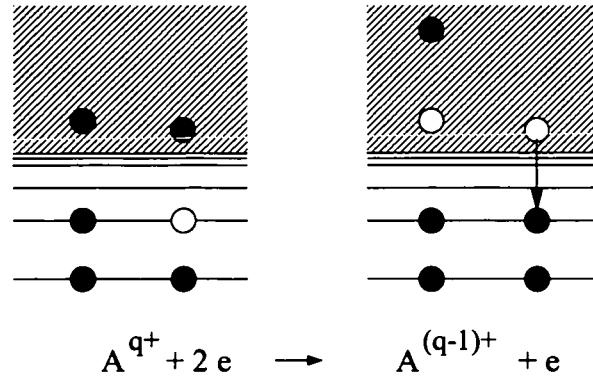


Figure 2.7: Schematic picture of three-body recombination (TBR): a free electron is captured into a bound state of an ion. The excess energy and momentum are imparted to a neighboring free electron.

where the excess energy and momentum are transferred to another free electron of the gas. This is the inverse process of electron collisional ionization. It is important at high electron densities and low collision energies, since the probability for two electrons to be close to the same ion must be high enough and the $e - e$ scattering cross section must be sufficient in magnitude. An illustrative picture of TBR is shown in Figure 2.7. Explaining the measured enhancement by contributions from TBR faces the difficulty that the electron density n_e is quite low ($n_e \approx 10^7 \text{ cm}^{-3}$) in the experiments and the observed recombination rates have been shown to be insensitive to a variation of n_e by a factor of 5 [10]. Since the probability for TBR should scale as n_e^2 , considerable effects from TBR can be excluded likewise.

Therefore, for bare ions radiative recombination remains as the only dominant recombination mechanism prevailing at the experimental storage ring conditions.

2.4 Review of Experimental Results

The observation of anomalously enhanced electron-ion recombination rates compared to the predictions of standard two-body radiative recombination theory (section 2.2 and Refs. [5, 6, 7]) has been a major surprise. Below a brief overview of various experiments performed at different facilities will be given.

Recombination rate enhancement was first observed in 1989 in an experiment with U^{28+} ions at the GSI in Darmstadt [34]. The uranium ions passing a cold dense electron target at the UNILAC accelerator of the GSI revealed a recombination rate at zero relative energy between electrons and ions which was about a factor of 200 higher than the theoretically calculated value. This enormous discrepancy between

experiment and theory stimulated continuous efforts in the investigation of RR of bare ions as well as of multicharged ions.

The pioneering experiment on radiative recombination of bare ions was performed by Andersen *et al.* [35] (see also [30]) in 1990. Absolute rate coefficients were measured for C^{6+} ions in a merged beam single pass experiment at Aarhus finding a reasonably good agreement between experiment and theory in the investigated relative energy range from $E_{rel} = 0$ to 1 eV. In fact, the measured rate coefficients at seemingly zero relative energy were even slightly below the theoretical predictions. In a number of consecutive measurements different bare ions (such as D^+ , He^{2+} , N^{7+} , Ne^{10+} and Si^{14} at the CRYRING [8, 9, 36], C^{6+} and Cl^{17+} at the TSR [10, 37] and Ar^{18+} at the UNILAC of the GSI [22]) have been investigated at several facilities. All measured rate coefficients have been in agreement with RR theory for relative energies $E_{rel} \geq 0.01$ eV. Nevertheless, in contrast to Andersen's observation, in these measurements strong deviations of the experimental findings from the theoretical predictions have been found at very low electron-ion relative energies ($E_{rel} \leq 0.01$ eV): towards lower energies the measured rate coefficient α typically shows an enhancement of $\Delta\alpha = \alpha - \alpha_{RR}$ on top of the theoretical rate coefficient α_{RR} for RR. The resulting rate enhancement factor $\epsilon = \alpha/\alpha_{RR}$ at $E_{rel} = 0$ increases from 1.6 (He^{2+}) to 10 (Ar^{18+}) for the explored bare ions. More recent measurements at the ESR focus on the recombination of very highly charged bare ions such as Bi^{83+} [11] and U^{92+} [12]. Note that although the RR cross section diverges at $E_{rel} = 0$, the measured rate coefficient attains a finite value at zero average relative energy due to the experimental electron and ion velocity spreads.

Moreover, since the first observation of the enhancement phenomenon in U^{28+} [34], also a series of measurements with non-bare ions (such as Au^{25+} at the UNILAC of the GSI [21], $Au^{49+,50+,51+}$ at the TSR [38] and $Pb^{52+,53+,54+}$ in the Low Energy Antiproton Ring (LEAR) at CERN [39]) have been performed. In such complex multielectron ions much higher enhancement factors can be observed. For example, for Au^{25+} ions it results in a value as high as 365 at zero relative energy. Thereby the electronic structure of the ion (for example, for Au^{50+} and Pb^{53+}) has a great influence on the magnitude of the enhancement. Whereas these very high rate enhancement factors of such complex ions could be partly traced back to the presence of additional recombination channels, *i.e.* mainly due to dielectronic recombination [40], the origin of the remaining discrepancies between experiment and theory for bare ions, where DR cannot occur, is still unknown.

For the further exploration and clarification of the enhancement phenomenon, its dependences on external experimental parameters such as the electron density n_e , the electron beam temperatures T_{\perp} and T_{\parallel} , the ion charge Z and the magnetic guiding field B have been investigated at the different storage ring and merged beam facilities. Variations of the electron density within a total range of 10^6 cm^{-3} up to about 10^9 cm^{-3} [10, 11, 21, 36] have not shown any considerable effect on the en-

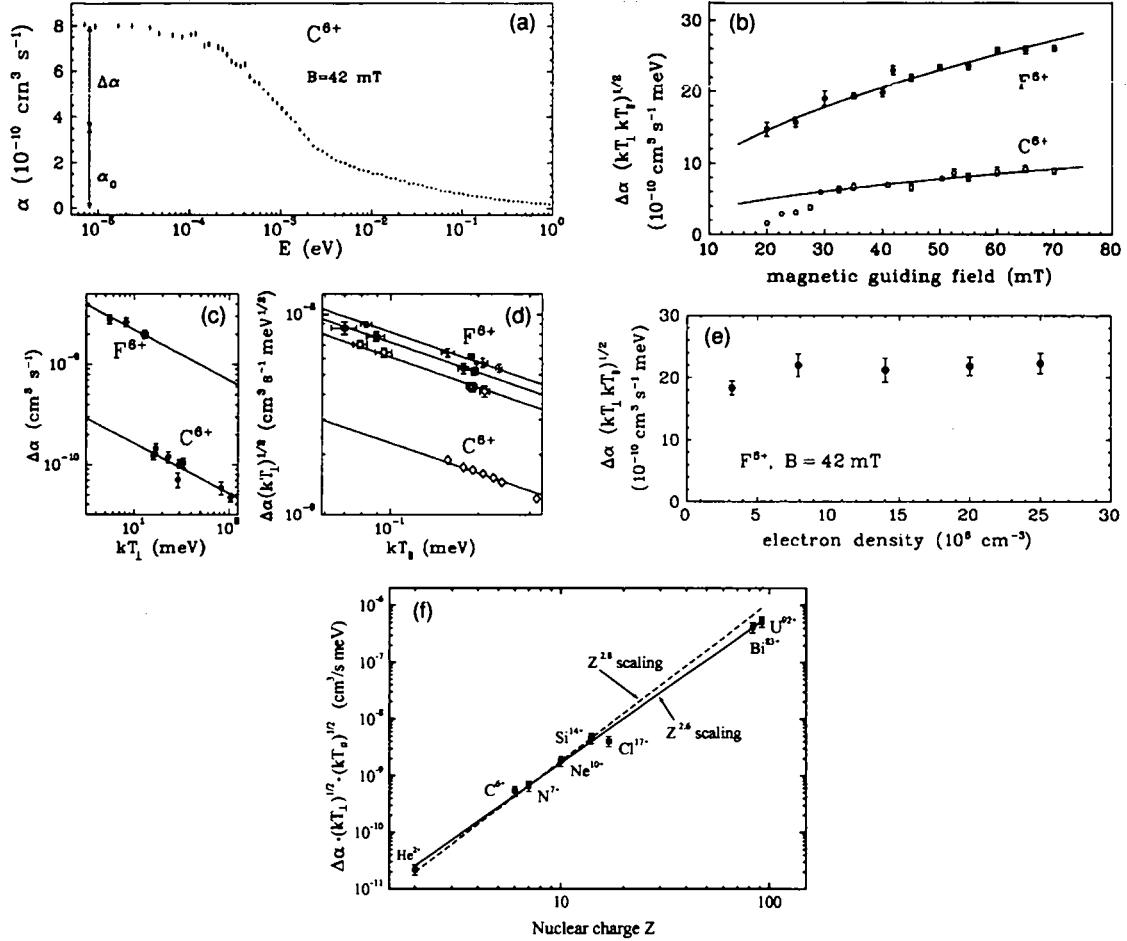


Figure 2.8: Experimental results of the RR rate enhancement. The recombination rate α versus the relative energy between electrons and ions (a) and the excess rate coefficients $\Delta\alpha = \alpha - \alpha_{RR}$ at $E_{rel} = 0$ as a function of the magnetic field (b), the transverse temperature (c), the longitudinal temperature (d), the electron density (e) and the ion charge (f) are illustrated. Note that the rates in (b), (e) and (f) are scaled with $\sqrt{kT_\perp kT_\parallel}$ according to the observed temperature dependence. The data (a)-(e) is taken from the TSR experiment [10], whereas the measurements of the nuclear charge dependence of the excess recombination for fully stripped ions (f) originate from different storage ring experiments, *i.e.* the CRYRING facility for He²⁺, N⁷⁺, Ne¹⁰⁺ and Si¹⁴⁺ [9], the TSR for C⁶⁺ [10] and Cl¹⁷⁺ [37] and the ESR for Bi⁸³⁺ [11] and U⁹²⁺ [12].

hancement. Furthermore, the excess recombination rate $\Delta\alpha$ has been observed to scale with the transverse electron temperature as $T_{\perp}^{-1/2}$, as expected for the standard rate coefficient α_{RR} alone as well, and, surprisingly, also with the longitudinal electron temperature as $T_{\parallel}^{-1/2}$ [10]. A systematic study of the ion charge-state dependence of the excess rate coefficients for bare ions has yielded approximately a $Z^{2.8}$ behavior [9] for smaller charges $1 \leq Z \leq 14$ and, later on, a similar $Z^{2.6}$ dependence [12] for all the ions investigated up to $Z = 92$. In addition, also the magnetic guiding field B in the interaction region influences the experimental enhancement: the excess rates at $E_{rel} = 0$ increase with B according to an approximate B^x scaling with $0.5 \leq x \leq 1$ [10, 21, 41]. In particular, the recent systematic measurements at the TSR [10] have shown a $B^{0.5}$ dependence.

Figure 2.8 shows a sample of experimental results thus displaying the dependence of the poorly understood rate enhancement phenomenon on the different experimental parameters. To summarize, the measured excess recombination rates $\Delta\alpha$ have been found to scale as $(kT_{\perp})^{-1/2}$, $(kT_{\parallel})^{-1/2}$, $Z^{2.6}$, increase with B and are insensitive to n_e .

2.5 Alternative Theoretical Proposals

Several theoretical proposals have been put forward to explain the anomalously enhanced electron-ion recombination rates. They range from the influence of three-body recombination [9] and density enhancement due to plasma screening effects [42, 43, 44] to transient electric field-induced recombination [13, 45]. We note that the density independence of the experimental rates renders an explanation in terms of three-body effects unlikely. In [42] molecular dynamics simulations on the electron density enhancement near an ion in a magnetized electron plasma have been performed and a self-consistent screening model [43] in terms of extended pseudo-electrons accounting for the effect of a magnetic field has been developed. The latter approach, however, includes an adjustable effective temperature T_{eff} ($T_{\parallel} \leq T_{eff} \leq T_{\perp}$) drastically influencing the overall size of the calculated rate enhancement. A similar ansatz for the magnetic field with the electron smeared over a Landau disk with radius r_c (r_c : cyclotron radius) has also been employed in [46]. Moreover, in [44] a lowering of the ionization threshold at low temperatures for the nonlinear electron density enhancement has been discussed.

The proposal of field-induced recombination during the electron-ion beam merging followed by radiative stabilization inside the solenoid has first been made by Gwinner *et al.* [45]. A quantitative analysis of the associated recombination rates, which has been outstanding so far, will be presented in chapter 4 of this thesis. Finally, we point out that also in the approach by Heerlein *et al.* [13] the enhancement has been traced to the process of beam merging. In their letter [13] they

report rate coefficients in good agreement with the experimental data. However, in this model recombination turns out to be induced by an instantaneous switch-on of the electron-ion interaction without considering the electric field distribution in the merging region, the kinematics of merging or the properties of the radiative stabilization process. A more detailed discussion of these deficiencies is raised in chapter 5.

In summary, none of these models can, so far, account satisfactorily and consistently for the observed enhancement.

Chapter 3

Classical Chaotic Dynamics in a Magnetic Field

To understand the fundamental mechanism of the underlying recombination process in the presence of a magnetic field we explore in this chapter the scattering dynamics between an electron and an ion inside the solenoidal interaction region of the electron cooler. For the regime of magnetic field strengths available in the experiment, the electron can be found, as will be discussed in detail in section 3.1, on the average, in initial states with high Landau quantum numbers for which a classical description should be valid. The classical description has the advantage that the electron dynamics can easily be treated non-perturbatively, while a quantum mechanical treatment would necessitate a perturbative approach, since a full non-perturbative solution of the electronic wavefunction for an incident scattering state in the simultaneous presence of Coulomb and magnetic fields is not known.

In the magnetic guiding field of the cooler the classical motion of an electron becomes chaotic in the Coulomb field of the target ion. The analysis of individual trajectories and selected phase space portraits shows that the magnetic field dramatically changes the phase space structure of the system compared to the pure Coulomb field: the smooth deflection function (*i.e.* the deflection of the particle induced by the scattering) for an electron in the Coulomb potential of the ion gets highly irregular in the presence of a magnetic field. This generalized deflection function, specifically the visit function to be discussed, modifies the net flux of electrons towards the immediate vicinity of the ion. However, the value of such a visit function, *i.e.* the number of close encounters of an electron to the target ion, is not unique. Electronic visits to the ion depend on the representation in coordinate or momentum space as a result of the gauge freedom available for the description of a magnetic field.

The influence of the magnetic field on the radiative recombination cross section will be considered by incorporating the effect of the chaotic dynamics into the eval-

uation of the recombination rates. We thus discuss an appropriate representation of quantum mechanical rate coefficients by means of our CTMC calculations. While exploring the effect of the chaotic scattering dynamics on the recombination process in this chapter, the influence of the bound-state motion will be addressed in chapter 4. Correspondingly, radiative recombination of low-energy continuum electrons is studied throughout this chapter, whereas radiative stabilization of highly excited bound states will be treated in the next chapter.

After a brief examination of the electronic and ionic motion in the laboratory frame we treat the system exclusively in the rest frame of the ion. The chaotic scattering dynamics is visualized by individual trajectories of electrons and Poincaré surfaces of section. Moreover classical scaling relations of the Hamiltonian are discussed. Based on the significant role of chaotic dynamics we develop a modification of the standard RR theory by means of the visit function V . The behavior of V in the Coulomb and magnetic field as well as in the pure Coulomb field is investigated and illustrated for different subspaces of phase space. The ambiguity of calculating V in the magnetic field is discussed. Finally, we evaluate recombination rates within this modified theory and study their dependencies on the different experimentally accessible parameters such as the average relative energy between electrons and ions E_{rel} , the magnetic field strength B , the ion charge Z and the longitudinal and transverse electron beam temperatures kT_{\parallel} and kT_{\perp} .

3.1 Influence of a Magnetic Field

The standard RR theory as described in section 2.2 does not take into account the magnetic field prevailing in the experiments (beyond the obvious corrections due to the anisotropic velocity distribution Eq. (2.12)). Therefore, in the following this standard theory is re-analyzed for effects due to the presence of the magnetic field. Under the influence of a magnetic field the wavefunctions used to evaluate the recombination cross section σ_{RR} (Eq. (2.6)) need to be modified.

Starting point of our analysis are the different length scales present in the system (Figure 3.1). The recombination process is governed by two vastly different length scales: the characteristic distances $r \leq r^{RR}$ from which contributions to the RR matrix element (Eq. (2.6)) originate and the classical cyclotron radius $r_c = v_{\perp}/\omega_c = v_{\perp}c/B$ which delimits the lateral confinement of the incident electronic wavefunction in the asymptotic regime. For typical field strengths ($B \approx 30$ mT) and transverse beam energies ($T_{\perp} \approx 10$ meV) in the cooler the cyclotron radius amounts to an order of magnitude of $r_c \approx 10^5$ a.u. By comparison, the final state of the recombined electron is localized around the ion with a radius $r^{RR} \approx n_r^2/Z$ of the order of 10 - 100 a.u. Higher n states are quenched by motional electric fields in the demerging toroid, the subsequent correction dipoles and the charge analyzing bending magnet

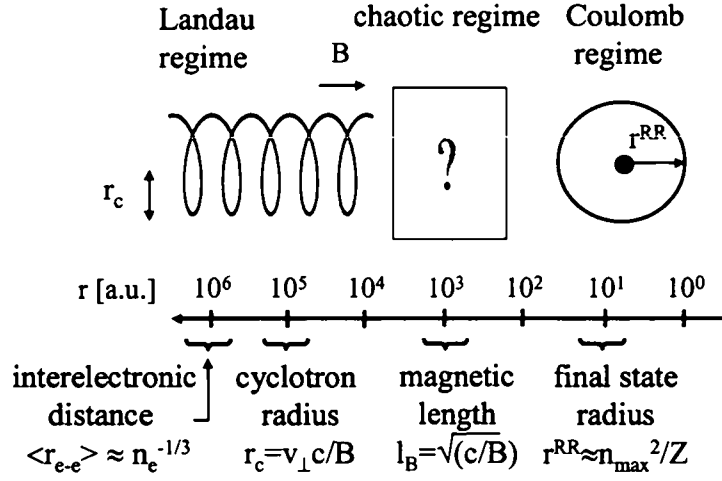


Figure 3.1: Characteristic scales pertaining to a recombination experiment in the electron cooler of a storage ring. In the Landau and Coulomb regimes the corresponding classical motion is regular, whereas in the intermediate region it is chaotic.

prior to detection. For example, for initially bare C^{6+} ions the principal quantum numbers for recombined electrons are limited to $n_r \approx 30$. Thus, generally $r^{RR} \ll r_c$.

In the asymptotic region of large distances to the ion the magnetic interaction dominates and the electron moves on Landau orbits. The typical cyclotron radius itself is large compared to the magnetic length $l_B = \omega_c^{-1/2} = \sqrt{c/B} \approx 10^3$ a.u.. Note that l_B is given by the radius of the quantized circular orbit of the electron in the magnetic field B (without a Coulomb potential present). This implies that the electron is, on the average, in high Landau states with Landau quantum numbers $N \approx (r_c/l_B)^2 \gg 1$.

On the other hand, near r^{RR} the Coulomb field dominates and the influence of the magnetic field is entirely negligible. Therefore, the final states strongly localized around the ion $\langle \vec{r} | u_n \rangle$ entering the cross section (Eqs. (2.6) - (2.10)) are well approximated using the unperturbed hydrogenic bound states. Only the initial wavefunction for the Coulomb continuum state $\langle \vec{r} | u_k \rangle$ needs to be modified, *i.e.* replaced by a new wavefunction $\langle \vec{r} | u_k^B \rangle$ taking into account the simultaneous presence of a Coulomb and a magnetic field. With the knowledge of such a wavefunction $\langle \vec{r} | u_k^B \rangle$ a direct evaluation of the cross section for RR (Eq. (2.6)) in a magnetic field would be possible. Unfortunately, no full non-perturbative solution of the wavefunction for an incident scattering state $\langle \vec{r} | u_k^B \rangle$ in the combined Coulomb and magnetic fields is available. Perturbative approaches turn out to be difficult if not even impossible because of the large difference in length scales of r_c and r^{RR} . A perturbative expansion

of the wavefunction $\langle \vec{r} | u_k^B \rangle$ using either Coulomb waves or Landau states requires a huge number of basis set in order to represent the wavefunction $\langle \vec{r} | u_k^B \rangle$ accurately both in the asymptotic region and near the target ion. A perturbative evaluation of Eq. (2.6) by employing Landau states as initial states rather than Coulomb continuum states has failed to give any significant modification of the recombination rates due to the fact that r_c/l_B is very large compared to one [46].

In between these two regimes of r^{RR} and r_c , however, there exists a region where the Lorentz force and the Coulomb force are of comparable strengths. Contrary to the integrable motions of the electron on cyclotron orbits in the asymptotic region and on Kepler orbits near the target ion the dynamics in this intermediate region is classically chaotic. The associated electron motion becomes thus very complicated as will be later visualized by individual trajectories. Whereas in the asymptotic region of dominant magnetic field the electron ensemble can be described by the anisotropic velocity distribution of Eq. (2.12), the electronic flux changes towards the ion due to the underlying chaotic dynamics. Accordingly, the presence of the B field is expected to lead to a profound alteration of the phase space density of electrons available for recombination. Thus, the mapping of the asymptotic electron flux defined in the Landau regime down to the Coulomb zone $r \leq r^{RR}$ will be the key point of this chapter.

The strategy of modifying the recombination theory in the presence of a magnetic field becomes therefore obvious: while the transition matrix element for radiative recombination pertaining to the Coulomb zone remains unchanged, it is the effective flux of electrons entering from the Landau region into the Coulomb zone that will be modified within the present framework. To obtain this change in electron flux we employ a classical trajectory Monte Carlo (CTMC) method whose justification relies on the fact that the typically populated Landau quantum numbers are very large, *i.e.* $N \approx 10^4$. For such high Landau states a classical description should be valid.

In order to determine the electron density $|\langle \vec{r} | u_k^B \rangle|^2$ near the ion under the influence of a magnetic field the electron distribution is treated as an ensemble of classical trajectories with randomly generated initial conditions which mimic the Maxwell-Boltzmann distribution (Eq. (2.12)) in the asymptotic region. The biggest advantage of using classical trajectories is that they can be treated non-perturbatively and, thus, the modification of the electronic flux can be properly described. By means of the CTMC an entire beam of electrons is simulated from the asymptotic region down to distances close to the target ion in the presence of the magnetic field. These simulations will provide, on a classical level, the mapping of the asymptotic distribution Eq. (2.12) onto the Coulomb orbits near the nucleus. Assuming that a modification of the recombination rate is due to the enhanced transport of flux into the Coulomb dominated region the excess recombination $\Delta\alpha$ relative to the standard rate α_{RR} could be extracted from the simulation.

Finally we point out that the electron densities available in the experiments are rather low (typically $n_e \approx 10^6 - 10^7 \text{ cm}^{-3}$) resulting in interelectronic distances $r_{e-e} \approx n_e^{-1/3}$ of the order of 10^6 a.u. For such large distances, *i.e.* $r_{e-e} \gg r^{RR}$ and even $r_{e-e} > r_c$, three body recombination is expected to play a minor role in agreement with the density independence observed in the measurements (Figure 3.1).

In the subsequent sections the influence of the classical chaotic dynamics on the recombination rates will be studied.

3.2 Electron-Ion Motion: Lab, Center of Mass, and Ionic Rest Frames

First the general two-body problem of the motion of an electron and an ion (charge Z , mass m_{ion}) in the presence of a homogeneous magnetic field $\vec{B} = B\hat{e}_z$ will be investigated. Later on, the electron will be treated in the rest frame of the ion. The electron-ion dynamics through the solenoid region of the electron cooler is governed in the laboratory frame by the two-particle Hamiltonian

$$H^{e-ion} = \frac{1}{2m_{ion}} \left(\vec{p}_{ion} - \frac{Z}{c} \vec{A}(\vec{r}_{ion}) \right)^2 + \frac{1}{2} \left(\vec{p}_e + \frac{1}{c} \vec{A}(\vec{r}_e) \right)^2 - \frac{Z}{|\vec{r}_e - \vec{r}_{ion}|}, \quad (3.1)$$

where $\vec{p}_e = (p_{ex}, p_{ey}, p_{ez})$, $\vec{r}_e = (x_e, y_e, z_e)$, $\vec{p}_{ion} = (p_{ionx}, p_{iony}, p_{ionz})$ and $\vec{r}_{ion} = (x_{ion}, y_{ion}, z_{ion})$ denote the canonical momenta and coordinates of the electron and ion, respectively. We express the vector potential in the symmetric gauge, $\vec{A} = 1/2 (\vec{B} \times \vec{r}) = 1/2 (-By, Bx, 0)$. Employing $\nabla \vec{A} = 0$ and $\vec{p} (\vec{B} \times \vec{r}) = \vec{B} (\vec{r} \times \vec{p}) = BL_z = B(xp_y - yp_x)$ the Hamiltonian is written as

$$\begin{aligned} H^{e-ion} = & \frac{1}{2m_{ion}} \vec{p}_{ion}^2 + \frac{Z^2}{8m_{ion}c^2} B^2 (x_{ion}^2 + y_{ion}^2) - \frac{Z}{2m_{ion}c} B (x_{ion}p_{iony} - y_{ion}p_{ionx}) \\ & + \frac{1}{2} \vec{p}_e^2 + \frac{1}{8c^2} B^2 (x_e^2 + y_e^2) + \frac{1}{2c} B (x_ep_{ey} - y_ep_{ex}) - \frac{Z}{|\vec{r}_e - \vec{r}_{ion}|}. \end{aligned} \quad (3.2)$$

Since it is the relative motion between an individual electron-ion pair which eventually decides whether recombination can occur (the cross section depends on the relative energy as illustrated in Figure 2.3), it is advantageous to treat the two-body system Eq. (3.2) in center of mass (CM) variables

$$\vec{R}_{CM} = \frac{1}{M} \vec{r}_e + \frac{m_{ion}}{M} \vec{r}_{ion} \quad \vec{P}_{CM} = \vec{p}_e + \vec{p}_{ion} \quad (3.3)$$

and internal variables

$$\vec{R} = \vec{r}_e - \vec{r}_{ion} \quad \vec{P} = \frac{m_{ion}}{M} \vec{p}_e - \frac{1}{M} \vec{p}_{ion} \quad (3.4)$$

with the total mass given by $M = 1 + m_{ion}$. These transformations can be obtained from the generating function F_2

$$\begin{aligned} F_2(\vec{r}_e, \vec{r}_{ion}, \vec{P}_{CM}, \vec{P}) &= \vec{P}_{CM} \cdot \vec{R}_{CM}(\vec{r}_e, \vec{r}_{ion}) + \vec{P} \cdot \vec{R}(\vec{r}_e, \vec{r}_{ion}) \\ &= \vec{P}_{CM} \left(\frac{1}{M} \vec{r}_e + \frac{m_{ion}}{M} \vec{r}_{ion} \right) + \vec{P} (\vec{r}_e - \vec{r}_{ion}). \end{aligned} \quad (3.5)$$

For a more detailed description of canonical transformations and the associated generating functions see appendix A or Ref. [47]. To derive the Hamiltonian in CM and internal degrees of freedom we insert the inverted equations

$$\vec{r}_e = \vec{R}_{CM} + \frac{m_{ion}}{M} \vec{R} \quad \vec{p}_e = \frac{1}{M} \vec{P}_{CM} + \vec{P} \quad (3.6)$$

and

$$\vec{r}_{ion} = \vec{R}_{CM} - \frac{1}{M} \vec{R} \quad \vec{p}_{ion} = \frac{m_{ion}}{M} \vec{P}_{CM} - \vec{P} \quad (3.7)$$

into the Hamiltonian Eq. (3.2) and obtain

$$H^{e-ion} = H_{CM}^{e-ion} + H_{rel}^{e-ion} \quad (3.8)$$

$$H_{CM}^{e-ion} = \frac{1}{2M} \left(\vec{P}_{CM} - \frac{Z-1}{2c} (\vec{B} \times \vec{R}_{CM}) + \frac{m_{ion}+Z}{2Mc} (\vec{B} \times \vec{R}) \right)^2 \quad (3.9)$$

$$H_{rel}^{e-ion} = \frac{1}{2\mu} \left(\vec{P} - \frac{-m_{ion}^2+Z}{2M^2c} (\vec{B} \times \vec{R}) + \frac{m_{ion}+Z}{2Mc} (\vec{B} \times \vec{R}_{CM}) \right)^2 - \frac{Z}{|\vec{R}|}. \quad (3.10)$$

$\mu = m_{ion}/(1+m_{ion})$ represents the reduced mass. Thus, in the presence of a magnetic field the CM and internal motions are no longer separable, but they are coupled. The coupling appears in both the CM and internal degrees of freedom: the CM kinetic energy Eq. (3.9) contains the internal coordinates \vec{R} as well as the relative kinetic energy in Eq. (3.10) depends on the coordinates \vec{R}_{CM} of the CM. Referring to the electric dipole moment of the electron and ion with respect to the CM

$$\vec{d} = (-1)(\vec{r}_e - \vec{R}_{CM}) + Z(\vec{r}_{ion} - \vec{R}_{CM}) = -\frac{m_{ion}+Z}{M} \vec{R} \quad (3.11)$$

the coupling in Eq. (3.9) may be regarded as a dipole contribution. $Z-1$ denotes the total charge of the electron-ion system. As required, in the field free case $\vec{B} = 0$ the coupling between the CM and internal variables vanishes and the motions become separable.

Note that the coupling in Eqs. (3.9) and (3.10) is the same, *i.e.* the coefficients of \vec{R} in Eq. (3.9) and of \vec{R}_{CM} in Eq. (3.10) are identical. Taking advantage of this

fact the coupling between the CM and internal variables can be minimized [48, 49] (Power-Zienau-Woolley (PZW) transformation). The classical analog of the PZW transformation is a point transformation $(\vec{r}_e, \vec{r}_{ion}, \vec{p}_e, \vec{p}_{ion}) \rightarrow (\vec{R}, \vec{R}_{CM}, \vec{P}, \vec{P}_{CM})$ which uses the gauge freedom to specify new CM and internal momenta \vec{P}_{CM} and \vec{P} , while retaining the standard CM and relative coordinates of Eqs. (3.3) and (3.4). For this purpose the F_2 generating function (Eq. (3.5)) is modified to

$$F_2 = \vec{P}_{CM} \cdot \vec{R}_{CM}(\vec{r}_e, \vec{r}_{ion}) + \vec{P} \cdot \vec{R}(\vec{r}_e, \vec{r}_{ion}) - \frac{m_{ion} + Z}{2Mc} \vec{R}(\vec{r}_e, \vec{r}_{ion}) \vec{B} \times \vec{R}_{CM}(\vec{r}_e, \vec{r}_{ion}). \quad (3.12)$$

This extended form for F_2 now provides more involved relations between \vec{p}_e and \vec{p}_{ion} and \vec{P}_{CM} and \vec{P} respectively given by

$$\vec{p}_e = \frac{1}{M} \vec{P}_{CM} + \vec{P} - \frac{m_{ion} + Z}{2Mc} \vec{B} \times \left(\vec{R}_{CM} - \frac{1}{M} \vec{R} \right) \quad (3.13)$$

$$\vec{p}_{ion} = \frac{m_{ion}}{M} \vec{P}_{CM} - \vec{P} + \frac{m_{ion} + Z}{2Mc} \vec{B} \times \left(\vec{R}_{CM} + \frac{m_{ion}}{M} \vec{R} \right) \quad (3.14)$$

and vice versa

$$\vec{P}_{CM} = \vec{p}_e + \vec{p}_{ion} - \frac{m_{ion} + Z}{2Mc} \vec{B} \times (\vec{r}_e - \vec{r}_{ion}) \quad (3.15)$$

$$\vec{P} = \frac{m_{ion}}{M} \vec{p}_e - \frac{1}{M} \vec{p}_{ion} + \frac{m_{ion} + Z}{2Mc} \vec{B} \times \left(\frac{1}{M} \vec{r}_e + \frac{m_{ion}}{M} \vec{r}_{ion} \right), \quad (3.16)$$

whereas the Hamiltonian in terms of these newly introduced CM and internal variables adopts the simpler form

$$H^{e-ion} = H_{CM}^{e-ion} + H_{rel}^{e-ion} \quad (3.17)$$

$$H_{CM}^{e-ion} = \frac{1}{2M} \left(\vec{P}_{CM} - \frac{Z-1}{2c} (\vec{B} \times \vec{R}_{CM}) + \frac{m_{ion} + Z}{Mc} (\vec{B} \times \vec{R}) \right)^2 \quad (3.18)$$

$$H_{rel}^{e-ion} = \frac{1}{2\mu} \left(\vec{P} - \frac{m_{ion}^2 + Z}{2M^2c} (\vec{B} \times \vec{R}) \right)^2 - \frac{Z}{|\vec{R}|}. \quad (3.19)$$

Here the only coupling between the CM and internal coordinates arises in the CM kinetic energy (Eq. (3.18)). In comparison to Eq. (3.9) this coupling has been doubled, while the coupling term in the relative kinetic energy (Eq. (3.19)) has been eliminated.

Thus, depending on the definition of the CM and internal momenta used, the electron-ion relative energy $E_{rel}^{e-ion} = 1/2 \mu \dot{\vec{R}}^2 - Z/|\vec{R}|$ is given either by Eq. (3.19) or (3.10), likewise the electron-ion center of mass energy $E_{CM}^{e-ion} = 1/2 M \dot{\vec{R}}_{CM}^2$ follows either from Eq. (3.18) or (3.9).

However, due to the heavy ion mass $m_{ion} \gg 1$ and thus $M \gg \mu$ the coupling between the CM and internal degrees of freedom is small as can be seen from a direct comparison of the $\vec{B} \times \vec{R}$ terms in Eqs. (3.18) and (3.19). As will be shown below, the CM and relative energies will be approximately conserved during the combined propagation of the electron and ion throughout the solenoid region.

As an example we study the motion of an electron and C^{6+} ion for the parameters available at the TSR experiment [10], where the region of straight overlap of electron and ion beam inside the solenoid is about 1.5 m and beam velocities of about $0.1c$ (c : velocity of light) are realizable. We choose the lab frame as the frame of reference for our simulation. The time evolution of the electron and the ion is described by the classical Hamilton's equations of motion derived from the Hamiltonian Eq. (3.2). Figure 3.2 shows sample trajectories for both electron and ion propagated in a magnetic field of $B = 42$ mT for a time duration of $\tau_c = 60$ ns. The electron performs a cyclotron motion with radius $r_c = 1.19 \times 10^5$ a.u. and frequency $\omega_c = B/c \simeq 1.79 \times 10^{-7}$ a.u. with the guiding center of the spiral shaped trajectory deflected somewhat from a straight line by the ionic Coulomb potential, whereas the ion moves along approximately a straight line throughout the solenoid and is hardly disturbed by the Coulomb and magnetic fields due to its much larger mass (Figure 3.2a). However, for only slightly different longitudinal (*i.e.* $\parallel B$) velocities the electron and ion can effectively interact through their Coulomb potentials: the electron, if trailing the ion, is accelerated towards the ion until reaching its maximum velocity during passage of the ion and is, thereupon, decelerated such that the ion can again catch up with the electron. Therefore, during the time evolution the electron is found to overtake the ion and vice versa in the direction parallel to B (Figure 3.2b). Nevertheless, the electron-ion relative energy E_{rel}^{e-ion} is only insignificantly influenced by this mutual Coulomb interaction in the magnetic field, exhibiting tiny oscillations with ω_c while retaining its overall magnitude within a small error bar (Figure 3.2c and 3.2d). The relative change of E_{rel}^{e-ion} with time, *i.e.* the quantity $(E_{rel}^{e-ion}(t) - E_{rel}^{e-ion}(t=0))/E_{rel}^{e-ion}(t=0)$, remains within an upper limit of 5×10^{-4} for the trajectories illustrated in Figure 3.2.

Using the CTMC method we investigate the electron-ion dynamics in the solenoid region for an entire ensemble of trajectories. The initial ensemble of electrons is distributed uniformly within a sphere with diameter $d = n_{ion}^{-1/3}$ in coordinate space (n_{ion} corresponds to a typical ion density available in the TSR experiment) and Maxwell-Boltzmann distributed (Eq. (2.12)) in velocity space with electron temperatures kT_{\perp} and kT_{\parallel} and an average detuning energy E_{rel} with respect to the ion motion. The ion is always located at the center of the electron ensemble. The electronic (*i.e.* on top of the thermal distribution) and ionic velocities are fixed to $0.1c$ along the direction of B in our lab frame simulation. We thus test the non-conservation of the electron-ion relative energy due to the breakdown of separability for the ensemble. In Figure 3.3 the change of E_{rel}^{e-ion} obtained at the end of the time propagation is explored, both

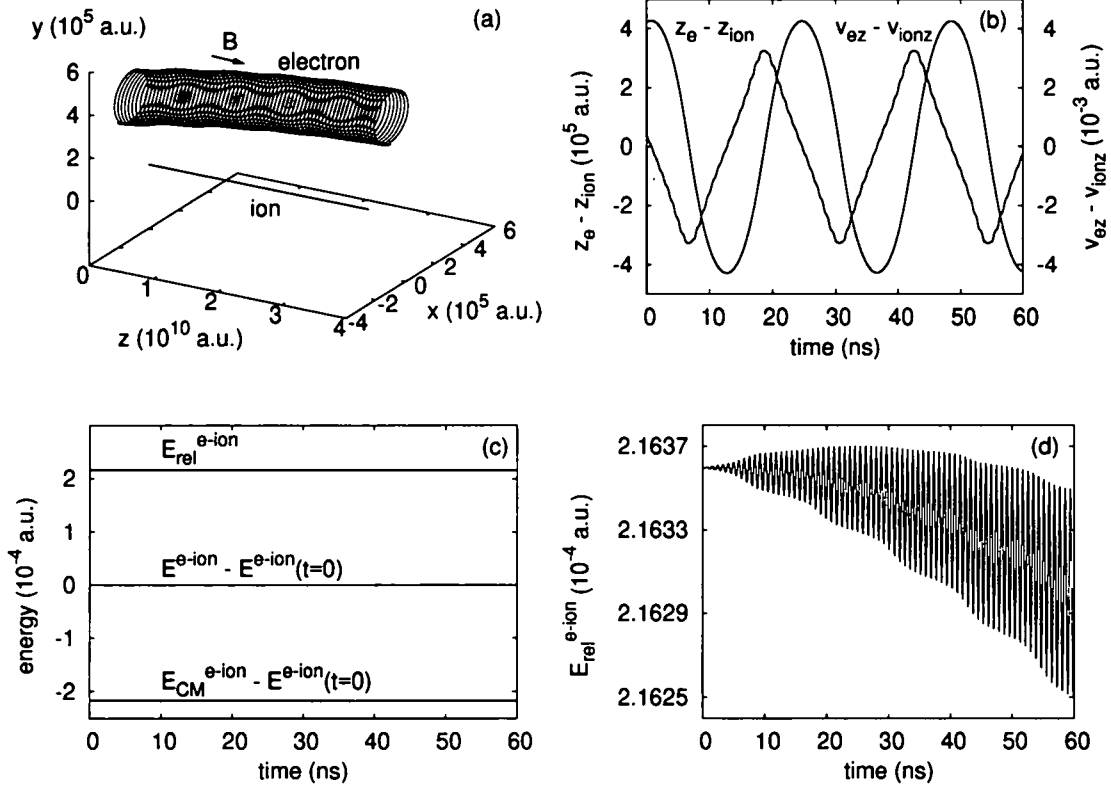


Figure 3.2: Simultaneous propagation of an electron and C^{6+} ion at $B = 42$ mT in the lab frame. Initial velocities are $v_{ionz} = 0.1c$ for the ion and $v_{ez} = 0.1c + 4.46 \times 10^{-4}$ a.u. and $v_{e\perp} = 2.13 \times 10^{-2}$ a.u. for the electron with an initial displacement of $R = 5.5 \times 10^5$ a.u. from the ion. Thus, initially $E_{rel}^{e-ion} \simeq 2.16 \times 10^{-4}$ a.u. The three-dimensional trajectories (a), the longitudinal relative coordinate and velocity components (b), the total, CM and relative energies (c) and the relative energy on a magnified scale (d) are shown. Note that in (c) E_{CM}^{e-ion} and E^{e-ion} are displayed only after subtraction of the initial total energy value $E^{e-ion}(t=0)$.

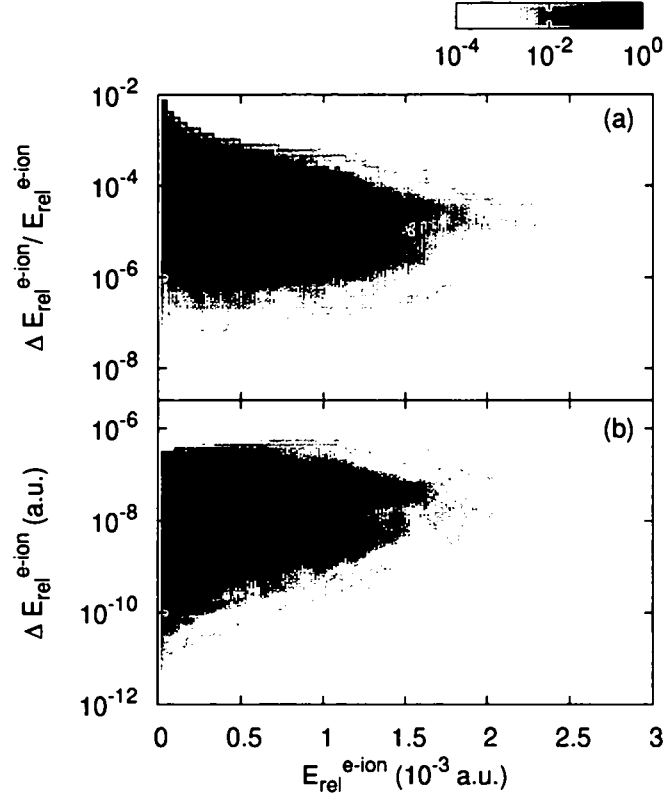


Figure 3.3: Analysis of the non-conservation of the electron-ion relative energy within the solenoid: a density plot of the relative (a) and the absolute (b) change of E_{rel}^{e-ion} at time $t = \tau_c$ relative to the initial value and the corresponding initial energies at $t = 0$ is drawn. $kT_{\perp} = 10$ meV, $kT_{\parallel} = 0.06$ meV, $E_{rel} = 0.03$ meV, $d = 1.765 \times 10^6$ a.u. and $B = 42$ mT are used. Electron and ion (C^{6+}) beam velocities are $0.1c$. Note that the density is plotted on a logarithmic scale and the peak height is normalized to 1.

the absolute change $\Delta E_{rel}^{e-ion}(t = \tau_c) = E_{rel}^{e-ion}(t = \tau_c) - E_{rel}^{e-ion}(t = 0)$ (Figure 3.3b) and the relative change of $\Delta E_{rel}^{e-ion}(t = \tau_c)/E_{rel}^{e-ion}(t = 0)$ (Figure 3.3a) with respect to the initial energy value at $t = 0$ are displayed on a logarithmic density plot. τ_c denotes the time available inside the solenoid. Accordingly, for typical experimental parameters the CM and relative energies change only by a diminutive amount during the combined propagation of the electron and ion through the solenoidal interaction region. We find that E_{rel}^{e-ion} is conserved to better than 10^{-7} a.u. Therefore, to a good approximation, the transfer of CM energy to relative energy can be entirely neglected. Under this assumption the transformation to the rest frame of the ion (denoted by the superscript R), which is numerically advantageous since the beam velocities ($0.1c$) are much larger than the relative velocity between electron and ion, can be immediately accomplished. With the ion a priori fixed in R , *i.e.* $\vec{p}_{ion}^R = 0$ and $\vec{r}_{ion}^R = 0$, only the motion of the electron in the presence of the magnetic field B and the fixed ionic charge Z needs to be studied. Thus, in the symmetric gauge the resultant Hamiltonian in the rest frame of the ion reads

$$(H_{rel}^{e-ion})^R = \frac{1}{2} \left(\vec{P}^R + \frac{1}{2c} (\vec{B} \times \vec{R}^R) \right)^2 - \frac{Z}{|\vec{R}^R|} = \frac{1}{2} \left(\vec{p}_e^R + \frac{1}{2c} (\vec{B} \times \vec{r}_e^R) \right)^2 - \frac{Z}{|\vec{r}_e^R|} \quad (3.20)$$

with the relative momenta and coordinates between electron and ion \vec{P}^R and \vec{R}^R given by the electronic degrees of freedom \vec{p}_e^R and \vec{r}_e^R , respectively. Below the chaotic dynamics described by Eq. (3.20) will be investigated in detail.

3.3 Classical Chaotic Dynamics

The dynamics of an electron incident from the asymptotic region and approaching the target ion of charge Z in the presence of a homogeneous magnetic field $\vec{B} = B\hat{e}_z$ is thus governed by the reduced Hamiltonian (compare Eq. (3.20))

$$H = \frac{p^2}{2} - \frac{Z}{r} + \frac{1}{2c} B(xp_y - yp_x) + \frac{1}{8c^2} B^2(x^2 + y^2), \quad (3.21)$$

where $\vec{p} = (p_x, p_y, p_z)$ and $\vec{r} = (x, y, z)$ are the Cartesian momentum and coordinate of the electron in the rest frame of the target ion (with the subscript e and superscript R omitted henceforth). Applying the canonical transformation technique [47] (appendix A) the Hamiltonian can as well be expressed in cylindrical coordinates

$$H = \frac{1}{2} \left(p_\rho^2 + \frac{L_z^2}{\rho^2} + p_z^2 \right) - \frac{Z}{\sqrt{\rho^2 + z^2}} + \frac{1}{2c} B L_z + \frac{1}{8c^2} B^2 \rho^2 \quad (3.22)$$

exploiting the axial symmetry of the system imposed by the magnetic field B along the solenoid of the electron cooler, *i.e.* along z in our notation. ρ denotes the

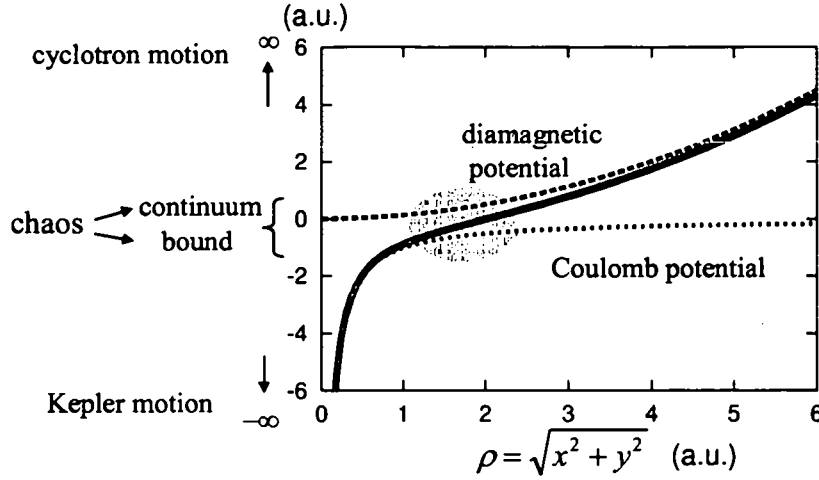


Figure 3.4: Schematic picture of the Coulomb (blue) and diamagnetic (green) potentials of the Hamiltonian Eq. (3.22) as a function of the transverse coordinate ρ ($z = 0$) with $Z = 1$ and $B/c = 1$. For potential energies of competitive strength the underlying classical motion is chaotic (shaded area). The red line indicates the sum of the two contributions.

transverse distance to the ion and L_z the angular momentum component along the direction of the magnetic field. $p_\rho = (xp_x + yp_y)/\rho$ and $L_z = xp_y - yp_x$ are the canonically conjugate momenta with respect to the coordinate $\rho = \sqrt{x^2 + y^2}$ and the polar angle $\phi = \arctan(y/x)$.

This Hamiltonian (Eq. (3.21) or (3.22)) has two constants of motion in involution, the energy E and the angular momentum component L_z . Since the magnetic field along the solenoid breaks the spherical symmetry, the total angular momentum L^2 is not a constant of motion any longer as compared to the pure Coulomb field. The distribution of L^2 in a magnetic field may influence the RR rate (Eq. (2.11)) considerably, because only small L^2 significantly contribute.

In order to be integrable a system with N degrees of freedom requires N constants of motion in involution. For the three degrees of freedom of Eq. (3.22) we find only two constants of motion (E and L_z). Thus, the electronic motion in the combined Coulomb and magnetic fields is not integrable and classical chaotic motion can occur. Note that both the pure Coulomb field (constants of motion: E , L_z and L^2) and the pure magnetic field $\vec{B} = B\hat{e}_z$ (constants of motion: E , L_z and p_z) alone would constitute integrable systems.

Figure 3.4 displays a schematic picture of the potential energy terms in the Hamiltonian Eq. (3.22) as a function of the transverse coordinate ρ ($z = 0$). For small ρ the Coulomb potential ($\propto 1/r$) dominates, whereas for large ρ the diamag-

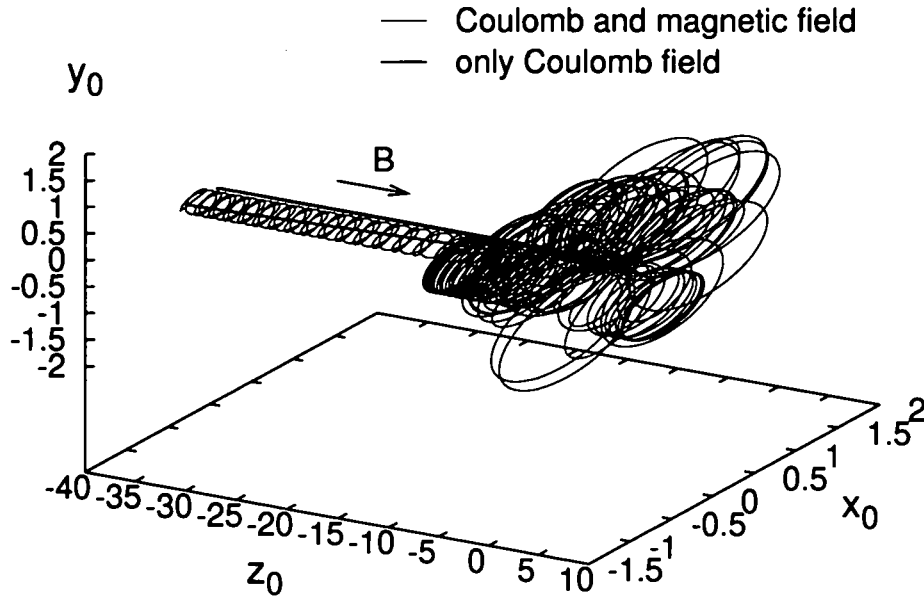


Figure 3.5: Electron trajectory near the target ion in the combined Coulomb and magnetic fields (red) as well as in the pure Coulomb field (green). In the presence of a magnetic field the electron comes close to the ion located at $(0, 0, 0)$ several times. The coordinates are given in scaled units according to Eq. (3.23). The scaled initial velocities have been fixed to $v_{z0} = 0.17$ parallel to and $v_{\perp 0} = 0$ perpendicular to the magnetic field direction.

netic potential ($\propto \rho^2$) dominates with the underlying motion becoming regular in both cases (Kepler motion in the former and cyclotron motion in the latter case). In between, however, for intermediate values of ρ the two potential energies are of comparable strength and the associated motion is classically chaotic. For recombination to take place the incident electron resides in the continuum. Hence, throughout this chapter the chaotic domain at $E > 0$, *i.e.* chaotic scattering dynamics, will be explored. The chaotic motion is, however, also important for small negative energies (see chapter 4).

For a given set of initial conditions the dynamics of the system is determined by the classical Hamilton's equations of motion (appendix A). By integrating these equations numerically (using either a Runge-Kutta method [50] or a symplectic

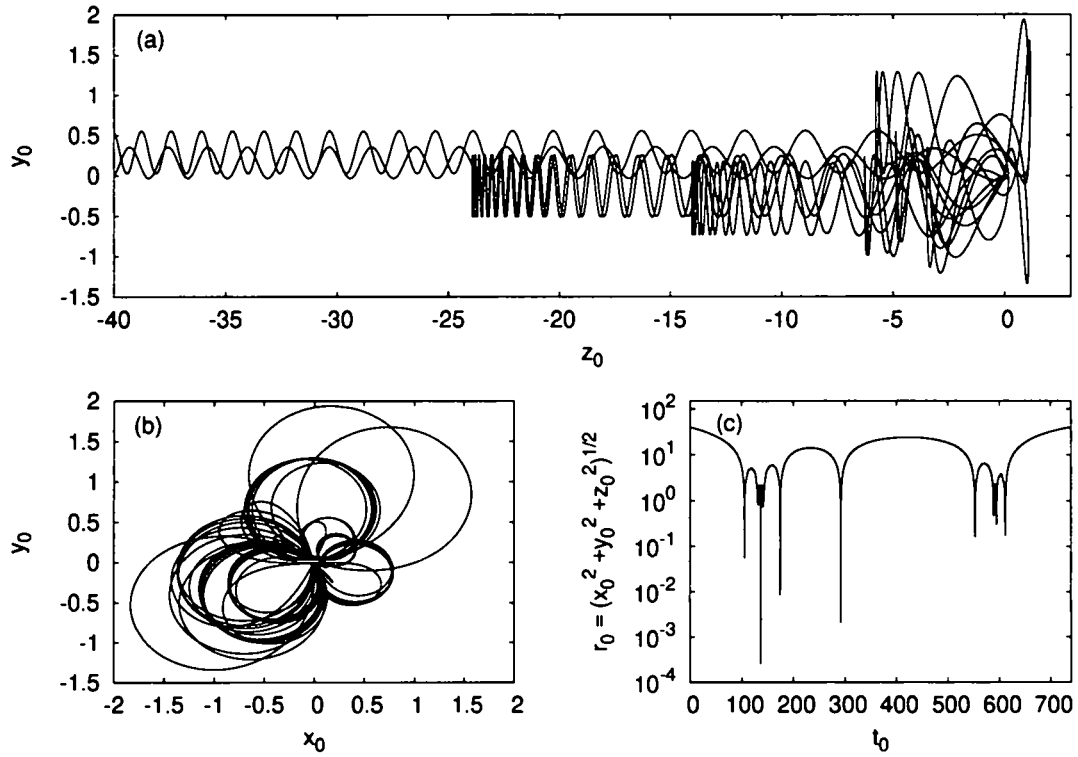


Figure 3.6: Electron trajectory in the combined Coulomb (ion fixed at $(0, 0, 0)$) and magnetic fields ($B \parallel z_0$). The projections onto the $z_0 - y_0$ plane (a) and onto the $x_0 - y_0$ plane (b) and the total distance to the nucleus as a function of the evolved time (c) are shown in scaled coordinates (Eq. (3.23)). The scaled incoming velocities are $v_{\perp 0} \approx 0.19$ and $v_{z0} \approx 0.27$.

integrator [51, 52] (appendix C)) the motion of an electron scattered by the Coulomb potential of the target ion in a magnetic field can be studied. Typical trajectories near the ion are depicted in Figures 3.5 and 3.6 with the electron moving back and forth around the nucleus (situated at the origin of the coordinate system) several times. In the region of comparable strength of the Coulomb force and the Lorentz force the electronic motion is thus a complicated combination of a (fast) Kepler orbit and the (slower) cyclotron motion. The key observation is that trajectories which reach the immediate vicinity of the target ion may return to its proximity a couple of times before leaving to the asymptotic region. By comparison, in the pure Coulomb field the electron moves on a hyperbolic Kepler orbit passing by the ion just once (see Figure 3.5). These multiple traversals in the magnetic field, if as close as $r \leq r^{RR}$, will enhance the radiative recombination rate, since each of them increases the probability for recombination. However, as Figure 3.6c presents, many of the electronic encounters to the ion proceed at distances by far larger than r^{RR} . Accordingly, most of the passings of the ion cannot contribute to the recombination. To estimate the effect of these repeated traversals on the RR rates quantitatively the simulation of an ensemble of trajectories is required.

The Hamiltonian (Eq. (3.21) or (3.22)) exhibits classical scaling invariance [53, 54]. In our problem the scaling reveals the systematic dependence on B and Z . We scale the variables by the transformations (appendix B)

$$\begin{aligned}\vec{r}_0 &= (B/c)^{2/3} Z^{-1/3} \vec{r}, \\ \vec{p}_0 &= (B/c)^{-1/3} Z^{-1/3} \vec{p}, \\ L_{z0} &= (B/c)^{1/3} Z^{-2/3} L_z,\end{aligned}\tag{3.23}$$

where scaled quantities are denoted by the subscript 0. Applying these scaling relations the scaled Hamiltonian, H_0 , becomes

$$H_0 = (B/c)^{-2/3} Z^{-2/3} H = \frac{p_0^2}{2} - \frac{1}{r_0} + \frac{1}{2} L_{z0} + \frac{1}{8} \rho_0^2.\tag{3.24}$$

In the scaled system the only relevant control parameter is the scaled energy H_0 . Different combinations of $\{H, B, Z\}$ with the same H_0 result in the same dynamics. Accordingly, exploring the dynamics for different H_0 covers all possible realizations: the B and Z dependencies are, in turn, completely contained in the scaling transformations of Eq. (3.23).

The classical simulation is, however, not as simple as it might appear because, the system has two vastly different length scales, the "target space" ($r^{RR} \approx 10 - 100$ a.u.) and the asymptotic Landau region ($r_c \approx 10^5$ a.u.). This disparity in length scales implies that classical scattering trajectories have to be followed from "infinity" at almost macroscopic distances down to microscopic distances from the target ion for reliable predictions. Due to the chaotic dynamics this amounts to

the proverbial search for a needle in the hay stack. To find systematic dependences (such as on E , Z or B) among such small probabilities requires large ensemble sizes. Typically, millions of trajectories are necessary for a given set of experimental parameters in order to represent the electronic phase space distribution near the ion properly. Because of the chaotic dynamics the propagation of these trajectories is not an easy task: very small time steps have to be chosen to maintain the accuracy of the calculation. This is due to the fact that the numerical error associated with each trajectory is exponentially enlarged with time, an inherent feature of chaotic dynamics. However, by the help of parallel processing different trajectories can be distributed to different processors and, accordingly, the computing time required to get converged results is reduced by a factor $1/N$ with N representing the number of available processors.

3.4 Classical Phase Space Structure: Poincaré Surfaces of Section

In order to analyze the classical phase space structure and to view the chaotic nature of the underlying trajectories we employ a modified version of Poincaré surfaces of section applicable to scattering systems proposed by Jung [55].

A Poincaré surface of section [56] is the representation of trajectories in a subspace of phase space. Points of the Poincaré surface of section represent points of intersections of trajectories with the two-dimensional subspace (plane) of phase space. For a meaningful representation the intersections should be densely distributed. This technique has been used extensively for bounded systems whose trajectories are localized in a finite region of space: a bound-state trajectory can cross the surface of section many times and becomes visualized as an ensemble of dots indicating either regular (only finite number of points or a one-dimensional set for periodic or quasi-periodic motion, respectively) or chaotic motion (points lie dense in a two-dimensional subset).

However, for scattering systems trajectories are not bounded but they spread over the phase space: the projectile comes in from infinity, interacts with the target only for a finite time interval and then goes off to infinity again. Therefore any surface S is pierced only a finite number of times by a generic scattering trajectory. Accordingly, only few points can be accumulated on the corresponding Poincaré surface of section (even if the analyzed scattering potential induces chaotic behavior). Thus, in order to map out structures in phase space a more involved technique is required in the case of scattering problems: the method proposed by Jung [55] suggests that once a projectile leaves the target region, the trajectory is mapped back onto the entrance region of the phase space to the target zone again. This map

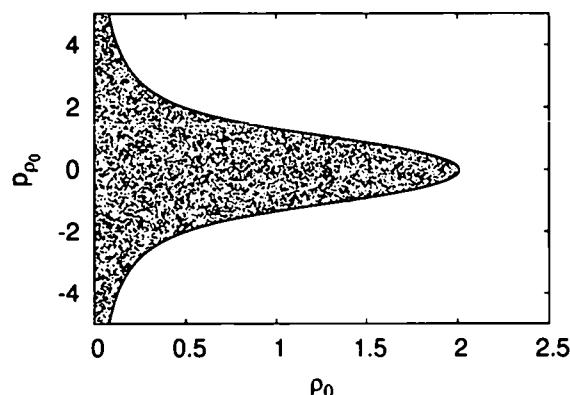


Figure 3.7: Poincaré surface of section at $z_0 = 0$ generated from the trajectory of Figure 3.5 by propagating it up to 100 reflections at $z_0 = z_c = 100$. The transverse coordinate ρ_0 is plotted against the corresponding transverse momentum p_{ρ_0} . The trajectory reaches the entire classically allowed region of phase space indicated by the red line. It is given by $p_{\rho_0} = \sqrt{2E_0 - L_{z0} - L_{z0}^2/\rho_0^2 - 1/4\rho_0^2} + 2/\rho_0$.

should be: 1) independent of the scattering potential and 2) identical to periodic boundary conditions in the absence of the scattering potential. The resulting map illustrates regions of phase space which are filled by stable or unstable trajectories. In our case the motion in the transverse direction is confined due to the magnetic field. However, a trajectory is unbounded in the longitudinal direction, *i. e.* parallel to the magnetic field, chosen as z -axis in our coordinate system. Once z becomes larger than a given boundary value z_c , we map $z \rightarrow -z$. In this way a Poincaré surface of section for our scattering problem can be constructed. The boundary z_c is chosen such that the Coulomb potential of the ion has already decreased to a small strength compared to the magnetic field contribution which is present also in the asymptotic regime far away from the ion to be scattered at. Thus, in terms of the two assumptions specified above only the Coulomb potential is regarded as the "scattering potential" in our case.

Figure 3.7 illustrates a Poincaré surface obtained from the trajectory depicted in Figure 3.5. The surface of section is taken at the origin where the target ion is situated. The trajectory lies densely in the entire region of classical phase space accessible for the chosen initial conditions. We investigated surfaces of section for different positive energies. In all cases we obtained pictures similar to Figure 3.7 with no regular structures visible at all indicating that the system features hard chaos. The nature of chaotic trajectories implies that a small change in the initial conditions dramatically affects the time evolution and, as time proceeds, the sensitivity on the

initial conditions becomes stronger and stronger. This intrinsic feature of chaos manifests itself in the random distribution of points, *i. e.* a dense two-dimensional set, shown on the Poincaré surface of section (Figure 3.7). Precisely this chaotic behavior makes the propagation from the asymptotic region to the target ion very difficult.

3.5 Modification of the Recombination Rate

From the CTMC simulation the change of the electron density $|\langle \vec{r} | u_k^B \rangle|^2$ near the ion in the presence of a magnetic field relative to the pure Coulomb case $|\langle \vec{r} | u_k \rangle|^2$ can be extracted: following the discussion of section 3.1 we define the Coulomb zone $S_C = \{\vec{r} | r < r^{RR}\}$ as the region where radiative recombination takes place and, below, investigate the probability for finding an electron within S_C . We determine the change of probability density in terms of a visit function $V(\vec{r}, \vec{v})$, which denotes the number of visits, *i. e.* the number of encounters, of a given trajectory with asymptotic phase space coordinates (\vec{r}, \vec{v}) to the Coulomb zone S_C . For a schematic picture see Figure 3.8. The visit function V plays the role of a generalized time-delay function of irregular scattering [57, 58, 59, 60]. The corresponding visit functions are evaluated with (V) and without a magnetic field (V_C).

Since each visit is considered to contribute to the recombination, the ratio V/V_C corresponds to the enhancement of the recombination rate for given initial conditions (\vec{r}, \vec{v}) . Accordingly, the enhancement for a fixed asymptotic velocity \vec{v} is given by

$$h(\vec{v}) = \frac{\int d\vec{r} V(\vec{r}, \vec{v})}{\int d\vec{r} V_C(\vec{r}, \vec{v})} \quad (3.25)$$

with V_C denoting the visit function in the pure Coulomb field. In the presence of a magnetic field the asymptotic Maxwell-Boltzmann velocity distribution for the incident electrons needs to be properly weighted according to the modification of the electron beam flux in coordinate space characterized by Eq. (3.25). Thus, the radiative recombination rate can be written as

$$\alpha(v_{rel}) = \int \sigma_{total} v h(\vec{v}) f_{MB}(\vec{v}, v_{rel}) d\vec{v}. \quad (3.26)$$

Note that even though the Hamiltonian and the resulting equations of motion are derived in the symmetric gauge (Eq. (3.21)), the recombination rate is gauge invariant due to the fact that all the functions in the integrand are evaluated in terms of gauge independent quantities such as \vec{r} and \vec{v} .

We emphasize that the visit functions both $V(\vec{r}, \vec{v})$ and $V_C(\vec{r}, \vec{v})$ are evaluated in terms of asymptotic phase space coordinates, *i. e.* the initial ensemble is taken on the surface of a sphere with radius r or more precisely, exploiting the axial symmetry

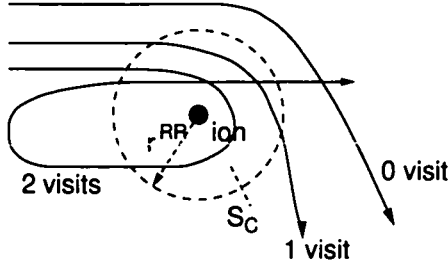


Figure 3.8: Trajectories that enter $S_C(r < r^{RR} = n_r^2/Z)$ around the target ion are counted as 'visits' to the ion.

for finite field strengths B , on a plane with initial coordinate $z = r$ (for a more detailed discussion see section 3.7). Hence the integration $\int d\vec{r} = d^2r$ in Eq. (3.25) has the dimension of an area and can be interpreted as the corresponding classical analog of a cross section. The new rate formula can intuitively be understood: in Eq. (3.26) an appropriate weighting of the RR cross section σ_{total} with the ratio of the classical flux for radiative recombination in the combined fields versus the corresponding flux in the pure Coulomb field needs to be taken into account.

3.6 Determination of the Visit Function

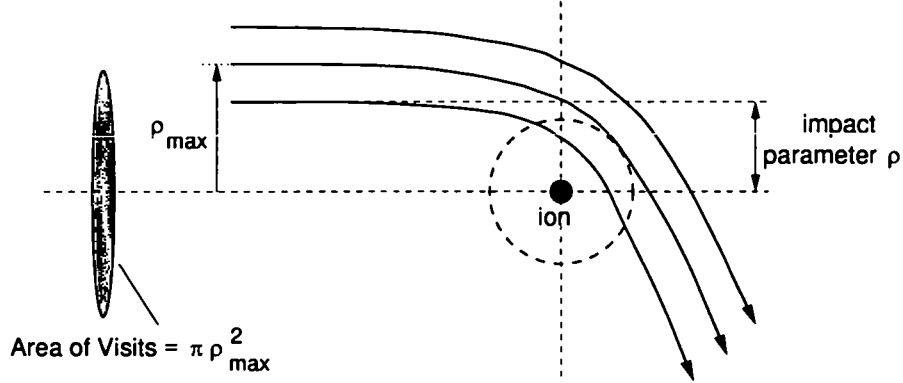
Evaluation of the modified RR rate formula (Eq. (3.26)) requires only the determination of the visit function $V(\vec{r}, \vec{v})$.

In the pure Coulomb case the visit function V_C is easy to evaluate since the underlying dynamics is regular, *i. e.* the motion proceeds on hyperbolic Kepler orbits (Figure 3.9). Accordingly V_C takes only the values 0 and 1 (Figure 3.12b) and is non-zero only in a single connected phase space region (Figures 3.11b and 3.13b), whose size can be readily calculated. For a hyperbola the distance of the perihelion from the focus, where the ion is located, is given in terms of the semi-axis a and the eccentricity ε [61]. This distance of closest approach of an electron to the ion, denoted by r_{min} , must be smaller than r^{RR} for a visit to occur, *i. e.*

$$r^{RR} \geq r_{min} = a(\varepsilon - 1) = \frac{Z}{2E} \left(\sqrt{1 + \frac{2EL^2}{Z^2}} - 1 \right). \quad (3.27)$$

The angular momentum L and the energy E of the electron are expressed in terms of asymptotic quantities such as the impact parameter ρ_∞ and the velocity v_∞ at infinity as

$$L = L_z = \rho_\infty v_\infty, \quad E = \frac{1}{2} v_\infty^2. \quad (3.28)$$


 Figure 3.9: Contribution to the visit function V_C in the pure Coulomb field.

Since we want to compare V_C with the corresponding value of V being determined from the CTMC at the SAME initial phase space coordinates (\vec{r}, \vec{v}) (chosen at large distances from the ion, but definitely not at infinity), we actually employ

$$L = \rho v, \quad E = \frac{v^2}{2} - \frac{Z}{r} \quad (3.29)$$

to account for the contribution of the Coulomb field at large, but still finite distances \vec{r} . Exploiting the spherical symmetry of the Coulomb potential for the evaluation of V_C the coordinate system can be chosen such that the initial velocity of the electron becomes parallel to the z -axis, *i.e.* $\vec{v} = v\hat{e}_z = \sqrt{v_{\parallel}^2 + v_{\perp}^2}\hat{e}_z$, where v_{\parallel} and v_{\perp} denote the corresponding longitudinal ($\parallel B$) and transverse ($\perp B$) velocity components of V in the magnetic field to be compared with. Thus, all electrons with initial impact parameter $\rho \leq \rho_{max}$ contribute to V_C (Figure 3.9) and the coordinate space integration of V_C results in

$$V_C(\vec{v}) = \int d\vec{r} V_C(\vec{r}, \vec{v}) = \pi \rho_{max}^2 = \pi \frac{2r^{RR}(Er^{RR} + Z)}{v^2} \quad (3.30)$$

with the maximum impact parameter $\rho_{max} = \rho(r_{min} = r^{RR})$ having a visit to the ion being determined by the equality sign in Eq. (3.27). The values obtained for V_C are displayed in the subsequent figures (Figure 3.11b, 3.12b and 3.13b).

The visit function V in the magnetic field is determined numerically from our CTMC simulation. Due to the chaotic dynamics in the presence of B the electron can be scattered by the ion many times allowing for multiple visits (Figure 3.5). The longer the total propagation time, the higher is the sensitivity of the visit function V on its initial conditions. Therefore, it is very difficult to analytically predict for given

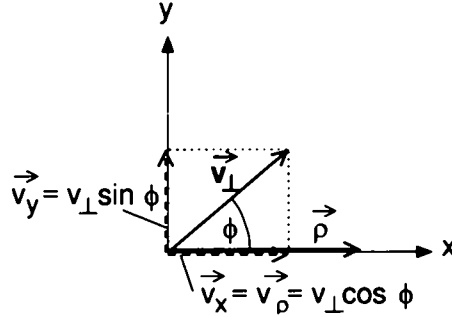


Figure 3.10: The initial coordinates and velocities as chosen in the simulations. Due to the cylindrical symmetry of the system we set $\vec{\rho} = x\hat{e}_x$. ϕ denotes the angle between $\vec{\rho}$ and \vec{v}_\perp .

initial conditions (\vec{r}, \vec{v}) in the asymptotic region whether the electron visits the target ion within a finite time period and, if it does, how many times. Nevertheless, some geometrical restrictions on the initial conditions can be made due to the fact that the angular momentum component L_z is preserved in the magnetic field $\vec{B} = B\hat{e}_z$ within the symmetric gauge. Since $L^2 = L_x^2 + L_y^2 + L_z^2 \geq L_z^2$, in analogy to Eq. (3.27) at least a lower limit for the distance of closest approach r_{min} can be established for given initial conditions by

$$r_{min} \geq \frac{Z}{2E} \left(\sqrt{1 + \frac{2E}{Z^2} L_z^2} - 1 \right). \quad (3.31)$$

Equating the lower boundary for r_{min} with the relevant length scale r^{RR} for RR, *i.e.*

$$r^{RR} = \frac{Z}{2E} \left(\sqrt{1 + \frac{2E}{Z^2} L_z^2} - 1 \right), \quad (3.32)$$

constraints on the initial conditions contributing to V can be derived. Exploiting the cylindrical symmetry of the Hamiltonian Eq. (3.22) we choose the initial electronic coordinates and velocities as (Figure 3.10)

$$\begin{aligned} x &= \rho, & v_x &= v_\rho = v_\perp \cos \phi \\ y &= 0, & v_y &= v_\perp \sin \phi \end{aligned} \quad (3.33)$$

whereupon the angular momentum L_z becomes

$$L_z = xp_y - yp_x = \rho v_\perp \sin \phi - \frac{1}{2c} B \rho^2. \quad (3.34)$$

Solving Eq. (3.32) with this expression for L_z with respect to ρ and ϕ finally leads to the intervals of initial conditions

$$\rho \in [0, \rho_{max}], \quad \phi \in [\phi_1, \phi_2] \quad (3.35)$$

where

$$\rho_{max} = \frac{c}{B} \left(v_{\perp} + \sqrt{2 \frac{B}{c} \sqrt{2 r^{RR} (E r^{RR} + Z)} + v_{\perp}^2} \right) \quad (3.36)$$

$$\phi_1 = \arcsin \left(\frac{1}{2 \rho v_{\perp}} \left(\frac{B}{c} \rho^2 - 2 \sqrt{2 r^{RR} (E r^{RR} + Z)} \right) \right) \quad (3.37)$$

$$\phi_2 = \arcsin \left(\frac{1}{2 \rho v_{\perp}} \left(\frac{B}{c} \rho^2 + 2 \sqrt{2 r^{RR} (E r^{RR} + Z)} \right) \right). \quad (3.38)$$

3.7 The Visit Function: Numerical Results

In this section we investigate the visit functions, V and V_C , for fixed initial velocities $(v_{\perp 0}, v_{z0})$. To determine $V(\vec{r}, \vec{v})$ an ensemble of electrons incident from the asymptotic region is simulated subject to the restrictions Eqs. (3.35) - (3.38). All scattering trajectories are calculated from the asymptotic incoming region through the immediate vicinity of the ion (with multiple forward and backward encounters possible) to the asymptotic outgoing region without any limitation in propagation time. In Figures 3.11a and 3.13a the set of initial conditions (ρ_0, ϕ_0) with non-zero values of V is plotted as dots on the corresponding plane. In Figures 3.12a and 3.14 the visit function $V(\rho_0)$ is displayed for fixed values of the initial angle ϕ_0 . As a reference, also V_C is shown (Figures 3.11b, 3.12b and 3.13b). As seen from the figures V can take any integer value and is a highly irregular function with fractal structure because of the chaotic dynamics in the presence of a magnetic field.

In Figure 3.11a, where the perpendicular velocity is fixed at $v_{\perp 0} = 0.15$, in the magnetic field a connected region at $\rho_0 \approx 0.3$ (Figure 3.12a) can be found as in the pure Coulomb case (Figure 3.12b), however at larger impact parameter. In addition to this connected region with one visit to the ion multiple visits appear spread over wide regions in phase space with a fractal-like structure. To emphasize these fractal structures a magnification of a small range of V is drawn in the inset of Figure 3.12a. The overall contribution of the visit function $\int d\vec{r}_0 V(\vec{r}_0, \vec{v}_0) = \int d\rho_0 \rho_0 \int d\phi_0 V(\rho_0, \phi_0)$ amounts to about 0.101 in the presence of the magnetic field and only to 0.078 in the pure Coulomb field (*i.e.* for V_C) thus leading to an enhancement ratio of $h(\vec{v}_0) \approx 1.29$ for $(v_{\perp 0}, v_{z0}) = (0.15, 0.3)$. The horizontal line in Figure 3.11 indicates the cut through phase space investigated further in Figure 3.12.

The origin of the fractal-like structure of V can be understood by investigating the dynamics of the associated trajectories. The analysis of individual trajec-

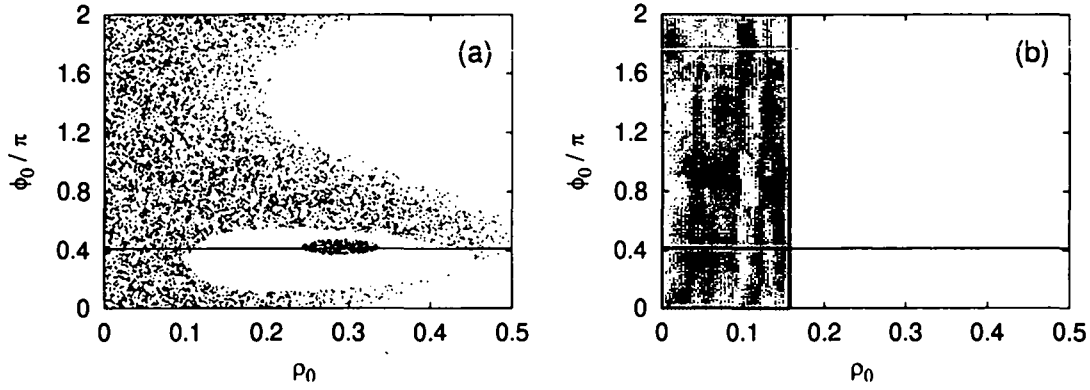


Figure 3.11: Phase space region of non-zero visit function $V(\vec{r}_0, \vec{v}_0)$ (a) and $V_C(\vec{r}_0, \vec{v}_0)$ (b) at fixed scaled perpendicular and parallel velocities $v_{\perp 0} = 0.15$, $v_{z0} = 0.3$ and scaled coordinate $z_0 = -100$. Visits are defined for $r_0 < 1.4 \times 10^{-3}$ scaled units. ρ_0 denotes the impact parameter and ϕ_0 the angle between $\vec{\rho}_0$ and $\vec{v}_{\perp 0}$. The lines refer to the subspace of phase space illustrated in Figure 3.12.

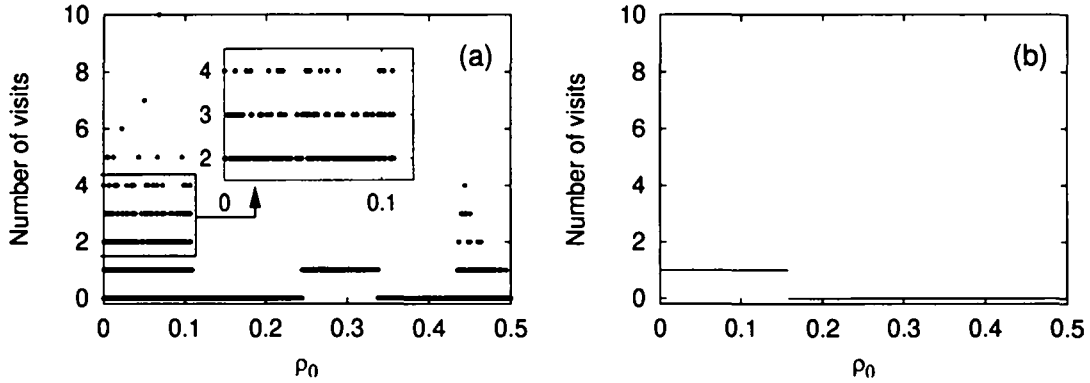


Figure 3.12: Visit function V along the cut $\phi_0/\pi \approx 0.41$ (indicated by the horizontal line in Figure 3.11) with magnetic field (a) and without magnetic field (b). The inset in (a) is a magnification of the window around $\rho_0 = 0$ displaying the fractal-like structure of V .

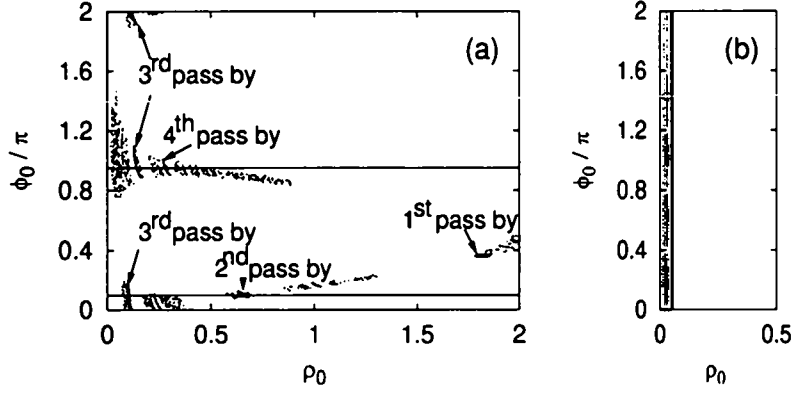


Figure 3.13: Phase space portraits of $V(\vec{r}_0, \vec{v}_0)$ (a) and $V_C(\vec{r}_0, \vec{v}_0)$ (b) recorded at a larger perpendicular velocity of $v_{\perp 0} = 1.0$. The other parameters are the same as in Figure 3.11. The various structures visible in V can be assigned to different types of trajectories as indicated in (a). The two horizontal lines denote the subspaces of phase space depicted in Figure 3.14.

ries (Figure 3.15) reveals that the dense black spot at $(\rho_0, \phi_0/\pi) \approx (1.82, 0.36)$ in Figure 3.13a represents a small connected area of points with non-zero V which correspond to the initial conditions of trajectories visiting the ion when the electron passes by the ion for the first time. Similarly, the spot at $(\rho_0, \phi_0/\pi) \approx (0.65, 0.1)$ is associated with electrons having a visit at their second pass by. Furthermore, also the connected regions pertaining to visits at the third and fourth traversals of the ion appear. As already pointed out, the later a visit occurs the higher its sensitivity on the initial conditions becomes. Therefore, the size of the connected regions to be formed is decreasing for visits happening at later times. Piling up these smaller and smaller structures in the initial conditions the fractal-like structure of the visit function $V(\vec{r}, \vec{v})$ is obtained. The profile of V depicted in Figure 3.14 for two fixed angles ϕ_0 illustrates the fractal behavior of the visit function with magnifications of connected regions of non-zero values of V . Figure 3.15 displays sample trajectories related to the connected regions of visits from the first and second pass by.

For the larger velocity component $v_{\perp 0} = 1.0$ fewer visits occur (Figure 3.14). V extends to larger values of the impact parameter ρ_0 as a result of the increased cyclotron radius ($r_{\infty} \propto v_{\perp 0}$) whereas being much more restricted in the initial angle ϕ_0 for individual values of ρ_0 (Figure 3.13a). This is due to the fact that a small angular momentum L_{z0} (Eq. (3.34)) is required for a visit to occur. $L_{z0} = 0$ is given by $\phi_0 = \arcsin(\rho_0/(2v_{\perp 0}))$. In the case of Figure 3.13 the enhancement ratio (Eq. (3.25)) is calculated as $h(\vec{v}_0) = 1.88$, which is considerably larger than for the smaller perpendicular velocity $v_{\perp 0} = 0.15$ discussed above.

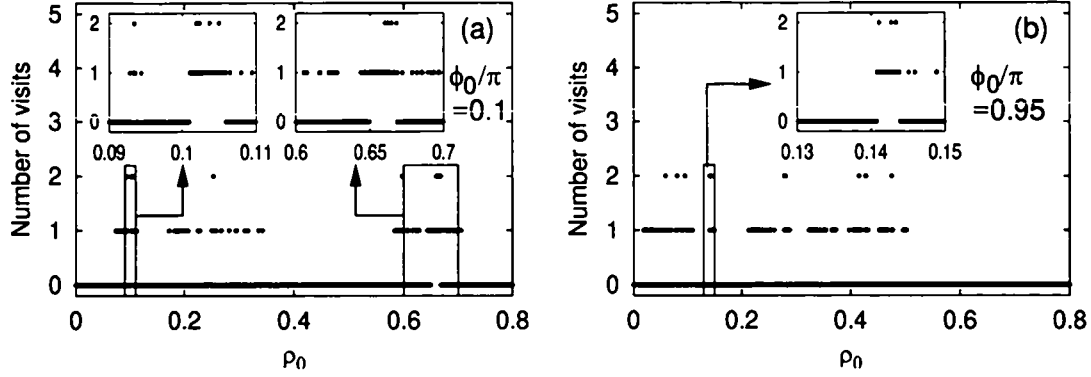


Figure 3.14: Visit function V along $\phi_0/\pi = 0.1$ (a) and $\phi_0/\pi = 0.95$ (b). Note that ρ_0 has been restricted to ≤ 0.8 . The left inset in (a) enlarges the connected region around $\rho_0 = 0.1$ associated with visits from electrons passing by the ion for the third time and the right inset in (a) zooms at the connected region around $\rho_0 = 0.65$ caused by visits of the second pass by of the electron. The inset in (b) is a magnification around $\rho_0 = 0.14$, where again visits from the third electronic traversal are located.

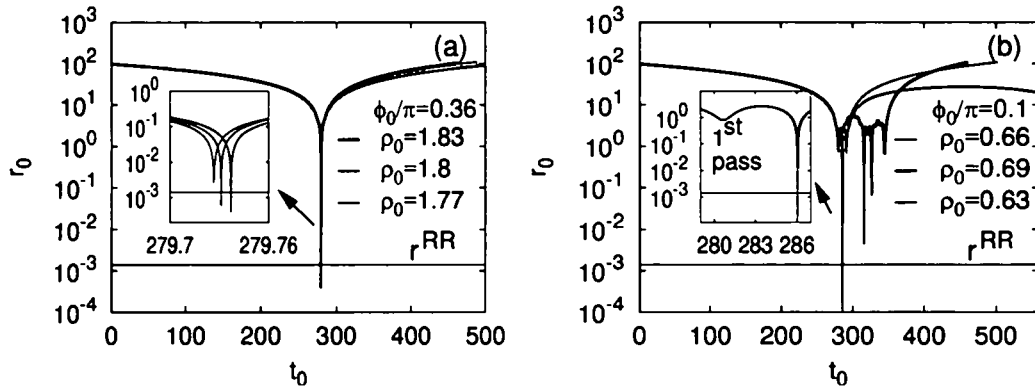


Figure 3.15: Trajectories originating from the phase space region of Figure 3.13 around $\rho_0 \approx 1.8$, $\phi_0/\pi = 0.36$, *i.e.* close to or within the connected region related to visits from the first pass by (a), and trajectories from the region around $\rho_0 \approx 0.66$, $\phi_0/\pi = 0.1$, *i.e.* close to or within the connected region representing visits from the second pass by (b). The distance to the ion is shown as a function of scaled time. Visits are assumed for $r_0 < r^{RR} = 1.4 \times 10^{-3}$ scaled units (horizontal line). In the inset the region around the closest approach to the ion is magnified. Note that in (a) two trajectories visit the ion, whereas in (b) only one does.

Note that in the phase space portrait of Figure 3.11a only one connected area, situated at $(\rho_0, \phi_0/\pi) \approx (0.29, 0.42)$, is visible representing visits to the ion at the first pass by of the electron. All the other structures in V have already become so tiny at the given velocity that they could not be resolved within the available Monte Carlo statistics (with 6456 trajectories contributing to V) thus demonstrating the extremely high sensitivity of the dynamics on the chosen initial conditions in the very low velocity regime.

The accurate determination of V and its integration over phase space coordinates (Eqs. (3.25) and (3.26)) is therefore very difficult. High levels of Monte Carlo statistics are required to reach converged results for measures of irregular scattering. Certainly, this difficulty limits the accuracy of the presented results. Finally we emphasize that the visit functions presented throughout this section do not include a time limit for visits to the ion.

3.8 Weighted Visit Function

The flux of electrons near the target ion in the presence of a magnetic field is determined by means of the visit function $V(\vec{r}, \vec{v})$. So far, V has been defined by applying a sharp cutoff to the contribution to recombination at $r = r^{RR}$ (with r^{RR} decided by the maximum principal quantum number n_r not being field-ionized in the subsequent charge-analyzing dipole magnet in the experiment). However, a sharp cutoff in n irrespective of the angular momentum l definitely constitutes an oversimplified description for RR to take place. To attain a more realistic characterization of the RR process, each visit into the Coulomb zone S_C by a given trajectory should be weighted with a weighting function $w(r_{min})$, where r_{min} corresponds to the minimum distance to the ion associated with this visit. The weighting function is obtained by breaking the Coulomb zone S_C down into different n, l subshells and by assuming each visit has a weight according to the unperturbed cross section σ_{nl}^{RR} for RR into the (n, l) state, *i.e.*

$$w(r) = \frac{1}{\sigma_{total}} \sum_{n=1}^{n_r} \sum_{l=0}^{n-1} \sigma_{nl}^{RR} \Theta\left(\frac{ln}{Z} - r\right), \quad (3.39)$$

where $\Theta(r)$ represents the step function. σ_{nl}^{RR} can be approximated within a non-relativistic treatment in the electric dipole approximation [5, 62] by

$$\sigma_{nl}^{RR} \approx \frac{\pi^2}{3} \alpha_f^3 [(l+1)c_{l+1}^2(n, l) + lc_{l-1}^2(n, l)] \frac{E_{nl}}{E_e} \quad (3.40)$$

in the limit of low electron energy, *i.e.* $E_e \ll E_{nl}$. α_f denotes the fine structure constant, E_e the free electron kinetic energy (see Eq. (2.7)), E_{nl} the electron binding

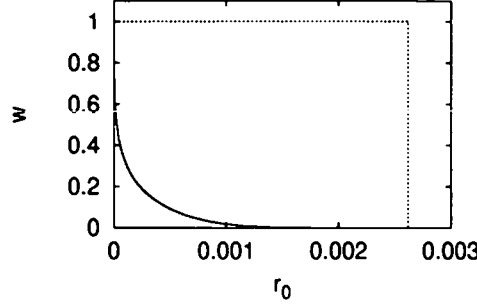


Figure 3.16: Weighting functions (line for Eq. (3.39) and dashed line for Eq. (3.41)) employed to determine the number of visits to the ion. $n_r = 30$ and $Z = 6$.

energy in the final state and $c_{l\pm 1}(n, l)$ the reduced electric dipole matrix elements given by [62]

$$\begin{aligned}
 c_{l-1}(n, l) &= \frac{2^{2l} n^{l-1} e^{-2n}}{(2l-1)!} \left[\frac{(n+l)!}{(n-l-1)!} \right]^{1/2} \\
 &\quad \times [F(l-n+1, 2l; 4n) - F(l-n-1, 2l; 4n)] \\
 c_{l+1}(n, l) &= \frac{2^{2l+4} n^{l+1} e^{-2n}}{(2l+1)!} \left[\frac{(n+l)!}{(n-l-1)!} \right]^{1/2} \\
 &\quad \times \left[F(l-n+1, 2l+2; 4n) - \frac{l-n+1}{l+1} F(l-n+2, 2l+3; 4n) \right]
 \end{aligned}$$

with the confluent hypergeometric function $F(\beta, \gamma; z)$ [63]. A plot of the resulting weighting function Eq. (3.39) with $n_r = 30$ is shown in Figure 3.16 and compared with that of a sharp cutoff of V at $r = r^{RR}$,

$$w^{sharp}(r) = \Theta \left(\frac{n_r^2}{Z} - r \right). \quad (3.41)$$

Accordingly, the visit function $V(\vec{r}, \vec{v})$ is evaluated by summing up all the weighted visits of a trajectory launched from the asymptotic coordinate (\vec{r}, \vec{v}) , *i.e.* $V(\vec{r}, \vec{v}) = \sum_i w(r_{min}^i)$ where the index $i = 1, 2, \dots$ counts the number of repeated visits (if any) for a given trajectory. The visit functions with (V) and without a magnetic field (V_C) are thus determined.

By the weighting according to Eq. (3.39) the visit function changes from an integer-valued quantity to a real-valued function. Since in the pure Coulomb field $i = 0$ or 1 , $V_C \leq 1$, that is at most one visit per trajectory takes place. V_C is a smooth function and as before non-zero only in a single connected phase space region

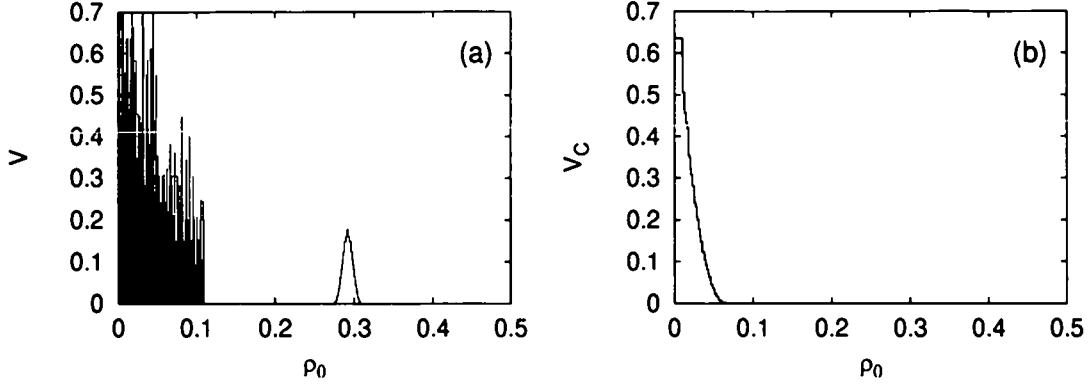


Figure 3.17: Visit function V weighted according to Eq. (3.39) as a function of the scaled impact parameter ρ_0 with magnetic field (a) and without magnetic field (b) for the data of Figure 3.12 with scaled velocities of $v_{\perp 0} = 0.15$ and $v_{z0} = 0.3$ and scaled coordinates of $z_0 = -100$ and $\phi_0/\pi \approx 0.41$.

(Figure 3.17b). In the presence of a magnetic field the visit function becomes a highly fluctuating function exhibiting a fractal-like structure (Figure 3.17a). Multiple visits appear in addition to the connected region at $\rho_0 \approx 0.3$. In the simulation, a point by point integration of V is performed over the phase space coordinates. With a longer total time propagation V shows a high sensitivity to the scaled initial coordinate ρ_0 (Figure 3.17a). Figure 3.17 illustrates V and V_C after weighting with Eq. (3.39) for the same data set as in Figure 3.12 where V and V_C have both been evaluated using the weighting of Eq. (3.41).

3.9 Magnetic Field Dependence of the Visit Function

In order to understand the effect of the magnetic field on the enhancement of the recombination we first investigate the phase space region of non-zero visit function V for different magnetic field strengths at fixed initial velocities. For a comparison of $V(\vec{r}, \vec{v})$ at the same velocities (v_{\perp}, v_z) given in a.u. but different magnetic fields the corresponding phase space portraits (Figure 3.18) are shown in a.u. rather than scaled units, where different B would lead to different \vec{r}_0 and \vec{v}_0 . The trajectories are launched from a plane perpendicular to B with initial coordinate $z = -7.167 \times 10^6$ a.u. With decreasing magnetic field the cyclotron radius increases ($r_c \propto 1/B$) and the dynamics allowing for visits to the ion extends to larger transverse coordinates ρ . In contrast, the range of initial angles ϕ contributing to V becomes narrower at

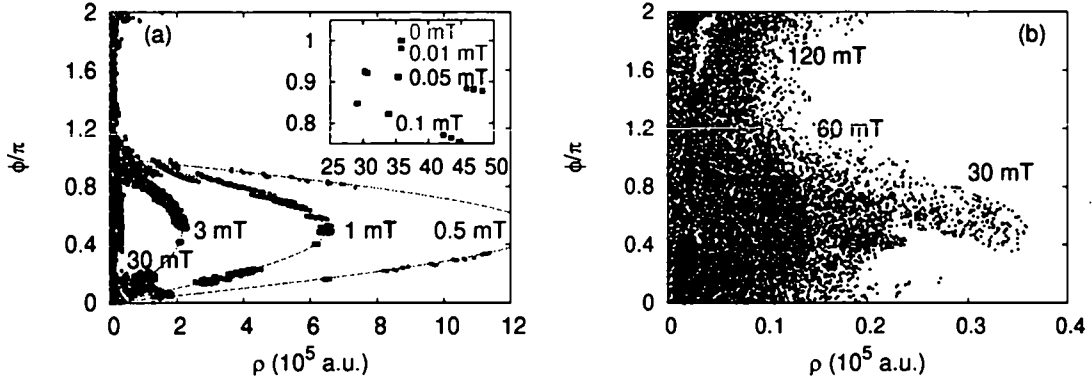


Figure 3.18: Phase space region of non-zero visit function $V(\vec{r}, \vec{v})$ for lower (a) and higher magnetic field strengths (b). The initial velocities are fixed to $v_z = 2.744 \times 10^{-3}$ a.u. and $v_\perp = 1.372 \times 10^{-3}$ a.u., the initial coordinate to $z = -7.167 \times 10^6$ a.u. and visits are defined for $r < r^{RR} = 100$ a.u. The dashed lines in (a) indicate $L_z = 0$ given by $\phi = \arcsin(1/(2c) B\rho/v_\perp)$ (compare Eq. (3.34)).

individual values of ρ in order to preserve an angular momentum L_z small enough for a visit to take place. Thus, a decrease in B modifies the phase space structure of $V(\rho, \phi)$ in the same manner as an increase in v_\perp (discussed in section 3.7) does. For magnetic fields such as $B \lesssim 3$ mT V is essentially non-zero only in a narrow strip around $L_z = 0$ (Eq. (3.34)) given by $\phi = \arcsin(1/(2c) B\rho/v_\perp)$. For small values of B the dynamics gets more Coulomb-like with V becoming less irregular in (ρ, ϕ) space approaching the distribution in a single region of phase space. Note that with decreasing B it is increasingly difficult to determine V with sufficient accuracy due to its sparser representation in the available (ρ, ϕ) space. Correspondingly, in our simulation the sampling of initial conditions according to Eqs. (3.35) - (3.38) becomes more and more inefficient for lower values of B . Table 3.1 displays the fraction of the trajectories launched which has at least one visit to the ion as obtained for the phase space portraits of Figure 3.18.

In Figure 3.18a the Coulomb contribution $V_{C,sim}$ ($V_{C,sim}$ refers to the visit function obtained from the simulation in contrast to the analytically determined value V_C) is situated at $\rho \gg 1$ and $\phi \approx \pi$, since in our simulation for $B = 0$ we do not rotate the coordinate system in order to achieve $\vec{v} \parallel \hat{e}_z$ as it is done for the analytical determination of the visits in Eq. (3.30), whereupon non-zero values of V_C reside at $\rho \leq \rho_{max}$ with $0 \leq \phi \leq 2\pi$ (Figures 3.11b and 3.13b). In the simulation contributing values to $V_{C,sim}$ are found at the larger transverse coordinates ρ the larger the ratio v_\perp/v_z becomes in order to obtain an impact parameter small enough for reaching the ion. The contribution $V_{C,sim}(\vec{v}) = \int d\vec{r} V_{C,sim}(\vec{r}, \vec{v})$ if evaluated at

magnetic field (mT)	fraction of sampled phase space contributing to V
0.05	4.44×10^{-5}
0.1	6.29×10^{-4}
0.5	0.0039
1.0	0.0074
3.0	0.019
10.0	0.067
15.0	0.099
30.	0.18
60.0	0.30
120.0	0.36

Table 3.1: Fraction of trajectories with non-zero values of V obtained for the phase space portraits of Figure 3.18.

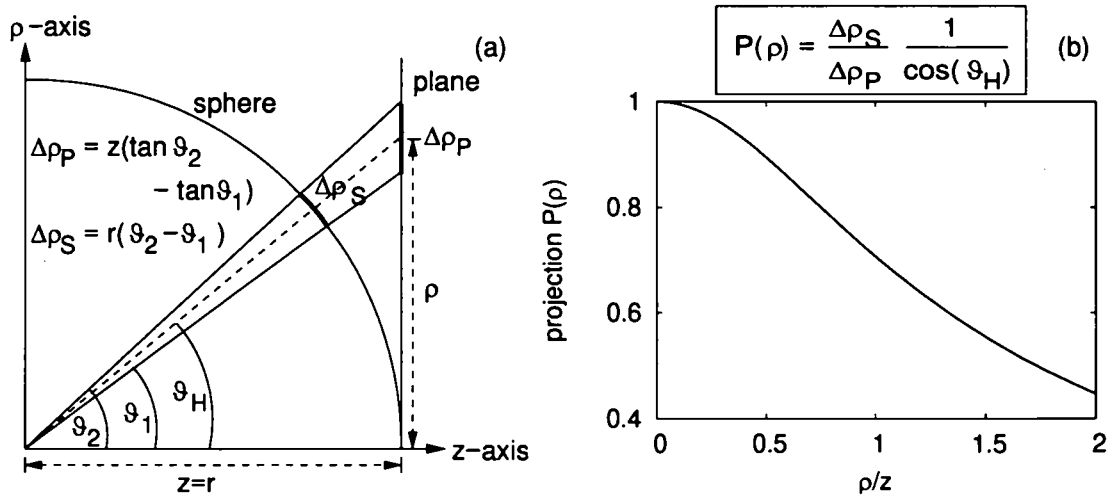


Figure 3.19: Projection factor required to account for the deviation of the visit function evaluated at a fixed z -plane from the corresponding contribution at the sphere with $r = z$. A schematic picture (a) and the dependence on ρ (Eq. (3.42)) (b) are shown.

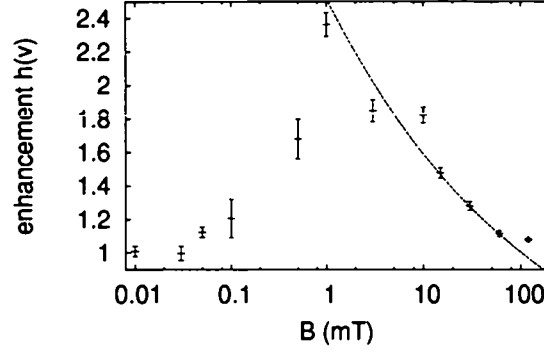


Figure 3.20: Enhancement ratio $h(\vec{v})$ (Eq. (3.25)) for $V^r(\vec{v})$ at different magnetic fields but fixed initial velocity ($v_z = 2.744 \times 10^{-3}$ a.u., $v_\perp = 1.372 \times 10^{-3}$ a.u.). The corresponding phase space portraits are illustrated in Figure 3.18. The dashed line is $\propto B^{-0.2}$.

the surface of a sphere in the asymptotic region does not depend on the orientation of the underlying coordinate system due to the spherical symmetry of the Coulomb potential and $V_{C,sim} = V_C$. However, since we initiate our simulation at a fixed z -plane perpendicular to the magnetic field, $V_{C,sim}(\vec{v})$ as obtained in the limit of $B \rightarrow 0$ is overestimated compared to the corresponding evaluation on the sphere (Figure 3.19). To compensate for this overestimate of visits, which is by no means negligible for $v_\perp \gtrsim v_\parallel$ (given by $\vartheta \gtrsim \pi/4$), we introduce the projection function

$$P(\vec{r}) = P(\rho) = \frac{\vartheta_2 - \vartheta_1}{\tan(\vartheta_2) - \tan(\vartheta_1)} \frac{1}{\cos((\vartheta_1 + \vartheta_2)/2)} \quad (3.42)$$

with $\vartheta_{2,1} = \arctan((\rho \pm \Delta\rho_P/2)/z)$ (Figure 3.19b). Visit functions including this projection should henceforth be labeled by the superscript r , *i.e.*

$$V^r(\vec{r}, \vec{v}) = P(\vec{r})V(\vec{r}, \vec{v}) \quad \text{and} \quad V_{C,sim}^r(\vec{r}, \vec{v}) = P(\vec{r})V_{C,sim}(\vec{r}, \vec{v}). \quad (3.43)$$

Employing $V_{C,sim}^r(\vec{v}) = \int d\phi \int d\rho \rho V_{C,sim}^r(\rho, \phi, \vec{v})$ the Coulomb contribution of visits is properly determined given by $h(\vec{v}) = 1$ (*i.e.* $V_{C,sim}^r(\vec{v}) = V_C(\vec{v})$). With $V_{C,sim}(\vec{v})$, however, the enhancement ratio at $B = 0$ would be $h(\vec{v}) \approx 1.12$ thus causing a 12 percent error even for the small velocity ratio of $v_\perp/v_z = 0.5$ studied in Figures 3.18 and 3.20.

Similarly, the projection Eq. (3.42) is required for small magnetic fields, where the lateral confinement of the dynamics imposed by B is so weak that visits to the ion can occur at such large transverse distances ρ of the order of the initial coordinate z . Only for higher magnetic fields $B \gtrsim 10$ mT non-zero values of V are

well localized at small ρ with $\rho/z \ll 1$ (compare Figure 3.18) so that $P(\rho)$ is close to 1 and hence $V^r(\vec{r}, \vec{v}) \approx V(\vec{r}, \vec{v})$. Nevertheless, for accuracy, we will retain $V^r(\vec{r}, \vec{v})$ at all field strengths for the determination of the recombination rates below.

For larger magnetic field strengths, V^r is laterally more confined, more irregular, and multiple visits to the target ion get more pronounced (Figure 3.18). However, the integration of V^r over ρ and ϕ reveals that its contribution is not necessarily increasing with the irregularity of the scattering dynamics, *i.e.* with increasing B . In fact, for the phase space portraits of Figure 3.18, the integrated visit function $V^r(\vec{v})$ and the resulting enhancement ratio $h(\vec{v})$ at first increase with the magnetic field with a maximum found at $B \approx 1$ mT and, thereafter, decrease with B obeying an approximate $B^{-0.2}$ scaling (Figure 3.20). This decrease in $h(\vec{v})$ can be attributed to the increased lateral confinement of the motion by the magnetic field which, eventually, leads to a strong reduction of the effective phase space volume (due to the decreased impact parameter ρ) contributing to V^r .

3.10 Velocity Projection of Visits

In this section an alternative determination of the visit function in a magnetic field will be discussed. According to Eq. (3.25) the definition of visits should, first, be independent of the specific orientation of the coordinate system used within our simulation and, secondly, converge to the Coulomb contribution (Eq. (3.30)) in the limit of $B \rightarrow 0$. In the pure Coulomb field, the area $V_C(\vec{v})$ with visits to the ion is evaluated perpendicular to the incident velocity of the electron. Note that this is the case for the analytical calculation of $V_C(\vec{v})$ via Eq. (3.30), where $\vec{v} = v_z \hat{e}_z$ is assumed, as well as for the determination of $V_{C,sim}^r(\vec{v})$ in our simulation, since in the pure Coulomb potential the transverse coordinate ρ and the transverse velocity v_\perp for an electron reaching the ion are directly related.

The projection perpendicular to \vec{v} might be performed in velocity space instead (see inset in Figure 3.21) according to the trigonometric relation

$$P(\vec{v}) = |\sin(\arctan(v_z/v_\perp))|. \quad (3.44)$$

We will denote visit functions accounting for this projection function in velocity space by the superscript v ,

$$V^v(\vec{r}, \vec{v}) = P(\vec{v})V(\vec{r}, \vec{v}) \quad \text{and} \quad V_{C,sim}^v(\vec{r}, \vec{v}) = P(\vec{v})V_{C,sim}(\vec{r}, \vec{v}). \quad (3.45)$$

The evaluation $V_{C,sim}^v(\vec{v}) = \int d\phi \int d\rho \rho V_{C,sim}^v(\rho, \phi, \vec{v})$ yields the correct contribution of visits in the Coulomb field with an enhancement ratio of $h(\vec{v}) = 1$ (Eq. (3.25)). Note that the application of both projections, the spatial projection of Eq. (3.42) and the velocity projection of Eq. (3.44), *i.e.* $V_{C,sim}^{rv}(\vec{r}, \vec{v}) = P(\vec{v})P(\vec{r})V_{C,sim}(\vec{r}, \vec{v})$, is obviously inconsistent and results in $h(\vec{v}) < 1$.

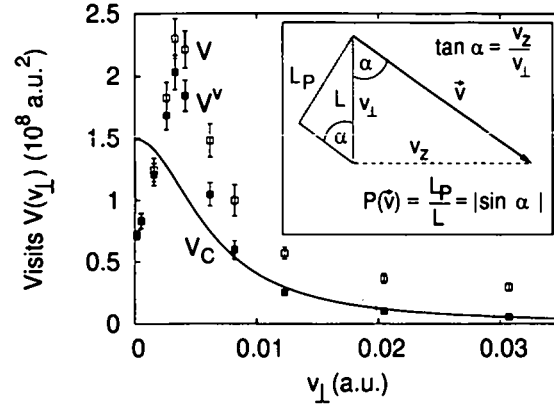


Figure 3.21: Visit functions V (red) and V^v (blue) integrated over coordinate space, i.e. $V^{(v)}(\vec{v}) = \int d\phi \int d\rho \rho V^{(v)}(\rho, \phi, \vec{v})$, as a function of the initial electron velocity v_{\perp} perpendicular to the magnetic field. For comparison, the Coulomb contribution of visits according to Eq. (3.30) (green) is also shown. The longitudinal velocity of the incident electrons has been fixed to $v_z = 6.141 \times 10^{-3}$ a.u.; $B = 42$ mT, $Z = 6$ and $r^{RR} = 150$ a.u.

Analogously, also the visit function in the combined Coulomb and magnetic fields could be evaluated as $V^v(\vec{r}, \vec{v})$ instead of $V^r(\vec{r}, \vec{v})$. Figure 3.21 illustrates the visit functions V and V^v for different transverse velocities and fixed longitudinal velocity of the incident electrons after integration over coordinate space. $V(v_{\perp})$ significantly exceeds the contribution of visits in the pure Coulomb field even at higher values of v_{\perp} ($v_{\perp} = 0.03$ a.u. corresponds to a perpendicular energy of $E_{\perp} \approx 12$ meV), whereas $V^v(v_{\perp})$ is reduced at large v_{\perp} thus compensating for the discrepancy between $V(v_{\perp})$ and $V_C(v_{\perp})$. For $v_{\perp} \rightarrow 0$ $P(\vec{v})$ tends to unity and V and V^v become identical. Note that at very small v_{\perp} , $V(v_{\perp})$ and $V^v(v_{\perp})$ fall below the Coulomb contribution V_C . In this case the magnetic field prevents an electron from visiting the target ion. For example, Figure 3.22a shows an electron trajectory with initial velocity into the z -direction ($v_{\perp} = 0$) with and without the presence of a magnetic field. Correspondingly, the magnetic field appears to counteract the deflection of the electron towards the nucleus induced by the Coulomb potential resulting in a larger distance of closest approach to the ion than in the pure Coulomb field (inset in Figure 3.22a). In addition, in Figure 3.22b the coordinate space integrated visit functions $V(v_z)$ ($= V^v(v_z)$) and $V_C(v_z)$ are illustrated for $v_{\perp} = 0$ (i.e. $P(\vec{v}) = 1$). V exhibits enhanced values at intermediate values of v_z ($v_z = 0.02$ a.u. corresponds to an energy of $E_z = 5.44$ meV), whereas approaching V_C for high v_z and falling below V_C for small v_z .

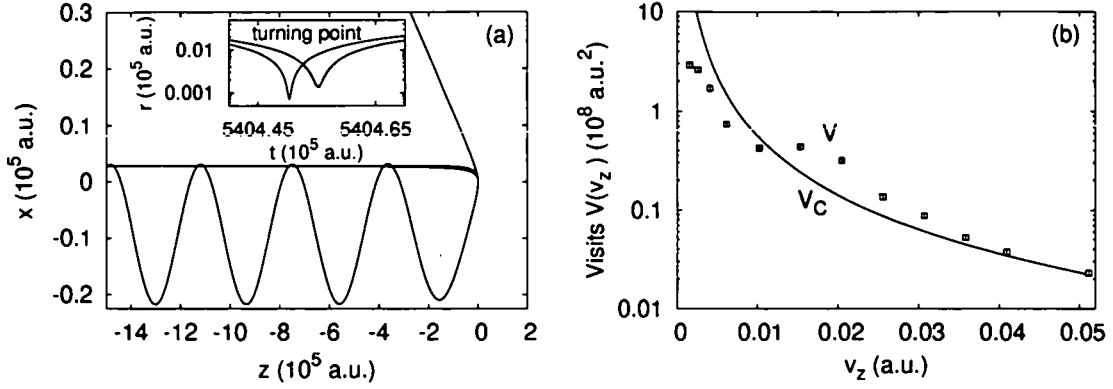


Figure 3.22: Electron trajectory with initial velocity $v_z = 0.01$ a.u. and $v_\perp = 0$ in the presence of Coulomb and magnetic fields (red) and the pure Coulomb field (green) depicted in (a) and the obtained visit function $V(v_z)$ after coordinate space integration shown in (b) as a function of v_z ($v_\perp = 0$, thus $P(\vec{v}) = 1$) in the combined fields (red) and the pure Coulomb field (green). The inset in (a) reflects the absolute distance to the ion versus the elapsed time around the distance of closest approach. Visits are defined for $r \leq r^{RR} = 150$ a.u. in (b); $B = 42$ mT and $Z = 6$.

3.11 Relative Energy Dependence of the Recombination Rate

As a first application we compare our simulation with the experimental data for C^{6+} observed at the TSR in Heidelberg [10]. The electron temperatures in this experiment are $kT_\parallel \approx 0.2$ meV and $kT_\perp \approx 10$ meV and the magnetic guiding field of the electron beam is $B = 42$ mT. Figure 3.23 shows the recombination rate as a function of the average relative energy E_{rel} between electrons and ions obtained with the visit function V^r . The standard RR theory (section 2.2), the experimental data and our CTMC results are displayed. We define V^r and V_C either with the sharp cutoff of contributions at $r^{RR} = n_r^2/Z$ (Eq. (3.41)) or via the weighting with σ_{nl}^{RR} (Eq. (3.39)). The calculated recombination rates (Eqs. (3.25), (3.26) and (3.30)) qualitatively agree with the measurements both in terms of the energy dependence and the overall magnitude of the effect. In fact, the CTMC calculation seems to overestimate the enhancement by 20 to 30 percent. Furthermore, the rate coefficients obtained with the different weighting functions for V^r (Eqs. (3.39), (3.41)) agree well. Therefore, the recombination rate does not appear to be sensitive to the shape of the effective region chosen for RR to take place, which confirms the validity of our simple classical description. In the subsequent analysis we confine ourselves to the

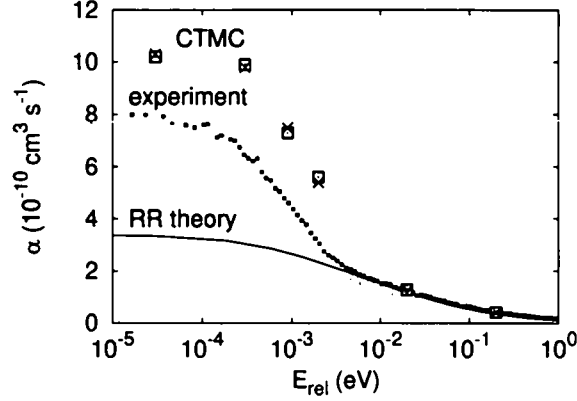


Figure 3.23: Radiative recombination rate for C^{6+} ions at $B = 42$ mT as a function of relative energy between electrons and ions. The standard RR theory (Eqs. (2.9), (2.11) and (2.12)) (green line), the experimental data [10] (red full squares) and the CTMC results for V^r (blue open squares, magenta crosses) (Eq. (3.26)) are shown. The blue squares correspond to a weighting of V^r according to Eq. (3.41) and the magenta crosses to a weighting with Eq. (3.39) respectively. $kT_{\parallel} = 0.2$ meV, $kT_{\perp} = 10$ meV and $n_r = 30$ are used.

definition of V^r using the step function weighting of Eq. (3.41).

We note that the number of visits is counted only within a time duration τ_c corresponding to the temporal overlap between electron and ion beam in the cooler. For the TSR experiment [10] $\tau_c \approx 60$ ns. In the CTMC, where the electron ensemble is launched from the asymptotic region according to a Maxwell-Boltzmann distribution in velocity space (Eq. (2.12)) and a uniform distribution in coordinate space, the interaction time is counted starting when the distance between electron and ion has reached typical interionic distances $r_{ion} = n_{ion}^{-1/3}$ (n_{ion} : ion density). We start the clock randomly at distances to the ion ranging from $r_{ion}/4$ to $3r_{ion}/4$. As Figure 3.24 presents within the time limit of $t \leq \tau_c$ the effect of multiple visits to the ion is comparatively small even at very low relative energies such as $E_{rel} = 0.03$ meV. Clearly, were a longer propagation time available multiple visits would become more important. The peak of the first visit in Figure 3.24 can be attributed to electrons visiting the ion at their first pass by. Accordingly, an electron with $v_z = v_{rel} = 1.485 \times 10^{-3}$ a.u. reaches the ion after 1.4 ns, 4.2 ns and 8.0 ns respectively depending on whether the time counting is initiated at a distance of $r_{ion}/4$, $r_{ion}/2$ or $3r_{ion}/4$ (with $r_{ion} = 1.765 \times 10^6$ a.u.) between electron and ion. Most of the irregular forth and back motion of typical trajectories around the ion (Figure 3.6) proceeds at distances to the ion much larger than the Coulomb zone S_C characteriz-

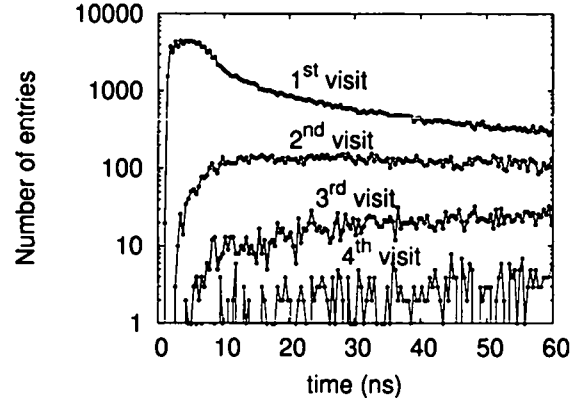


Figure 3.24: Number of first, second, third and fourth visits to the ion as a function of time duration inside the cooler. For the electronic ensemble shown about 1.56×10^5 trajectories contribute to V . The parameters are $Z = 6$, $B = 42$ mT, $n_r = 30$, $E_{rel} = 0.03$ meV, $kT_{\perp} = 5$ meV, $kT_{\parallel} = 0.06$ meV and $r_{ion} = 1.765 \times 10^6$ a.u.

ing the effective region for RR. Therefore, multiple visits are found to play a minor role for the enhancement of the recombination. For comparison, in Figure 3.25 the calculated recombination rates including all the visits within τ_c are compared with the rate coefficients resulting from only the first visits to the ion ($V^r \leq 1$). Nevertheless, the presence of the magnetic field enhances the recombination rate efficiently when using the visit function V^r , since due to the chaotic dynamics an increased volume of asymptotic phase space contributes with visits to the ion compared to the pure Coulomb field.

We have also evaluated the recombination rates applying the visit function V^v (Figure 3.26). While the calculated rates agree with the experimental data and the standard RR theory at $E_{rel} \geq 10$ meV, the behavior of α at smaller relative energies is remarkable. An increase of α towards lower E_{rel} is observed but stops at $E_{rel} \approx 1$ meV and for still smaller values of E_{rel} , even gets reversed into a decrease. At relative energies close to zero the CTMC rates are reduced to only one half of the value predicted by the standard theory and cover not even 20 percent of the measured rate coefficient. This drop of α below α_{RR} is consistent with the behavior of V^v at small longitudinal velocities (Figure 3.22b), where the Kepler motion in the pure ionic Coulomb potential brings an electron closer to the ion than the dynamics in the combined Coulomb and magnetic fields. While with V^r enhanced recombination can be mainly observed at larger transverse velocities (compare Figure 3.21), a large part of this enhancement is, however, removed in V^v thus leading to a much smaller effect on the recombination rate. In short, the interplay between the suppression of

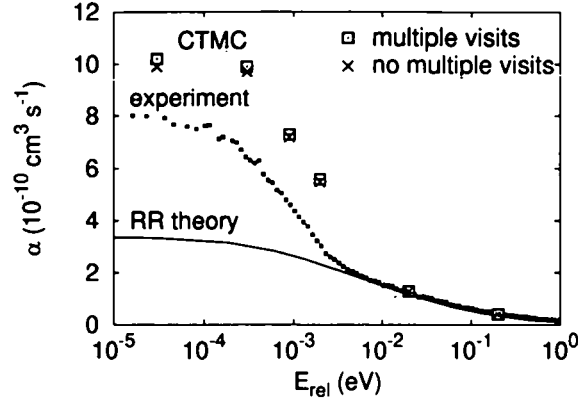


Figure 3.25: Radiative recombination rate for C^{6+} ions at $B = 42$ mT as a function of relative energy between electrons and ions. The standard RR theory (Eqs. (2.9), (2.11) and (2.12)) (green line), the experimental data [10] (red full squares) and the CTMC results for V^r (Eq. (3.26)) with (blue open squares) and without (magenta crosses) multiple visits taken into account are drawn. Same parameters as in Figure 3.23.

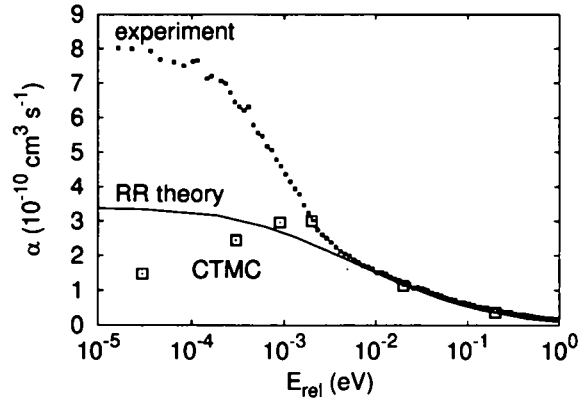


Figure 3.26: Radiative recombination rate for C^{6+} ions and $B = 42$ mT as a function of relative energy between electrons and ions. The CTMC results for V^v (blue open squares) are compared with the standard RR theory (green line) and the experimental data [10] (red full squares). Parameters are the same as in Figure 3.23.

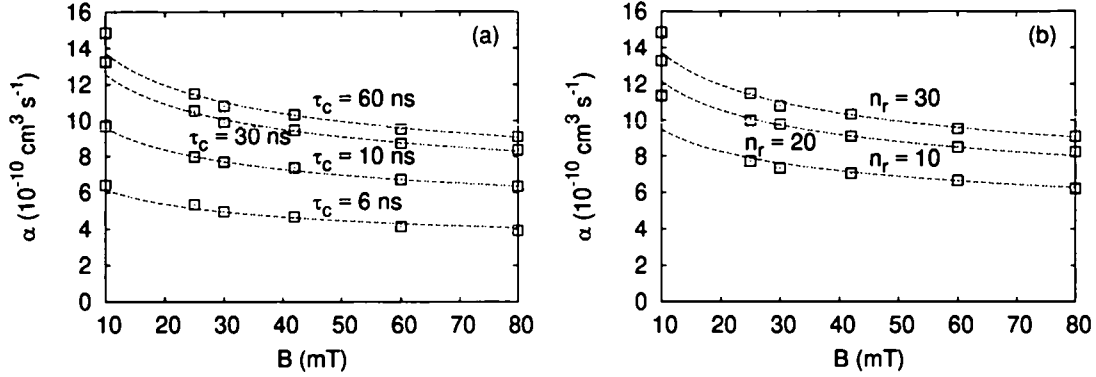


Figure 3.27: Radiative recombination rate with V^r for C^{6+} ions at $E_{\text{rel}} = 0.03$ meV as a function of the magnetic guiding field in the electron cooler. Variations in the interaction time τ_c between electrons and ions (a) or the maximum principal quantum number n_r of the recombined ions (b) do not change the scaling of the rate coefficients with B . Electron temperatures are fixed to $kT_{\parallel} = 0.06$ meV and $kT_{\perp} = 5$ meV; $n_r = 30$ in (a) and $\tau_c = 60$ ns in (b). The lines drawn to guide the eye are $\propto B^{-0.2}$.

V at small v_{\perp} and the enhancement of V at higher v_{\perp} (large contribution to V^r , but only small-sized for V^v) determines the shape of the resulting recombination rates.

In the following systematic studies of the dependence of α on B , Z , kT_{\parallel} and kT_{\perp} will be presented. First we focus on the results for V^r . Only later we will discuss the effect of V^v on the recombination rates.

3.12 Magnetic Field and Charge Dependence of the Recombination Rate

First we study the recombination rates at low relative energies between the electron and the ion for different magnetic field strengths B . Henceforth we use the visit function V^r for the evaluation of α . The magnetic field dependence of α acquired for an ensemble of electrons representing the electron beam in the cooler reflects the B behavior of the enhancement ratio $h(\vec{v})$ found for fixed electron velocities (compare Figure 3.20). Accordingly, for magnetic field strengths accessible in the experiment (at the TSR $20 \text{ mT} \leq B \leq 70 \text{ mT}$ [10]) α is seen to decrease approximately as $B^{-0.2}$ (Figure 3.27). In Figure 3.27 the calculated recombination rates are shown for varying interaction times τ_c between electron and ion and different principal quantum numbers $n \leq n_r$ contributing to recombination. Neither a variation in τ_c

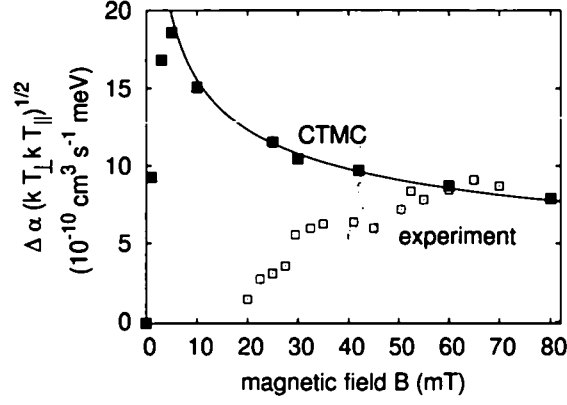


Figure 3.28: Magnetic field dependence of the excess recombination for C^{6+} ions. The CTMC results with V^r (blue full squares) are compared with the experimental data of the TSR experiment [10] (red open squares). The excess rates $\Delta\alpha = \alpha - \alpha_{RR}$ are scaled with $\sqrt{kT_{\perp}kT_{\parallel}}$ according to the temperature dependence found in [10]. In the CTMC $E_{rel} = 0.03$ meV, $kT_{\parallel} = 0.2$ meV, $kT_{\perp} = 10$ meV and $n_r = 30$. The line is $\propto B^{-1/3}$. Note that the error bar is within the symbol size for all datapoints.

nor in n_r noticeably influences the observed scaling with B .

Furthermore, Figure 3.28 compares the computed absolute excess rate coefficients $\Delta\alpha = \alpha - \alpha_{RR}$ (α_{RR} : standard RR rate) with the corresponding measurements of the TSR experiment [10]. Note that $\Delta\alpha$ is scaled with $\sqrt{kT_{\perp}kT_{\parallel}}$ according to the temperature dependence observed in [10]. Similarly, as for the enhancement ratio illustrated in Figure 3.20 the maximum excess rate emerges at a comparatively small magnetic field such as $B \approx 5$ mT. For lower values of B the excess recombination decreases and approaches zero at $B = 0$, *i.e.* the standard RR rate is recovered at zero magnetic field. Due to the increasing inefficiency of our simulation with decreasing field strength (compare Table 3.1) huge ensemble sizes are required for the representation of the recombination rate at the smallest values of B in Figure 3.28. For $B \geq 10$ mT $\Delta\alpha$ scales approximately as $B^{-1/3}$. This $B^{-1/3}$ dependence is in contrast to the experimental observation of $\Delta\alpha \sim B^{0.5}$ [10]. Thus, the chaotic dynamics inside the solenoid fails to account for the magnetic field dependence of the excess rate observed in the measurements. As pointed out previously (section 3.9) the decreasing cyclotron radius, $r_c \propto 1/B$, reduces the number of visits to the ion with increasing B which, in turn, leads to a smaller recombination rate.

In addition, we have investigated the Z dependence of $\Delta\alpha$. Figure 3.29 illustrates our CTMC results and the appropriate experimental data from the CRYRING experiment [9]. The chaotic dynamics increases the recombination with increasing

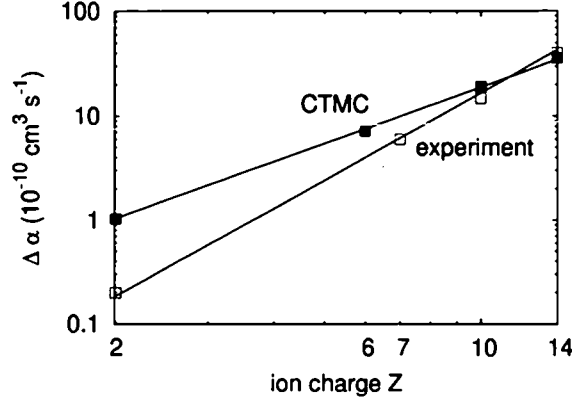


Figure 3.29: Charge dependence of the excess recombination rate $\Delta\alpha = \alpha - \alpha_{RR}$ at $B = 30$ mT. The CTMC results with V^r (blue full squares) for $E_{rel} = 0.03$ meV, $kT_{\parallel} = 0.12$ meV and $kT_{\perp} = 10$ meV and the corresponding experimental data of the CRYRING experiment [9] (red open squares) are shown. n_r is set to 10, 23, 35 and 43 for He^{2+} , C^{6+} , Ne^{10+} and Si^{14+} , respectively. The lines indicate a $Z^{1.8}$ behavior found for our CTMC data and the $Z^{2.8}$ trend observed in the measurements of Ref. [9].

nuclear charge due to an enhanced flux of electrons visiting the ion. We find that the scaling with Z exhibits a trend in agreement with the measurements, however, the calculated excess recombination rate scales approximately as $Z^{1.8}$ while the experimental data in [9] was fitted by $\Delta\alpha \sim Z^{2.8}$.

We note that the dependence of α on Z and B , *i.e.* increasing with Z and decreasing with B , is consistent with the classical scaling relations of Eq. (3.23), whereupon the characteristic length scale r^{RR} for RR to take place obeys counteracting scaling laws with Z and B , namely $\propto Z^{-1/3}$ and $\propto (B/c)^{2/3}$. Correspondingly, the scaling of r^{RR} is found to influence the Z and B dependence of the recombination rate. Along those lines, a cutoff in momentum space, $p \geq p^{RR}$, which scales with Z and B in the same way (Eq. (3.23)), appears to be more suitable for the definition of V^r and thus the determination of α . A representation of visits in momentum space and the resulting gauge dependence of the classical description will be discussed in section 3.15.

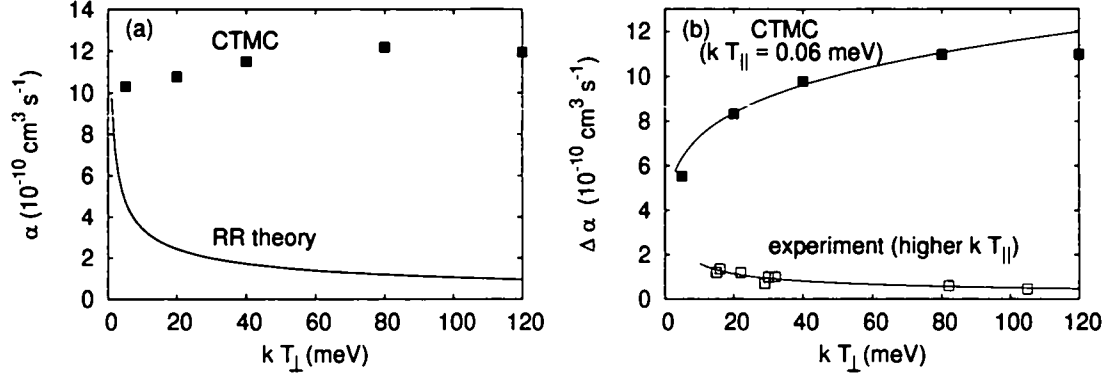


Figure 3.30: Recombination rate for C^{6+} ions at $B = 42$ mT and $E_{rel} = 0.03$ meV as a function of the perpendicular electron temperature. The rate coefficients α with V^r (Eq. (3.26)) (blue full squares) and α_{RR} (Eq. (2.11)) (green line) are illustrated in (a) and the resulting excess rates $\Delta\alpha = \alpha - \alpha_{RR}$ (blue full squares) are compared with the experimental data [10] (red open squares) in (b). The lines in (b) are $\propto (kT_{\perp})^{-0.5}$ for the measurements and $\propto (kT_{\perp})^{0.2}$ for the CTMC data. $n_r = 30$ and $kT_{\parallel} = 0.06$ meV in the simulation, whereas kT_{\parallel} has been higher in the measurements.

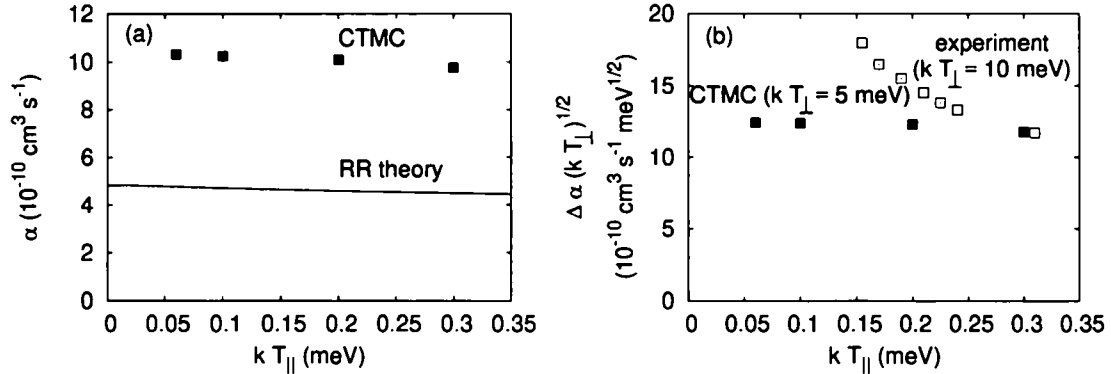


Figure 3.31: Recombination rate for C^{6+} ions at $B = 42$ mT and $E_{rel} = 0.03$ meV as a function of the parallel electron temperature. The CTMC results for α using V^r (blue full squares) and the standard rates α_{RR} (green line) (a) and the corresponding scaled excess rates $\Delta\alpha (kT_{\perp})^{0.5}$ (blue full squares) together with the experimental data of [10] (red open squares) (b) are shown; $n_r = 30$. Note that $kT_{\perp} = 5$ meV in the CTMC, whereas $kT_{\perp} \approx 10$ meV in the experiment.

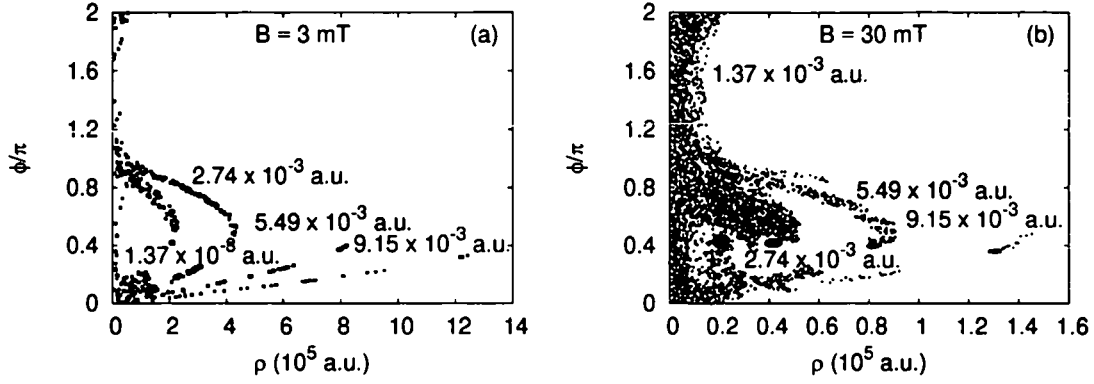


Figure 3.32: Phase space region of non-zero visit function $V(\vec{r}, \vec{v})$ at $B = 3$ mT (a) and $B = 30$ mT (b) for different fixed initial velocities v_\perp (values indicated) transverse to the magnetic field. The longitudinal initial velocity is $v_z = 2.744 \times 10^{-3}$ a.u. and the initial coordinate $z = -7.167 \times 10^6$ a.u. Visits are defined for $r < r^{RR} = 100$ a.u.

3.13 Temperature Dependence of the Recombination Rate

We have also analyzed the dependence of the recombination rate on the electron beam temperatures at low relative energy. Figures 3.30a and 3.31a display the rate coefficients at $E_{rel} = 0.03$ meV as a function of kT_\perp and kT_\parallel respectively both for the calculated rates α in the combined Coulomb and magnetic fields and the standard radiative recombination rates α_{RR} . Whereas α_{RR} decreases with kT_\perp (i.e. $\alpha_{RR} \sim (kT_\perp)^{-0.5}$), the CTMC rates, however, are seen to increase with the perpendicular temperature (Figure 3.30a). This remarkable trend of α is consistent with its scaling with B and the observation that the phase space structure of non-zero visit function is altered in the same way by a decrease of B as by an increase of v_\perp (compare section 3.9 and Figures 3.18 and 3.32). To emphasize this similarity between small v_\perp and large B in $V(\vec{r}, \vec{v})$ Figure 3.32 illustrates the phase space region of non-vanishing values of V for fixed magnetic field strength and parallel velocity but different perpendicular velocities of the incident electron. Therefore, analogous to the behavior of the enhanced recombination with B , a reduction in α will become visible only at high transverse temperatures. The resulting excess recombination rate $\Delta\alpha = \alpha - \alpha_{RR}$ follows approximately a $(kT_\perp)^{0.2}$ scaling in our simulation in contrast to the experimental finding of $\Delta\alpha \sim (kT_\perp)^{-0.5}$ (Figure 3.30b). Hence, also the scaling of the excess recombination with the perpendicular electron temperature contradicts the measurements.

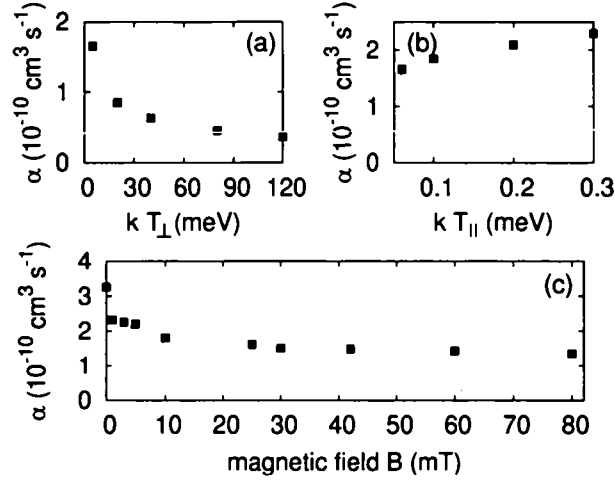


Figure 3.33: Radiative recombination rates evaluated with V^v . The dependence of α on kT_{\perp} (a), kT_{\parallel} (b) and the magnetic guiding field (c) is displayed. $E_{rel} = 0.03$ meV, $Z = 6$ and $n_r = 30$; $B = 42$ mT (a), (b), $kT_{\parallel} = 0.06$ meV (a), $kT_{\perp} = 5$ meV (b) and $kT_{\parallel} = 0.2$ meV, $kT_{\perp} = 10$ meV (c).

On the other hand, the recombination rate, α as well as α_{RR} , exhibits a slight decrease with kT_{\parallel} (Figure 3.31a). The obtained excess rate coefficient $\Delta\alpha$ though reduces only marginally with increasing parallel temperature with a scaling much weaker than the experimentally established $\Delta\alpha \sim (kT_{\parallel})^{-0.5}$ dependence (Figure 3.31b).

3.14 Parameter Dependences for the Velocity Projection of Visits

Finally, we investigate the behavior of the recombination rates with the electron beam temperatures and the magnetic guiding field using the velocity projected visit function V^v (Figure 3.33). Whereas a decrease of α with kT_{\perp} is obtained, an increase with kT_{\parallel} is found in agreement with the increase of α observed at low relative energies (compare Figure 3.26). The magnetic field dependence of the recombination now exhibits an increasing trend all the way down to $B = 0$, where α_{RR} is recovered again. Therefore, by evaluating α with V^v , the enhancement of the recombination is not only suppressed but even reversed into a decline of the rate below the prediction of the standard RR theory at small relative energies. This implies that the chaotic dynamics in the magnetic field rather reduces than increases the probability for radiative recombination at matched beam velocities. On top of this overall reduction

the scaling of α with B and kT_{\parallel} contradicts the measurements.

3.15 Visits in Momentum Space

The visit function V discussed so far represents close encounters of an electron to the target ion in coordinate space. With increasing magnetic field strength B , however, the effective spatial volume traversed by an electron decreases (cyclotron radius $\sim 1/B$) and the number of visits to the ion gets reduced. Correspondingly, the recombination rate (no matter whether evaluated with V^r or V^v) decreases with B , which contradicts the measurements. The reduction of this effective spatial volume can also be seen from the classical scaling relations (compare Eq. (3.23))

$$H = (B/c)^{2/3} Z^{2/3} H_0 = (B/c)^{2/3} Z^{2/3} \left(\frac{p_0^2}{2} - \frac{1}{r_0} + \frac{1}{2} L_{z0} + \frac{1}{8} (x_0^2 + y_0^2) \right) \quad (3.46)$$

$$\vec{r} = (B/c)^{-2/3} Z^{1/3} \vec{r}_0, \quad (3.47)$$

$$\vec{p} = (B/c)^{1/3} Z^{1/3} \vec{p}_0, \quad (3.48)$$

where the subscript 0 again refers to scaled quantities. According to Eq. (3.47) coordinate space gets enlarged with increasing ion charge Z , but reduced with increasing magnetic field strength B , a behavior reflected in the recombination rate (Eq. (3.26)). On the other hand, in momentum space (Eq. (3.48)) the same scaling with both Z and B is observed. This opposite scaling of \vec{p} with B compared to the scaling of \vec{r} indicates that the effective volume in momentum space, or in other words, visits of the electron towards the nucleus in momentum space, increases as a function of the magnetic field. Such a different behavior of V with \vec{r} and \vec{p} respectively originates from the gauge dependence of the classical approach. The precise value of p is different for different gauges used for the representation of the magnetic field. The more appropriate the chosen gauge is, the better description of the measurements can be expected.

Visits in momentum space can be represented, in analogy to the coordinate space definition (section 3.5), by the condition $p \geq p^{RR}$, where p^{RR} denotes the minimum momentum required for a visit to occur. This definition, however, faces serious difficulties for electrons launched at larger transverse distances from the ion. Since the absolute momentum (using the symmetric gauge again) is calculated as $p = \sqrt{(v_x + 1/(2c)By)^2 + (v_y - 1/(2c)Bx)^2 + v_z^2}$, large transverse coordinates x or y are seen to dramatically increase its value. Multiple visits in momentum space are thus determined for trajectories with high transverse displacements from the ion, for which radiative recombination could never occur. Note that these artificially created multiple visits get more pronounced the larger the magnetic field strength B becomes. Figure 3.34 shows two sample trajectories at $B = 90$ mT, one behaving

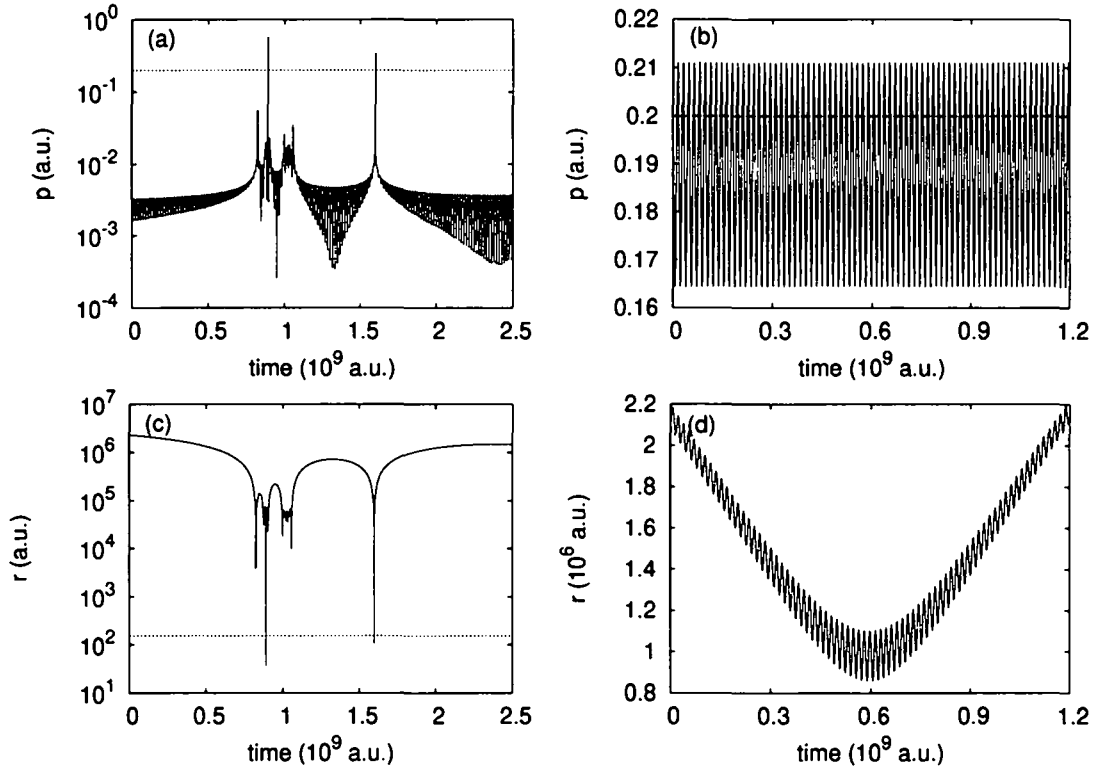


Figure 3.34: Absolute value of momentum (a), (b) and distance to the ion (c), (d) as a function of propagated time for two different electron trajectories ((a), (c) and (b), (d) respectively) at $B = 90$ mT and $Z = 6$. The electron is initiated from a fixed z -plane and a transverse distance from the nucleus of $\rho \approx 2.772 \times 10^3$ a.u. (c) and $\rho = 8.630 \times 10^5$ a.u. (d). Note that with $n_r = 30$ the upper limit in r amounts to $r^{RR} = n_r^2/Z = 150$ a.u. and the lower limit in p to $p^{RR} = Z/n_r = 0.2$ a.u. (horizontal dashed lines). Whereas the first trajectory exhibits two visits in momentum space (a) and in coordinate space (c), the second trajectory reveals multiple visits in momentum space (b) but no visit in coordinate space (d).

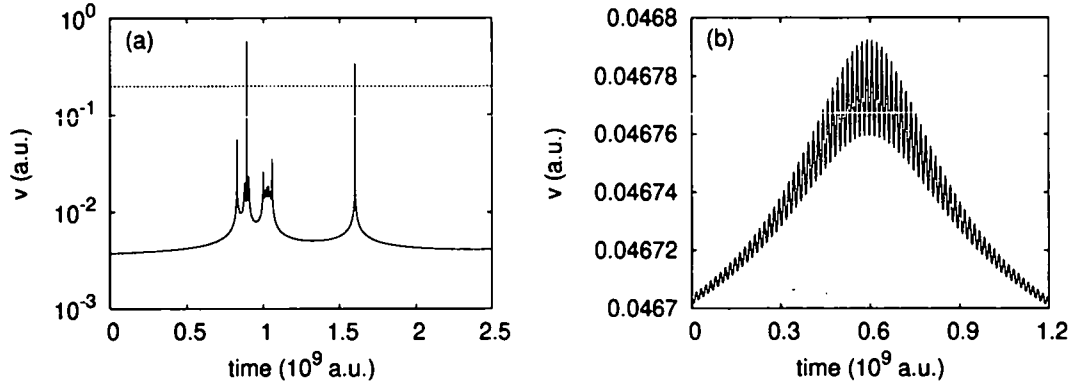


Figure 3.35: Absolute value of velocity as a function of propagated time for the two electron trajectories of Figure 3.34. $v^{RR} = Z/n_r = 0.2$ a.u. (dashed line in (a)). The first trajectory exhibits two visits in velocity space (a) and the second one none (b) in agreement with the coordinate space behavior in Figures 3.34c, 3.34d.

as desired with visits in momentum space at simultaneous small spatial distances from the ion (Figures 3.34a and 3.34c) and the second one demonstrating the effect of artificial multiple visits in momentum space observed at spatial distances as large as 10^6 a.u. (Figures 3.34b and 3.34d). Accordingly, a simple classification of visits analogous to the coordinate space approach is not applicable. In appendix D alternative considerations towards a calculation of recombination rates in momentum representation are given and a perturbative model for the quantum rate with Landau states as initial wavefunctions for the incident electrons is discussed. However, a satisfying description of the recombination of a continuum electron in the combined Coulomb and magnetic fields could not be given.

A more promising possibility is to define visits via the mechanical momentum (*i.e.* velocity) instead of the canonical one (Figure 3.35). A determination of visits according to $v \geq v^{RR}$ (v^{RR} : lower cutoff in velocity for $V > 0$) agrees with the coordinate space representation of visits (compare Figures 3.34c, 3.34d and 3.35). The problem of artificial multiple visits at large spatial distances from the nucleus does not occur. Therefore, a definition of V via a velocity based selection criterion seems to be more reasonable than a corresponding cutoff in momentum space. Note that both \vec{r} and \vec{v} are gauge independent quantities. The recombination rates determined from the velocity and coordinate space evaluation of visits agree.

3.16 Formation of Bound States in the Solenoid: Coupling between the Center of Mass and Relative Motions

The possibility of forming bound states within the solenoid can be considered as well. As discussed in section 3.2, the center of mass (CM) and relative motions are coupled in the presence of a magnetic field B . Even if this coupling is weak, the relative energy E_{rel}^{e-ion} between electron and ion could be reduced such that a bound state is formed inside the solenoid given by $E_{rel}^{e-ion} < 0$. Figure 3.36 shows an electron captured by a C^{6+} ion during its passage through the solenoid according to the parameters of the TSR experiment [10]. However, the observed binding energy is very small. Neglecting at the moment the magnetic field, the relation $n = Z/\sqrt{2|E_{rel}^{e-ion}|}$ is used to assign a principal quantum number n to the populated bound state at the end of the solenoid. For instance, the C^{5+} Rydberg state of Figure 3.36 with $E_{rel}^{e-ion} \approx -8 \times 10^{-8}$ a.u. at $t = 60$ ns possesses a quantum number as high as $n = 15000$. The electron and ion motions parallel to the magnetic field direction proceed such that the electron passes the ion and vice versa (Figure 3.36b). Since the CM and total energies E_{CM}^{e-ion} and E^{e-ion} are more than 10 orders of magnitude larger than the relative energy E_{rel}^{e-ion} (in Figure 3.36 $E^{e-ion} \approx 2.1 \times 10^6$ a.u. compared to the small value of $E_{rel}^{e-ion}(t=0) \approx 6.3 \times 10^{-8}$ a.u.), the determination of E_{CM}^{e-ion} and E^{e-ion} up to an accuracy of better than 10^{-8} a.u. is numerically difficult. In fact, the limitation in representation of a double precision real number in Fortran given by 16 significant digits is almost reached in Figure 3.36a thus some numerical uncertainties and fluctuations become visible in the representation of E_{CM}^{e-ion} and E^{e-ion} . By contrast, E_{rel}^{e-ion} , the quantity of interest for recombination, can be very precisely determined during the calculation.

We have investigated the formation of bound states inside the solenoid for a typical ensemble of electrons available at the TSR experiment. The total fraction of bound states accumulated at the end of the solenoid is very small. For the ensemble of Figure 3.37 (with $E_{rel}^{e-ion}(t=0) > 0$) the acquired bound-state fraction is approximately 1.0×10^{-4} . Figure 3.37 depicts the bound states formed at the end of the solenoid as a function of the initial relative energy at the beginning of the solenoid. Only extremely high Rydberg states get populated inside the solenoid, *i.e.* $n \geq 8000$ for the parameters of Figure 3.37. These highly excited states cannot be observed in the measurements. In the electron cooler such high-lying Rydberg states will be field-ionized again during the separation of the electron and ion beams in the toroidal demerging section adjacent to the solenoid. In addition, radiative decay of these Rydberg states to lower lying bound states before the demerging toroid is by far too slow to populate low n states that could survive the demerging region

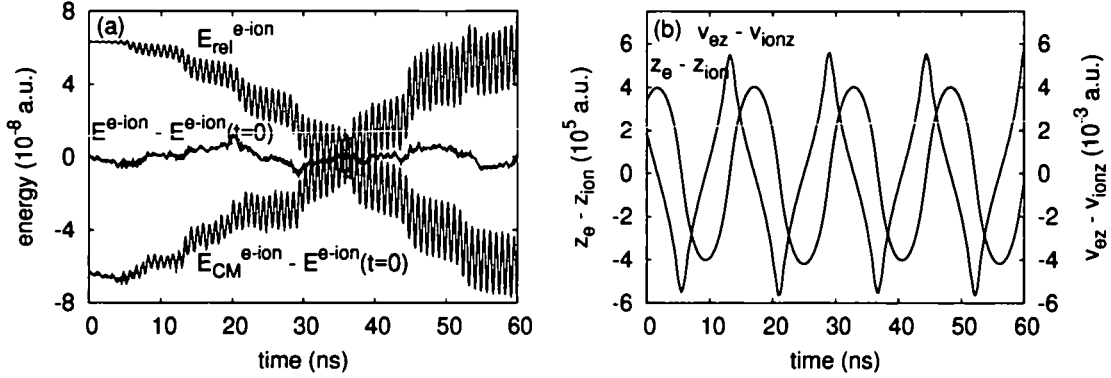


Figure 3.36: Electron captured by a C^{6+} ion ($E_{rel}^{e-ion} < 0$) during the combined propagation of the electron and ion (beam velocities of $0.1c$) through the solenoid with $B = 42$ mT. The total, CM and relative energies (a) and the relative coordinate and velocity components parallel to the magnetic field (b) are illustrated. Note that in (a) E_{CM}^{e-ion} and E^{e-ion} are shown with reference to the total energy at the beginning of the solenoid $E^{e-ion}(t=0)$. The initial electron-ion relative distance and velocity have been $r = |\vec{r}_e - \vec{r}_{ion}| \approx 4.1415 \times 10^5$ a.u. and $v = |\vec{v}_e - \vec{v}_{ion}| \approx 5.3947 \times 10^{-3}$ a.u. respectively.

of the cooler let alone the subsequent charge analyzing bending magnet prior to the recombination detector. A detailed discussion of field-ionization in the various magnets of the experimental setup and radiative stabilization of high Rydberg states inside the solenoid can be found in the next chapter. At this point, we can state that the generation of bound states inside the solenoid due to the coupling of the internal and CM energies of individual electron-ion pairs can be safely neglected for the investigation of the experimental rate enhancement.

3.17 Summary

We have shown that the classical dynamics of an electron in the simultaneous presence of the Coulomb field of an ion and the magnetic guiding field in the cooler is dramatically changed compared to the Kepler motion in a pure Coulomb field. We have presented a quantitative analysis of the chaotic scattering dynamics in a magnetic field in terms of the visit function characterized by close encounters in phase space (coordinate, velocity) of an electron to the target ion. Depending on whether the electronic visits to the ion are evaluated at an asymptotic sphere around the nucleus (V^r) or perpendicular to the incident velocity of the incoming electron (V^v) an enhancement or a reduction of the radiative recombination process can be

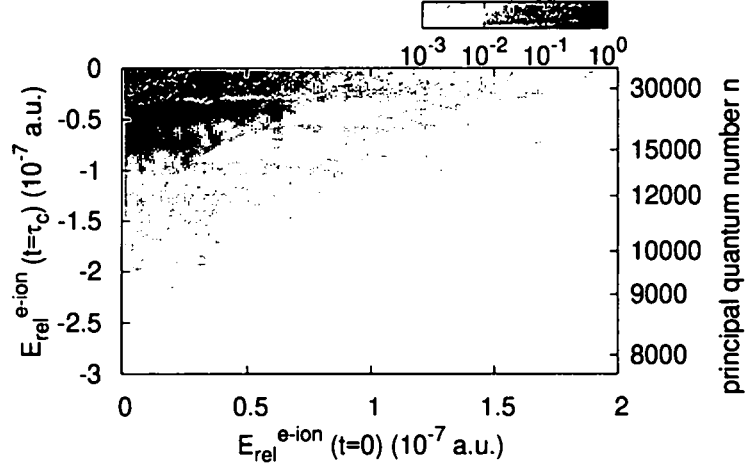


Figure 3.37: Negative energies ($E_{rel}^{e-ion} < 0$) obtained inside the solenoid due to the small but finite coupling between the CM and relative motions of individual electron-ion pairs. A density plot of the initial energies $E_{rel}^{e-ion}(t=0)$ and the reached binding energies $E_{rel}^{e-ion}(t=\tau_c) < 0$ at the end of the solenoid is displayed. As a reference, the corresponding principal quantum numbers n are also given. The parameters are the same as in Figure 3.3: $Z = 6$, $B = 42$ mT, $kT_{\perp} = 10$ meV, $kT_{\parallel} = 0.06$ meV, $E_{rel} = 0.03$ meV, the spatial diameter of the initial electron ensemble is 1.765×10^6 a.u. and the overall beam velocities are 0.1c. Note that the total fraction of bound states at $t = \tau_c$ amounts to 1.0×10^{-4} for the investigated ensemble. The density is plotted on a logarithmic scale and the peak height is normalized to 1.

observed at small relative velocities between electron and ion. In both cases at zero magnetic field the standard RR rate is recovered rendering a decision of whether V^r or V^v is more appropriate for the calculation of α in a magnetic field difficult.

However, even with V^r , where enhanced recombination rates at low relative velocities are obtained in accordance with the measurements, neither the dependence of the excess recombination on kT_{\parallel} and kT_{\perp} nor on Z and B can be reproduced within our CTMC calculations. Concerning Z and kT_{\parallel} at least the general trend of $\Delta\alpha$ observed in the experiments is confirmed by our simulations, with $\Delta\alpha \sim Z^{1.8}$, whereas the experimental finding is $\Delta\alpha \sim Z^{2.6}$ (with ions up to $Z = 92$ included), and $\Delta\alpha$ only weakly decreasing with kT_{\parallel} compared to an experimental scaling of $\Delta\alpha \sim (kT_{\parallel})^{-0.5}$. The calculated B and kT_{\perp} dependences contradict the measurements. In the simulation we find $\Delta\alpha \sim B^{-1/3}$ and $\Delta\alpha \sim (kT_{\perp})^{0.2}$ in contrast to the experimental observations of $\Delta\alpha \sim B^{0.5}$ and $\Delta\alpha \sim (kT_{\perp})^{-0.5}$ respectively. Thus, the chaotic dynamics inside the solenoid (as determined from the visit function V^r) cannot satisfactorily account for the experimentally observed enhancement of the recombination. Employing V^v the enhancement of the recombination persists only for a narrow interval of relative energies, while it has completely disappeared at zero relative energy. This is due to the fact that at small longitudinal and transverse velocities of the electron the magnetic field rather prevents than assists the recombination with the target ion.

In summary, we have presented various visit functions satisfying 1) the convergence towards the standard rate α_{RR} as $B \rightarrow 0$ and 2) the gauge independence of the recombination rate. However, V^v and V^r produce non-unique recombination rates ranging from a reduction of the standard RR rate to an overestimation of the measurements. Furthermore, we have shown that the formation of bound states inside the solenoid due to the small coupling between the center of mass (CM) and relative energies of individual electron-ion pairs can be safely neglected.

Chapter 4

Merging of Electron and Ion Beam

While our simulations of the solenoid region inside the electron cooler presented in the previous chapter have shown either enhanced or reduced recombination rates at low relative velocities depending on the specific visit function V^r or V^v employed, the scaling of the calculated rate coefficients with the magnetic field strength contradicts the measurements in both cases. Therefore an additional field dependent mechanism contributing to the enhancement of the recombination appears to be operative. Another mechanism which may influence the electron-ion recombination rates was suggested by Gwinner *et al.* [45]: during the merging of an electron and an ion beam in the electron cooler of the storage ring a transient motional electric field is present in the rest frame of the ion which, in turn, may open an additional pathway for free-bound transitions of electrons. In this chapter the efficiency of this alternative route to recombination will be investigated.

We present simulations performed for the toroidal merging geometry of the Test Storage Ring (TSR) electron cooler. After a detailed discussion of the merging geometry and the involved electric field strengths we analyze the field-induced formation of Rydberg states during the merging followed by radiative stabilization inside the solenoid. While we have explored direct radiative recombination of an electron with the target ion in the previous chapter, kinematic recombination into high Rydberg states in combination with subsequent radiative decay of these high-lying bound states is the topic of the present chapter. The dynamics of weakly bound Rydberg electrons in comparably strong magnetic and Coulomb fields will be visualized. We will show that the bound-state motion (chaotic or quasi-periodic) results in an invariant distribution of angular momentum states during propagation through the solenoid. Computing radiative decay rates we find a significant contribution to recombination into experimentally observable low-lying Rydberg states. The scaling of the obtained excess recombination rates with the ion charge Z and the magnetic guiding field B will be discussed.

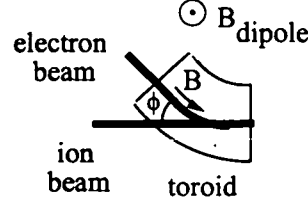


Figure 4.1: Electron and ion beam are merged in the toroidal region of the electron cooler. The magnetic field consists of a toroidal component and a dipole field perpendicular to the toroid plane.

4.1 Recombination in Transient Electric Fields

Gwinner *et. al.* [45] studied the influence of motional electric fields at the toroidal merging and demerging sections in the electron cooler (Figures 4.1 and 4.3a). In the cooler the electron beam is brought to overlap with the ion beam by a toroidal magnetic field strength B , aligned along the curvature of the toroid, *i. e.* $B_x = -B \sin \phi$ and $B_y = B \cos \phi$, where $\phi \leq 0$ denotes the opening angle with respect to the entrance plane of the solenoid ($\phi = 0$ inside the solenoid) with Cartesian coordinates (x, y) defining the toroid bending plane at $z = 0$. For a schematic picture of the coordinate system see Figure 4.4a. This longitudinal magnetic field guides the electrons along the bending of the toroid while avoiding a geometric expansion of the beam due to space charge effects (Coulomb repulsion between the electrons). In addition, also a magnetic dipole field perpendicular to the plane of the toroid $B_z = B_{dipole}$ is required to ensure the complete merging of the electron beam (Figure 4.1). Without such a perpendicular dipole field applied, the electrons would drift away in the direction perpendicular to the toroid plane due to the Lorentz force $F_z = v_{ex}B_y - v_{ey}B_x$ (Figure 4.2). Thus, the strength of the dipole field must be chosen such as to compensate this undesirable drift motion.

We investigate the electronic motion using the data for the merging geometry available at the TSR where the toroid has a bending radius of $r_t = 80$ cm and an opening angle of $\phi_t = 45$ degrees. At $B = 42$ mT B_{dipole} is estimated to be about 0.2 mT in order to obtain an electron trajectory bending properly along the curvature of the toroid (Figure 4.2). For simplicity, we did not consider the decrease of B_{dipole} at the end of the toroid within our simulation.

To ensure the guiding of the electrons, the magnetic field strength B and the central bending r_t of the toroid must fulfill $Br_t \gg v_{ec}$ [64]. Here v_{ec}/B denotes the pitch s_c ($\times 1/(2\pi)$) of the cyclotron orbit. s_c must be small compared to the circumference of the circle, $2\pi r_t$, along which the electron beam is to be guided. From $2\pi r_t \gg s = v_{ec}t_c = v_e 2\pi/\omega_c = v_e 2\pi c/B$ (t_c and ω_c signify the electronic

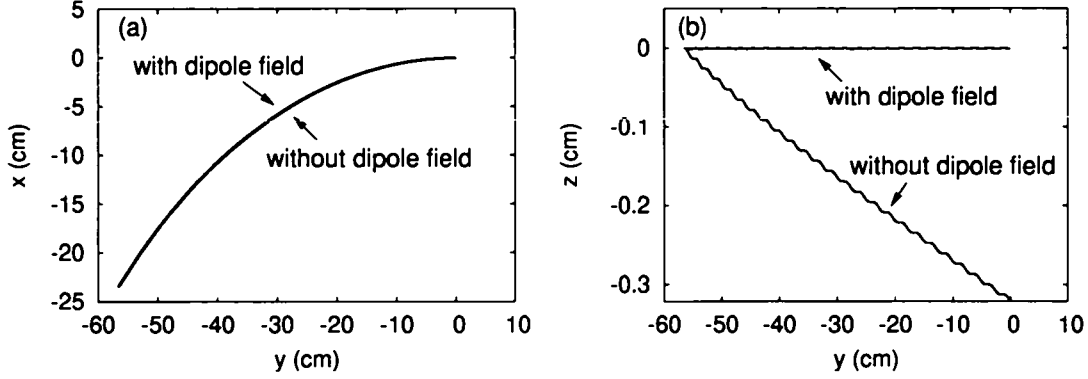


Figure 4.2: Electron trajectory propagated through the merging toroid with beam velocity of $0.1c$ at $B = 42$ mT with (red) and without (cyan) the perpendicular dipole field $B_{dipole} \approx 0.2$ mT. (a) shows the projection of the trajectory onto the toroid plane $z = 0$ and (b) depicts one direction along the toroid and the direction perpendicular to it. Whereas the trajectories coincide in (a) since they both bend in the (x, y) plane, the trajectory without the dipole field applied drifts off perpendicular to the toroid plane.

cyclotron period and frequency, respectively) the above condition is derived. The characterization of the cyclotron motion in terms of s_c has the advantage of being independent of the thermal perpendicular excitation of the electrons. Furthermore, the dipole field satisfies the relation $B_{dipole} = v_e c / r_t \ll B$. With $v_e \approx 0.1c$ and $r_t = 80$ cm $B_{dipole} \approx 0.2$ mT can be determined.

When the ions cross this toroidal region, they are exposed to magnetic field components transverse to their direction of motion $\vec{v}_{ion} = v_{ion} \hat{e}_y$ resulting in a non-vanishing Lorentz force. Transforming to the rest frame of an ion these magnetic field components give rise to motional transverse electric fields. An electric field tilts the ionic Coulomb potential as illustrated in Figure 4.3b. Accordingly, the Coulomb potential barrier gets depressed near a saddle, the so-called Stark saddle, within the toroidal section and is raised again when the ions enter the solenoid region. Initially free electrons can thus become trapped inside the potential of the ion when the tilted potential is restored to a Coulomb one at the end of the toroidal merging section [45]. This capture by the Stark saddle was recently observed in an experiment with a trap-like arrangement [65, 66]. Note that it is the inverse process to field ionization.

For typical storage ring conditions, the observed binding energies of the captured electrons are estimated to be small, *i.e.* only very high Rydberg states will get populated. These highly excited states will most likely get reionized again at the toroidal

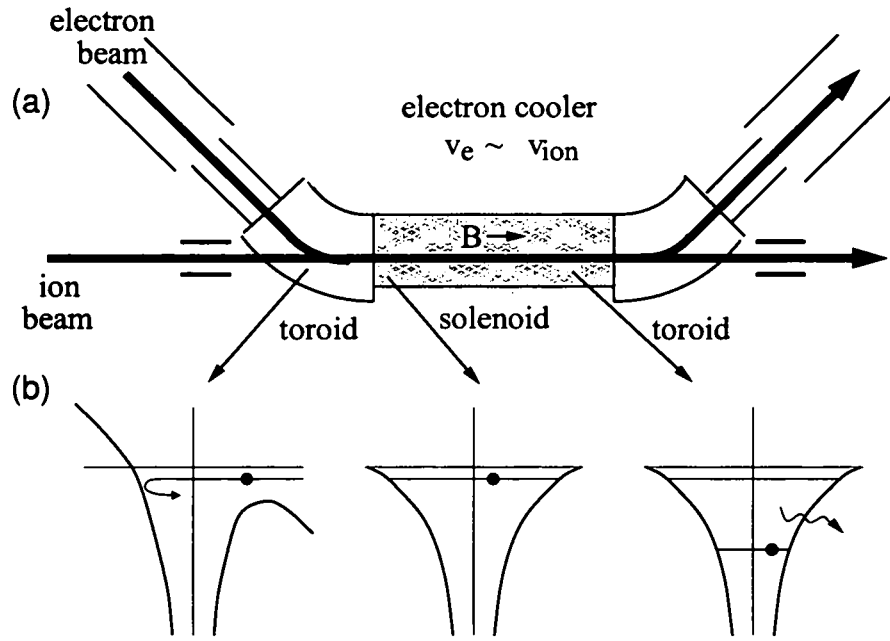


Figure 4.3: Schematic picture of the TSR electron cooler (a) and Gwinner's proposal [45] (b): In the rest frame of the ion motion induced transverse electric field components appear in the toroidal region. This electric field modifies the ionic Coulomb potential such that a Stark saddle allows passage into the Coulomb zone. Initially free electrons can pass over the saddle and get trapped inside it when the transient field disappears upon entering the solenoidal region. Radiative decay of Rydberg states inside the solenoid could then prevent them from being field-ionized again at the toroidal demerging section.

demerging section where the Coulomb barrier gets depressed once more. However, a fraction of Rydberg states might radiatively decay to more deeply bound states inside the solenoid and can then pass the demerging toroid without field ionization. Thus, sufficiently deeply bound electrons, *i.e.* with principal quantum numbers $n \leq n_r$ (with n_r being determined by field ionization in the charge analyzing dipole magnet downstream from the electron cooler), can then effectively contribute to the electron-ion recombination rate. Since the probability for radiative stabilization inside the solenoid strongly depends on the quantum numbers n and l of the populated Rydberg state, a realistic simulation of the merging section is required to determine the distribution of the obtained Rydberg states at the end of the toroid and thus to estimate the contribution from transient bound states. The influence of this additional recombination channel initially suggested by Gwinner *et al.* [45] on the observed recombination rates will be investigated in this chapter.

4.2 Electron-Ion Merging in the Lab Frame

In the laboratory frame the electron and ion (charge Z) are both exposed to the toroidal and dipole magnetic field and to the Coulomb field. In the symmetric gauge, $\vec{A} = 1/2 (\vec{B} \times \vec{r})$, the Hamiltonian of the electron-ion two-body system becomes

$$H = \frac{1}{2m_{ion}} \left(\vec{p}_{ion} - \frac{Z}{2c} \left(\vec{B}(\vec{r}_{ion}) \times \vec{r}_{ion} \right) \right)^2 + \frac{1}{2} \left(\vec{p}_e + \frac{1}{2c} \left(\vec{B}(\vec{r}_e) \times \vec{r}_e \right) \right)^2 - \frac{Z}{|\vec{r}_e - \vec{r}_{ion}|}, \quad (4.1)$$

where the electron is described by the position \vec{r}_e and the momentum \vec{p}_e and the ion by \vec{r}_{ion} and \vec{p}_{ion} , respectively, and the magnetic field in the lab frame is given by

$$\vec{B}(\vec{r}) = \begin{pmatrix} -B(\vec{r}) \sin \phi \\ B(\vec{r}) \cos \phi \\ B_{dipole}(\vec{r}) \end{pmatrix}. \quad (4.2)$$

Note that the magnetic field strength depends on the local position of the particle or, equivalently, on the time elapsed during the merging process. For a given set of initial conditions the dynamics of the system is determined by the classical Hamilton's equations of motion (appendix E).

We study the electron-ion merging for the TSR geometry with a toroid of $r_t = 80$ cm and $\phi_t = 45$ degrees. For $B = 42$ mT and $B_{dipole} \approx 0.2$ mT the electronic trajectory follows the curvature of the toroid (Figure 4.2), whereas the incoming ion is displaced perpendicular to the toroid due to the non-vanishing Lorentz force $F_z \approx -v_{ion} B_x$ (Figure 4.4b). This ion drift can be compensated, as in the case

of the electrons, by applying another dipole field. For simplicity, however, we omit this dipole field, and choose, instead, initial conditions for the ion beam with a displacement perpendicular to the toroid plane such that a proper merging with the electron beam at the end of the toroid is achieved. Figure 4.4b shows sample trajectories for both the electron and the ion. The ion trajectories with and without an initial displacement are drawn. In addition, Figure 4.4a depicts a sketch of the coordinate system used for our simulations.

The relative energy of the electron-ion system is calculated as

$$E_{rel}^{e-ion} = \frac{1}{2}\mu |\vec{v}|^2 - \frac{Z}{|\vec{r}|}, \quad (4.3)$$

where $\mu = m_{ion}/(1 + m_{ion}) \approx 1$ is the reduced mass, $\vec{r} = \vec{r}_e - \vec{r}_{ion}$ the relative coordinate and $\vec{v} = \vec{v}_e - \vec{v}_{ion}$ the relative velocity. The relative energy determines whether a bound state is formed during the merging process, *i.e.* whether $E_{rel}^{e-ion} < 0$ can be reached. It is invariant under frame transformation from the lab system to the rest frame of the ion. Thus, the distribution of E_{rel}^{e-ion} at the end of the toroid will eventually determine the efficiency of the proposed recombination mechanism [45]. Moreover, the distribution among angular momentum states controls the efficiency of radiative stabilization in the solenoid region. To obtain these distributions the electron and ion beams are propagated through the toroidal section where the two beams exhibit an overlap in coordinate space since only in this region (prior to the solenoid) the electron and ion can effectively interact through their Coulomb potentials. For beams of 2 mm in diameter the coordinate space overlap extends over the last 5.6 cm of the toroid of the TSR prior to entering the solenoid. This corresponds to about 4 degrees in opening angle or 1.86 ns in time for $|\vec{v}_e| \approx 0.1c$. Only during the short time $[t_0, t_1]$ between entering the overlap region at t_0 and entering the solenoid at t_1 the relative internal energy of the electron-ion system is reduced such that recombination can occur. This time interval $t_1 - t_0$ of coordinate space merging will also be referred to as $t_m(r)$ (chapter 5).

As discussed in section 3.2 already the constant magnetic field in the solenoid led to a break-down of the separation of the center of mass (CM) and relative motions for the electron-ion system. However, due to the heavy ion mass the transfer of energy between these two degrees of freedom turned out to be very small within the solenoid ($\leq 10^{-7}$ a.u., see Figure 3.3). During the merging, the magnetic field (Eq. (4.2)) is implicitly time dependent thus allowing for a much larger energy transfer between the CM and relative motions and, correspondingly, a much larger fraction of electrons captured by the ion, *i.e.* $E_{rel}^{e-ion} < 0$, at the end of the toroid (see Figure 3.37 for a comparison with the solenoid). Before presenting the bound state distributions obtained for an ensemble of electrons, the electron-ion merging will be treated in the rest frame of the ion first.

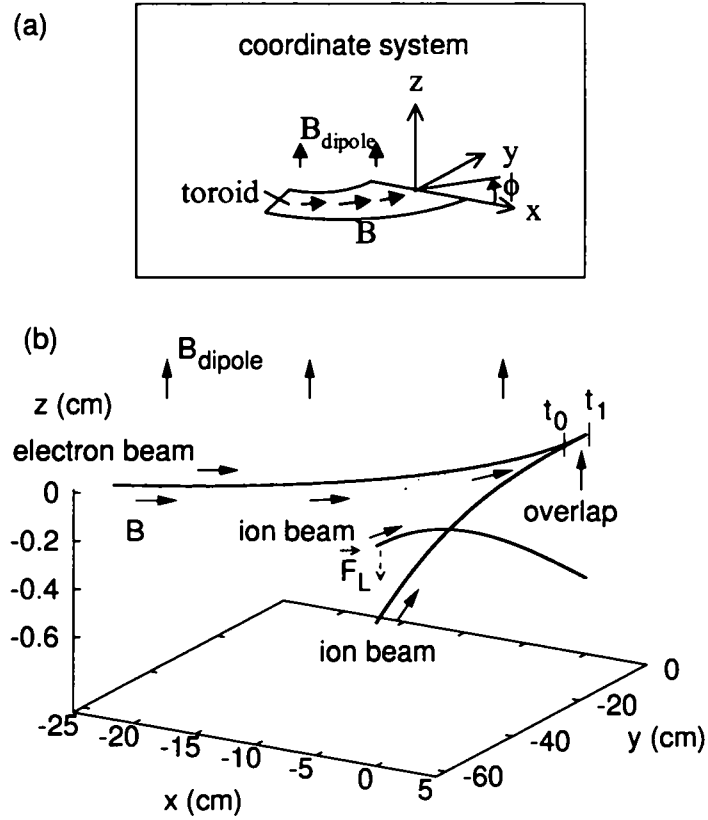


Figure 4.4: Coordinate system employed in the merging region (a) and merging of trajectories of an electron and C^{6+} ion (b) propagated over the entire length of the toroid ($\phi_t = 45$ degrees) for the geometry at the TSR. t_0 and t_1 mark the region of overlap of the two beams in coordinate space (with beam diameters chosen to be 2 mm). Without proper alignment the ion beam does not merge with the electron beam due to the Lorentz force \vec{F}_L .

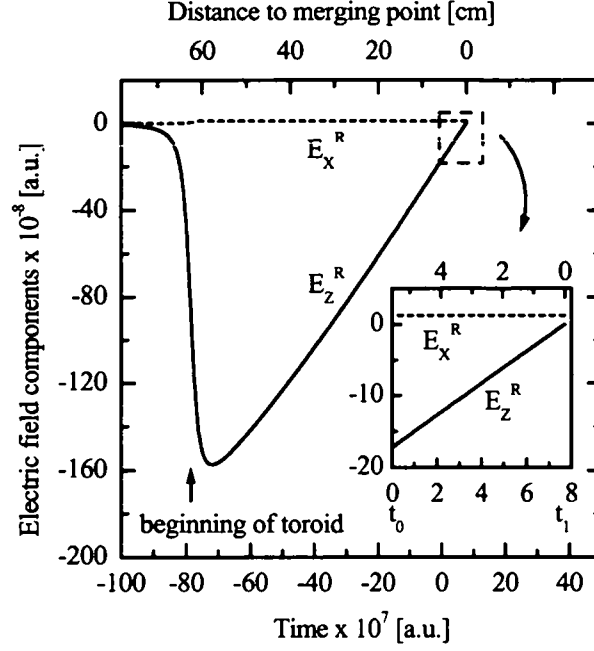


Figure 4.5: Schematic picture of the transient electric field \vec{E}^R over the toroidal merging section of the TSR electron cooler: the elapsed time and distance towards the end of the merging section are shown. The time scale is chosen such that at $t_0 = 0$ the beams start to have an overlap in coordinate space. The inset depicts only the short time interval of non-zero overlap $[t_0, t_1]$ (see also Figure 4.4b) during which the electron and ion can interact with each other before reaching the solenoid with $\vec{E}^R = 0$.

4.3 Transformation to the Rest Frame of the Ion

Alternatively, the electron-ion system can be treated in the rest frame of the ion (denoted by the superscript R). Due to the much larger ion mass ($m_{ion} \gg 1$) the ionic accelerations in the magnetic field Eq. (4.2) in the lab frame can be, to a good approximation, neglected during the time interval $[t_0, t_1]$ (Figure 4.6a). Therefore, the ion is assumed to move with constant velocity $\vec{v}_{ion} = v_{iony}\hat{e}_y$ throughout the merging section. Applying the Lorentz transformation from the lab frame to the internal frame R , the electric and magnetic field components in the rest frame of the ion can be obtained. For a boost along the y -axis with speed $c\beta$ from the lab frame to the rest frame of the ion the transformation equations for classical electromagnetic

fields read [67]

$$\begin{aligned} B_x^R &= \gamma(B_x - \beta E_z) & E_x^R &= \gamma(E_x + \beta B_z) \\ B_y^R &= B_y & E_y^R &= E_y \\ B_z^R &= \gamma(B_z + \beta E_x) & E_z^R &= \gamma(E_z - \beta B_x). \end{aligned} \quad (4.4)$$

In the case of the TSR $\beta = v_{ion}/c \approx 0.1$ and $\gamma = 1.0/\sqrt{1 - \beta^2} \approx 1$. Thus, relativistic effects can be neglected. For $\vec{E} = 0$ and \vec{B} according to Eq. (4.2) the rest frame components of the electric and magnetic fields are determined as

$$\vec{B}^R(\vec{r}^R, t) = \begin{pmatrix} -B(\vec{r}, t) \sin \phi(t) \\ B(\vec{r}, t) \cos \phi(t) \\ B_{dipole}(\vec{r}, t) \end{pmatrix} \quad \vec{E}^R(\vec{r}^R, t) = \frac{v_{ion}}{c} \begin{pmatrix} B_{dipole}(\vec{r}, t) \\ 0 \\ B(\vec{r}, t) \sin \phi(t) \end{pmatrix}. \quad (4.5)$$

They depend on the time elapsed during the merging process. Figure 4.5 shows a schematic picture of the transient electric field components over the entire merging region for the merging geometry of the TSR. The onset of the electric fields is determined by the rising transverse magnetic field components the ion encounters when entering the toroidal region, whereas the decrease in E_z^R is due to the decrease of B_x towards the end of the toroid. The inset in Figure 4.5 illustrates the region of interaction between electrons and ions $[t_0, t_1]$ simulated in our CTMC calculations. Note that we did not take into account the decrease of E_x^R (*i.e.* the decrease of B_{dipole}) at the end of the merging.

Figure 4.6a illustrates the acceleration of the (initially displaced) C^{6+} ion in the lab frame during the investigated time interval $[t_0, t_1]$ as obtained from the time evolution of the Hamiltonian Eq. (4.1). For comparison, the electric field components Eq. (4.5) (see also Figure 4.5) are displayed for the same time interval in Figure 4.6b. The ionic acceleration \vec{a}_{ion} is about three orders of magnitude (factor Z/m_{ion} , compare appendix F) smaller than the electric field \vec{E}^R thus confirming the validity of the assumption of a constant ion velocity throughout the merging region used to derive Eq. (4.5).

A more general derivation of the electric and magnetic field components in the rest frame of the ion is presented in appendix F by allowing for an acceleration of the ion in the laboratory frame. It is demonstrated that the electric field components are well approximated by those in Eq. (4.5). Eq. (4.5) thus constitutes a sufficient description of the electric and magnetic fields present during the merging of electrons in the cooler.

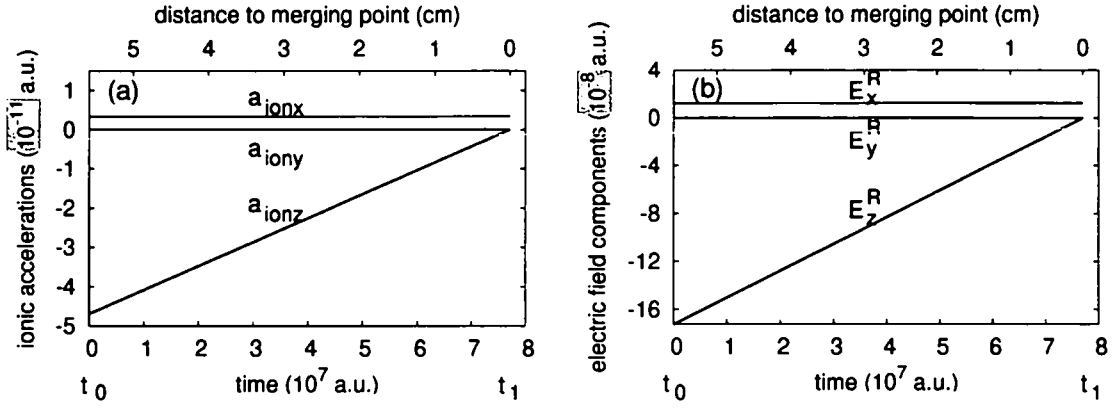


Figure 4.6: The ionic acceleration in the lab frame (a) and the electric field components in R Eq. (4.5) (b) shown as a function of merging time respectively distance for the merging of a C^{6+} ion (with initial displacement) and an electron at the TSR electron cooler with $B = 42$ mT and $B_{dipole} \approx 0.2$ mT. Only the short time interval of interaction $[t_0, t_1]$ is considered.

4.4 Electron-Ion Merging in the Rest Frame of the Ion

In the rest frame of the ion (superscript R) the electron-ion merging is described by propagating only the electron. The Hamiltonian is given by

$$H = \frac{1}{2} \left(\vec{p}_e^R + \frac{1}{2c} \left(\vec{B}^R(\vec{r}_e^R, t) \times \vec{r}_e^R \right) \right)^2 - \frac{Z}{|\vec{r}_e^R|} + \vec{r}_e^R \vec{E}^R(\vec{r}_e^R, t) \quad (4.6)$$

with the electric and magnetic fields of Eq. (4.5). Note that this Hamiltonian does not obey the scaling relations Eq. (3.23) applicable in the solenoidal region, since the electric field $\vec{E}^R = \vec{v}_{ion}/c \times \vec{B}$ breaks the scaling invariance. \vec{E}^R allows for an acceleration or deceleration of the electron changing its energy during the merging process. The electron energy in R is equivalent to the relative energy of the electron-ion system Eq. (4.3),

$$E_{rel}^{e-ion} = E_e^R = \frac{1}{2} (\vec{v}_e^R)^2 - \frac{Z}{|\vec{r}_e^R|}, \quad (4.7)$$

since $\vec{r} = \vec{r}_e - \vec{r}_{ion} = \vec{r}_e^R$, $\vec{v} = \vec{v}_e - \vec{v}_{ion} = \vec{v}_e^R$ and $\mu \approx 1$. Figure 4.7 illustrates an electron trajectory in R and the associated relative energy E_{rel}^{e-ion} during the simulated time interval $[t_0, t_1]$. The observed change in E_{rel}^{e-ion} is due to the variation of the magnetic field Eq. (4.2) during the merging section which generates, as already pointed out, a much larger energy transfer $E_{rel}^{e-ion} \longleftrightarrow E_{cm}^{e-ion}$ between the relative

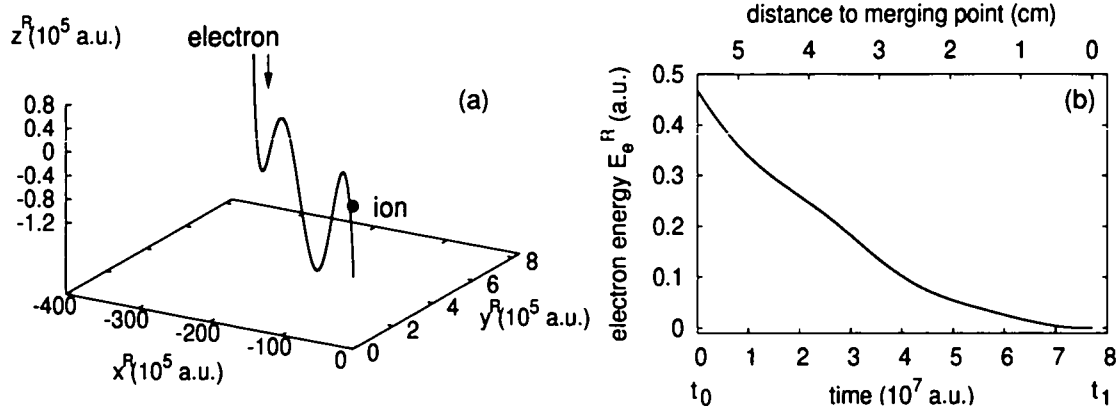


Figure 4.7: Merging of a C^{6+} ion and an electron for the TSR geometry at $B = 42$ mT and $B_{dipole} \approx 0.2$ mT: the electron trajectory in R (a) and the corresponding relative energy between electron and ion (Eq. (4.7)) (b) are displayed for the time interval $[t_0, t_1]$.

and CM motions than the homogeneous magnetic field in the solenoid (see also sections 3.2 and 3.16).

4.5 CTMC Simulation of the Merging

To determine the contribution of the transient electric field-induced recombination to the observed recombination rates the electron-ion merging needs to be investigated for an ensemble of electrons. Using a classical trajectory Monte Carlo (CTMC) method we first study the merging of C^{6+} ions with electrons at the TSR electron cooler. The electrons are initially distributed uniformly within a sphere with radius $R = 1/2 r_{ion}$ ($r_{ion} = n_{ion}^{-1/3}$ denotes a typical interionic distance in the experiment given by the ion density n_{ion}) in coordinate space and Maxwell-Boltzmann distributed in velocity space with electron temperatures kT_{\perp} and kT_{\parallel} . The transverse and longitudinal velocity spreads refer to the direction of the toroidal magnetic field B . The ensemble has an average detuning energy E_{rel} with respect to the ion motion. Note that E_{rel} characterizes the average relative energy between the electron and ion beam after the merging and is not to be confused with the relative energy E_{rel}^{e-ion} of an individual electron-ion pair. For beam velocities $\beta = v/c \approx 0.1$ and typical magnetic guiding fields at the TSR ($20 \text{ mT} \leq B \leq 70 \text{ mT}$ according to Ref. [10]) the strength of the dipole field amounts to $B_{dipole} \approx 0.2$ mT in order to achieve a properly merged electron beam. Accordingly, the center of the initial

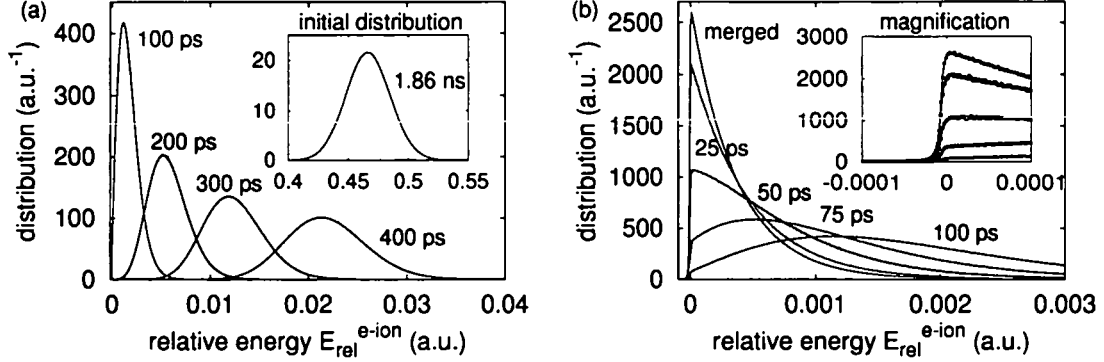


Figure 4.8: Snapshots of the relative energy distribution (Eq. (4.3)) recorded at different times during the merging of C^{6+} ions with electrons at the TSR electron cooler with $B = 42$ mT and $B_{dipole} \approx 0.2$ mT. The inset in (a) displays the initial distribution at time t_0 . The values for the time indicated are measured relative to the completion of the merging process, *i.e.* $t = 0$ as the end of the toroid ($\phi = 0$) is reached. The inset in (b) is a magnification of the distributions around $E_{rel}^{e-ion} = 0$. All distributions are normalized, $\int P(E_{rel}^{e-ion}) dE_{rel}^{e-ion} = 1$. The parameters of the initial electronic ensemble are $kT_{\perp} = 10$ meV, $kT_{\parallel} = 0.06$ meV, $E_{rel} = 0.03$ meV and $r_{ion} = 1.765 \times 10^6$ a.u.

electron distribution is shifted such that at the end of the toroid the electron at the center merges exactly towards the target ion. We simulate only the short time interval of interaction $[t_0, t_1]$ thus starting the propagation of the electron and ion beams at a distance of 5.6 cm prior to the solenoid and we choose the lab frame for our calculations.

In Figure 4.8 the distribution of the electron-ion relative energies E_{rel}^{e-ion} (Eq. (4.3)) is shown for different points in time during the merging simulation. At time t_0 the relative energies are all positive with a broad distribution around the peak value at $E_{rel}^{e-ion} \approx 0.465$ (inset in Figure 4.8a). As time proceeds throughout the merging the energy distribution gets narrower and shifts to lower E_{rel}^{e-ion} due to the gradual approach of the electrons towards the ions with increasing alignment of \vec{v}_e parallel to \vec{v}_{ion} as ϕ tends to zero. Bound states are found to be formed only during about the last 100 ps of the merging process (inset in Figure 4.8b and Table 4.1). Table 4.1 presents the total bound-state fractions accumulated in the course of the merging process.

Furthermore, Figure 4.9a depicts the distribution of the magnitude of the relative velocity $|\vec{v}|$ between electron and ion during the merging region. $|\vec{v}|$ is smallest at the end of the toroid where the electron and ion beam velocities have become parallel.

time prior to the merging point (ps)	fraction of bound states
200	≈ 0
100	0.00055
75	0.00279
50	0.00833
25	0.01682
0	0.02119

Table 4.1: Total fraction of bound states present at different times during the merging process as obtained for the distributions of Figure 4.8.

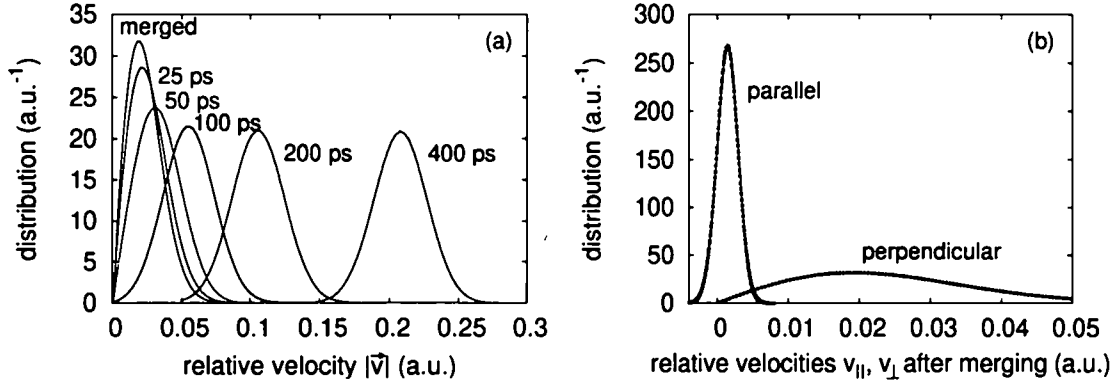


Figure 4.9: Distribution of magnitude of relative velocity ($|\vec{v}| = |\vec{v}_e - \vec{v}_{ion}|$) at different times during the merging process (a) and the velocity components along the longitudinal and transverse (*i.e.* \parallel and $\perp B$) directions after the merging (b). The given times in (a) refer to the end of the merging section and the underlying black lines in (b) represent the parallel, $\sqrt{1/(2\pi kT_{||})} \exp(-(v_{||} - v_{rel})^2/(2kT_{||}))$, and perpendicular, $2\pi v_{\perp} 1/(2\pi kT_{\perp}) \exp(-v_{\perp}^2/(2kT_{\perp}))$, Maxwell-Boltzmann distributions. Same parameters as in Figure 4.8.

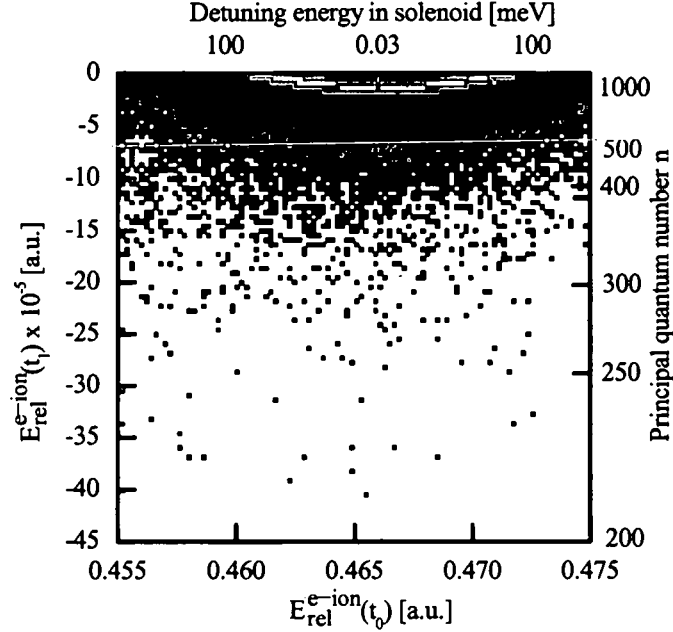


Figure 4.10: Bound-state formation during the merging of C^{6+} ions with electrons at the TSR ($B = 42$ mT, $B_{dipole} \approx 0.2$ mT): a density plot of the electron-ion relative energies (Eq. (4.3)) before the merging $E_{rel}^{e-ion}(t_0)$ and after the merging $E_{rel}^{e-ion}(t_1)$ is shown. The density is plotted on a logarithmic scale. As a reference, for electrons moving along the trajectory of the center of the Maxwell-Boltzmann distribution the detuning energy reached in the solenoid is also given. Same parameters as in Figure 4.8.

However, the thermal distribution of the electronic velocity components remains essentially unchanged throughout the merging. Figure 4.9b displays the relative velocities parallel and perpendicular to the magnetic field as obtained at the end of the toroid. Their distributions agree well with the Maxwell-Boltzmann distribution (Eq. (2.12)) of the initial electronic ensemble. Moreover, from Figure 4.9a the time scale for the merging in velocity space $t_m(v)$ can be determined. Along the lines of the coordinate space overlap discussed in section 4.2, $t_m(v)$ is estimated via a non-zero overlap of the "initial" velocity distribution with the corresponding merged one and, thus, approximately amounts to $0.05 - 0.1$ ns (Figure 4.9a). $t_m(v)$ is shorter than the time scale in coordinate space $t_m(r) \approx 1.86$ ns.

We thus find that the vast majority of electrons features $E_{rel}^{e-ion} > 0$ at the end of the toroid at time t_1 . Only a minor fraction of the electrons forms bound states after merging is completed. In the case of our CTMC data illustrated in

Figure 4.8 the bound-state fraction is approximately two percent (see Table 4.1). In the following the bound-state distributions from our simulation will be examined in detail. Figure 4.10 displays the distribution of Rydberg states formed for our currently studied CTMC ensemble. Both the binding energies $E_{rel}^{e-ion}(t_1) < 0$ (a.u.) and the corresponding principal quantum numbers n are shown as a function of the initial energy before the merging process $E_{rel}^{e-ion}(t_0)$. Accordingly, very high Rydberg states get populated during the merging process. For example, the probability for forming Rydberg states with $n \leq 400$, $\sum_{n=1}^{400} P(n) < 2 \times 10^{-5}$, is very small.

4.6 Analysis of Bound-State Distributions

The challenge of the determination of the contribution of this pathway to recombination lies in the accurate calculation of the bound-state n , l distribution after the merging. Large ensemble sizes ($\gtrsim 10^8$ trajectories) are required for the miniscule fractions of bound states (compare Table 4.1) obtained at typical storage ring conditions. We investigate bound-state spectra for different ion charges Z and magnetic guiding field strengths B at the end of the merging section. In Figure 4.11 the probability distributions for the binding energies $P(E_B)$ ($E_B = -E_{rel}^{e-ion}$) and the corresponding principal quantum numbers $P(n)$ are compared. The field-free relation $n = Z/\sqrt{2E_B}$ is used. The peak in the n distribution (Figure 4.11b) can be assigned to the spatial extent of the initial electronic ensemble, *i.e.* a sphere with radius R . Correspondingly, the position of the peak is roughly estimated as $n_{peak} \approx \sqrt{RZ}$ and a variation in R or rather in Z shifts the peak position and, in addition, changes the overall amount of the associated production of bound states. Therefore, the observed reduction of $P(n)$ at $n > n_{peak}$ is a beam density effect: for higher values of n Rydberg orbitals of neighboring ions would overlap. Due to the presence of field non-uniformities and thus small electric stray fields inside the solenoid, a cutoff appears at smaller n for any realistic experimental setup.

The distribution of bound states (Figure 4.11) falls off precipitously towards lower n (or higher binding energies E_B). The probability that electrons are populated at low-lying Rydberg states becomes thus very small and is even less than 10^{-8} at $n = 100$. For such small probabilities the Monte Carlo statistics is insufficient to resolve the actual bound-state distributions with reasonable accuracy even with our large ensembles employed. For example, the curves presented in Figure 4.11 are obtained from 3.5×10^8 trajectories. Consequently, probabilities of the order of 10^{-8} correspond to only few trajectories contributing and the lowest value resolvable at all resulting from the contribution of a single electron amounts to approximately 3×10^{-9} . Thus, typically less than one event can be found for $n \lesssim 100$ and, accordingly, the determination of $P(n)$ for such small n requires the controlled smooth extrapolation of $P(n)$ from higher n values with a continuous slope (indicated by

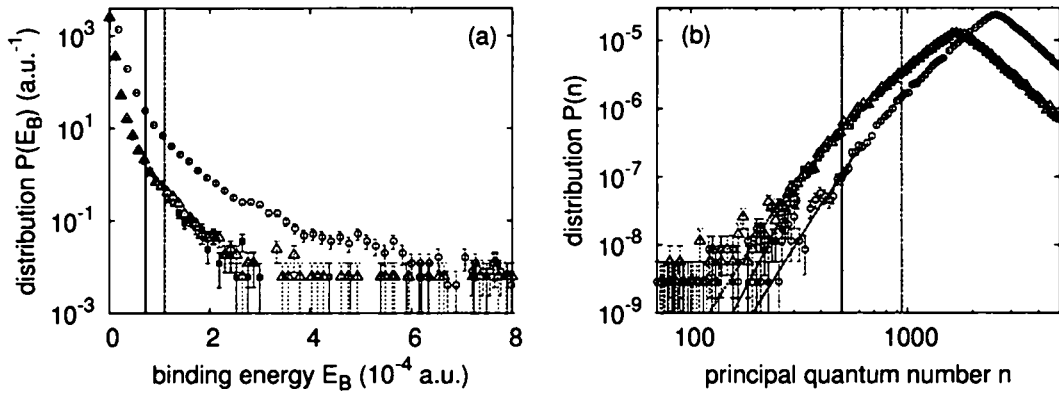


Figure 4.11: Binding energy E_B (a) and principal quantum number n (b) distributions after the merging between the electron and ion beams at the TSR electron cooler with $kT_{\perp} = 10$ meV, $kT_{\parallel} = 0.06$ meV, $E_{rel} = 0.03$ meV and $R = 8.825 \times 10^5$ a.u.; blue Δ (dotted line): $B = 42$ mT, $Z = 6$, green \circ (dashed line): $B = 42$ mT, $Z = 14$, red \blacksquare (full line): $B = 10$ mT, $Z = 6$. The distributions are normalized, $\int_{-\infty}^{\infty} P(E_{rel}^{e-ion}) dE_{rel}^{e-ion} = 1$ (likewise the n distributions), and obtained with 3.5×10^8 trajectories. The vertical lines (red, blue for $Z = 6$ and green for $Z = 14$) refer to the approximate cutoff in the distributions due to stray fields in the experiment. Accordingly, lower E_B and higher n values do not contribute to the field-induced recombination. The lines through the CTMC data in (b) indicate the extrapolation for low n .

parameters		fraction of bound states			
Z	B (mT)	P_B	$P(n \leq 1000)$	$P(n \leq 500)$	$P(n \leq 200)$
2	42	0.00511	1.75×10^{-3}	1.67×10^{-4}	4.13×10^{-6}
6	42	0.0212	1.01×10^{-3}	5.42×10^{-5}	7.11×10^{-7}
14	42	0.0551	3.68×10^{-4}	1.08×10^{-5}	4.00×10^{-7}
6	10	0.0210	9.96×10^{-4}	4.92×10^{-5}	3.23×10^{-7}
6	42	0.0212	1.01×10^{-3}	5.42×10^{-5}	7.11×10^{-7}
6	90	0.0212	1.01×10^{-3}	5.51×10^{-5}	9.54×10^{-7}

Table 4.2: Cumulative fractions of bound states for different Z and B at the end of the merging process. P_B : total bound-state fraction, $P(n \leq n_0)$: the probability for forming Rydberg states with $n \leq n_0$. Same parameters as in Figure 4.11.

the lines in Figure 4.11b).

Table 4.2 displays the fraction of bound states obtained for different values of Z and B . The total bound-state fractions as well as the probabilities for forming Rydberg states with $n \leq 1000$, $n \leq 500$ and $n \leq 200$ are given. Whereas an increase in Z considerably enhances the cumulative bound-state fraction due to the increased Coulomb potential, an increase of B and thus of the transient electric field E_z^R (Eq. (4.5)) during the merging displays a more subtle effect on the population of Rydberg states increasing the relative probability of low-lying bound states (*i.e.* at low n or, correspondingly, high E_B values). The latter follows from the classical over-the-barrier relation for the critical quantum number $n_F \propto (Z^3/F)^{1/4}$ (with F denoting the electric field strength) matching the Stark saddle (for a more detailed discussion see section 4.9 and Eq. (4.14) therein). Moreover, the distribution among bound states in Figure 4.11 clearly demonstrates that the majority of the captured electrons exhibits very small binding energies ($\leq 10^{-4}$ a.u.) at the end of the toroid, *i.e.* on the average very high Rydberg states get populated during the merging.

The calculated angular momentum distribution $P(n, l)$ (with n fixed) of trapped electrons at the end of the merging is shown in Figure 4.12. The distribution in l (with the field-free relation $l = |\vec{r} \times \vec{v}|$) follows the statistical weight $g_n = 2l + 1$ corresponding to the m degeneracy for a fixed value of n and, up to rather high values of l , closely follows the prediction of a microcanonical ensemble,

$$P(n, l) = P(n) \frac{2l + 1}{n^2}. \quad (4.8)$$

Deviations from the purely statistical occupation can only be found for very high l close to the cutoff in n . Since only states with low l can effectively contribute to radiative stabilization, the l distribution can be approximated by Eq. (4.8) without significant error. Due to the dipole selection rules high values of l with $l \gg n_r$ do

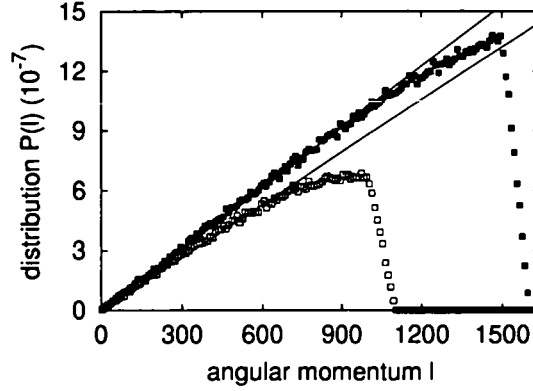


Figure 4.12: Angular momentum distribution of Rydberg electrons with $1000 \leq n \leq 1100$ (\square) and $1500 \leq n \leq 1600$ (\blacksquare) after the merging of C^{6+} ions with electrons at the TSR for $B = 42$ mT and otherwise the same parameters as in Figure 4.11. The lines are proportional to $2l + 1$.

not contribute to radiative decay into low lying states with $n \leq n_r$. In Figure 4.12 n has not been fixed to a certain value but rather confined to a small interval to increase the statistics within the CTMC. Note that $P(n)$ (likewise $P(E_B)$) represents a reduced distribution of $P(n, l)$.

The statistical distribution of angular momentum states originates from the bound-state motion of electrons in high Rydberg states in the presence of a magnetic field. Electrons are found to move along either chaotic or regular trajectories depending on the respective binding energy and therefore the strength of the magnetic field compared to the Coulomb potential of the parent ion. Correspondingly, the angular momentum l exhibits (quasiperiodic) fluctuations in the magnetic field in contrast to analytically known elliptic Kepler orbits in the pure Coulomb field where l is conserved. The dynamics of electrons in high Rydberg states inside the solenoid will be studied in the next section.

4.7 Bound-State Evolution in the Solenoid

Starting from the distribution $P(n, l)$ (Eq. (4.8)) at the end of the merging section, the time evolution through the solenoidal region needs to be analyzed in order to evaluate the rate for radiative decay. Since in the solenoid the electron-ion relative energy E_{rel}^{e-ion} is well conserved (the transfer of center of mass energy to relative energy due to the coupling by the constant field strength B is negligible and energy is conserved within an error bar of 10^{-7} a.u., see section 3.2 and Figure 3.3 therein), the

reduced distribution $P(n)$ can be considered to be invariant during the propagation. Accordingly, the bound-state dynamics inside the solenoid can easily be studied in the rest frame of the ion using the Hamiltonian Eq. (3.21). Figures 4.13 and 4.14 show sample electron trajectories.

The two trajectories visualized in Figure 4.13 correspond to very weakly bound states with binding energies ($E_B = -E_{rel}^{e-ion}$) of $E_B \approx 0.209$ meV ($n \approx 1529$) and $E_B \approx 0.025$ meV ($n \approx 4392$) respectively. Because of the weak binding and the comparatively strong magnetic field ($B = 42$ mT) the electron motion is very different from a high n Kepler orbit. For an instructive illustration of the dynamics the trajectories are propagated for a time interval much longer than the cooler time in Figure 4.13. The characteristic cyclotron radius for the electron $r_c = v_\perp c/B$ is much smaller than the separation between the electron and the ion. We denote the separation transverse to the magnetic field direction (here assumed as the z axis) by $r_\perp = \sqrt{(x_e - x_{ion})^2 + (y_e - y_{ion})^2}$. Therefore, $r_c \ll r_\perp$ for the trajectories of Figure 4.13. Likewise, the cyclotron frequency for the electron $\omega_c = B/c$ is much larger than the other dynamical frequencies of the system. In addition to the cyclotron motion the electron in Figure 4.13 oscillates back and forth along the magnetic field in the Coulomb field of the ion (frequency ω_c) and $\vec{E} \times \vec{B}$ drifts around the ion (frequency ω_D) with the frequency ordering given by $\omega_c \gg \omega_z \gg \omega_D$. Note that also the frequency of the corresponding unperturbed Kepler motion, $\omega_k = 2/Z\sqrt{2(E_B)^3}$ [61], is small compared to ω_c . The dynamics of these weakly bound and strongly magnetized atoms has been investigated in Refs. [68, 69], where the term "guiding center drift atoms" has been appropriately introduced for such atoms. With the magnetic field sufficiently strong that the electron cyclotron frequency is the largest of the frequencies and the cyclotron radius the smallest of the length scales such as in Figure 4.13, the rapid cyclotron motion may be averaged out and the dynamics of the electron treated by guiding center drift theory.

The electron trajectory visualized in Figure 4.14 is much deeper bound with $E_B \approx 2.87$ meV or, correspondingly, $n \approx 413$. In this case the cyclotron radius is found to be much larger than the electronic distance to the ion, $r_c \gg r_\perp$. The frequencies due to the cyclotron, field aligned and $\vec{E} \times \vec{B}$ drift motions become comparable to each other and, moreover, comparable to the Kepler frequency ω_k . The trajectory in Figure 4.14 ($\omega_k \approx 3\omega_c$) looks like a strongly perturbed Kepler orbit. Finally, for sufficiently deeply bound states, *i.e.* $\omega_k \gg \omega_c$, the electronic motion can be well approximated by the unperturbed Kepler motion.

Whereas E_{rel}^{e-ion} and hence the principal quantum number n remain conserved throughout the solenoid, the angular momentum l is no longer a good quantum number in the presence of a magnetic field. The analysis of individual trajectories shows that l rapidly fluctuates during the propagation through the solenoid region. In Figure 4.15 the time evolution of l inside the solenoid is illustrated for the trajectories visualized in Figures 4.13 and 4.14. However, the l distribution acquired for

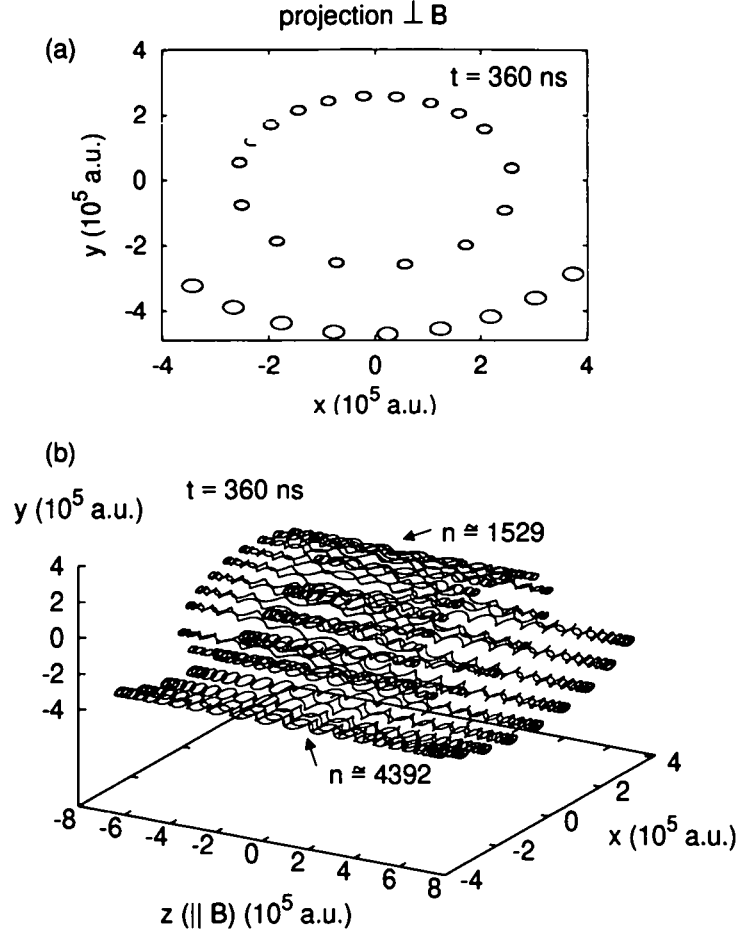


Figure 4.13: Two electron trajectories for $E_{rel}^{e-ion} \approx -7.695 \times 10^{-6}$ a.u. ($n \approx 1529$) (red) and $E_{rel}^{e-ion} \approx -9.332 \times 10^{-7}$ a.u. ($n \approx 4392$) (green) propagated through a magnetic field of $B = 42$ mT (along z) and the Coulomb field of a C^{6+} ion (situated at the origin) for a time of 360 ns (corresponding to $6 \times \tau_c$ at the TSR). The three-dimensional trajectories (b) as well as their projections to the $x-y$ plane (*i.e.* $\perp B$) around the turning points at $z > 0$ (a) are drawn. In detail, for the deeper bound state (red trajectory) the transverse electron-ion separation is $r_{\perp} \approx 2.5 \times 10^5$ a.u., the electron cyclotron radius $r_c \approx 1.35 \times 10^4$ a.u., the cyclotron frequency $\omega_c \approx 1.8 \times 10^{-7}$ a.u., the frequency of the field aligned oscillations $\omega_z = 7.0 \times 10^{-9}$ a.u. and the frequency of the $\vec{E} \times \vec{B}$ drift rotation $\omega_D \approx 5.5 \times 10^{-10}$ a.u., whereas for the weaker bound electron (green trajectory) one finds $r_{\perp} \approx 4.8 \times 10^5$ a.u., $r_c \approx 1.91 \times 10^4$ a.u., $\omega_c \approx 1.8 \times 10^{-7}$ a.u., $\omega_z = 3.6 \times 10^{-9}$ a.u. and $\omega_D \approx 1.25 \times 10^{-10}$ a.u.

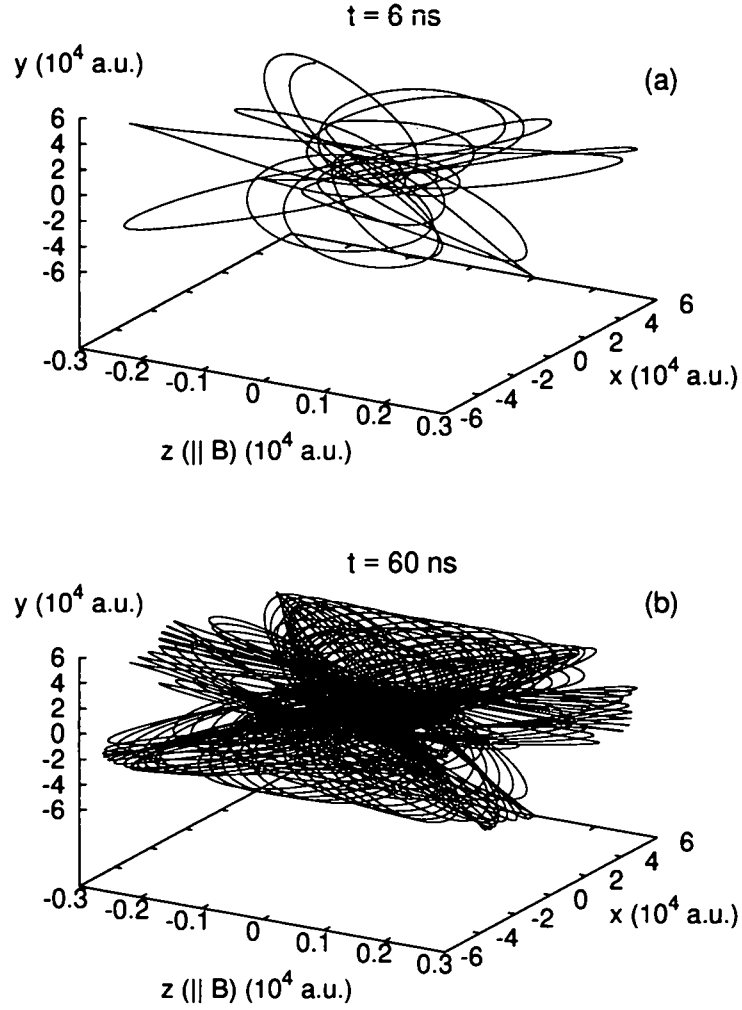


Figure 4.14: Bound-state trajectory for $E_{rel}^{e-ion} \approx -1.054 \times 10^{-4}$ a.u. ($n \approx 413$) in the Coulomb field of a C^{6+} ion and a magnetic field of $B = 42$ mT (along z) evolved for a time of 6 ns (a) and 60 ns (b). The initial transverse electron-ion separation amounts to $r_{\perp} = 7.51 \times 10^3$ a.u., the cyclotron radius to $r_c = 2.1 \times 10^5$ a.u. and the cyclotron and Kepler frequencies are given by $\omega_c \approx 1.8 \times 10^{-7}$ a.u. and $\omega_k \approx 5.1 \times 10^{-7}$ a.u. respectively.

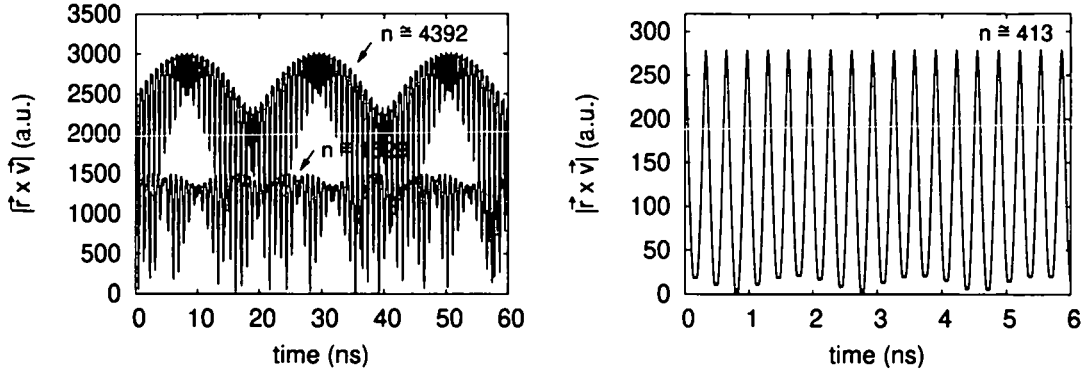


Figure 4.15: The angular momentum $l = |\vec{r} \times \vec{v}|$ shown as a function of propagation time through the solenoid for the trajectories of Figure 4.13 (a) and the trajectory of Figure 4.14 (b). In the presence of the magnetic field ($B = 42$ mT) l is no longer conserved.

an ensemble of electrons does not noticeably change during its passage through the solenoid, but retains the form adopted at the end of the merging process (Eq. (4.8)). Figure 4.16 displays snapshots of the reduced angular momentum distribution $P(l)$ from our CTMC calculation taken at different times within the solenoid. Correspondingly, also $P(n, l)$ is found to be invariant throughout the solenoid. This invariance and maximum randomness of $P(n, l)$ mirrors the classical (chaotic or quasiperiodic) dynamics of weakly bound Rydberg electrons in a relatively strong magnetic field compared to the Coulomb field of the parent ion. Therefore, to determine the probability for radiative stabilization inside the solenoid, the propagation of the formed Rydberg states through the solenoid becomes dispensable and the decay rates may be directly evaluated from the CTMC distributions at the end of the toroid instead.

4.8 Semiclassical Lifetime Estimate

The lifetime of a given Rydberg state with quantum numbers n and l can be determined by the semiclassical estimate [70],

$$\tau(n, l) = \tau_0 \frac{n^3 l(l+1)}{Z^4} \quad (4.9)$$

with $\tau_0 = 93$ ps. Strictly speaking, Eq. (4.9) is only valid for the field-free case ($B = 0$) and does not accurately present the lifetime of individual, magnetized high Rydberg states. Nevertheless, it may serve as a first-order estimate for the

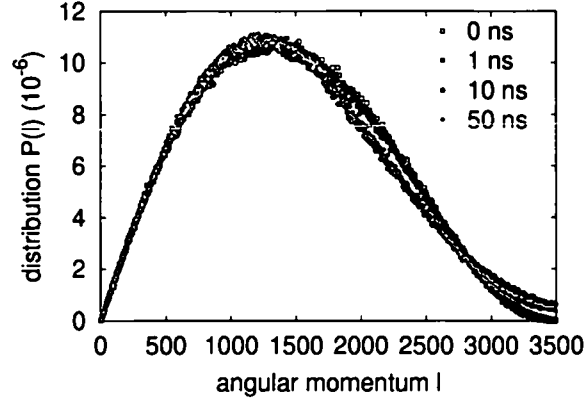


Figure 4.16: Angular momentum distribution of the bound-state electrons, as they follow from the merging with C^{6+} ions at the TSR with $B = 42$ mT, recorded at different times during the propagation through the solenoid. $t = 0$ refers to the entrance into the solenoid region. In detail, the parameters of the initial ensemble are $kT_{\perp} = 10$ meV, $kT_{\parallel} = 0.06$ meV, $E_{rel} = 0.03$ meV and $R = 8.825 \times 10^5$ a.u.

statistically populated Rydberg manifolds since state mixing leads to a redistribution rather than an overall change in the transition probabilities (see also section 4.7). Moreover, the precise value of individual $\tau(n, l)$ does not enter the final analysis. Taking, for example, $n = 1000$, $Z = 6$ and $l = 1$, τ amounts to a value of 1.4×10^5 ns. By comparison, the time τ_c available for radiative stabilization within the solenoidal region of the TSR electron cooler is approximately 60 ns. Therefore, for Rydberg states typically obtained in the simulation $\tau(n, l) \gg \tau_c$. Accordingly, the vast majority of the formed bound states will be reionized again in the toroidal demerging section where the Coulomb barrier gets depressed a second time. Just a small fraction of the captured electrons is observed at lower lying Rydberg states (*i.e.* with n of the order of few hundred) (see Table 4.2) after the merging. In view of the long lifetimes of these bound states (even $\tau(200, 1) \approx 1.1 \times 10^3$ ns and $\tau(100, 1) \approx 1.4 \times 10^2$ ns with $Z = 6$) only a miniscule fraction of the recombined electrons will thus have radiatively decayed to a state sufficiently deeply bound to escape the demerging toroid without field ionization. For instance, for typical TSR parameters recombined C^{5+} ions are ionized for Rydberg states with $n \gtrsim 60$ by demerging and for $n > n_r \approx 30$ by the subsequent bending magnet (compare Figure 4.17).

4.9 Properties of the Stark Saddle

In this section the potential generated by the Coulomb field of an ion (charge Z) and a homogeneous electric field $\vec{F} = F\hat{e}_z$ is analyzed. The position and energy of the obtained saddle point, the so-called Stark saddle, and the critical principal quantum number n_F with respect to field ionization will be given [71]. Classically, field ionization, or vice versa, recombination as discussed previously is possible above the Stark saddle. Its position \vec{r}_0 is determined (in a.u.) with $F > 0$ by

$$\frac{d}{d\vec{r}} \left(-\frac{Z}{|\vec{r}|} + Fz \right)_{\vec{r}=\vec{r}_0} = 0 \implies \vec{r}_0 = (0, 0, -\sqrt{Z/F}) \quad (4.10)$$

and the energy at \vec{r}_0 follows as

$$E(\vec{r}_0) = -\frac{Z}{|\vec{r}_0|} + F z_0 = -2\sqrt{ZF}. \quad (4.11)$$

The absolute value of this energy $|E(\vec{r}_0)|$ is referred to as the depth of the Stark saddle. The electric field strength for which the energy of this saddle point equals the field free energy of the electron in a given Rydberg state n , *i.e.* $E(\vec{r}_0) = -Z^2/(2n^2)$, is calculated as

$$F_{sp}(n) = \frac{Z^3}{16n^4} = \xi^{sp} \frac{Z^3}{n^4} F_0. \quad (4.12)$$

$\xi^{sp} = 1/16$ (with the index *sp* for "saddle point" emphasizing the simple energy argument used to derive Eq. (4.12)) and F_0 refers to the atomic field strength $F_0 = e/a_0^2 = 1 \text{ a.u.} = 5.142 \times 10^9 \text{ V/cm}$. Generally, the critical electric field strength for field ionization of the Rydberg electron in state n is given by

$$F_c(n) = \xi \frac{Z^3}{n^4} F_0. \quad (4.13)$$

For hydrogenlike systems the parameter ξ has been established as $\xi \approx 1/8$ from experiments with field-ionization [72]. From Eq. (4.13) the critical quantum number n_F for ionization by the field F is obtained by solving the relation $F_c(n_F) = F$ with respect to n_F , which leads to

$$n_F = \xi^{1/4} \frac{Z^{3/4}}{(F/F_0)^{1/4}} = \left(\frac{6.43 \times 10^8 Z^3}{(F/(V/cm))} \right)^{1/4}. \quad (4.14)$$

Thus, the threshold for field ionization or field-induced recombination increases with the ion charge, $n_F \propto Z^{3/4}$, and decreases with the electric field strength, $n_F \propto F^{-1/4}$. Since $F \approx E_z^R \propto B$ (Eq. (4.5)) during the merging, n_F scales with the magnetic guiding field B as $n_F \propto B^{-1/4}$. Accordingly, the lower tail of the bound state

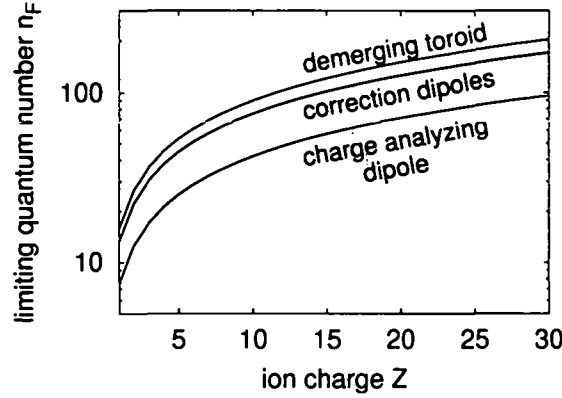


Figure 4.17: Critical principal quantum numbers n_F with respect to field ionization obtained for the demerging toroid ($F \approx 10$ kV/cm), the adjacent correction dipoles ($F \approx 20$ kV/cm) and the subsequent charge analyzing dipole magnet ($F \approx 200$ kV/cm) of the TSR electron cooler as a function of the ionic charge Z . The values for F are taken from Ref. [73].

distributions in Figure 4.11b shifts to higher n values with increasing Z , whereas to lower n with increasing B (see also Table 4.2). Figure 4.17 displays the critical quantum numbers n_F according to Eq. (4.14) as encountered in the various magnets at the TSR electron cooler [73].

Comparing the depth of the Stark saddle with the transverse electron-ion collision energies [45] a qualitative estimate for the time scale at which the formation of bound states sets in during the merging process (see Table 4.1) can be obtained. For the straight-lined ion trajectories $\vec{v}_{ion} = v_{ion} \hat{e}_y$ (section 4.3) the electron-ion collision energy $E_{col\perp}^{e-ion}$ perpendicular to the ion motion is given by the electron energies into the x and z directions. Neglecting the small velocity spreads due to the Maxwell-Boltzmann distribution of the velocities in the beam the electrons propagate with a beam velocity of $v_{e\parallel} \approx 0.1c$ along the curvature of the toroid. Thus, the transverse electron-ion collision energy is calculated as

$$E_{col\perp}^{e-ion} \approx \frac{1}{2} (v_{e\parallel} \sin \phi_e)^2. \quad (4.15)$$

On the other hand, the depth of the Stark saddle due to the electric field $E_z^R = v_{ion}y/c B \sin \phi$ (Eq. (4.5)) follows according to Eq. (4.11) with $F = E_z^R \leq 0$ as

$$E_{Stark} = |E(\vec{r}_0)| = 2\sqrt{Z |E_z^R|}. \quad (4.16)$$

It varies along the path of the ion because of the decrease of $|E_z^R|$ during the toroidal merging region. In Figure 4.18 the transverse collision energy Eq. (4.15) with $v_{e\parallel} =$

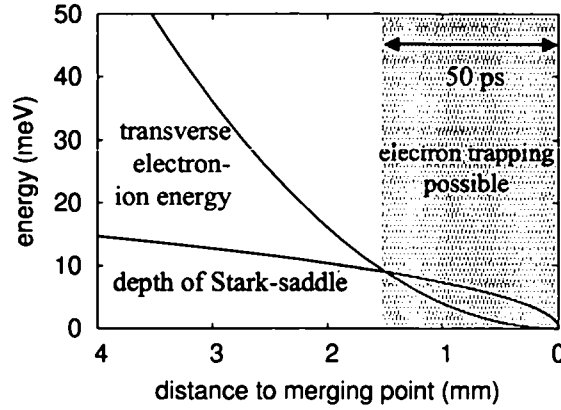


Figure 4.18: The electron-ion collision energy transverse with respect to the ion motion $E_{col\perp}^{e-ion}$ (Eq. (4.15)) and the depth of the Stark saddle E_{Stark} (Eq. (4.16)) generated by the Coulomb and electric fields are shown for the end of the merging section. The region for electron trapping to occur is estimated by $E_{col\perp}^{e-ion} < E_{Stark}$.

$v_{iony} = 0.1c$ and the depth of the Stark saddle Eq. (4.16) with $Z = 6$ are compared. Accordingly, if $E_{col\perp}^{e-ion} < E_{Stark}$ electron trapping is expected to become possible. Thus, for C^{6+} ions at the TSR experiment [10] illustrated in Figure 4.18, electrons are estimated to be captured into bound states within the last 1.6 mm of the toroid or, correspondingly, the last 50 ps in time before merging is completed. A comparison with Table 4.1 shows that this simple estimate yields the right order of magnitude in time for electron capture to occur during the merging region.

4.10 Evaluation of Radiative Decay Rates

To determine the efficiency of the field-induced recombination (FIR) mechanism the radiative stabilization of the formed Rydberg states by transitions to states with $n \leq n_r$ has to be computed in detail. The probability for a given Rydberg state with quantum numbers n and l to radiatively decay to a state n', l' inside the solenoid per unit time is given by [7] (appendix G)

$$W(n, l \rightarrow n', l' = l \pm 1) = \frac{4}{3} \frac{\omega^3}{c^3} \frac{\max(l, l')}{2l + 1} \left(R_{nl}^{n'l \pm 1} \right)^2 \quad (4.17)$$

where ω denotes the energy of the emitted photon. The integral over the radial wave-functions $R_{nl}^{n'l \pm 1} = \int_0^\infty R_{nl} R_{n'l \pm 1} r^3 dr$ can be evaluated in closed form. According to

Ref. [7] $R_{nl}^{n'l-1}$ is calculated as

$$R_{nl}^{n'l-1} = \frac{(-1)^{n'-l}}{4(2l-1)!} \sqrt{\frac{(n+l)!(n'+l-1)!}{(n-l-1)!(n'-l)!}} \frac{(4nn')^{l+1}(n-n')^{n+n'-2l-2}}{(n+n')^{n+n'}} \times$$

$$\left[{}_2F_1\left(-n_r, -n'_r, 2l; -\frac{4nn'}{(n-n')^2}\right) - \left(\frac{n-n'}{n+n'}\right)^2 {}_2F_1\left(-n_r-2, -n'_r, 2l; -\frac{4nn'}{(n-n')^2}\right) \right] \quad (4.18)$$

with the hypergeometric function ${}_2F_1(\alpha, \beta, \gamma; z)$ [63] and the radial quantum numbers $n_r = n - l - 1$ and $n'_r = n' - l$ of the initial and final states. We assume, for simplicity, that the field free ($B = 0$) rates can be used. Due to the invariance of $P(l)$ within the solenoid (section 4.7 and Figure 4.16) this approximation may be justified for averages over a very large number of contributing l, l' states while it is clearly inappropriate for individual state-to-state transitions. The total rate for radiative stabilization of a given high n, l state to low-lying states is given by the sum over the decay rates into all final states ($n' \leq n_r$), *i.e.*

$$W(n, l) = \sum_{n' \leq n_r, l'} W(n, l \rightarrow n', l'). \quad (4.19)$$

Figure 4.19 displays $W(n, l)$ due to radiative decay of highly excited C^{5+} ions into experimentally observable final states with $n' \leq 30$ for the TSR. $W(n, l)$ scales as n^{-3} for not too small values of n (deviations from this scaling arise at smaller n values for larger values of l , however, even for $l = 30$ the n^{-3} scaling is approximately appropriate for $n \gtrsim 200$) and also strongly decreases with increasing l hence varying over many orders of magnitude for the Rydberg states typically obtained in the simulation. Correspondingly, radiative stabilization is highly favored for initial states with lower n and l quantum numbers.

We note that for the investigated n range ($n \approx 10^2 - 10^3$) the indices in the hypergeometric functions of Eq. (4.18), $-n_r$ and $-n_r - 2$ respectively, become large negative numbers. The determination of ${}_2F_1$, *i.e.* ${}_2F_1(\alpha, \beta, \gamma; z) = \sum_{\nu} \alpha(\alpha+1)\dots(\alpha+\nu-1)\beta(\beta+1)\dots(\beta+\nu-1)/(\gamma(\gamma+1)\dots(\gamma+\nu-1))z^{\nu}/\nu!$ [63], then involves the multiplication and subsequent summation of rather large numbers which, in turn, leads to instabilities in the numerical evaluation of $R_{nl}^{n'l'}$, essentially given by the difference of two hypergeometric functions, at higher n values. Eventually, for $n \gg 1$, $R_{nl}^{n'l'}$ is found to diverge at all. Therefore, asymptotic expansions of ${}_2F_1$ must be used. Since for larger values of n $W(n, l)$ is well described by a n^{-3} dependence we can extrapolate $R_{nl}^{n'l'}$ into the high n region according to this scaling, *i.e.* $R_{nl}^{n'l'} \propto n^{-3/2}$.

With Eq. (4.19) the recombination probability per ion through radiative stabi-

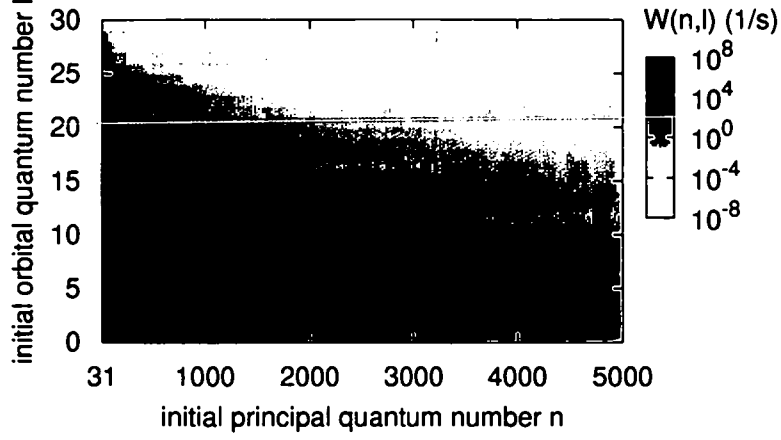


Figure 4.19: Density plot of the rate for radiative stabilization $W(n, l)$ (Eq. (4.19)) into final states with $n' \leq 30$ of recombined C^{5+} ions shown as a function of the initial quantum numbers n and l . Note that $W(n, l)$ (given in units of s^{-1}) is drawn on a logarithmic scale and extends over 16 (!) orders of magnitude for the parameter range displayed. Only the lower left corner is of relevance for the experiment.

lization can be estimated as

$$P_s = \sum_{n, l} \bar{P}(n, l) (1 - e^{-\tau_c W(n, l)}) \approx \tau_c \sum_{n, l} \sum_{n', l'} \bar{P}(n, l) W(n, l \rightarrow n', l'), \quad (4.20)$$

where $\bar{P}(n, l)$ represents the average number of electrons found in the state n, l at the end of the merging process and $\tau_c \approx 60$ ns (τ_c : time within the solenoid at the TSR). $\bar{P}(n, l)$ is associated with the distribution of Rydberg states from the CTMC obtained per incident electron $P(n, l)$ through the relation $\bar{P}(n, l) = n_e V P(n, l)$. Here n_e is the electron density available in the experiment and $V = 4/3 \pi R^3$ the coordinate space volume of the initial ensemble in the CTMC. In our case, $n_e = 7.0 \times 10^6 \text{ cm}^{-3}$ [10] and $R = 8.825 \times 10^5 \text{ a.u.}$ (corresponding to $n_{ion} = 1.23 \times 10^6 \text{ cm}^{-3}$), i.e. about three electrons are found, on the average, in the simulated volume. Using Eq. (4.8) $\bar{P}(n, l)$ can be expressed as

$$\bar{P}(n, l) = n_e V P(n, l) = n_e V P(n) \frac{(2l+1)}{n^2} = \bar{P}(n) \frac{(2l+1)}{n^2}. \quad (4.21)$$

The evaluation of P_s (Eq. (4.20)) thus only requires the distribution of the principal quantum numbers $P(n)$ (determined at the end of the merging region as discussed in section 4.7, see also Figure 4.11b) from the simulation. Finally, the probability for radiative stabilization of transient bound states per ion and per revolution in the

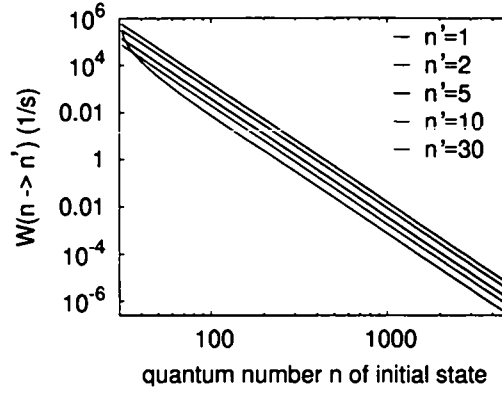


Figure 4.20: The transition rates $W(n \rightarrow n')$ summed over l and l' (Eq. (4.22)) plotted as a function of the initial quantum number n for radiative decay into different final states n' as indicated. $W(n \rightarrow n')$ decreases $\propto n^{-5}$.

ring reads

$$\begin{aligned}
 P_s &= \tau_c \sum_{n > n_r} \bar{P}(n) \sum_{n'=1}^{n_r} W(n \rightarrow n') = \\
 &= \tau_c \sum_{n > n_r} \bar{P}(n) \sum_{n'=1}^{n_r} \frac{4\omega^3}{3c^3} \frac{1}{n^2} \sum_{l'=0}^{n'-1} \sum_{l=l'-1}^{l'+1} \max(l, l') \left(R_{nl}^{n'l'} \right)^2. \quad (4.22)
 \end{aligned}$$

Figure 4.20 presents the involved transition rates $W(n \rightarrow n')$ after summation over l and l' . Their scaling with n^{-5} clearly demonstrates the importance of lower n states for radiative stabilization. For example, we find a probability of $P_s \approx 2.76 \times 10^{-10}$ for radiative stabilization into states with $n' \leq 30$ for the ensemble investigated in section 4.5, where $B = 42$ mT, $Z = 6$, $kT_{\perp} = 10$ meV, $kT_{\parallel} = 0.06$ meV and $E_{rel} = 0.03$ meV. By comparison, the probability for radiative recombination $P_{RR} = n_e \alpha_{RR} \tau_c$ amounts to 1.45×10^{-10} with $n_e = 7 \times 10^6$ cm $^{-3}$ and a standard rate coefficient (Eq. (2.11)) of $\alpha_{RR} = 3.45 \times 10^{-10}$ cm 3 /s. Accordingly, the field-induced formation of Rydberg states during the merging followed by radiative stabilization is almost twice the contribution from radiative recombination.

For the RR process free electrons are available all over the cooling solenoid. The rate coefficient α_{RR} , which measures the probability for recombination of an incident electron and a given ion per unit volume and unit of time (compare Eqs. (2.4) and (2.11)), is well-defined. In contrast, the additional contribution due to the merging (Eq. (4.20)) faces the conceptual difficulty that the feeding mechanism of the radiative decay channel by the formation of bound states during the merging is

transient and stops after the merging is completed. Thus, inside the solenoid the source term for radiative stabilization continuously gets depleted, conflicting with the concept of a constant rate coefficient. However, for long-lived high-lying states $\tau(n, l) \gg \tau_c$ this depletion, *i.e.* the decrease of available Rydberg states due to preceding radiative decay processes, can be safely neglected as long as the linear approximation used to derive Eq. (4.20) and, thus, the conversion of Eq. (4.22) into a constant rate inside the solenoid is valid. In analogy to RR, a rate coefficient α_s can be defined for the radiative stabilization channel as

$$\alpha_s = \frac{P_s}{n_e \tau_c}. \quad (4.23)$$

In fact, this recombination rate converges towards the standard RR rate in the limit that the initial electron energy becomes positive. Note that in view of the low probability for forming bound states (see Table 4.2) and the slow decay rate to lower n , the recombination probability per ion via this additional recombination channel is a very small number. Nevertheless, as the numerical example given above clearly shows, it is competitive with radiative recombination, a similarly improbable process requiring an ion circulating in the storage ring, on the average, for billions of times before recombination takes place.

Finally we point out that the l and l' sums in Eq. (4.22) can be eliminated by using an approximate expression for the oscillator strength summed over l, m, l' and m' [7]. The oscillator strength f (n, l, m and n', l', m' denote the principal, orbital and magnetic quantum number of the initial and final state, respectively)

$$f_{nlm \rightarrow n'l'm'} = 2\omega |x_{nlm \rightarrow n'l'm'}|^2 \quad (4.24)$$

is a dimensionless quantity and corresponds to the effective number of classical electron harmonic oscillators that would emit (or absorb) radiation as strongly as the atom does. For a one electron atom or ion $\sum_{n'l'm'} f_{nlm \rightarrow n'l'm'} = 1$ (Thomas-Reiche-Kuhn sum rule). Note that the definition of f contains only one polarization direction of the emitted radiation. Therefore, $f_{nlm \rightarrow n'l'm'} = 2\omega/3 |\vec{r}_{nlm \rightarrow n'l'm'}|^2$. The summed oscillator strength (compare with Eq. (G.9))

$$f_{n \rightarrow n'} = \sum_{l, l'} \sum_{m, m'} f_{nlm \rightarrow n'l'm'} = \frac{2\omega}{3} \sum_{l, l'} \max(l, l') \left(R_{nl}^{n'l'} \right)^2 \quad (4.25)$$

can be approximated according to Ref. [7] by

$$f_{n \rightarrow n'} \approx \frac{2^5}{3\sqrt{3}\pi} \left(\frac{1}{n'^2} - \frac{1}{n^2} \right)^{-3} \frac{1}{n'^3 n^3}. \quad (4.26)$$

This expression represents the sums accurately for large n and n' and to within a factor of about two for all values of $n \neq n'$, whereat for small n and n' the exact

expression Eq. (4.25) is overestimated. Hence Eq. (4.22) can be approximately evaluated as

$$P_s(\tau_c) \approx \tau_c \sum_{n > n_r} \bar{P}(n) \sum_{n'=1}^{n_r} \frac{2\omega^2}{c^3} \frac{2^5}{3\sqrt{3}\pi} \left(\frac{1}{n'^2} - \frac{1}{n^2} \right)^{-3} \frac{1}{n'^3 n^5}. \quad (4.27)$$

Similarly, as for the calculation of the standard RR rates (section 2.2), this approximation can be improved by including Gaunt factors (Eq. (2.13)) thus approaching the exact expression of Eq. (4.22). However, in the following we do not employ Eq. (4.27) but rather Eq. (4.22) for the determination of the recombination rates via Eq. (4.23).

4.11 Alternative Approach to Radiative Decay

Before presenting the obtained excess rate coefficients α_s , first, an alternative approach to determine the radiative stabilization of the formed Rydberg states will be pursued [64]. The formalism given below clearly demonstrates the equivalence of the standard RR rates established for positive initial electron energies and the radiative decay rates evaluated for bound-state electrons.

Starting from radiative recombination we rewrite the rate coefficient in a way which allows its immediate extension to weakly bound states. The RR rate coefficient (Eq. (2.11)) may be transformed to an integral over the energy scale ($E = E_{\text{rel}}^{e-\text{ion}}$ characterizes the relative energy between electron and ion)

$$\alpha_{RR} = \int \sigma_{\text{total}} v f(\vec{v}) d^3v = \sqrt{2} \sum_{n'} \int_{E>0} \sigma_{RR}(n', E) \frac{f(E)}{\sqrt{E}} E dE \quad (4.28)$$

for the isotropic RR cross section (compare Eq. (2.7), for simplicity Gaunt factors are omitted) given in a.u. by

$$\sigma_{RR}(n', E) = \frac{32\pi}{3\sqrt{3}c^3} \frac{Z^4/4}{n'E(Z^2/2 + n'^2E)} = \frac{16\pi}{3\sqrt{3}c^3} \frac{Z^2}{n'E} \frac{-E_{n'}}{E - E_{n'}} \quad (4.29)$$

with $E_{n'} = -Z^2/(2n'^2)$. For the anisotropic Maxwell-Boltzmann velocity distribution $f(\vec{v})$ (Eq. (2.12)) the energy distribution $f(E)/\sqrt{E} = \sqrt{2} \int f(\vec{v}) d\Omega$ (Ω denotes the solid angle) is calculated as

$$\begin{aligned} \frac{f(E)}{\sqrt{E}} &= \frac{1}{kT_{\perp} \sqrt{kT_{\parallel}}} \exp\left(-\frac{E - E_{\text{rel}}/\xi}{kT_{\perp}}\right) \frac{1}{\sqrt{\xi E/(kT_{\parallel})}} \times \\ &\times \frac{1}{2} \left[\text{erf}\left(\sqrt{\frac{\xi E}{kT_{\parallel}}} + \sqrt{\frac{E_{\text{rel}}/\xi}{kT_{\parallel}}}\right) + \text{erf}\left(\sqrt{\frac{\xi E}{kT_{\parallel}}} - \sqrt{\frac{E_{\text{rel}}/\xi}{kT_{\parallel}}}\right) \right] \end{aligned} \quad (4.30)$$

where $\xi = 1 - T_{\parallel}/T_{\perp}$ and $E_{rel} = v_{rel}^2/2$. Using Eq. (4.29) with the approximation $-E_{n'}/(E - E_{n'}) \approx 1$ justified for incident electrons in the energy range of few meV the rate coefficient becomes

$$\alpha_{RR} = \gamma_E \sqrt{2\pi^2} \sum_{n'} \frac{Z^2}{n'} \int_{E>0} \frac{f(E)}{\sqrt{E}} dE \quad (4.31)$$

after having introduced the universal constant $\gamma_E = 16/(3\sqrt{3}\pi c^3)$.

In order to rewrite the integrand of Eq. (4.31) we express the average number of electrons $\bar{f}(E)dE$ found in the energy interval dE in terms of the density of available states D_{free} and the probability of occupation $N(E)$, *i.e.*

$$\bar{f}(E)dE = n_e V f(E)dE = D_{free}(E)N(E)dE \quad (4.32)$$

with the electron density n_e and the spatial volume V . Employing the density of states for free electrons disregarding the spin degeneracy

$$D_{free}(E) = \frac{V\sqrt{2E}}{2\pi^2} \quad (E > 0) \quad (4.33)$$

the phase space occupation for the continuum states is thus obtained as

$$N(E) = n_e V \frac{f(E)}{D_{free}(E)} = \sqrt{2\pi^2} n_e \frac{f(E)}{\sqrt{E}}. \quad (4.34)$$

With this relation the rate coefficient Eq. (4.31) finally yields

$$\alpha_{RR} = \gamma_E \sum_{n'} \frac{Z^2}{n'} \int_{E>0} \frac{N(E)}{n_e} dE. \quad (4.35)$$

The quantity $N(E)/n_e$ has the dimension of a volume and may be interpreted as a kind of reaction volume. Since quantum states closely below and closely above the ionization threshold contribute with about the same strength to radiative decay into lower lying states, the corresponding occupation numbers $N(E)$ for continuum and bound states can be directly compared in order to estimate the radiative stabilization of free and bound electrons, respectively. Thus, Eq. (4.35) can be analogously applied to Rydberg state electrons,

$$\alpha_s = \gamma_E \sum_{n'} \frac{Z^2}{n'} \int_{E<0} \frac{N(E)}{n_e} dE, \quad (4.36)$$

where the integrand is determined by

$$\frac{N(E)}{n_e} = \frac{\bar{P}(E)}{n_e D_{Ryd}(E)}. \quad (4.37)$$

The average number of electrons $\bar{P}(E)$ is established from the energy distribution per electron $P(E)$ of the CTMC (Figure 4.11a with $E_B = -E$) by the relation $\bar{P}(E) = n_e V P(E)$ and $D_{Ryd}(E)$ represents the density of Rydberg states on the energy scale neglecting the spin of the electron

$$D_{Ryd}(E) = \frac{Z^3}{(-2E)^{5/2}} \quad (E < 0). \quad (4.38)$$

From the rate coefficient α the probability for stabilization follows by multiplication with the electron density n_e and the cooler time τ_c (Eq. (4.23)). Accordingly, the contribution from radiative recombination per ion and per revolution in the storage ring is given by

$$P_{RR}(\tau_c) = n_e \tau_c \alpha_{RR} = \tau_c \gamma_E \frac{\sqrt{2}\pi^2}{V} \sum_{n'=1}^{n_r} \frac{Z^2}{n'} \int_{E>0} \frac{\bar{f}(E)}{\sqrt{E}} dE, \quad (4.39)$$

whereas the contribution from radiative decay of the formed bound states amounts to

$$P_s(\tau_c) = n_e \tau_c \alpha_s = \tau_c \gamma_E 4\sqrt{2} \sum_{n'=1}^{n_r} \frac{1}{Z n'} \int_{E<0} \bar{P}(E) (-E)^{5/2} dE. \quad (4.40)$$

The analytically known distribution $\bar{f}(E)$ in Eq. (4.39) should be better replaced by the positive electron energy distribution from the simulation, *i.e* by $\bar{P}(E)$ with $E > 0$. Then the RR rate is accurately determined taking into account also the effect of FIR during the merging whereupon the electron energy distribution starts leaking into the $E < 0$ region due to the transient electric field. Correspondingly, $\int_{E>0} P(E) dE = 1 - \int_{E<0} P(E) dE$ after the merging instead of $\int_{E>0} f(E) dE = 1$ used for the calculation of the conventional RR rate. Figure 4.21 displays the Maxwell-Boltzmann energy distribution $f(E)$ of Eq. (4.30) and the calculated relative energy distribution $P(E)$ at the end of the merging section. $P(E)$ gets shifted somewhat towards smaller energies compared to the pure Maxwell-Boltzmann distribution. The total change in the positive energy distribution, however, remains small. For example, with the data of Figure 4.21 and $n_r = 30$ the recombination rate is computed as $\alpha_{RR} = 3.53 \times 10^{-10} \text{ cm}^3/\text{s}$, whereas the usual rate coefficient with $f(E)$ amounts to $\alpha_{RR} = 3.45 \times 10^{-10} \text{ cm}^3/\text{s}$. Therefore, the standard RR rate is not significantly modified by the formation of bound states during the merging due to the overall shift of $P(E)$ towards lower E and the conventional determination of α_{RR} according to Eq. (2.11) may be still applied.

Note that the probability for radiative stabilization according to Eq. (4.40) agrees with the value previously determined from the n distribution Eq. (4.27) (appendix H). Moreover, in appendix H also the continuity of the transition rates across the ionization threshold

$$\lim_{n \rightarrow \infty} D_{Ryd}(n) W(n \rightarrow n') = \lim_{E \rightarrow 0} D_{free}(E) W(E \rightarrow n') \quad (4.41)$$

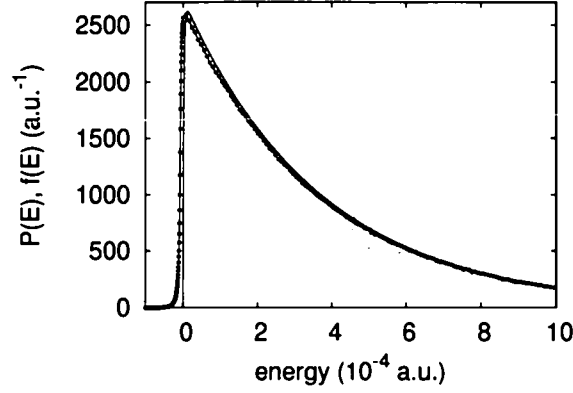


Figure 4.21: Energy distribution $P(E)$ (red points connected with line) after the merging between electrons and ions at the TSR with $kT_{\perp} = 10$ meV, $kT_{\parallel} = 0.06$ meV, $E_{rel} = 0.03$ meV, $Z = 6$ and $B = 42$ mT; $\int_{E>0} P(E)dE \approx 0.9788$ and $\int_{E<0} P(E)dE \approx 0.0212$. For comparison, the Maxwell-Boltzmann distribution $f(E)$ according to Eq. (4.30) (blue line) is also shown.

is verified. Here $W(n \rightarrow n')$ and $W(E \rightarrow n')$ denote the transition probabilities per unit of time for bound (due to Eq. (4.27) or (4.40)) and free electrons (following from Eq. (4.39)), respectively.

However, to calculate the magnetic field and the nuclear charge dependence of FIR in the following, we explicitly evaluate the l and l' sums (see also Eq. (4.25)) in the transition probabilities during our calculation. The presented rates are thus determined via Eqs. (4.22) and (4.23).

4.12 Magnetic Field and Charge Dependence of the Field-Induced Recombination

Since the measured rate is a combination of RR and radiative stabilization, *i.e.* $\alpha = \alpha_{RR} + \alpha_s$, α_s can be identified with the excess recombination rate observed in the measurements $\Delta\alpha = \alpha_s$. Note that in this section the effect of the chaotic scattering dynamics onto the RR rates discussed in the previous chapter is neglected. Only the enhancement of the recombination due to the merging of electron and ion beams will be compared with the experimental data.

Figure 4.22 illustrates the magnetic field dependence and Figure 4.23 the charge dependence of α_s determined from Eqs. (4.22) and (4.23). The calculated absolute excess rate coefficient as a function of B agrees with the experimental data quite

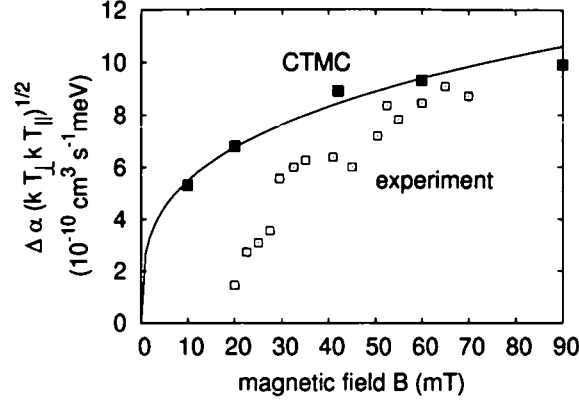


Figure 4.22: Magnetic field dependence of the excess recombination rate for C^{6+} ions. The blue full squares denote the rate coefficients due to FIR (Eq. (4.23)) and the red open squares represent the excess rates of the TSR experiment [10]. The rates are scaled with $\sqrt{kT_{\perp}kT_{\parallel}}$ according to the temperature dependence found in [10]. In the CTMC $kT_{\perp} = 10$ meV, $kT_{\parallel} = 0.2$ meV, $E_{rel} = 0.03$ meV and $n_r = 30$. The line drawn to guide the eye is proportional to $B^{0.3}$. Stray fields inside the solenoid are not considered. The statistical error bar is within the symbol size.

well, in particular for higher magnetic fields (Figure 4.22). The field dependence of the excess rate $\Delta\alpha \sim B^{0.3}$ is somewhat weaker than observed in the measurements ($\sim B^{0.5}$). However, in the experiment electron cooling did not work well for small magnetic field strengths ($B \lesssim 25$ mT) [74], which is possibly reflected in the strong drop of the experimental $\Delta\alpha$ below 30 mT (see Figure 4.22). Furthermore, measurements below 20 mT could not be performed. Hence the experimental $B^{0.5}$ scaling of $\Delta\alpha$ might contain a slight overestimate of the actual B dependence of the enhancement. Similarly, the charge dependence of the field-induced recombination follows a $Z^{2.4}$ scaling in close agreement with the experimentally observed $Z^{2.8}$ dependence of Ref. [9] and the $Z^{2.6}$ dependence established after including charges up to $Z = 92$ [12] (Figure 4.23).

We note that uncertainties in the determination of the recombination rates α_s may arise from the extrapolation performed for low values of n (compare Figure 4.11b). These low-lying Rydberg states, although very infrequently populated, nevertheless significantly contribute to the observed recombination into $n' \leq n_r$ due to the n^{-5} dependence of the transition probability $W(n \rightarrow n')$ (see Figure 4.20). In particular, the B dependence of α_s resulting from the preferential population of lower lying bound states (see Table 4.2) is likely affected by statistical uncertainties and the extrapolation error. CTMC simulations with much larger ensemble sizes,

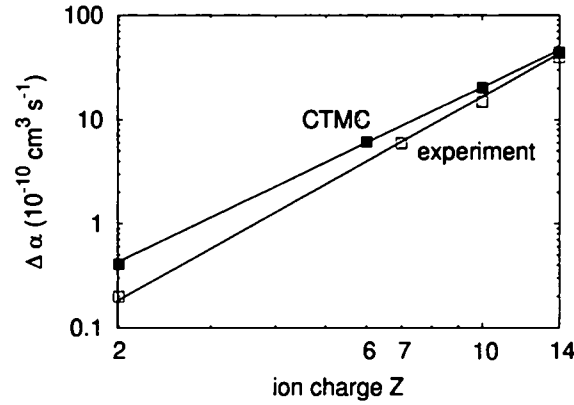


Figure 4.23: Charge dependence of the excess recombination rate. The blue full squares present the rate coefficients due to FIR (Eq. (4.23)) for the TSR merging geometry using $B = 42$ mT, $E_{rel} = 0.03$ meV, $kT_{\perp} = 10$ meV and $kT_{\parallel} = 0.06$ meV. n_r is set to 10, 23, 35 and 43 for He^{2+} , C^{6+} , Ne^{10+} and Si^{14+} , respectively. For comparison, the experimental data from the CRYRING experiment [9] (red open squares) although recorded for a different merging geometry with $B = 30$ mT and $kT_{\parallel} = 0.12$ meV is also shown. The lines indicate a $Z^{2.4}$ behavior for the CTMC data and the $Z^{2.8}$ trend observed in the measurements of Ref. [9]. Field non-uniformities inside the solenoid are neglected. The statistical error bar is within the symbol size.

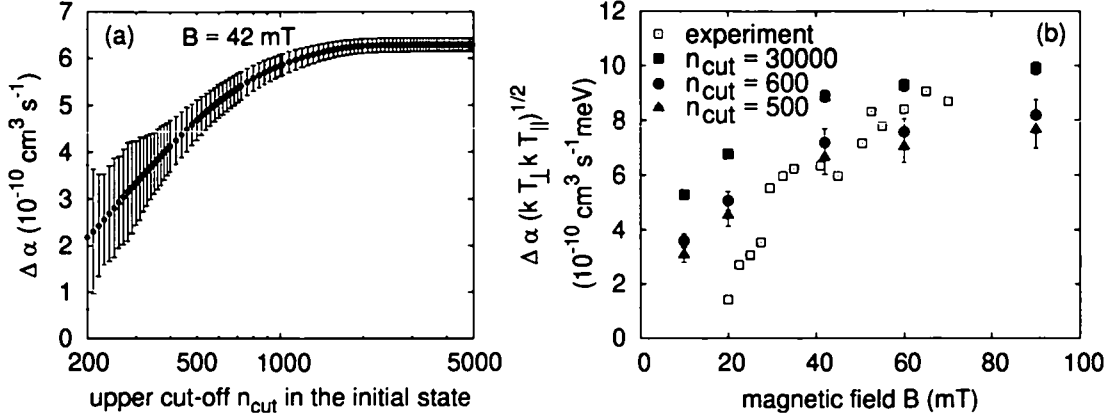


Figure 4.24: Effect of stray fields inside the solenoid. The FIR rate for C^{6+} at $B = 42$ mT as a function of the upper cutoff n_{cut} in the principal quantum number n of the initial state (a) and the B dependence of the thus determined excess rate coefficients (b). The blue full squares and red open squares in (b) denote the temperature rescaled CTMC and experimental data of Figure 4.22 respectively. In addition, the excess rates for $n_{cut} = 600$, *i.e.* a stray field of $\vec{F}_{stray} \approx 1.07$ V/cm (Eq. (4.14)) (magenta circles) and $n_{cut} = 500$ ($\vec{F}_{stray} \approx 2.22$ V/cm) (cyan triangles) are given. Same parameters as in Figure 4.22.

although at present computationally unfeasible, would be desirable.

Due to the rapid decrease of $W(n \rightarrow n')$ with increasing n , very high-lying initial states will hardly contribute to the FIR rate. In our simulations with C^{6+} , for instance, only Rydberg states with $n \lesssim 2000$ are found to noticeably influence the recombination rate into final states with $n' \leq n_r = 30$ (Figure 4.24a).

Moreover, field non-uniformities and electric stray fields inside the solenoid provide an effective upper cutoff at $n = n_{cut}$ for the n distribution of the formed Rydberg states (see also Figure 4.11). In the presence of these small stray fields the Stark saddle cannot completely close. Thus, electrons bound more weakly than the average remaining Stark-saddle energy in the solenoid are in fact not really bound in the experiment. At the TSR electric stray fields of $\vec{F}_{stray} < 2.6$ V/cm are estimated [74, 64] for the C^{6+} and F^{6+} measurements of Ref. [10]. The resulting limitation in n then follows from Eq. (4.14). For example, for $Z = 6$ cutoffs in n at $n_{cut} = 500$ and $n_{cut} = 600$ correspond to fields of $\vec{F}_{stray} = 2.22$ V/cm and $\vec{F}_{stray} = 1.07$ V/cm, respectively. Figure 4.24a shows the obtained excess rate coefficient for C^{6+} with the summation over n restricted to $n \leq n_{cut}$ in Eq. (4.22). In particular, low n states significantly influence the value of α_s (remember $W(n \rightarrow n') \propto n^{-5}$). The error bars refer to the statistical uncertainty within our simulation. In Figures 4.24b and 4.25

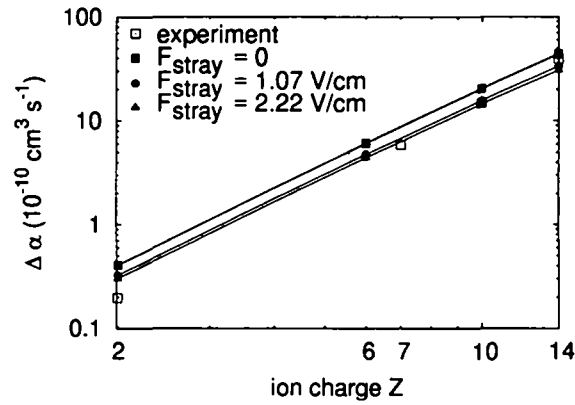


Figure 4.25: Stray fields included into the Z dependence of the excess recombination rate. The blue full squares (points connected with line to guide the eye) and red open squares represent the CTMC and CRYRING data depicted in Figure 4.23. In addition, the rate coefficients obtained for electric stray fields of 1.07 V/cm (magenta circles) and 2.22 V/cm (cyan triangles) inside the solenoid are also shown. According to Eq. (4.14) $\vec{F}_{stray} = 1.07$ V/cm (2.22 V/cm) corresponds to $n_{cut} = 263$ (219) for He^{2+} , $n_{cut} = 600$ (500) for C^{6+} , $n_{cut} = 880$ (733) for Ne^{10+} and $n_{cut} = 1133$ (944) for Si^{14+} , respectively. Same parameters as in Figure 4.23.

the B and Z dependences of the excess recombination rates are illustrated including now the effect of electric stray fields. Accordingly, α_s is reduced somewhat, but not dramatically, by the experimental stray fields. Note that with increasing Z , n_{cut} is shifted to higher values (compare Eq. (4.14)). The inclusion of stray fields thus yields a good agreement of $\Delta\alpha$ with the experimental results at moderate magnetic fields such as $B = 42$ mT while underestimating the measured values somewhat at higher field strengths. Also the Z dependence of the excess recombination comes even closer to the experimental findings.

4.13 Summary

To conclude, transient field-induced recombination due to the merging of electron and ion beams in the electron cooler of a storage ring presents a competitive route to recombination. The magnitude of the resulting recombination rates matches the experimentally observed excess rate coefficients quite well. Also the scaling of the excess recombination with Z and B qualitatively agrees with the measurements. One important point to note is that this enhancement of the recombination rate depends on the geometry of the merging and demerging sections. However, current coolers in different ion storage rings feature similar geometries such that these dependences have not yet been explored. Correspondingly, present results obtained at different facilities closely resemble each other.

Moreover, $\Delta\alpha$ would also depend on the total propagation time τ_c through the solenoid in the limit of long electron coolers (large τ_c) where the linear approximation used to derive Eq. (4.20) fails. For all current cooler setups though the lifetimes of the transiently formed high-lying Rydberg states are much longer than the available cooler times τ_c . Therefore, the observed stabilization is, to a good approximation, linear and no dependency on τ_c can be obtained. We note that CTMC calculations with much larger ensemble sizes would be worthwhile, first of all, to improve the representation of the calculated binding energy (E_B) and the principal quantum number (n) distributions at high E_B and low n values respectively, and, secondly, to try also to tackle a description in terms of n and l quantum numbers, *i.e.* the distribution $P(n, l)$, without making use of the l averaging of Eq. (4.8).

4.14 Sum of the Field-Induced Recombination and the Radiative Recombination in the Magnetic Field

Finally, the radiative recombination (RR) due to the chaotic dynamics in the magnetic field (rate coefficient α) investigated in the previous chapter and the field-induced recombination during the merging followed by radiative stabilization inside the solenoid (FIR) (rate coefficient α_s) treated in the present chapter should be combined. As a first approximation, we simply add the rate coefficients from the two contributions. The magnetic field and charge dependence of the obtained absolute excess recombination rates, *i.e.* $\Delta\alpha = (\alpha - \alpha_{RR}) + \alpha_s$ (α_{RR} : standard RR rate), will be explored in the following. In chapter 3 we have presented the visit functions V^r and V^v resulting in different recombination rates α in a magnetic field. The calculated RR rates led either to an enhancement or a suppression of the recombination process at almost zero relative energy. Now the total excess rate coefficients $\Delta\alpha$ obtained with the two values of α should be compared with each other and with the experimental data. The agreement with the measurements may eventually favor one of the two scenarios for the evaluation of visits to the target ion.

Using V^r the resulting B and Z dependences of $\Delta\alpha$ are depicted in Figures 4.26 and 4.27. In this case the agreement of the calculated values for $\Delta\alpha$ with the measurements is not satisfactory. The combined excess rate coefficients are seen to overestimate the experimental data by at least a factor of two with scaling laws of $B^{-0.08}$ and $Z^{2.1}$ in terms of the magnetic guiding field and the ion charge, respectively. On the other hand, by employing V^v , the RR rates for the solenoid are reduced in certain velocity regions compared to the standard RR rate prediction therefore giving rise to negative "excess" recombination rates $\alpha - \alpha_{RR}$. The resulting sum of the RR and FIR channels exhibits excess rate coefficients with respect to α_{RR} in quite close agreement with the measurements (Figures 4.28 and 4.29). $\Delta\alpha$ is observed to scale as $B^{0.3}$ and $Z^{2.4}$ approximately. The good agreement with the experimental data thus lends support to the latter scenario for the calculation of visits to the ion, *i.e.* in terms of the visit function V^v .

From the comparison with the experiment we can conclude that the magnetic field inside the solenoid appears to modify the probability for recombination of an electron with the target ion with both enhancement and reduction possible. Nevertheless, a significant enhancement of the recombination rate can be found in storage ring experiments with electron cooling. This enhancement originates to a large extent from the finite angle merging of the electron and ion beams in the electron cooler of the ring, which induces an additional channel for free-bound transitions of electrons. The total excess rates calculated are in good agreement with the experimental data.

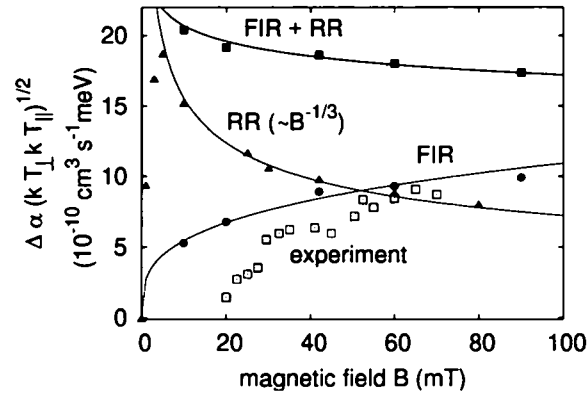


Figure 4.26: Magnetic field dependence of the excess recombination obtained from our simulations of the merging and solenoid regions using V^r for the calculation of the RR rate. The experimental data for C^{6+} [10] (red open squares), the CTMC results from FIR for the TSR merging (magenta circles) (see Figure 4.22, magenta line: $\propto B^{0.3}$), the corresponding data for enhanced RR (cyan triangles) (see Figure 3.28, cyan line: $\propto B^{-1/3}$) and the sum of the two contributions (blue full squares) are shown. Note that the RR rates at $B = 20$ mT and $B = 90$ mT are estimated by extrapolation according to the observed $B^{-1/3}$ dependence. The combined CTMC results are found to scale as $B^{-0.08}$ (blue line).

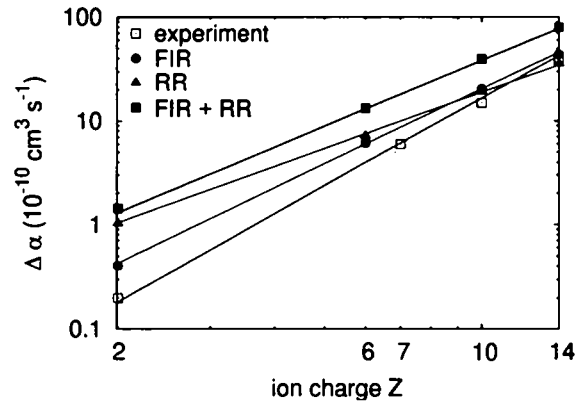


Figure 4.27: Charge dependence of the excess recombination for the combined merging and solenoid calculations using V^r for the evaluation of the RR rate. The measurements from the CRYRING facility [9] (red open squares) are compared with the CTMC results for FIR (magenta circles, data from Figure 4.23), enhanced RR (cyan triangles, data from Figure 3.29) and the sum (blue full squares). The lines reflect the $Z^{2.8}$ dependence of the experimental data in [9] (red), the $Z^{2.4}$ behavior observed for FIR (magenta), the $Z^{1.8}$ scaling of enhanced RR (cyan) and a $Z^{2.1}$ trend for the combined CTMC contributions (blue).

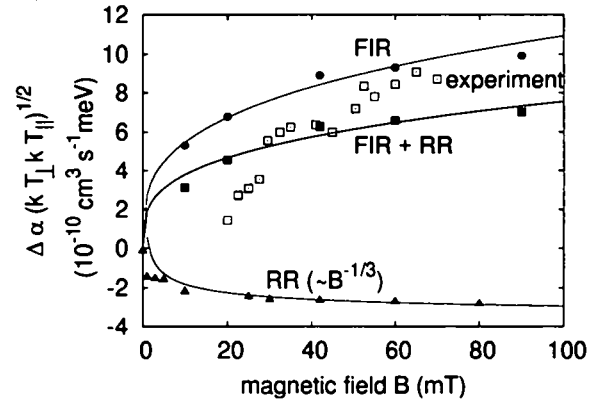


Figure 4.28: Magnetic field dependence of the excess recombination by employing V^v for the calculation of the RR rate. The experimental data for C^{6+} [10] (red open squares), the CTMC results for FIR (magenta circles) (see Figure 4.22, magenta line: $\propto B^{0.3}$) and reduced RR (cyan triangles) (data from Figure 3.33c, cyan line: $\propto B^{-1/3}$) and the sum of the two contributions (blue full squares) are illustrated. The RR rates at $B = 20$ mT and $B = 90$ mT are again estimated by extrapolation according to $B^{-1/3}$. The combined CTMC results scale as $B^{0.3}$ (blue line).

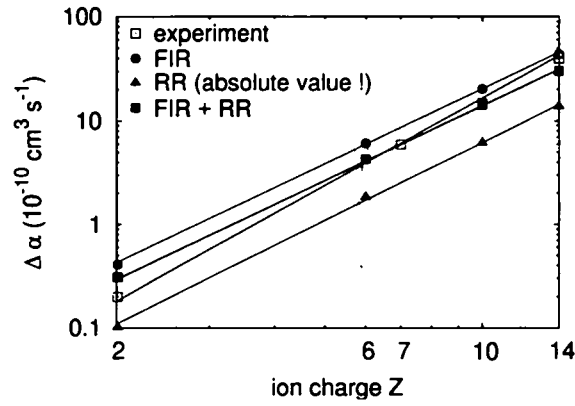


Figure 4.29: Charge dependence of the excess recombination by employing V^v for the evaluation of the RR rate. The measurements from CRYRING [9] (red open squares) are compared with our CTMC data for FIR (magenta circles, data from Figure 4.23), reduced RR (cyan triangles) (absolute value of the negative "excess" rate is plotted) and the sum (blue full squares). The lines indicate the $Z^{2.8}$ dependence of the experimental data [9] (red), the $Z^{2.4}$ scaling of FIR (magenta), a $Z^{2.5}$ behavior seen for the absolute value of the "excess" RR rate (cyan) and another $Z^{2.4}$ trend for the combined CTMC contributions (blue).

Chapter 5

An Alternative Model for the Enhancement

Recently Heerlein, Zwicknagel and Toepffer [13, 75, 76, 77, 78] have proposed an alternative model for the radiative recombination enhancement. In this model the enhancement of the recombination rate α for highly charged ions relative to the standard rate α_{RR} is also attributed to the bound-state density generated during the merging process of the electron and ion beams. The purpose of this chapter is to compare and contrast our present approach to this model. We point to serious difficulties of the model and, therefore, emphasize that this alternative approach does not lead to an understanding of the anomalous rate coefficients. The major issues raised here have been published in form of a comment [14] to the original letter [13] of the authors.

5.1 Sudden Turn-On of the Coulomb Field

In [13] a Vlasov equation is employed to describe the time evolution of the classical phase space density of electrons inside the solenoid in order to investigate whether concentrated electronic density near the ion enhances radiative recombination in the presence of a magnetic field. However, both electron-electron scattering and mean fields are neglected. In this limit the ensemble of electrons evolves as independent particles under the combined influence of the Coulomb field of the ion and the magnetic field in the cooler and, correspondingly, the solution of the Vlasov equation becomes equivalent to the present CTMC calculation. Thus, the electronic dynamics inside the solenoid is treated in the same way as by our approach.

In [13] the process of beam merging is approximated by a sudden switch-on of the Coulomb potential of the target ion, $-\theta(t)Z/|\vec{r}_e - \vec{r}_{ion}|$, where $\theta(t)$ denotes the step function, Z the charge of the ion, and \vec{r}_e and \vec{r}_{ion} the electron and ion coordinates,

respectively. During a sudden turn-on of the Coulomb field of the ion immersed in the gas of electrons bound-state formation results for electrons that suddenly acquire large negative potential energy when located in the vicinity of the ion at the moment of switch-on of the nuclear charge. This nonadiabatic turn-on has to be contrasted with the merging between electron and ion beams in the experiment, where a transient electric field in the rest frame of the ion provides an additional channel for free-bound electron transfer as studied in detail in the previous chapter.

A sudden turn-on should be checked against the experimental time scales involved. At the TSR experiment [10] the characteristic merging time to reach the region of full density n of the cooler is $t_m^{TSR}(r) \approx 1.9$ ns (8×10^7 a.u.) (deduced from the geometric overlap of electron and ion beams, see section 4.2), while the change of relative velocity during the bend occurs on a time scale of $t_m^{TSR}(v) \approx 0.05 - 0.1$ ns ($2 - 4 \times 10^6$ a.u.) (section 4.5). Both time scales $t_m^{TSR}(r)$ and $t_m^{TSR}(v)$ are several orders of magnitude longer than the characteristic orbital period of even the highest surviving Rydberg state in the cooler. Taking $n_r = 30$ for recombined C^{5+} ions the orbital period is approximately 1×10^{-13} sec (5×10^3 a.u.) providing the characteristic time scale and upper bound below which non-adiabatic processes may set in and, therefore, a sudden approximation for the formation of Rydberg states may hold. This large difference in time scales points to the need to form surviving bound states by radiative stabilization inside the solenoid. The latter is, however, not calculated within that model.

The measured enhancement factor $\epsilon = \alpha/\alpha_{RR}$ in [13] is assumed to be represented by the ratio

$$\tilde{\epsilon} = \frac{\langle n_{free} + n_{bound} \rangle}{\langle n_{free} \rangle}, \quad (5.1)$$

where n_{free} and n_{bound} denote the densities of free and bound electrons, respectively. The average $\langle \rangle$ is taken over the velocity and coordinate (*i.e.* phase space) distribution of the electrons in the cooler. Note that this description in terms of the total density of electrons $\langle n_{free} \rangle$ or $\langle n_{bound} \rangle$ is different from the spectral density $P(E_{rel}^{e-ion})$ discussed in the previous chapter. According to Ref. [13] the coordinate space average is restricted to a cylinder with a radius given by the average cyclotron radius r_c and a length along the direction of the magnetic field given by the longitudinal Debye length $r_{d\parallel}$. This volume is considered as the relevant region for radiative recombination to take place.

The definition of the enhancement factor according to Eq. (5.1) implies conceptual difficulties due to the non-equivalent role of n_{bound} and n_{free} . n_{bound} describes the density of bound electrons formed during the "merging" by a non-radiative redistribution process and n_{free} represents the density of free electrons after the merging being the source for radiative recombination. While n_{bound} is the result of a mechanical capture of electrons caused by the sudden turn-on of the ionic

Coulomb field in [13], n_{free} is subject to radiative electron capture. Adding these two densities without weighting factors that contain the information on radiative and non-radiative recombination probabilities and radiative stabilization appears to be poorly justified.

The instantaneous turn-on of the ionic Coulomb field will now be analyzed and compared to the realistic beam merging process treated in chapter 4.

5.2 Test of the Sudden Approximation

In order to test the validity of the sudden approximation employed in [13] the degree of non-adiabaticity of the electron-ion merging has to be quantified. In the adiabatic limit of a merging process the electron-ion internal energy would be - as in the solenoid region - approximately conserved. According to our analysis in section 3.2 the transfer of electron-ion center of mass energy to relative energy due to the coupling by a constant magnetic field is very small (energy conservation to better than 10^{-7} a.u.). Thus, for an adiabatic beam merging transitions from free to (experimentally resolvable) bound states and, consequently, the formation of a non-zero $\langle n_{bound} \rangle$ are precluded. Non-vanishing values of $\langle n_{bound} \rangle$ originate from a non-adiabatic turn-on of external fields in the merging region.

To study the degree of non-adiabaticity we have simulated the merging of an ensemble of electrons with an initially spatially homogeneous electron density n_{free}^0 with transverse T_{\perp} and longitudinal T_{\parallel} temperatures pertaining to the TSR experiment with an ion beam in a two-body CTMC calculation. Note that the CTMC is equivalent to the solution of the Vlasov equation in the regime discussed above (*i.e.* the mean field and electron-electron collisions are neglected). We consider a cylindrically shaped segment of the electron beam with radius $r_c = (kT_{\perp})^{1/2}/\omega_c$ (ω_c : cyclotron frequency) and length $r_{d\parallel} = (kT_{\parallel}/(4\pi n_{free}^0))^{1/2}$ as suggested in [13] (Figure 5.1). For simplicity and also to deal with the same axially symmetric ensemble as used in [13], the calculation has been restricted to straight line trajectories of the merged beam with the correct relative velocity after the bend. For the discussion of the effect of non-adiabaticity induced by the sudden turn-on of the Coulomb field this simplification of geometry is irrelevant. At $t = 0$, the moment of switch-on of the nuclear charge, the center of this cylinder has a distance z_m from the highly charged ion. After a time $t_m = z_m/v_{beam}$ (v_{beam} denotes the beam velocity in the lab frame, at the TSR [10] $v_{beam} = 0.09c$ whereas the relative velocity corresponds to $E_{rel} = 0.03$ meV) the ion is fully immersed in the electron gas. With increasing interaction time the electron density rearranges itself due to Coulomb scattering as the ion approaches the beam segment. A sudden turn-on corresponds to $t_m = z_m = 0$ and the adiabatic turn-on to the limit $t_m, z_m \rightarrow \infty$. Figure 5.1 shows the fraction

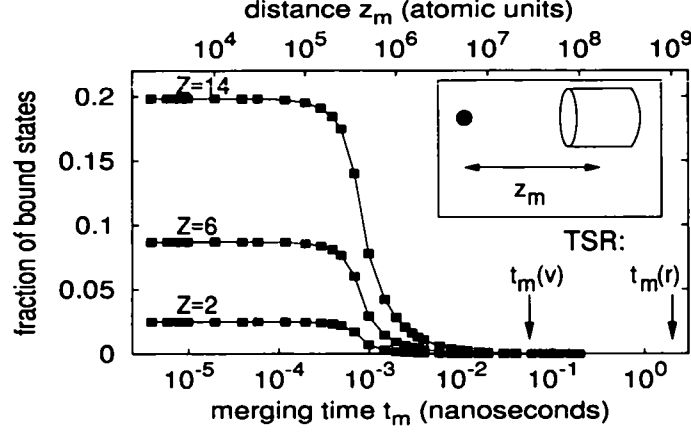


Figure 5.1: Fraction of bound states after the merging between electron and ion beams (He^{2+} , C^{6+} and Si^{14+}) as a function of the effective merging time $t_m = z_m/v_{\text{beam}}$. z_m is the distance of the center of the beam segment relative to the ion at the moment of switch-on of the Coulomb potential. Parameters are taken from the TSR experiment [10]: $B = 42$ mT, $kT_{\parallel} = 0.2$ meV, $kT_{\perp} = 10$ meV, $n_{\text{free}}^0 = 7 \times 10^6 \text{ cm}^{-3}$ and $E_{\text{rel}} = 0.03$ meV. All bound states in arbitrary high Rydberg states, $n_r = \infty$, are included.

of bound states

$$P_{\text{bound}} = \frac{\langle n_{\text{bound}} \rangle}{\langle n_{\text{free}} + n_{\text{bound}} \rangle} \quad (5.2)$$

formed as a function of the merging time t_m . For $t_m \rightarrow 0$ we recover an increase of the bound-state fraction with the nuclear charge Z , however, at lower magnitude than observed in [13]. In Figure 5.1 all Rydberg states up to $n_r = \infty$ are taken into account thus by far overestimating the experimentally observable recombined states. The corresponding probabilities for radiative stabilization of these high Rydberg states inside the solenoid are not taken into account. At the experimental merging times $t_m^{\text{TSR}}(v)$ or $t_m^{\text{TSR}}(r)$ the effective formation of bound states is completely suppressed and $\tilde{\epsilon}$ is very close to unity, *i.e.* an enhancement is not operative since the time scale for Rydberg state formation is much shorter.

5.3 Magnetic Field Dependence

The magnetic field dependence of the enhancement as treated in [13] should be briefly discussed. The free and bound electron densities in Eqs. (5.1) and (5.2) are averaged over a cylinder (volume V_C) with decreasing radius for increasing magnetic field, *i.e.* $V_C \propto r_c^2 \propto 1/B^2$, thus leading to a larger fraction of bound-state electrons for higher

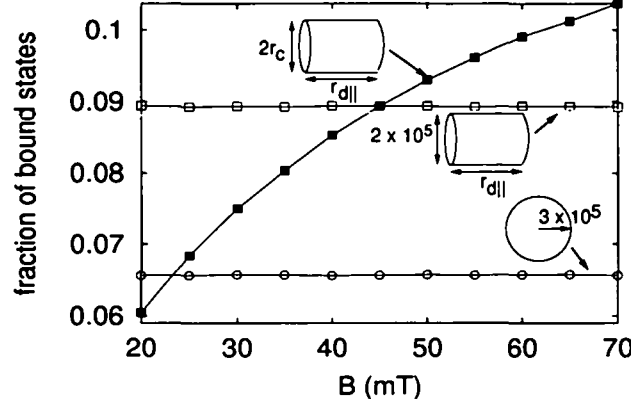


Figure 5.2: Fraction of bound states due to the sudden turn-on of the ionic Coulomb field as a function of the magnetic field for different volumes (as indicated in the figure) taken for the average $\langle \rangle$ in Eq. (5.2). Parameters according to the TSR experiment [10]: $Z = 6$, $kT_{\parallel} = 0.2$ meV, $kT_{\perp} = 10$ meV, $n_{free}^0 = 7 \times 10^6$ cm $^{-3}$ and $E_{rel} = 0.03$ meV are assumed; $n_r = \infty$.

values of B . This scaling of the reference volume, the volume where one electron-ion pair is to be found on average (*i.e.* an inverse density), with B presumes that the effective density in the cooler increases when the magnetic guiding field becomes stronger. This assumption is clearly at variance with the experiments, where the electron density is kept fixed for different magnetic field strength measurements. Figure 5.2 presents the fraction of bound states P_{bound} with the average $\langle \rangle$ calculated over different spatial volumes. For the volume used in [13] P_{bound} increases with B , whereas the choice of a B independent volume (for example a cylinder or a sphere with fixed size) yields a constant P_{bound} as a function of B .

5.4 Comparison with Realistic Merging Process

We shall compare the mechanical electron capture due to the sudden turn-on of the Coulomb field with the capture induced by the transient motional electric field during the realistic beam merging treated in the previous chapter. Figure 5.3 illustrates the distribution of bound states obtained after suddenly switching on the ionic Coulomb potential immersed in a Maxwell-Boltzmann distributed ensemble of electrons with a uniform distribution inside a sphere of diameter $d = r_{ion} = n_{ion}^{-1/3}$ (r_{ion} and n_{ion} refer to the interionic distance and ion density in the experiment) in coordinate space (same ensemble size as in chapter 4). Both the binding ener-

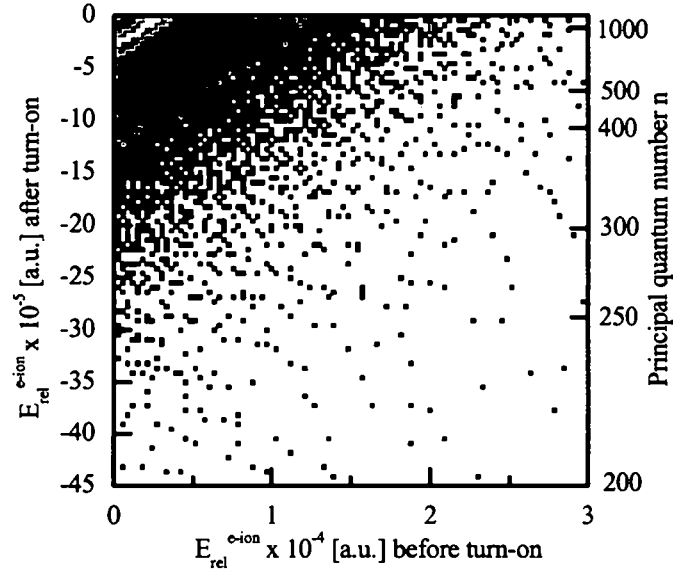


Figure 5.3: Bound-state formation at $B = 42$ mT after the merging induced by the sudden turn-on of the Coulomb potential of a C^{6+} ion fully immersed in the electron ensemble with $kT_{\perp} = 10$ meV, $kT_{\parallel} = 0.06$ meV and $E_{rel} = 0.03$ meV distributed within a sphere with diameter $r_{ion} = 1.765 \times 10^6$ a.u. A density plot of the electron-ion relative energies before the merging $E_{rel}^{e-ion} = v^2/2$ and after the merging $E_{rel}^{e-ion} = v^2/2 - Z/r$ is shown. The density is plotted on a logarithmic scale.

parameters		fraction of bound states within a sphere of diameter r_{ion}			
Z	B (mT)	P_{bound}	$P(n \leq 1000)$	$P(n \leq 500)$	$P(n \leq 200)$
2	42	0.00516	1.77×10^{-3}	1.70×10^{-4}	5.25×10^{-6}
6	42	0.0216	1.04×10^{-3}	6.70×10^{-5}	1.16×10^{-6}
14	42	0.0564	4.46×10^{-4}	2.03×10^{-5}	1.94×10^{-7}
6	10	0.0216	1.04×10^{-3}	6.70×10^{-5}	1.16×10^{-6}
6	42	0.0216	1.04×10^{-3}	6.70×10^{-5}	1.16×10^{-6}
6	90	0.0216	1.04×10^{-3}	6.70×10^{-5}	1.16×10^{-6}

Table 5.1: Fractions of bound states for different Z and B after an instantaneous turn-on of the Coulomb field of the ion fully immersed in the electron gas. The electron ensemble has a spatial extent of typical interionic distances in the experiment ($r_{ion} = 1.765 \times 10^6$ a.u.). P_{bound} : total bound-state fraction, $P(n \leq n_0)$: the probability for forming Rydberg states with $n \leq n_0$. Same parameters as in Figure 5.3.

gies $E_{rel}^{e-ion} = v^2/2 - Z/r$ ($r = |\vec{r}_e - \vec{r}_{ion}|$ and $v = |\vec{v}_e - \vec{v}_{ion}|$ denote the absolute relative coordinate and velocity between electron and ion) and the corresponding principal quantum numbers n are plotted as a function of the kinetic initial energy $E_{rel}^{e-ion} = v^2/2$ before the turn-on. High Rydberg states are generated by the instantaneous switch-on. The comparison with the electron-ion merging process at the TSR studied in Figure 4.10 shows that the sudden approximation overestimates the bound-state population at lower values of n . Table 5.2 lists the fraction of bound states induced by the sudden turn-on for different ion charges Z and magnetic field strengths B . The total bound-state fractions as well as the probabilities for forming Rydberg states with $n \leq 1000$, $n \leq 500$ and $n \leq 200$ are given. These values should be compared with the formation of bound states at the end of the realistic merging process given in Table 4.2. Correspondingly, we find larger bound-state fractions within the sudden approximation for lower lying Rydberg states, in particular for $n \lesssim 500$ (see also Figure 5.4), which, in turn, lead to larger recombination rates α_s , due to radiative stabilization into low Rydberg states ($n' \leq n_r$) surviving in the cooler. The resulting values of α_s (Eqs. (4.22) and (4.23)) are about a factor of 2 to 3 higher than the excess rates from the TSR merging calculation (see Table 5.3) and thus the experimental rate coefficients. By adopting a B independent spatial volume for the initial ensemble of electrons the sudden turn-on cannot account for a magnetic field dependence of the recombination rate (see also section 5.3). Therefore, a sudden turn-on of the ionic Coulomb field considering effective densities available in the experiment significantly overestimates the measured rate coefficients while it

parameters		fraction of bound states within the cylinder of [13]			
Z	B (mT)	P_{bound}	$P(n \leq 1000)$	$P(n \leq 500)$	$P(n \leq 200)$
2	42	0.0422	0.0371	0.0221	1.01×10^{-3}
6	42	0.130	0.0861	0.0130	2.23×10^{-4}
14	42	0.276	0.0808	3.93×10^{-3}	3.72×10^{-5}
6	10	0.0504	0.0110	7.34×10^{-4}	1.26×10^{-5}
6	42	0.130	0.0861	0.0130	2.23×10^{-4}
6	90	0.173	0.131	0.0479	1.03×10^{-3}

Table 5.2: Fractions of bound states for different Z and B after the sudden turn-on of the ionic Coulomb field. According to Ref. [13] the electron ensemble is distributed within a cylinder of radius r_c and length $r_{d\parallel}$ in coordinate space ($n_{free}^0 = 7 \times 10^6 \text{ cm}^{-3}$). The total bound-state fractions (P_{bound}) and the probabilities for forming Rydberg states with $n \leq n_0$ ($P(n \leq n_0)$) are given. Parameters are otherwise the same as in Figure 5.3.

cannot explain the magnetic field dependence of the enhancement.

We have also calculated bound-state fractions due to the sudden turn-on for electron ensembles distributed uniformly inside a cylinder with radius r_c and length $r_{d\parallel}$ as proposed in [13] (Table 5.2). In this case we observe much larger bound-state fractions overestimating the number of bound states acquired at the end of the toroidal merging section of the TSR electron cooler (Table 4.2) by 1 to 2 orders of magnitude (see also Figure 5.4). The significant increase of the bound-state fractions with B results from the decreasing size of the underlying spatial volume. Similarly, the recombination rates α_s determined from radiative stabilization into $n' \leq n_r$ exceed the experimental excess rate coefficients by at least two orders of magnitude (see Table 5.3).

In [13], however, no radiative stabilization calculation is employed but the enhancement of the recombination is determined in terms of the ratio $\tilde{\epsilon}$ of electron densities given in Eq. (5.1) instead. Neglecting radiative stabilization, the sudden turn-on with the spatial volume of [13] used for the electron ensemble populates low-lying bound states (for example, $n_r = 30$ for C^{6+}) with very small probabilities. The enhancement ratio $\tilde{\epsilon}$ tends to unity for such low Rydberg states. Therefore, the sudden switch-on of the atomic Coulomb field with the enhancement ratio evaluated by Eq. (5.1) differs substantially from the transient trapping due to the motional electric field in the merging region followed by radiative stabilization in the solenoid.

parameters		recombination rate α_s after radiative stabilization ($10^{-10} \text{ cm}^3 \text{ s}^{-1}$)		
Z	B (mT)	merging (chapter 4)	sudden turn-on: sphere (diameter r_{ion})	sudden turn-on: cylinder of [13]
2	42	0.409	1.22	2.48×10^2
6	42	6.16	15.0	2.70×10^3
14	42	44.2	98.7	1.69×10^4
6	10	4.20	15.4	1.52×10^2
6	42	6.58	15.4	2.78×10^3
6	90	7.32	15.4	1.21×10^4

Table 5.3: Recombination rates α_s (Eq. (4.23)) induced by radiative stabilization of the formed Rydberg states (of Tables 4.2, 5.1 and 5.2) for different Z and B . The merging at the TSR electron cooler (chapter 4) is compared with the instantaneous switch-on of the Coulomb potential for electron ensembles located within a sphere (diameter $r_{ion} = 1.765 \times 10^6$ a.u.) or within the cylinder of [13]. $kT_{\perp} = 10$ meV, $kT_{\parallel} = 0.06$ meV, $E_{rel} = 0.03$ meV and $n_{free}^0 = n_e = 7 \times 10^6 \text{ cm}^{-3}$. $n_r = 10$ (He^{2+}), 23 (C^{6+}) and 43 (Si^{14+}) in the upper half of the table, whereas $n_r = 30$ in the lower part.

5.5 Densities and Rydberg States

The authors of [13] published meanwhile an erratum [15] to their PRL, where they specified a smaller reference volume for calculating the averages over the electron densities in Eqs. (5.1) and (5.2). According to this erratum the reported enhancement factors have been obtained by using a much smaller cylinder with radius $(T_{\parallel}/T_{\perp})^{1/2}r_c$ and length $2(T_{\parallel}/T_{\perp})^{1/2}r_{d\parallel}$. This new reference volume per electron-ion pair amounts to increasing the effective density in the cooler by about three orders of magnitude compared to the experimental value (for example, $n_{free}^0 = n_e = 7 \times 10^6 \text{ cm}^{-3}$ at the TSR experiment [10]). The resulting bound-state fractions now outperform the number of bound states populated during the realistic merging process by several orders of magnitude (Table 5.4). For comparison, the distribution of the principal quantum numbers n of the formed Rydberg states is displayed in Figure 5.4 for the merging of electrons and C^{6+} ions according to the TSR experiment (data from Figure 4.11b) as well as for the sudden approximation adopting the different reference volumes for the electron ensemble discussed so far. While the sudden approximation with realistic experimental densities still yields bound-state fractions of the right order of magnitude down to even the lowest values of n , the sudden turn-on utilizing the cylinder of [13] or yet the cylinder of [15] produces bound-state fractions far off the electric field-induced capture probabilities discussed in chapter 4.

parameters		fraction of bound states using the cylinder of [15]			
Z	B (mT)	P_{bound}	$P(n \leq 1000)$	$P(n \leq 500)$	$P(n \leq 200)$
2	42	0.320	0.317	0.305	0.221
6	42	0.644	0.627	0.568	0.180
14	42	0.877	0.839	0.643	0.0400
6	10	0.441	0.413	0.320	0.0136
6	42	0.644	0.627	0.568	0.180
6	90	0.671	0.655	0.600	0.247

Table 5.4: Fractions of bound states (P_{bound} and $P(n \leq n_0)$) for different Z and B after the sudden turn-on of the Coulomb field of the ion located at the center of an electron ensemble spatially distributed within a cylinder of radius $(T_{\parallel}/T_{\perp})^{1/2}r_c$ and length $2(T_{\parallel}/T_{\perp})^{1/2}r_{d\parallel}$ as in [15]. Same parameters as in Figure 5.3.

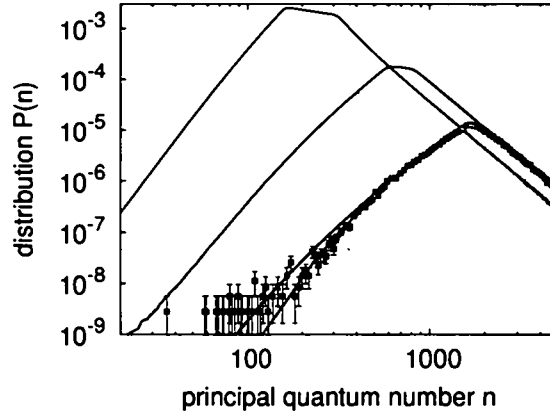


Figure 5.4: Principal quantum number (n) distribution after the merging between electrons and C^{6+} ions at $B = 42$ mT for the merging geometry at the TSR (red squares with errorbar, red line indicates the extrapolation for low n , see chapter 4) and the sudden turn-on of the ionic Coulomb field with electron ensembles distributed within a sphere representing the ion density in the experiment (blue) and within the cylinders of [13] (green) and [15] (magenta) respectively. $r_{ion} = 1.765 \times 10^6$ a.u., $n_{free}^0 = n_e = 7 \times 10^6 \text{ cm}^{-3}$ and otherwise the same parameters as in Figure 5.3.

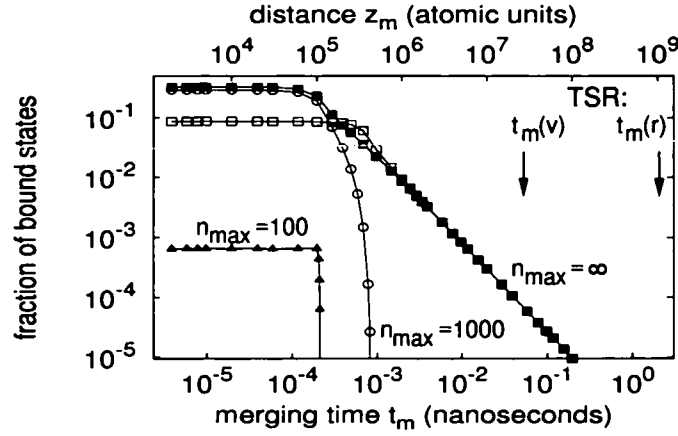


Figure 5.5: Fraction of bound states after the merging between electrons and C^{6+} ions as a function of $t_m = z_m/v_{beam}$ with parameters from the TSR experiment [10]. \square : reference volume in [13], $n_r = \infty$, \blacksquare : reference volume in [15], $n_r = \infty$, \circ : reference volume in [15], $n_r = 1000$, \blacktriangle : reference volume in [15], $n_r = 100$.

As in [13] we shall evaluate enhancement ratios according to Eq. (5.1). Figure 5.5 shows the fraction of bound states (Eq. (5.2)) as a function of the merging time t_m for the reference volumes of [13] and [15] with different limiting quantum number n_r considered for the enhancement of the recombination. Even with the unrealistic density of [15] the proposed recombination mechanism is ineffective (three orders of magnitude smaller than in the experiment) for the formation of any surviving Rydberg state in the cooler generously estimated to reach $n_r = 100$ due to the complete mismatch of time scales. As in [13] radiative stabilization of the formed Rydberg states inside the solenoid has still not been treated. Only if on top of the unrealistic sudden limit and the inflated density all bound states in arbitrary high Rydberg states are included finally seizable bound-state fractions can be obtained. However, at the experimental merging time $t_m^{TSR}(r)$ the bound-state contribution completely disappears (even if the increased densities are used and/or Rydberg states that cannot contribute are counted) with values less than 10^{-6} which could not be resolved within our Monte Carlo statistics.

To conclude, what has been observed in [13], is mechanical *recombination* due to an instantaneous turn-on of the electron-ion interaction assumed to mimic the electron-ion merging in the electron cooler. Neither the electric field distribution during the merging region nor the kinematics of the merging process have been considered which results in bound-state fractions exceeding those observed after the realistic beam merging process. In contrast to our analysis in chapter 4 radiative decay of the populated Rydberg states inside the solenoid has not been taken into

account within that model. While we could find a significant contribution from radiative stabilization to the observed electron-ion recombination rates in the previous chapter, the enhancement ratio evaluated with Eq. (5.1) yields values very close to unity for experimentally observable low-lying bound states. To obtain non-vanishing enhancement ratios in [13, 15] dramatically increased densities are employed and electrons in arbitrary high Rydberg states are considered. In summary, this alternative approach does not describe recombination in electron coolers in a realistic way.

Chapter 6

Electron Dynamics in Presence of Two Ions

So far, only the interaction between one electron and one ion in the presence of external fields has been investigated throughout this thesis. Effects due to neighboring ions and electrons in the plasma have been ignored. The existence of additional ions lowers the Coulomb potential barrier thus assisting the recombination of an electron with the target ion. However, in the experiment the ionic density is rather low. For example, ion beam currents of typically $100\ \mu\text{A}$ with a beam diameter of $2\ \text{mm}$ after the cooling result in an ion density of $n_{\text{ion}} \approx 1.2 \times 10^6\ \text{cm}^{-3}$, or, correspondingly, an interparticle distance of $r_{\text{ion}} = n_{\text{ion}}^{-1/3} \approx 1.8 \times 10^6\ \text{a.u.}$ between individual ions. In such a tenuous plasma the induced effective Coulomb potential only deviates from the Coulomb field of a single ion at quite large distances from the target ion ($r \gtrsim 10^5\ \text{a.u.}$). Nevertheless, even a drop in the effective potential at distances larger than $10^5\ \text{a.u.}$ can affect the chaotic dynamics of an electron in the magnetic field significantly (with an electron cyclotron radius of $r_c \approx 10^5\ \text{a.u.}$), which, in turn, may influence the observed electron-ion recombination rate. In addition, also neighboring electrons perturb the effective Coulomb field of the investigated electron. Their effects on the potential, however, are due to the smaller charge (in a.u. $e = -1$) by the value of Z smaller than the influence of neighboring ions for electron densities in the measurements comparable to the ion densities. Therefore, as a first approximation, only the influence of nearby ions onto the dynamics of the probed electron may be studied. Note that a many-body approach in terms of vicinal ions is different from attempts to explain the enhanced rates by three-body recombination or via plasma physics approaches modeling the electronic density near an ion, where the enhancement is assigned to the presence of neighboring electrons in the plasma.

In the following the classical description of the electron dynamics inside the solenoid region of the electron cooler presented in chapter 3 will be thus extended to the presence of an additional ion. The motion of an electron in the magnetic field

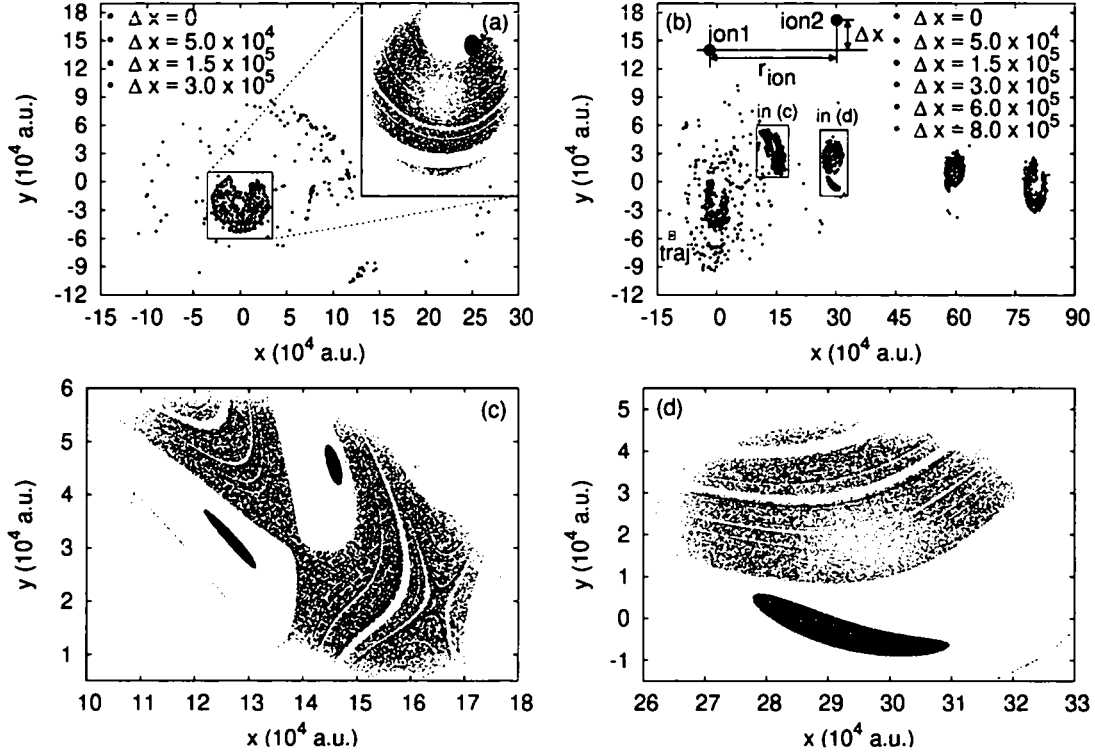


Figure 6.1: Phase space region of non-zero values of $V_t(\vec{r}, \vec{v})$ (visits to the target ion) (a) and $V_n(\vec{r}, \vec{v})$ (visits to the neighboring ion) (b-d) at $B = 42$ mT and $Z = 6$ for fixed initial velocities $v_x = 0.004$ a.u. and $v_z = 0.002$ a.u. ($v_y = 0$) and initial coordinate $z = -2.29 \times 10^6$ a.u. of the electrons. Visits are defined for $|\vec{r} - \vec{r}_{ion1,2}| \leq r^{RR} = 150$ a.u. The target ion is fixed at $\vec{r}_{ion1} = (0, 0, 0)$ and the second ion is placed at different transverse distances $x_{ion2} = \Delta x$ (values specified in the Figure), $y_{ion2} = 0$ and $z_{ion2} = r_{ion} = 1.765 \times 10^6$ a.u. The inset in (a) enlarges V_t for the indicated box around $(x, y) = (0, 0)$ when the second ion is found at $\Delta x = 3.0 \times 10^5$ a.u. Magnifications of V_n with $\Delta x = 1.5 \times 10^5$ a.u. (c) and $\Delta x = 3.0 \times 10^5$ a.u. (d) for the areas denoted in (b) are visualized with improved statistics. Note that the initial electron ensemble is restricted to $x^2 + y^2 \leq r_{ion}/2$ to aim solely at the target ion. The associated trajectory of the phase space point marked by "traj" in (b) is displayed in Figure 6.2.

$\vec{B} = B\hat{e}_z$ of the cooler and the combined Coulomb potential of two ions (both with charge Z) at positions \vec{r}_{ion1} and \vec{r}_{ion2} respectively is governed by the Hamiltonian

$$H = \frac{p^2}{2} - \frac{Z}{|\vec{r} - \vec{r}_{ion1}|} - \frac{Z}{|\vec{r} - \vec{r}_{ion2}|} + \frac{1}{2c}B(xp_y - yp_x) + \frac{1}{8c^2}B^2(x^2 + y^2), \quad (6.1)$$

where $\vec{p} = (p_x, p_y, p_z)$ and $\vec{r} = (x, y, z)$ denote the momentum and coordinate of the electron. We choose $\vec{r}_{ion1} = (0, 0, 0)$ and $\vec{r}_{ion2} = (x_{ion2}, y_{ion2}, z_{ion2})$ for the ionic positions fixed during the calculation. Hence only the electronic degrees of freedom are propagated according to the classical Hamilton's equations of motion, which we solve by means of a fourth order Runge Kutta integration method [50]. Here it is important to note that the existence of a second ion with a transverse displacement with respect to the original ion, *i.e.* $x_{ion2} \neq 0$ or $y_{ion2} \neq 0$, breaks the cylindrical symmetry of the system. Accordingly, the angular momentum component L_z of the electron along the direction of the magnetic field is not conserved any longer.

Again we quantify the motion of an electron in terms of visit functions $V_t(\vec{r}, \vec{v})$ and $V_n(\vec{r}, \vec{v})$ representing close encounters of the electron to the target ion (V_t) and the neighboring ion (V_n) for given asymptotic phase space coordinates (\vec{r}, \vec{v}) . Figure 6.1 illustrates phase space portraits of non-zero visit functions V_t and V_n for a fixed initial velocity of the incident electrons and different positions of the second ion. The electron ensemble is initiated from an area with $x^2 + y^2 \leq r_{ion}/2$ at a fixed z -plane, thus chosen such as to aim solely at the ion located at the origin of the coordinate system (also referred to as target ion). Due to the violation of the conservation of L_z in the presence of a transversely displaced second ion a restriction in the initial conditions according to Eqs. (3.35) - (3.38) is not applicable any more.

However, as long as the transverse displacement of the second ion x_{ion2} is large compared to the electron cyclotron radius r_c (in Figure 6.1 $r_c \approx 2.24 \times 10^4$ a.u.) the larger part of visits to the target ion V_t as well as to the displaced vicinal ion V_n (provided that $x_{ion2} < r_{ion}/2$ yet) is well localized in a small region of initial coordinates (x, y) around the transverse positions of the target and neighboring ions respectively in comparison with the spatial extent of the initial electronic ensemble. Magnifications of these regions (Figures 6.1c, 6.1d and inset in 6.1a) show that analogous to the one-ion system presented in chapter 3 the visiting functions exhibit fractal-like structures with connected regions of decreasing size for visits occurring at later times. For a more detailed discussion of these substructures in V see section 3.7. These visits with initial coordinates close to the transverse position of the respective ion are related to trajectories aiming at this ion straight ahead with the dynamics only weakly perturbed by the presence of the additional ion. Due to this small perturbation, for example, the positions of the connected regions of visits are shifted somewhat compared to the one-ion system, their overall sizes though remaining unchanged.

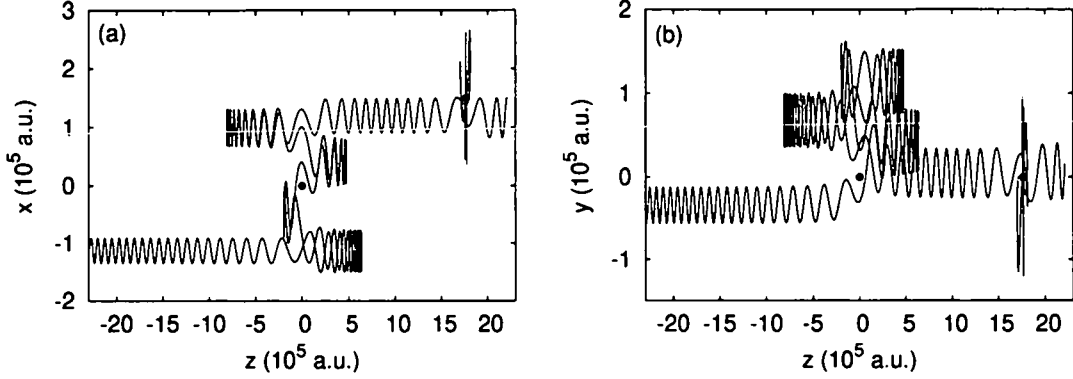


Figure 6.2: Electron trajectory at $B = 42$ mT (along z) and $Z = 6$ with initial conditions according to Figure 6.1b. The target ion is situated at $\vec{r}_{ion1} = (0, 0, 0)$ and the neighboring ion at $\vec{r}_{ion2} = (1.5 \times 10^5 \text{ a.u.}, 0, 1.765 \times 10^6 \text{ a.u.})$ (black points). The corresponding $z - x$ and $z - y$ projections are shown. The electron is deflected by the target ion such as to visit the neighboring ion. Propagation time is limited to 60 ns.

In addition, a few visits can be also observed at larger transverse distances from the corresponding ion (Figures 6.1a and 6.1b). The analysis of associated trajectories shows that the motion of such electrons is much more strongly affected by the Coulomb potential of the nearby second ion. Figure 6.2 shows an electron trajectory approaching first the target ion but then being deflected by its Coulomb potential such as to visit the displaced neighboring ion at a later time. Therefore, precisely those trajectories with visits at seemingly unpredictable initial positions (x, y) are most sensitive to the presence of the additional ion. In order to investigate these two-ion effects onto the electron dynamics, a restriction in the sampling of the initial electron ensemble appears not justified. However, the number of such visits resulting from a strong perturbation of the dynamics by the neighboring ion is small compared to the number of visits where the vicinal ion only exerts a weak influence anyway.

We have explored the visit functions for different magnetic field strengths with a fixed initial velocity of the incoming electrons. Figure 6.3 depicts phase space portraits of the resulting visits to the target ion V_t and the neighboring ion V_n located at $\vec{r}_{ion2} = (3.0 \times 10^5 \text{ a.u.}, 0, 1.765 \times 10^6 \text{ a.u.})$. These visit functions integrated over coordinate space, *i.e.* $V_{t,n}(\vec{v}) = \int dx \int dy V_{t,n}(x, y, \vec{v})$, again tend to decrease with B both for V_t and V_n .

Up to now we have only been able to determine $V_t(\vec{r}, \vec{v})$ and $V_n(\vec{r}, \vec{v})$ at fixed initial velocities \vec{v} and for a few selected positions of the additional ion. Calculations of an electron ensemble with Maxwell-Boltzmann distributed velocities and random

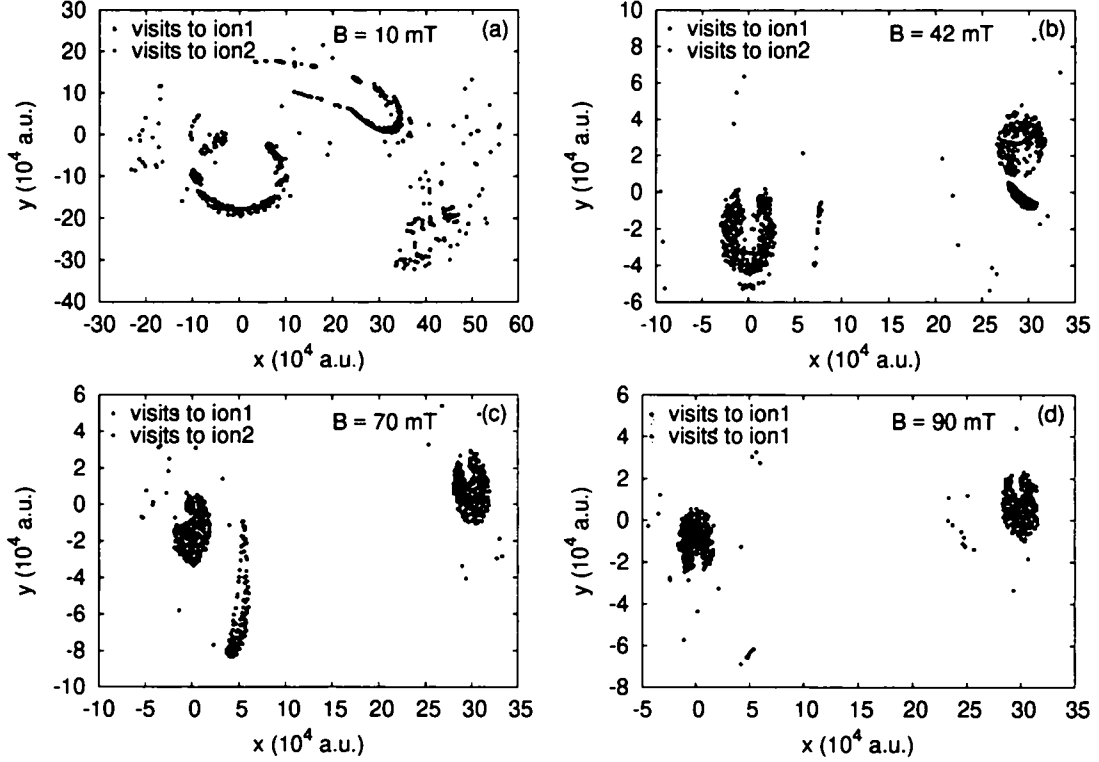


Figure 6.3: Phase space region of non-vanishing visit functions $V_i(\vec{r}, \vec{v})$ (red) and $V_n(\vec{r}, \vec{v})$ (green) displayed for magnetic field strengths of $B = 10$ mT (a), $B = 42$ mT (b), $B = 70$ mT (c) and $B = 90$ mT (d) with $Z = 6$ and initial electron velocity and coordinate of $v_x = 0.004$ a.u., $v_y = 0$, $v_z = 0.002$ a.u. and $z = -2.29 \times 10^6$ a.u. Visits are recorded for $|\vec{r} - \vec{r}_{ion1,2}| \leq 150$ a.u. The target ion is located at $\vec{r}_{ion1} = (0, 0, 0)$ and the second ion at $\vec{r}_{ion2} = (3.0 \times 10^5 \text{ a.u.}, 0, 1.765 \times 10^6 \text{ a.u.})$. The initial ensemble is launched from $x^2 + y^2 \leq r_{ion}/2$.

positions of the second ion turned out to be unfeasible within the available computing power with an estimated time of more than one year of simulations required to reach converged results. Therefore, a detailed microscopic analysis of the electron dynamics in the presence of several ions, let alone the investigation of the parameter dependences of the resulting recombination rates, is at present computationally impossible. However, in view of individual phase space portraits such as in Figures 6.1 and 6.3 the effect of neighboring ions in the beam onto the recombination rates can be estimated to be very small.

Chapter 7

Summary, Conclusions and Outlook

A detailed investigation of the classical dynamics between an electron and an ion in the toroidal and solenoidal regions of the electron cooler of a storage ring has been presented in this thesis. We have studied the chaotic scattering and bound-state motion of an electron in the simultaneous presence of Coulomb and magnetic fields. By including the chaotic effects into the evaluation of the quantum mechanical recombination rates we have thus accounted for the presence of the magnetic field in the cooler. We have treated radiative recombination inside the solenoid as well as non-radiative electron capture induced by the Stark saddle depression of a transient electric field during the beam merging region.

For the description of the electronic scattering dynamics the visit function has been introduced. It plays the role of a deflection function representing the number of close encounters of an electron to the target ion. However, its value is not unique but allows for different definitions such as V^r and V^v . In a non-zero magnetic field, V^r and V^v become highly irregular exhibiting a fractal-like structure in terms of the asymptotic initial phase space coordinates of the incident electrons. We have considered the effect of the magnetic field on the recombination cross section by incorporating the ratio of visits in the combined fields versus the pure Coulomb problem into the evaluation of the corresponding rate coefficients. Despite of the irregular scattering with multiple visits to the nucleus possible the total flux of electrons towards the immediate vicinity of the target ion is reduced as the magnetic field is increased. We find recombination rates smaller than the standard RR rate prediction at low relative velocities using V^v . Therefore, the magnetic field inside the solenoid appears not to enhance but suppress the radiative recombination process.

The enhancement of the recombination observed in storage ring experiments originates from an additional recombination mechanism available in the electron cooler. The alternative route to recombination is supplied by the merging of the

electron and ion beams in the toroidal-shaped entrance region of the cooler, where a transient motional electric field in the rest frame of an ion allows for additional free-bound electron transfer. We have simulated the effect of the induced transient field for the merging geometry of the TSR electron cooler. Accordingly, formation of bound states can be observed during passage of the very last part of the toroid, *i.e.* approximately during the last 100 picoseconds of the merging process at the given TSR experiment [10]. Typically very high Rydberg states are found to be populated during the merging. The probability for forming lower lying bound states is very small. Nevertheless, radiative decay of these Rydberg states inside the solenoid can stabilize a small fraction of the captured electrons by transitions to sufficiently deeply bound states observable in the measurements. As a result of the dynamics in comparable Coulomb and magnetic fields the overall angular momentum distribution of the weakly bound Rydberg electrons remains unchanged during propagation through the solenoid suggesting the application of field-free radiative transition rates. In view of the low probability for forming bound states and the slow radiative decay rates to lower lying Rydberg states CTMC calculations with huge ensembles are required to determine the contribution to the observed electron-ion recombination rate. With the calculated ensemble sizes controlled smooth extrapolation at low values of the principal quantum number n is indispensable at present. Due to the large expenditure of time of these simulations the dependences on the electron beam temperatures and the spectral shape of the enhancement have not yet been analyzed. Certainly, future investigations should tackle these parameter studies. We find absolute excess recombination rates in good agreement with the experimental data also after the summation of the field-induced recombination rates with the reduced radiative recombination rates within the magnetic field. The scaling of the excess rate with the ion charge ($\sim Z^{2.4}$) and the magnetic guiding field ($\sim B^{0.3}$) differs only slightly from the experimental findings.

In addition, the influence of neighboring ions and electrons in the beam onto the classical chaotic dynamics of the investigated electron has been discussed. We have presented a brief analysis of the electronic motion in the presence of two ions. Accordingly, effects from the neighboring ion appear to be small, however, the calculation of entire ensembles of electrons in the presence of randomly placed vicinal ions is at present computationally not yet feasible.

We point out that an enhancement of the recombination due to transient bound states formed during the merging between electrons and ions depends on the geometry of the merging and demerging regions. In fact, theoretical results of field-induced recombination rates for different geometries would be useful in order to explore what the expected influence might be. Current electron coolers such as at the TSR, the ESR and the CRYRING facilities all feature similar merging geometries thus leading to similar enhancement ratios. While in electron coolers the rate enhancement can be traced back to the process of beam merging, under different experimental

conditions an enhancement of the recombination within moderate magnetic field strengths cannot be a priori expected. Quite contrary, rather a reduction of the RR process might be inferred from the present analysis.

In summary, the understanding of the puzzling rate enhancement phenomenon, meanwhile an outstanding problem for more than a decade, has been considerably improved by the investigations of this thesis. A realistic model yielding, for the first time, a good quantitative agreement with the measurements both in terms of nuclear charge and magnetic field dependence of the enhanced rates has been developed and a deeper insight into the fundamental mechanism of the experimentally observed recombination has been obtained. The new electron target at the TSR and the even lower temperatures recently achieved open up new experimental possibilities to check scalings of the recombination rate over a wider range of external parameters in the near future.

Appendix A

The Hamiltonian in Cartesian and Cylinder Coordinates: Canonical Transformation Technique

We employ a classical trajectory Monte Carlo method (CTMC) to simulate an incoming beam of electrons from the asymptotic region to the target ion of charge Z in the presence of a homogeneous magnetic field $\vec{B} = B\hat{e}_z$. The Hamiltonian of this system reads

$$H = \frac{1}{2} (p_x^2 + p_y^2 + p_z^2) + \frac{1}{8c^2} B^2 (x^2 + y^2) + \frac{1}{2c} B (xp_y - yp_x) - \frac{Z}{\sqrt{x^2 + y^2 + z^2}} \quad (\text{A.1})$$

where $\vec{p} = (p_x, p_y, p_z)$ and $\vec{r} = (x, y, z)$ are the Cartesian momenta and coordinates of the electron in the rest frame of the ion. For a given set of initial conditions the classical dynamics of the electron is governed by the Hamilton equations of motion

$$\begin{aligned} \dot{x} &= v_x = \frac{\partial H}{\partial p_x} = p_x - \frac{1}{2c} B y \\ \dot{y} &= v_y = \frac{\partial H}{\partial p_y} = p_y + \frac{1}{2c} B x \\ \dot{z} &= v_z = \frac{\partial H}{\partial p_z} = p_z \\ \dot{p}_x &= -\frac{\partial H}{\partial x} = -\frac{1}{4c^2} B^2 x - \frac{1}{2c} B p_y - \frac{Zx}{(x^2 + y^2 + z^2)^{3/2}} \\ \dot{p}_y &= -\frac{\partial H}{\partial y} = -\frac{1}{4c^2} B^2 y + \frac{1}{2c} B p_x - \frac{Zy}{(x^2 + y^2 + z^2)^{3/2}} \\ \dot{p}_z &= -\frac{\partial H}{\partial z} = -\frac{Zz}{(x^2 + y^2 + z^2)^{3/2}}, \end{aligned}$$

where the dot indicates the derivative with respect to time. Since the magnetic field along the z axis gives rise to a cylinder symmetry of the system, the Hamiltonian may be treated more easily in cylindrical coordinates. The transformation from one set of phase space coordinates (\vec{r}, \vec{p}) to another one (\vec{R}, \vec{P}) is accomplished by a canonical transformation [47], which preserves the canonical character of the new coordinates \vec{R} and \vec{P} , i. e. \vec{R} and \vec{P} again obey Hamilton equations of motion for a new Hamiltonian $\tilde{H}(\vec{R}, \vec{P})$. Therefore, both (\vec{r}, \vec{p}) and (\vec{R}, \vec{P}) fulfill a modified Hamiltonian principle

$$\delta \int_{t_1}^{t_2} \left(\sum_i p_i \dot{r}_i - H(\vec{r}, \vec{p}, t) \right) dt = 0, \quad \delta \int_{t_1}^{t_2} \left(\sum_i P_i \dot{R}_i - \tilde{H}(\vec{R}, \vec{P}, t) \right) dt = 0.$$

The integrands of these two integrals may differ by the total time derivative of an arbitrary function F of the (old and new) canonical variables. The variation of the integral of such a difference term gives no contribution,

$$\delta \int_{t_1}^{t_2} \frac{dF}{dt} dt = \delta (F(t_2) - F(t_1)) = 0,$$

due to the vanishing variations of the canonical coordinates at the end points t_1 and t_2 . F is the so-called generating function of the transformation, which determines the transformation equations. It is given in terms of independent variables in one of the four forms

$$F_1(\vec{r}, \vec{R}, t) \quad F_2(\vec{r}, \vec{P}, t) \quad F_3(\vec{p}, \vec{R}, t) \quad F_4(\vec{p}, \vec{P}, t).$$

For a coordinate transformation $\vec{R} = \vec{R}(\vec{r}, t)$ a generating function of the type F_2 can be used, whose transformation equations read [47]

$$p_i = \frac{\partial F_2}{\partial r_i} \tag{A.2}$$

$$R_i = \frac{\partial F_2}{\partial P_i} \tag{A.3}$$

with

$$\tilde{H} = H + \frac{\partial F_2}{\partial t}. \tag{A.4}$$

The transformation from Cartesian coordinates $\vec{r} = (x, y, z)$ to cylindrical components $\vec{R} = (\rho, \phi, z)$ is described by F_2 according to

$$F_2(x, y, P_\rho, P_\phi) = \sqrt{x^2 + y^2} P_\rho + \arctan\left(\frac{y}{x}\right) P_\phi, \tag{A.5}$$

where for simplicity F_2 is restricted only to the four-dimensional subspace describing the canonical transformation from (x, y) Cartesian to planar polar coordinates (ρ, ϕ) , since z and p_z remain unaffected by the required transformation anyway. Eq. (A.3) leads to the (trivial) relations for the coordinates

$$\rho = \frac{\partial F_2}{\partial P_\rho} = \sqrt{x^2 + y^2} \quad \phi = \frac{\partial F_2}{\partial P_\phi} = \arctan\left(\frac{y}{x}\right), \quad (\text{A.6})$$

and their inverse forms

$$x = \rho \cos \phi \quad y = \rho \sin \phi, \quad (\text{A.7})$$

whereas Eq. (A.2) gives the transformation equations for the momenta

$$\begin{aligned} p_x &= \frac{\partial F_2}{\partial x} = \frac{x}{\sqrt{x^2 + y^2}} P_\rho - \frac{y}{x^2 + y^2} P_\phi = \cos \phi P_\rho - \frac{1}{\rho} \sin \phi P_\phi \\ p_y &= \frac{\partial F_2}{\partial y} = \frac{y}{\sqrt{x^2 + y^2}} P_\rho + \frac{x}{x^2 + y^2} P_\phi = \sin \phi P_\rho + \frac{1}{\rho} \cos \phi P_\phi, \end{aligned} \quad (\text{A.8})$$

and, by inversion, accordingly

$$P_\rho = \frac{xp_x + yp_y}{\sqrt{x^2 + y^2}} \quad P_\phi = L_z = xp_y - yp_x. \quad (\text{A.9})$$

Inserting the transformation equations (A.7) and (A.8) into Eq. (A.4) the Hamiltonian in cylindrical coordinates is found to be (since $\partial F_2/\partial t = 0$)

$$H = \frac{1}{2} \left(P_\rho^2 + \frac{L_z^2}{\rho^2} + P_z^2 \right) + \frac{1}{8c^2} B^2 \rho^2 + \frac{1}{2c} B L_z - \frac{Z}{\sqrt{\rho^2 + z^2}}. \quad (\text{A.10})$$

The coordinate ϕ is cyclic since it does not show up in Eq. (A.10) any more and the corresponding canonical momentum component L_z is thus a constant of motion. The time evolution of this system is described by the Hamilton equations as follows

$$\begin{aligned} \dot{\rho} &= v_\rho = \frac{\partial H}{\partial P_\rho} = P_\rho \\ \dot{\phi} &= v_\phi = \frac{\partial H}{\partial L_z} = \frac{L_z}{\rho^2} + \frac{1}{2c} B \\ \dot{z} &= v_z = \frac{\partial H}{\partial P_z} = P_z \\ \dot{P}_\rho &= -\frac{\partial H}{\partial \rho} = -\frac{1}{4c^2} B^2 \rho + \frac{L_z^2}{\rho^3} - \frac{Z\rho}{(\rho^2 + z^2)^{3/2}} \\ \dot{L}_z &= -\frac{\partial H}{\partial \phi} = 0 \quad \rightarrow \quad L_z \text{ is a constant of motion} \\ \dot{P}_z &= -\frac{\partial H}{\partial z} = -\frac{Zz}{(\rho^2 + z^2)^{3/2}}. \end{aligned}$$

Appendix B

Classical Scaling Invariance

The Hamiltonian for an electron in the Coulomb field of the ion and a uniform magnetic field B

$$H = \frac{1}{2} \left(p_\rho^2 + \frac{L_z^2}{\rho^2} + p_z^2 \right) + \frac{1}{8c^2} B^2 \rho^2 + \frac{1}{2c} B L_z - \frac{Z}{\sqrt{\rho^2 + z^2}} \quad (\text{B.1})$$

may be written in a scale invariant form such that the equations of motion depend only on a single parameter E_0 , rather than on the energy E , the magnetic field B and the ionic charge Z separately [53]. To show this we scale the Hamiltonian and the coordinates in terms of Z and B/c according to

$$H = \left(\frac{B}{c} \right)^\alpha Z^\beta H_0 \quad (\text{B.2})$$

$$r = \left(\frac{B}{c} \right)^\gamma Z^\delta r_0, \quad (\text{B.3})$$

where scaled quantities are denoted by the subscript 0 and α , β , γ and δ are the scaling exponents which have to be determined in the following. From Eqs. (B.2) and (B.3) the scaling of the momentum and the angular momentum can be derived immediately:

$$H \propto \frac{p^2}{2} \Rightarrow p = \left(\frac{B}{c} \right)^{\alpha/2} Z^{\beta/2} p_0 \quad (\text{B.4})$$

$$L_z = (xp_y - yp_x) \Rightarrow L_z = \left(\frac{B}{c} \right)^{\gamma+\alpha/2} Z^{\delta+\beta/2} L_{z0}. \quad (\text{B.5})$$

Applying the scaling relations Eqs. (B.2)-(B.5) to the potential energy terms of the Hamiltonian Eq. (B.1)

$$\begin{aligned} H \propto \frac{1}{8} \left(\frac{B}{c} \right)^2 \rho^2 &\Rightarrow \left(\frac{B}{c} \right)^\alpha Z^\beta = \left(\frac{B}{c} \right)^{2\gamma+2} Z^{2\delta} \\ H \propto \frac{1}{2} \left(\frac{B}{c} \right) L_z &\Rightarrow \left(\frac{B}{c} \right)^\alpha Z^\beta = \left(\frac{B}{c} \right)^{\gamma+\alpha/2+1} Z^{\delta+\beta/2} \\ H \propto -\frac{Z}{\sqrt{\rho^2 + z^2}} &\Rightarrow \left(\frac{B}{c} \right)^\alpha Z^\beta = \left(\frac{B}{c} \right)^{-\gamma} Z^{-\delta+1} \end{aligned}$$

we find the following equations for the scaling exponents

$$\alpha = 2\gamma + 2 \quad \beta = 2\delta \quad (\text{B.6})$$

$$\alpha/2 = \gamma + 1 \quad \beta/2 = \delta \quad (\text{B.7})$$

$$\alpha = -\gamma \quad \beta = -\delta + 1 \quad (\text{B.8})$$

Whereas Eqs. (B.6) and (B.7) are identical, Eqs. (B.6) and (B.8) can be solved and lead to the unique solution

$$\begin{aligned} \alpha &= \frac{2}{3} & \gamma &= -\frac{2}{3} \\ \beta &= \frac{2}{3} & \delta &= \frac{1}{3}. \end{aligned} \quad (\text{B.9})$$

Therefore, the desired scaling transformations read

$$\begin{aligned} H &= \left(\frac{B}{c} \right)^{2/3} Z^{2/3} H_0 \\ p &= \left(\frac{B}{c} \right)^{1/3} Z^{1/3} p_0 \\ r &= \left(\frac{B}{c} \right)^{-2/3} Z^{1/3} r_0 \\ L_z &= \left(\frac{B}{c} \right)^{-1/3} Z^{2/3} L_{z0} \end{aligned} \quad (\text{B.10})$$

resulting in a scaled Hamiltonian

$$H_0 = \frac{1}{2} \left(p_{\rho 0}^2 + \frac{L_{z0}^2}{\rho_0^2} + p_{z0}^2 \right) + \frac{1}{8} \rho_0^2 + \frac{1}{2} L_{z0} - \frac{1}{\sqrt{\rho_0^2 + z_0^2}}, \quad (\text{B.11})$$

which no longer depends on the field strength B and the nuclear charge Z . Thus, the associated classical dynamics depends, as required, only on the scaled energy $E_0 = (B/c)^{-2/3} Z^{-2/3} E$.

Appendix C

Equations of Motion: Symplectic Integration

For given initial conditions the time evolution of the classical dynamics of the electron is determined by the Hamilton equations of motion. In scaled cylindrical coordinates they are given by

$$\begin{aligned}\dot{\rho}_0 &= \frac{\partial H}{\partial p_{\rho_0}} = p_{\rho_0} \\ \dot{\phi}_0 &= \frac{\partial H}{\partial L_{z_0}} = \frac{L_{z_0}}{\rho_0^2} + \frac{1}{2} \\ \dot{z}_0 &= \frac{\partial H}{\partial p_{z_0}} = p_{z_0} \\ \dot{p}_{\rho_0} &= -\frac{\partial H}{\partial \rho_0} = -\frac{1}{4}\rho_0 + \frac{L_{z_0}^2}{\rho_0^3} - \frac{\rho_0}{(\rho_0^2 + z_0^2)^{3/2}} \\ \dot{L}_{z_0} &= -\frac{\partial H}{\partial \phi_0} = 0 \\ \dot{p}_{z_0} &= -\frac{\partial H}{\partial z_0} = -\frac{z_0}{(\rho_0^2 + z_0^2)^{3/2}}.\end{aligned}\tag{C.1}$$

To integrate these equations numerically we use a symplectic integrator [51, 52] within our simulations. In this section this method of integration will be briefly discussed.

Due to the canonical character of the Eqs. (C.1) their exact solution at a definite time t is given by a canonical transformation (or a symplectic map) from the initial conditions ($t = 0$) to the state at time t ,

$$\begin{pmatrix} \vec{r}_0(t) \\ \vec{p}_0(t) \end{pmatrix} = M(t) \begin{pmatrix} \vec{r}_0(0) \\ \vec{p}_0(0) \end{pmatrix},\tag{C.2}$$

where $M(t)$ denotes this map. In the following we would like to find a symplectic map $M_k(t)$ which approximates $M(t)$ through order t^k . Thus the difference between the two maps will be of order t^{k+1} ,

$$\|M(t) - M_k(t)\| = O(t^{k+1}). \quad (\text{C.3})$$

$M_k(t)$ can be determined by successive canonical transformations. These transformations are performed in such a way that the transformed Hamiltonian H' is expressed in terms of the exact initial conditions $\vec{r}_0(0)$ and $\vec{p}_0(0)$ through order t^{k-1} , *i. e.* H' vanishes through order t^{k-1} (since $\vec{r}_0(0)$ and $\vec{p}_0(0)$ are constants on which their corresponding Hamiltonian does not depend). Thus, the required transformation $(\vec{r}_0, \vec{p}_0, H) \rightarrow (\vec{r}_0', \vec{p}_0', H')$ is characterized by

$$H'(\vec{r}_0', \vec{p}_0', t) = O(t^k) \quad (\text{C.4})$$

with the corresponding equations of motion

$$\vec{r}_0' = \vec{r}_0(0) + O(t^{k+1}) \quad (\text{C.5})$$

$$\vec{p}_0' = \vec{p}_0(0) + O(t^{k+1}). \quad (\text{C.6})$$

where the new coordinates and momenta, \vec{r}_0' and \vec{p}_0' , differ from the exact initial conditions at order t^{k+1} . This means, if \vec{r}_0' and \vec{p}_0' are used as initial conditions within the calculation, the error introduced is of the order t^{k+1} .

For the explicit calculation of the symplectic map the generating function F_3 is employed for the canonical transformations,

$$F_3(\vec{r}_0', \vec{p}_0, t) = -\vec{r}_0' \vec{p}_0 - H(\vec{r}_0', \vec{p}_0) t, \quad (\text{C.7})$$

which is a function of the new (*i. e.* transformed) coordinates and the old momenta. Its transformation equations for a Hamiltonian $H(\vec{r}_0, \vec{p}_0) = T(\vec{p}_0) + V(\vec{r}_0)$ are given by [47, 51]

$$\vec{r}_0 = -\frac{\partial F_3}{\partial \vec{p}_0} = \vec{r}_0' + \frac{dT(\vec{p}_0)}{d\vec{p}_0} t \quad (\text{C.8})$$

$$\vec{p}_0 = -\frac{\partial F_3}{\partial \vec{r}_0'} = \vec{p}_0' + \frac{dV(\vec{r}_0')}{d\vec{r}_0'} t \quad (\text{C.9})$$

$$H' = H + \frac{\partial F_3}{\partial t} = V(\vec{r}_0) - V(\vec{r}_0'). \quad (\text{C.10})$$

After inverting the momentum equation Eq. (C.9) the two transformation equations Eqs. (C.8) and (C.9) are substituted into the Hamiltonian Eq. (C.10) and by expanding for a small time t a first-order symplectic map $M_1(t)$ can be found.

To construct a k -th order symplectic map $M_k(t)$ k transformation steps are necessary

$$\vec{p}_0^i = \vec{p}_0^{i-1} - c^i \frac{dV(\vec{r}_0^{i-1})}{d\vec{r}_0^{i-1}} t \quad (\text{C.11})$$

$$\vec{r}_0^i = \vec{r}_0^{i-1} + d^i \frac{dT(\vec{p}_0^i)}{d\vec{p}_0^i} t \quad (\text{C.12})$$

where i decreases from k to 1, $(\vec{r}_0^k, \vec{p}_0^k) = (\vec{r}_0, \vec{p}_0)$ and $(\vec{r}_0^0, \vec{p}_0^0) = (\vec{r}_0^j, \vec{p}_0^j)$. Note that the momenta at any given sub-step must be evaluated first followed by the coordinates' evaluation. The coefficients c^i and d^i are determined by successively inserting Eqs. (C.11) and (C.12) into the transformation equation for the Hamiltonian

$$H^{i-1}(\vec{r}_0^{i-1}, \vec{p}_0^{i-1}) = H^i(\vec{r}_0^i, \vec{p}_0^i) - d^i T(\vec{p}_0^i) - c^i V(\vec{r}_0^{i-1}) \quad (\text{C.13})$$

until for $i = 1$ finally an expression for the approximated initial Hamiltonian $H^0(\vec{r}_0^0, \vec{p}_0^0) = H^1(\vec{r}_0^j, \vec{p}_0^j)$ is reached. To obtain the required form of Eq. (C.4) for H' the coefficients c^i and d^i must satisfy a set of non-linear algebraic equations, which are thereupon solved for their unknowns c^i and d^i . Thus the explicit form of $M_k(t)$ is attained.

In our simulations we utilize a fourth order symplectic map $M_4(t)$, where the coefficients c^i and d^i are calculated to be [51]

$$\begin{aligned} c^1 &= x + \frac{1}{2} & d^1 &= 2x + 1 \\ c^2 &= -x & d^2 &= -4x - 1 \\ c^3 &= -x & d^3 &= 2x + 1 \\ c^4 &= x + \frac{1}{2} & d^4 &= 0 \end{aligned} \quad (\text{C.14})$$

with $x = (2^{1/3} + 2^{-1/3} - 1)/6$.

Once c_i and d_i are determined, the canonical transformations are applied in reverse sequence, *i. e.* $(\vec{r}_0^j, \vec{p}_0^j, H') \rightarrow (\vec{r}_0, \vec{p}_0, H)$, within the simulations and, accordingly, the coordinates and momenta (\vec{r}_0, \vec{p}_0) are evaluated from their initial values $(\vec{r}_0^j, \vec{p}_0^j)$. In this way the equations of motion can be solved numerically up to an error of order t^{k+1} by repeatedly applying the symplectic map $M_k(t)$.

Note that the Hamiltonian of our system Eq. (B.11) does not have the simple form $H(\vec{r}_0, \vec{p}_0) = T(\vec{p}_0) + V(\vec{r}_0)$ as assumed in the preceding considerations. However, if we perform the canonical transformation step for $(p_{\rho 0}, p_{z 0}, \phi_0)$ first and only afterwards that for $(\rho_0, z_0, L_{z 0})$ we obtain transformation equations of the form of Eqs. (C.11) and (C.12) again. Finally, explicitly inserting the Hamiltonian Eq.

(B.11), these canonical transformations are written as

$$\begin{aligned}
p_{\rho 0}^i &= p_{\rho 0}^{i-1} - c^i \left(\frac{\rho_0^{i-1}}{(\rho_0^{i-12} + z_0^{i-12})^{3/2}} + \frac{1}{4} \rho_0^{i-1} - \frac{L_{z0}^{i-12}}{\rho_0^{i-13}} \right) t \\
p_{z0}^i &= p_{z0}^{i-1} - c^i \frac{z_0^{i-1}}{(\rho_0^{i-12} + z_0^{i-12})^{3/2}} t \\
\phi_0^i &= \phi_0^{i-1} + c^i \left(\frac{L_{z0}^{i-1}}{\rho_0^{i-12}} + \frac{1}{2} \right) t \\
\rho_0^i &= \rho_0^{i-1} + d^i p_{\rho 0}^i t \\
z_0^i &= z_0^{i-1} + d^i p_{z0}^i t \\
L_{z0}^i &= L_{z0}^{i-1}.
\end{aligned} \tag{C.15}$$

For $M_4(t)$ $i = 1$ to 4 transforming the initial coordinates and momenta $(\vec{r}_0^i, \vec{p}_0^i)$ to their new values $(\vec{r}_0^i, \vec{p}_0^i)$ after time step t by the sequence of transformations $(\vec{r}_0^i, \vec{p}_0^i) = (\vec{r}_0^0, \vec{p}_0^0) \rightarrow (\vec{r}_0^1, \vec{p}_0^1) \rightarrow (\vec{r}_0^2, \vec{p}_0^2) \rightarrow (\vec{r}_0^3, \vec{p}_0^3) \rightarrow (\vec{r}_0^4, \vec{p}_0^4) = (\vec{r}_0^i, \vec{p}_0^i)$ with their coefficients c^i and d^i given by Eqs. (C.14). Note that the full integration step is the complete sequence of maps and the intermediate values of $(\vec{r}_0^i, \vec{p}_0^i)$ at the various sub-steps should not be interpreted as physical values. So, eventually we have managed to integrate Eqs. (C.1).

The time step t in Eqs. (C.15) has to be chosen carefully due to the Coulomb singularity of the problem. We proceed according to Ref. [82] and fix the next time step in terms of changes in position after that step. Thereby the relative error in position $|\Delta \vec{r}|/|\vec{r}|$ (with $\Delta \vec{r}$ being the change in position vector after one step) is confined by the assumption

$$|\Delta \vec{r}| \approx \epsilon |\vec{r}|. \tag{C.16}$$

ϵ is a positive error parameter which is less than unity. As our Hamiltonian in scaled cylindrical coordinates Eq. (B.11) has singularities both at $r_0 = 0$ and $\rho_0 = 0$ caused by the Coulomb potential $-1/r_0$ and the kinetic energy term $L_{z0}^2/(2\rho_0^2)$, the relative error in ρ_0 as well as in z_0 direction has to be kept small enough requiring the two conditions

$$|\Delta \rho_0| \approx \epsilon |\rho_0|, \quad |\Delta z_0| \approx \epsilon |z_0|.$$

A satisfactory time step t for the next integration step can be achieved as the

minimum of the two time steps [82]

$$t_\rho = \frac{\epsilon}{\sqrt{\frac{v_{\rho 0}^2}{\rho_0^2} + \frac{\epsilon}{2} \left| \frac{v_{\rho 0}}{\rho_0} \right|}},$$

$$t_z = \frac{\epsilon}{\sqrt{\frac{v_{z 0}^2}{z_0^2} + \frac{\epsilon}{2} \left| \frac{v_{z 0}}{z_0} \right|}},$$

obtained separately for the ρ_0 and z_0 directions, *i. e.* $t = \min(t_\rho, t_z)$. It is recalculated at every integration step. Note that the error parameter ϵ is the same for all trajectories and for all points on a given trajectory and is thus fixed once at the beginning of the CTMC.

To conclude this section a remark about the construction of higher order symplectic maps should be made. Given the fourth order symplectic integrator $M_4(t)$ a symplectic integrator of any higher even order can be obtained by a symmetric product of $M_4(t)$. For example, the 6th order symplectic map $M_6(t)$ is constructed by [52]

$$M_6(t) = M_4(y_1 t) M_4(y_0 t) M_4(y_1 t) \quad (\text{C.17})$$

with the coefficients y_0 and y_1 given by

$$y_0 = -\frac{2^{1/5}}{2 - 2^{1/5}}, \quad y_1 = \frac{1}{2 - 2^{1/5}}. \quad (\text{C.18})$$

Analogously, the 8th order symplectic integrator $M_8(t)$ involves the symmetric product of 3 times the map $M_4(t)$, *i. e.* 9 times the map $M_4(t)$. This procedure can be continued up to the $2n$ -th order symplectic map $M_{2n}(t)$.

Appendix D

Study of the Recombination in Momentum Space

D.1 Momentum Distributions of Bound and Free Electrons

Starting point of our investigations are the momentum distributions of bound and free electrons in a magnetic field, respectively. Since the bound-state wavefunctions ($n \leq n_r$) of recombined electrons are spatially localized around the ion, they can be well approximated using hydrogenic bound states in the absence of a magnetic field (see also section 3.1). For the spherically symmetric Coulomb potential in momentum space $V(p) = -Z/(2\pi^2 p^2)$ (*i.e.* the Fourier transform of the coordinate space potential $V(r) = -Z/r$) the wavefunction in momentum representation can be likewise expressed in terms of spherical polar coordinates, $\psi_{nlm}(\vec{p}) = F_{nl}(p)Y_{lm}(\theta, \phi)$, where F_{nl} denotes the radial wavefunction and Y_{lm} the corresponding spherical harmonic (as usual, n : principal quantum number, l : orbital quantum number and m : magnetic quantum number). The radial momentum space wavefunction for hydrogen-like ions with charge Z is given by [7]

$$F_{nl}(p) = \left[\frac{2}{\pi} \frac{(n-l-1)!}{(n+l)!} \right]^{1/2} n^2 2^{2(l+1)} l! Z^{-3/2} \frac{n^l (p/Z)^l}{(n^2 (p/Z)^2 + 1)^{l+2}} C_{n-l-1}^{l+1} \left(\frac{n^2 (p/Z)^2 - 1}{n^2 (p/Z)^2 + 1} \right), \quad (\text{D.1})$$

where $C_N^\nu(x)$ is the Gegenbauer polynomial, defined as the coefficient of h^N in the expansion of $(1 - 2hx + h^2)^{-\nu}$ in powers of h [63]. Thus, $|pF_{nl}(p)|^2$ represents the momentum distribution function of the recombined electron specifying the probability for the absolute value of the momentum p to lie between p and $p + dp$, *i.e.* $|pF_{nl}(p)|^2 dp$. To obtain a single final-state momentum distribution for an electron radiatively recombined into any of the (n, l) states with $n \leq n_r$, we weigh the dis-

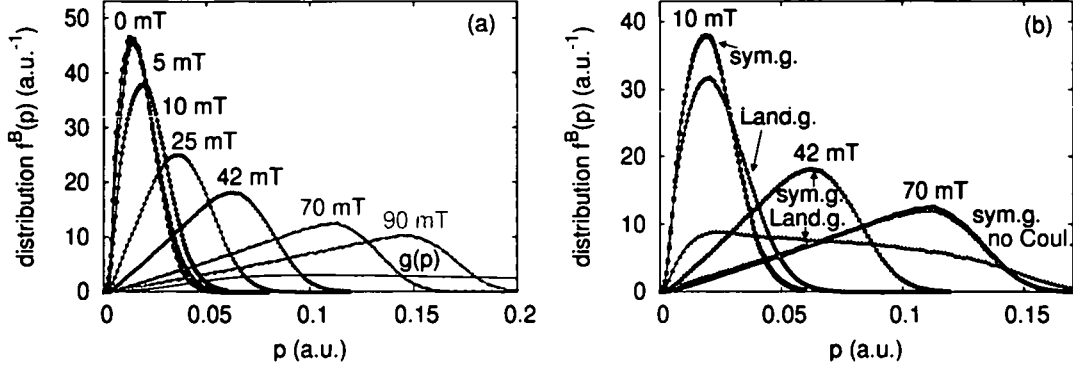


Figure D.1: Momentum distributions $f^B(p)$ of the electron ensemble for different magnetic field strengths (values indicated) (a). The momentum is recorded at random times within typical interionic distances ($r_{ion} = 1.765 \times 10^6$ a.u.). For comparison, the cross section weighted final-state momentum distribution $g(p)$ (Eq. (D.2)) (black line) with $n_r = 30$ and $E_e = 5.06$ meV is also shown in (a). The distributions obtained within the symmetric gauge (*i.e.* all distributions in (a)) and the Landau gauge are compared in (b). In addition, the distribution for $B = 70$ mT (symmetric gauge) accomplished by entirely neglecting the Coulomb potential of the ion is given by the magenta curve in (b). $Z = 6$, $kT_{\parallel} = 0.06$ meV, $kT_{\perp} = 5$ meV and $E_{rel} = 0.03$ meV.

tributions $|pF_{nl}(p)|^2$ with the corresponding unperturbed cross sections σ_{nl} for RR (given by Eq. (3.40)),

$$g(p) = \sum_{n=1}^{n_r} \sum_{l=0}^{n-1} |pF_{nl}(p)|^2 \sigma_{nl}. \quad (D.2)$$

On the other hand, the initial-state momentum distribution of the continuum electron needs to be determined in the presence of the magnetic field. Again, we perform a CTMC calculation justified for electrons in high Landau quantum numbers (section 3.1), from which the distribution at non-zero magnetic field strength can be easily determined. The initial electron ensemble is distributed uniformly in coordinate space (launched from a fixed z -plane with $|z| = r_{ion}/2$ spatially confined in the transverse direction to $\rho \leq r_{ion}/2$, r_{ion} denotes a typical interionic distance in the experiment estimated from the ion density n_{ion} as $r_{ion} = n_{ion}^{-1/3}$) and Maxwell-Boltzmann distributed (Eq. (2.12)) in velocity space. We confine the propagation of the electrons to a cylinder with radius $r_{ion}/2$ and length r_{ion} around the ionic position by imposing periodic boundary conditions, *i.e.* $x \rightarrow -x$ and $y \rightarrow -y$ if $\rho = \sqrt{x^2 + y^2} \geq r_{ion}/2$, likewise $z \rightarrow -z$ if $|z| \geq r_{ion}/2$. We record the abso-

lute momentum p of individual electrons at randomly chosen times. The obtained momentum distribution function $f^B(p)$ mimics the continuum momentum space wavefunctions of electrons in the cooler. Figure D.1 depicts $f^B(p)$ for different magnetic field strengths. All distributions are normalized, $\int_0^\infty \int f^B(p) dp = 1$. Note that $f^B(p)$ depends on the gauge chosen for the Hamiltonian. In the symmetric gauge, $\vec{A} = 1/2 (\vec{B} \times \vec{r}) = 1/2 (-By, Bx, 0)$, the Hamiltonian is described by Eq. (3.21). The obtained distributions $f^B(p)$ are shown in Figure D.1a. Alternatively, the Landau gauge $\vec{A} = (0, Bx, 0)$ could be employed, where the Hamiltonian reads

$$H = \frac{p^2}{2} - \frac{Z}{r} + \frac{1}{c} B x p_y + \frac{1}{2c^2} B^2 x^2. \quad (\text{D.3})$$

More details about the motion of an electron in a homogeneous magnetic field using the Landau gauge can be found for example in Refs. [79, 80]. Figure D.1b compares the distributions $f^B(p)$ for the Landau gauge and the symmetric gauge. The shape of these momentum distributions can be mainly attributed to the presence of the magnetic field, whereas the Coulomb field of the target ion plays only a minor role. In Figure D.1b $f^B(p)$ at $B = 70$ mT is additionally depicted omitting the ionic Coulomb potential. The curves with and without Coulomb field can hardly be distinguished.

Having determined the momentum distributions of free and recombined electrons, $f^B(p)$ and $g(p)$ respectively, we can investigate the overlap between the two distributions, given by

$$O(B) = \int f^B(p) g(p) dp. \quad (\text{D.4})$$

Figure D.2 displays the calculated overlap as a function of the magnetic field strength with $f^B(p)$ defined either in the symmetric gauge or in the Landau gauge. Although the corresponding distributions presented in Figure D.1b differ considerably, the momentum space overlap via Eq. (D.4) exhibits approximately the same increasing trend with B for both gauges. The obtained B dependence is in close agreement with the experimentally observed $B^{0.5}$ scaling of the excess recombination rate.

However, an evaluation of the RR rate via an overlap such as Eq. (D.4) faces the difficulty that multiplying the momentum distribution functions with the cross section, which already contains the momentum overlap in some form, looks like double counting. We point out that an incorporation of the ratio of overlaps in the combined fields versus the pure Coulomb problem, *i.e.* $\int dp f^B(p) |p F_{nl}(p)|^2 / (\int dp f^{B=0}(p) |p F_{nl}(p)|^2)$, into the recombination rate similarly as done for the visit function V in chapter 3 (compare Eq. (3.26)) is impossible due to a dramatic increase of this ratio for higher n, l states originating from the miniscule overlap of $f^{B=0}(p)$ with $|p F_{nl}(p)|^2$ at large (n, l) . To avoid such difficulties of a proper representation of the quantum RR rate by our CTMC calculations we instead pursue a perturbative

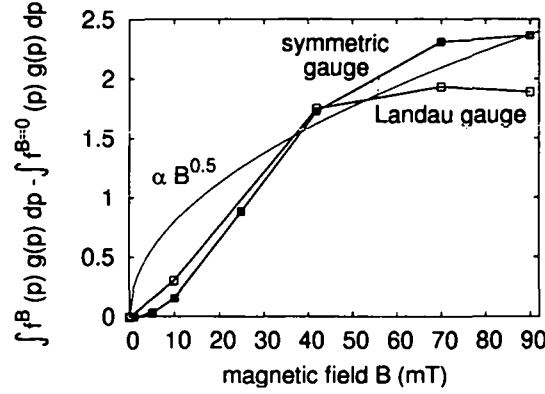


Figure D.2: Overlap (Eq. (D.4)) between the calculated momentum distribution $f^B(p)$ of the continuum electron (see also Figure D.1) and the cross section weighted final-state momentum distribution $g(p)$ of the bound-state electron (Eq. (D.2)) for different magnetic fields. Note that the overlap is drawn with reference to the corresponding quantity at $B = 0$. The results with $f^B(p)$ represented in the symmetric gauge and Landau gauge are compared. The black line is $\propto B^{0.5}$. Same parameters as in Figure D.1.

quantum mechanical approach to the rate coefficients in a magnetic field in momentum representation in the next section. Using first Born approximation, however, employing Landau states as initial wavefunctions, the effect of a magnetic field on the recombination rates will be explored.

D.2 Perturbative Quantum Mechanical Approach

The total probability for a transition of an atom or ion from an initial state ψ_i to a final state ψ_f accompanied by the emission of a photon is given in the electric dipole approximation in momentum representation by [7]

$$W = \frac{4}{3} \frac{\omega}{c^3} |\langle \psi_f | \vec{p} | \psi_i \rangle|^2 \quad (\text{D.5})$$

with the transition frequency ω and the velocity of light c . In the absence of a magnetic field the recombination of an electron with a fully stripped ion is described via Eq. (D.5) by employing a Coulomb continuum wavefunction for the initial state ψ_i of the incoming electron and the corresponding hydrogenic bound-state wavefunction for the final state ψ_f of the recombined electron. Note that the recombination cross section follows as $\sigma = W/j$, where j denotes the incident electron current.

In a magnetic field the initial wavefunction ψ_i needs to be properly modified. In the following we will account for the effect of a magnetic field by using Landau states as initial states. In other words, we will consider first order Born approximation, however, replacing the plane wave state by a Landau wavefunction. In the Landau gauge ($\vec{A} = (0, Bx, 0)$) the wavefunction for an electron in a homogeneous magnetic field $\vec{B} = (0, 0, B)$ is expressed in coordinate space as [79, 80]

$$\psi_i^L(\vec{r}) = \frac{1}{2\pi} e^{ik_z z} e^{-i\omega_c x_0 y} \phi_N(x - x_0), \quad (\text{D.6})$$

where $\phi_N(x - x_0)$ describes a displaced harmonic oscillator wavefunction centered around the guiding center coordinate x_0 ($x_0 = -k_y/\omega_c$)

$$\phi_N(x - x_0) = \frac{1}{\pi^{1/4} l_B^{1/2} \sqrt{2^N N!}} H_N \left(\frac{x - x_0}{l_B} \right) \exp \left[-\frac{(x - x_0)^2}{2l_B^2} \right] \quad (\text{D.7})$$

with Hermite polynomials H_N [63] and l_B denotes the magnetic length $l_B = \sqrt{c/B} = \omega_c^{-1/2}$. The quantum number N of this oscillator is referred to as Landau quantum number. The momentum representation of Eqs. (D.6) and (D.7) can be readily determined. Since the Hamilton operator of a harmonic oscillator in momentum space exhibits the same form as in coordinate space apart from the substitution $x \rightarrow p/\omega_c = pl_B^2$, the momentum oscillator wavefunction can be immediately obtained from its spatial counterpart (Eq. (D.7)) by replacing the argument x/l_B by pl_B . Furthermore, the momentum representation of a plane wave $\psi_{PW} = 1/\sqrt{2\pi} e^{ikx}$ is given by the delta function $\delta(p - k)$. Therefore, the Landau wavefunction in momentum space becomes

$$\psi_i^L(\vec{p}) = \delta(p_z - k_z) \delta(p_y + \omega_c x_0) e^{-ip_x x_0} \frac{l_B^{1/2}}{\pi^{1/4} \sqrt{2^N N!}} H_N(p_x l_B) e^{-p_x^2 l_B^2/2}. \quad (\text{D.8})$$

The additional phase factor $e^{-ip_x x_0}$ originates from the shift of x by x_0 and thus the replacement of $(x - x_0)/l_B$ by pl_B .

At typical experimental conditions the electron resides in high Landau states with quantum numbers $N \gg 1$ (section 3.1). In the limit of large N , however, the harmonic oscillator wavefunction $\phi_N(x - x_0)$ may be approximated by [63]

$$\phi_N(x - x_0) \xrightarrow{N \gg 1} \begin{cases} A \cos(\sqrt{2N+1}(x - x_0)/l_B) & N \text{ even} \\ A \sin(\sqrt{2N+1}(x - x_0)/l_B) & N \text{ odd} \end{cases} \quad (\text{D.9})$$

Taking into account that $H_N(0) = (-1)^{N/2} N!/(N/2)!$ for even N , the prefactor A is determined to be

$$A = \frac{1}{\pi^{1/4} l_B^{1/2} \sqrt{2^N}} \frac{\sqrt{N!}}{(N/2)!} (-1)^{N/2}. \quad (\text{D.10})$$

Since according to Eq. (D.9) in the asymptotic limit even and odd quantum numbers N have to be treated separately, it might be desirable to combine an even and an odd order for an appropriate representation of the incoming electron wave in the cooler. With Eqs. (D.9), (D.10) and $N = 2n$ a coordinate space Landau wavefunction can be written in the asymptotic form as [81]

$$\psi_i^{asym}(\vec{r}) = \frac{1}{2\pi} e^{ik_z z} e^{-i\omega_c x_0 y} \frac{\sqrt{(2n)!}}{\pi^{1/4} l_B^{1/2} 2^n n!} (-1)^n \left[C_{2n} \cos\left(\sqrt{4n+1} \frac{x-x_0}{l_B}\right) + C_{2n+1} \sin\left(\sqrt{4n+3} \frac{x-x_0}{l_B}\right) \right]. \quad (D.11)$$

For large values of n , the arguments of sine and cosine can be taken as equal, *i.e.* $\sqrt{4n+1} \approx \sqrt{4n+3} \approx \sqrt{4n}$. We may assume $\vec{k}_\perp = k_x \hat{e}_x$, so that the transverse energy E_\perp of the Landau state fulfills $E_\perp = \omega_c(N + 1/2) = 1/2 k_x^2$. Accordingly, N and k_x are related by $N \approx \text{int}(k_x^2/(2\omega_c))$ for $N \gg 1$. Thus, we have $\sqrt{4n}/l_B = \sqrt{2N\omega_c} = k_x$ in Eq. (D.11). Choosing

$$C_{2n} = \frac{(-1)^n \pi^{1/4} l_B^{1/2} 2^n n!}{\sqrt{2\pi} \sqrt{(2n)!}}, \quad C_{2n+1} = i C_{2n} \quad (D.12)$$

we find for the asymptotic Landau state of Eq. (D.11)

$$\psi_i^{asym}(\vec{r}) = \frac{1}{(2\pi)^{3/2}} e^{ik_z z} e^{-i\omega_c x_0 y} e^{ik_x(x-x_0)}. \quad (D.13)$$

Accordingly, the wavefunction in momentum representation at large N immediately follows as

$$\psi_i^{asym}(\vec{p}) = e^{-ik_x x_0} \delta(p_x - k_x) \delta(p_y + \omega_c x_0) \delta(p_z - k_z). \quad (D.14)$$

In the limit of $B \rightarrow 0$, or correspondingly $\omega_c \rightarrow 0$, a plane wave into the x - z plane is obtained apart from the phase factor $e^{-ik_x x_0}$. In the subsequent considerations we utilize this asymptotic momentum wavefunction to determine the transition matrix elements $\langle \psi_f | \vec{p} | \psi_i^{asym} \rangle$ in Eq. (D.5).

We investigate the recombination of an electron into the ground state of the ion. With the radial momentum wavefunction defined in Eq. (D.1) ($C_0^r = 1$) and the spherical harmonic $Y_{00} = 1/\sqrt{4\pi}$ the 1s bound-state wavefunction becomes

$$\psi_f^{1s} = \sqrt{\frac{8Z^5}{\pi^2}} \frac{1}{(p^2 + Z^2)^2}. \quad (D.15)$$

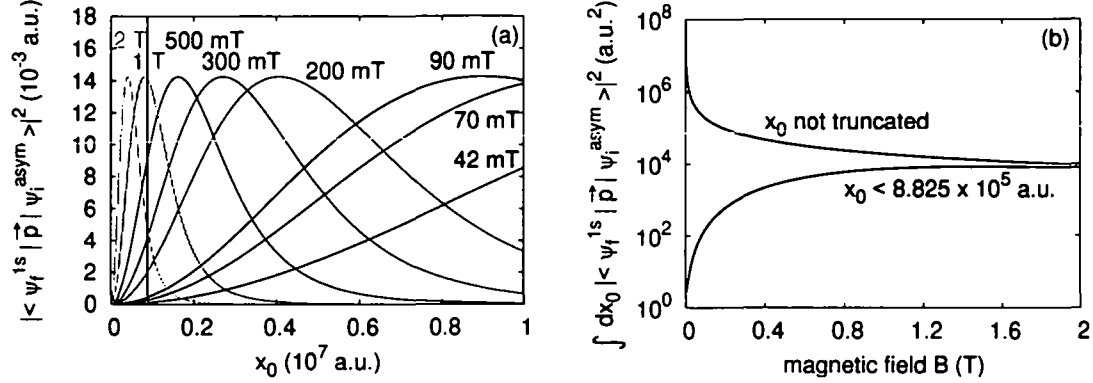


Figure D.3: Square of the dipole matrix element (Eq. (D.16)) between the asymptotic initial Landau wavefunction ψ_i^{asym} and the final hydrogenic ground state ψ_f^{1s} displayed in terms of the guiding center coordinate x_0 (a) and the corresponding quantity integrated over x_0 with no restriction in the x_0 range and $x_0 \leq r_{ion}/2 = 8.825 \times 10^5$ a.u. (b). Note that the vertical line in (a) denotes the cutoff in x_0 . $Z = 6$, $v_\perp = 0.0271$ a.u. and $v_\parallel = 0.0015$ a.u.

Correspondingly, the transition matrix element between ψ_i^{asym} and ψ_f^{1s} (Eqs. (D.14) and (D.15)) reads

$$M_{1s,i} = \langle \psi_f^{1s} | \vec{p} | \psi_i^{asym} \rangle = \sqrt{\frac{8Z^5}{\pi^2}} \frac{1}{(v_\perp^2 + \omega_c^2 x_0^2 + v_\parallel^2 + Z^2)^2} \begin{pmatrix} v_\perp \\ -\omega_c x_0 \\ v_\parallel \end{pmatrix} e^{-iv_\perp x_0}, \quad (\text{D.16})$$

where we have identified k_x and k_z with the transverse and longitudinal velocity of the electron according to the Maxwell-Boltzmann distribution in the experiment. Note that the guiding center coordinate x_0 constitutes an additional free parameter caused by the uncertainty of the guiding center position of the electron spiral orbit. Figure D.3a shows the square of the matrix element of Eq. (D.16) $|M_{1s,i}|^2$ as a function of x_0 for different magnetic fields. With increasing field strength $|M_{1s,i}|^2$ gets confined to smaller values of x_0 due to its scaling with ω_c^{-6} . The integration over the entire region of x_0 contributing to $|M_{1s,i}|^2$ results in a clear decrease of the dipole matrix element with B (Figure D.3b). However, since the average interionic distance r_{ion} is limited and we want to aim at a single ion in our one-particle approach, the range of x_0 should be rather restricted to $|x_0| \leq r_{ion}/2$. Within this limitation the x_0 -integrated squared transition matrix increases with B up to field strengths of $B \gtrsim 1$ T for typical interionic distances available in the experiment (for example, in Figure D.3b $r_{ion} = 1.765 \times 10^6$ a.u.). Only at even higher fields a reduction in the matrix element will be observed. Thus, the increase with B can be solely traced back

to the restriction of x_0 with the precise value of the peak position of $\int dx_0 |M_{1s,i}|^2$ tuned by the chosen cutoff in x_0 .

Once $|M_{1s,i}|^2$ has been determined the cross section for recombination into the ground state σ_{1s} can be calculated. The incident electron current generated by the initial wavefunction ψ_i^{asym} is determined by

$$\vec{j} = -\frac{i}{2} \left[\psi_i^{asym*} (\vec{\partial} \psi_i^{asym}) - \psi_i^{asym} (\vec{\partial} \psi_i^{asym*}) \right] + \frac{1}{c} \vec{A} \psi_i^{asym*} \psi_i^{asym} = \frac{1}{(2\pi)^3} \begin{pmatrix} v_{\perp} \\ 0 \\ v_{\parallel} \end{pmatrix}. \quad (D.17)$$

It can be easily derived from the coordinate representation of the asymptotic wavefunction Eq. (D.13) with the transverse energy $E_{\perp} = v_{\perp}^2/2$ of the Landau state taken into the x direction. Furthermore, the difference in cross section for the plane wave obtained in the $B \rightarrow 0$ limit and the $1s$ cross section calculated with a full Coulomb continuum state has to be taken into account. The quantum mechanical $1s$ recombination cross section σ_{1s}^{Coul} employing a Coulomb continuum wavefunction as initial state reads [7]

$$\sigma_{1s}^{Coul}(v) = \frac{2^8 \pi^2}{3c^3} \frac{Z^6}{(Z^2 + v^2)^2 v^2} \frac{\exp[-4Z/v \arctan(v/Z)]}{1 - \exp[-2\pi Z/v]}. \quad (D.18)$$

In the limit of $v \rightarrow 0$ applicable for the low-energy measurements of experimental rate coefficients $\exp[-4Z/v \arctan(v/Z)] \rightarrow \exp(-4)$ and $1 - \exp[-2\pi Z/v] \rightarrow 1$ and $\sigma_{1s}^{Coul}(v \rightarrow 0)$ becomes

$$\sigma_{1s}^{Coul}(v \rightarrow 0) = \frac{2^8 \pi^2}{3c^3} \frac{Z^6}{(Z^2 + v^2)^2 v^2} e^{-4}. \quad (D.19)$$

On the other hand, the cross section with an incident plane wave $\psi_i^{PW} = \delta^3(\vec{p} - \vec{v})$ is calculated by means of the electron current $\vec{j} = \vec{v}/(2\pi)^3$ and the transition probability W (Eq. (D.5)) with the energy of the emitted photon $\omega = 1/2 (v^2 + Z^2)$ and the hydrogenic ground-state wavefunction of Eq. (D.15) as

$$\sigma_{1s}^{PW}(v) = \frac{4}{3} \frac{\omega}{c^3} v^2 |\psi_f^{1s}(\vec{v})|^2 |\vec{j}|^{-1} = \frac{2^7 \pi}{3c^3} \frac{Z^5}{(Z^2 + v^2)^3} v. \quad (D.20)$$

Accordingly, the RR cross section $\sigma_{1s}^{Coul}(v \rightarrow 0)$ is related to the plane wave contribution $\sigma_{1s}^{PW}(v)$ by

$$\sigma_{1s}^{Coul}(v \rightarrow 0) = \sigma_{1s}^{PW}(v) \frac{2\pi Z(Z^2 + v^2)}{v^3} e^{-4}. \quad (D.21)$$

Thus, the cross section for RR into the ground state of an ion in the presence of a magnetic field can be determined. With Eqs. (D.5) ($\omega = 1/2 (v^2 + Z^2)$), (D.16),

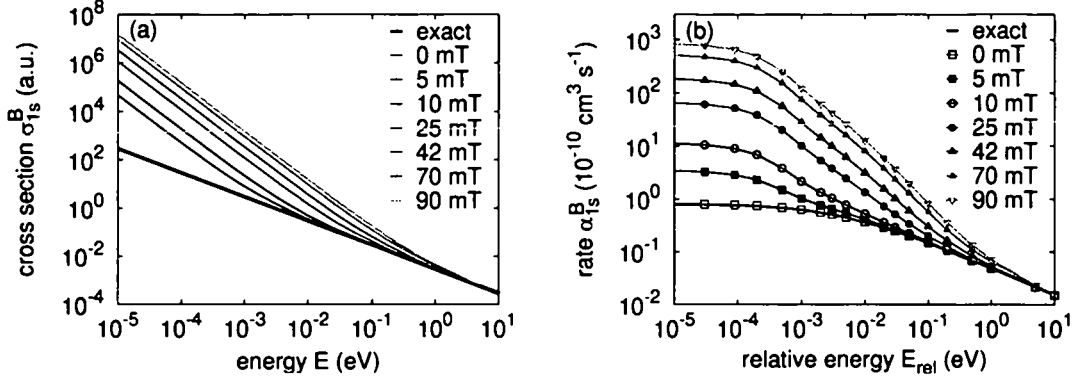


Figure D.4: The radiative recombination cross section $\sigma_{1s}^B(E = v^2/2)$ as a function of energy (Eq. (D.22)) (a) and the resulting recombination rate $\alpha_{1s}^B(E_{rel})$ versus the average relative energy (Eq. (D.23)) (b) for recombination into the ground state at different magnetic field strengths (values indicated in the figure). $Z = 6$ and $r_{ion} = 1.765 \times 10^6$ a.u. The temperatures for the Maxwell-Boltzmann distribution in (b) are $kT_{\parallel} = 0.2$ meV and $kT_{\perp} = 10$ meV.

(D.17) and (D.21) and an averaging over the guiding center coordinate x_0 it becomes

$$\sigma_{1s}^B(v) = \frac{2^8 \pi^2}{3c^3} \frac{Z^6 (Z^2 + v^2)^2}{v^4} e^{-4} \frac{1}{r_{ion}} \int_{|x_0| \leq r_{ion}/2} dx_0 \frac{v^2 + \omega_c^2 x_0^2}{(v^2 + \omega_c^2 x_0^2 + Z^2)^4} \quad (D.22)$$

with $v^2 = v_{\parallel}^2 + v_{\perp}^2$. Note that the integral over x_0 can be solved analytically.

Figure D.4a illustrates σ_{1s}^B as a function of energy $E = v^2/2$ for different magnetic field strengths and Figure D.4b depicts the corresponding recombination rate

$$\alpha_{1s}^B(E_{rel} = v_{rel}^2/2) = \int \sigma_{1s}^B(v) v f_{MB}(\vec{v}, v_{rel}) d\vec{v} \quad (D.23)$$

in terms of the parallel detuning energy E_{rel} between electrons and ions for the same values of B . The cross sections and rate coefficients are seen to dramatically increase with B thus by far overestimating the magnetic field dependence of the experimental rate enhancement.

Considering this enormous increase of α_{1s}^B with B the presented method to calculate RR rates appears to be too simplistic. For example, the initial Landau wavefunction could rather be taken without employing the asymptotic limit, i.e.

$$\psi_i = \frac{(-1)^n}{(\sqrt{2\pi})} \delta(p_z - k_z) \delta(p_y + \omega_c x_0) e^{-ip_x x_0} \frac{\pi^{1/4} 2^n n!}{l_B^{1/2} \sqrt{(2n)!}} [\phi_{2n}(p_x) + i\phi_{2n+1}(p_x)], \quad (D.24)$$

where $\phi_{2n}(p_x)$ and $\phi_{2n+1}(p_x)$ denote harmonic oscillator eigenfunctions in momentum space (compare Eq. (D.8)). It should be again noted that the given approach only represents first order Born approximation without considering the ionic Coulomb potential. The Coulomb field only enters through Eq. (D.21), *i.e.* the comparison of the cross sections for initial plane wave and Coulomb continuum states. Thus, a more realistic description including the Coulomb potential, preferably a non-perturbative model, would be highly welcome.

Appendix E

Electron-Ion Merging: Lab Frame

The Hamiltonian for the electron-ion system within the toroidal section of the electron cooler is given in the lab frame according to Eq. (4.1) in Cartesian coordinates by

$$H = \frac{1}{2m_{ion}} \left(\begin{pmatrix} p_{ionx} \\ p_{iony} \\ p_{ionz} \end{pmatrix} - \frac{Z}{2c} \begin{pmatrix} -B \sin \phi_{ion} \\ B \cos \phi_{ion} \\ B_{dipole} \end{pmatrix} \times \begin{pmatrix} x_{ion} \\ y_{ion} \\ z_{ion} \end{pmatrix} \right)^2 + \frac{1}{2} \left(\begin{pmatrix} p_{ex} \\ p_{ey} \\ p_{ez} \end{pmatrix} + \frac{1}{2c} \begin{pmatrix} -B \sin \phi_e \\ B \cos \phi_e \\ B_{dipole} \end{pmatrix} \times \begin{pmatrix} x_e \\ y_e \\ z_e \end{pmatrix} \right)^2 - \frac{Z}{|\vec{r}_e - \vec{r}_{ion}|}, \quad (E.1)$$

where we approximate $B(\vec{r}) = B = \text{const}$ and $B_{dipole}(\vec{r}) = B_{dipole} = \text{const}$. Exploiting the symmetry of the merging region we use cylindrical coordinates (polar coordinates in the plane of the toroid and a Cartesian component perpendicular to that plane) in our simulation. We apply the canonical transformation equations (see also Appendix A)

$$\begin{aligned} x &= \rho \cos \phi & p_x &= p_\rho \cos \phi - p_\phi / \rho \sin \phi \\ y &= \rho \sin \phi & p_y &= p_\rho \sin \phi + p_\phi / \rho \cos \phi \end{aligned} \quad (E.2)$$

to the ionic and electronic phase space coordinates in order to obtain the corresponding Hamiltonian in cylinder coordinates

$$H = \frac{1}{2m_{ion}} \left(\begin{pmatrix} p_{ion\rho} \\ p_{ion\phi}/\rho_{ion} \\ p_{ionz} \end{pmatrix} - \frac{Z}{2c} \begin{pmatrix} 0 \\ B \\ B_{dipole} \end{pmatrix} \times \begin{pmatrix} \rho_{ion} \\ 0 \\ z_{ion} \end{pmatrix} \right)^2 + \frac{1}{2} \left(\begin{pmatrix} p_{e\rho} \\ p_{e\phi}/\rho_e \\ p_{ez} \end{pmatrix} + \frac{1}{2c} \begin{pmatrix} 0 \\ B \\ B_{dipole} \end{pmatrix} \times \begin{pmatrix} \rho_e \\ 0 \\ z_e \end{pmatrix} \right)^2 - \frac{Z}{|\vec{r}_e - \vec{r}_{ion}|}. \quad (E.3)$$

ϕ_e and ϕ_{ion} denote the polar angles (≤ 0) with respect to the beginning of the solenoid region. The classical Hamilton's equations of motion

$$\begin{aligned} \frac{d\vec{r}_e}{dt} &= \frac{\partial H}{\partial \vec{p}_e} & \frac{d\vec{r}_{ion}}{dt} &= \frac{\partial H}{\partial \vec{p}_{ion}} \\ \frac{d\vec{p}_e}{dt} &= -\frac{\partial H}{\partial \vec{r}_e} & \frac{d\vec{p}_{ion}}{dt} &= -\frac{\partial H}{\partial \vec{r}_{ion}} \end{aligned} \quad (E.4)$$

govern the dynamics of the particles. In cylindrical coordinates they read

$$\begin{aligned} \dot{\rho}_e &= v_{e\rho} = \frac{\partial H}{\partial p_{e\rho}} = p_{e\rho} + \frac{1}{2c} B z_e \\ \dot{\phi}_e &= v_{e\phi} = \frac{\partial H}{\partial p_{e\phi}} = \frac{p_{e\phi}}{\rho_e^2} + \frac{1}{2c} B_{dipole} \\ \dot{z}_e &= v_{ez} = \frac{\partial H}{\partial p_{ez}} = p_{ez} - \frac{1}{2c} B \rho_e \\ \dot{p}_{e\rho} &= -\frac{\partial H}{\partial \rho_e} = \frac{p_{e\phi}^2}{\rho_e^3} - \frac{1}{4c^2} (B^2 + B_{dipole}^2) \rho_e + \frac{1}{2c} B p_{ez} - \frac{Z}{R^3} (\rho_e - \rho_{ion} \cos(\phi_e - \phi_{ion})) \\ \dot{p}_{e\phi} &= -\frac{\partial H}{\partial \phi_e} = -\frac{Z}{R^3} \rho_e \rho_{ion} \sin(\phi_e - \phi_{ion}) \\ \dot{p}_{ez} &= -\frac{\partial H}{\partial z_e} = -\frac{1}{4c^2} B^2 z_e - \frac{1}{2c} B p_{e\rho} - \frac{Z}{R^3} (z_e - z_{ion}) \\ \dot{\rho}_{ion} &= v_{ion\rho} = \frac{\partial H}{\partial p_{ion\rho}} = \frac{p_{ion\rho}}{m_{ion}} - \frac{Z}{2m_{ion}c} B z_{ion} \\ \dot{\phi}_{ion} &= v_{ion\phi} = \frac{\partial H}{\partial p_{ion\phi}} = \frac{p_{ion\phi}}{m_{ion}\rho_{ion}^2} - \frac{Z}{2m_{ion}c} B_{dipole} \\ \dot{z}_{ion} &= v_{ionz} = \frac{\partial H}{\partial p_{ionz}} = \frac{p_{ionz}}{m_{ion}} + \frac{Z}{2m_{ion}c} B \rho_{ion} \\ \dot{p}_{ion\rho} &= -\frac{\partial H}{\partial \rho_{ion}} = \frac{p_{ion\phi}^2}{m_{ion}\rho_{ion}^3} - \frac{Z^2}{4m_{ion}c^2} (B^2 + B_{dipole}^2) \rho_{ion} \\ &\quad - \frac{Z}{2m_{ion}c} B p_{ionz} - \frac{Z}{R^3} (\rho_{ion} - \rho_e \cos(\phi_e - \phi_{ion})) \\ \dot{p}_{ion\phi} &= -\frac{\partial H}{\partial \phi_{ion}} = +\frac{Z}{R^3} \rho_e \rho_{ion} \sin(\phi_e - \phi_{ion}) \\ \dot{p}_{ionz} &= -\frac{\partial H}{\partial z_{ion}} = -\frac{Z^2}{4m_{ion}c^2} B^2 z_{ion} + \frac{Z}{2m_{ion}c} B p_{ion\rho} + \frac{Z}{R^3} (z_e - z_{ion}) \end{aligned}$$

with

$$\begin{aligned} R = |\vec{r}_e - \vec{r}_{ion}| &= \sqrt{(x_e - x_{ion})^2 + (y_e - y_{ion})^2 + (z_e - z_{ion})^2} = \\ &= \sqrt{\rho_e^2 + \rho_{ion}^2 - 2\rho_e \rho_{ion} \cos(\phi_e - \phi_{ion}) + (z_e - z_{ion})^2}. \end{aligned}$$

The time evolution of the system is obtained by numerically integrating the equations of motion. We use a fourth order Runge Kutta method for the integration within our simulation. If B_{dipole} is chosen such that in the electronic equation of motion of $p_{e\rho}$ the terms $p_{e\phi}^2/\rho_e^3$ and $-1/(4c^2)B_{dipole}^2\rho_e$ approximately cancel each other, the undesired drift motion of the electron into the z -direction gets eliminated. Analogously, another dipole field of different strength would be needed for the compensation of the ionic drift motion. As discussed in section 4.2 we start the ionic trajectories with an initial displacement instead.

The velocities parallel and perpendicular to the electron and ion beam are given by

$$\begin{aligned} v_{e||} &= \rho_e v_{e\phi} \\ v_{e\perp} &= \sqrt{v_{ez}^2 + v_{e\rho}^2} \\ v_{ion||} &= v_{iony} = v_{ion\rho} \sin \phi_{ion} + \rho_{ion} v_{ion\phi} \cos \phi_{ion} \\ v_{ion\perp} &= \sqrt{v_{ionx}^2 + v_{ionz}^2} = \sqrt{(v_{ion\rho} \cos \phi_{ion} - \rho_{ion} v_{ion\phi} \sin \phi_{ion})^2 + v_{ionz}^2} \end{aligned}$$

and the relative energy of the electron-ion system Eq. (4.3) is calculated as

$$\begin{aligned} E_{rel} = & \frac{1}{2} \mu (v_{e\rho}^2 + \rho_e^2 v_{e\phi}^2 + v_{ion\rho}^2 + \rho_{ion}^2 v_{ion\phi}^2 - 2v_{e\rho}v_{ion\rho} \cos(\phi_e - \phi_{ion}) \\ & - 2v_{e\rho}\rho_{ion}v_{ion\phi} \sin(\phi_e - \phi_{ion}) + 2\rho_e v_{e\phi}v_{ion\rho} \sin(\phi_e - \phi_{ion}) \\ & - 2\rho_e v_{e\phi}\rho_{ion}v_{ion\phi} \cos(\phi_e - \phi_{ion}) + (v_{ez} - v_{ionz})^2) \\ & - \frac{Z}{\sqrt{\rho_e^2 + \rho_{ion}^2 - 2\rho_e\rho_{ion} \cos(\phi_e - \phi_{ion}) + (z_e - z_{ion})^2}}. \end{aligned}$$

Appendix F

Electron-Ion Merging: Ionic Rest Frame Transformation

In the following an alternative way of transformation to the rest frame of the ion is presented. This more general approach allows for an acceleration of the ion in the laboratory frame. According to the nonvanishing Lorentz force $F_z \approx -v_{ion} B_x$ perpendicular to the plane of the toroid the ionic beam is accelerated in the laboratory frame (see also Figure 4.4b). Due to the magnetic dipole field an additional, albeit small accelerating force component appears also into the x direction, $F_x \approx v_{ion} B_{dipole}$. Therefore, changing to the rest frame of the ion involves the transformation into an accelerated frame of reference. Relativistic effects can be neglected since $v_{ion} \approx 0.1c$ and $\gamma = 1.0/\sqrt{1 - (v_{ion}/c)^2} \approx 1$. We consider the equations of motion of an ion and an electron in the lab frame for the fields $\vec{E} = 0$ and \vec{B} according to Eq. (4.2),

$$\begin{aligned} m_{ion} \vec{a}_{ion} &= \frac{Z}{c} \vec{v}_{ion} \times \vec{B}(\vec{r}_{ion}) + \frac{Z}{|\vec{r}_e - \vec{r}_{ion}|^3} (\vec{r}_e - \vec{r}_{ion}) \\ \vec{a}_e &= -\frac{1}{c} \vec{v}_e \times \vec{B}(\vec{r}_e) - \frac{Z}{|\vec{r}_e - \vec{r}_{ion}|^3} (\vec{r}_e - \vec{r}_{ion}) \end{aligned} \quad (F.1)$$

with the electron being described by the position \vec{r}_e , velocity \vec{v}_e and acceleration \vec{a}_e and the ion by \vec{r}_{ion} , \vec{v}_{ion} and \vec{a}_{ion} , respectively. As already pointed out the magnetic field strength depends on the particular position of the ion or electron. We employ the frame transformation

$$\begin{aligned} \vec{a}_{frame}(t) &= \vec{a}_{ion}(t) \\ \vec{v}_{frame}(t) &= \int_0^t \vec{a}_{ion}(t') dt' = \vec{v}_{ion}(t) \\ \vec{r}_{frame}(t) &= \int_0^t \vec{v}_{ion}(t') dt' = \vec{r}_{ion}(t) \end{aligned} \quad (F.2)$$

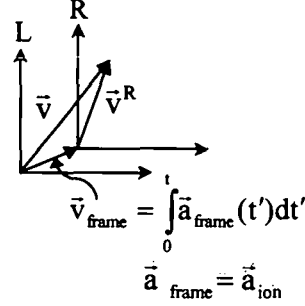


Figure F.1: Transformation from the lab frame to the rest frame of the ion R : The adding up of velocities is shown.

to transform to the rest frame of the ion R thus connecting the lab frame dynamics with the dynamics in R by

$$\begin{aligned}\vec{a} &= \vec{a}^R + \vec{a}_{ion} \\ \vec{v} &= \vec{v}^R + \vec{v}_{ion} \\ \vec{r} &= \vec{r}^R + \vec{r}_{ion}.\end{aligned}\tag{F.3}$$

Figure F.1 illustrates the relation between the lab frame and rest frame velocities. Inserting Eqs. (F.3) into Eqs. (F.1) the equations of motion in the rest frame of the ion are obtained. The ionic motion becomes trivial

$$\vec{r}_{ion}^R = 0 \quad \vec{v}_{ion}^R = 0 \quad \vec{a}_{ion}^R = 0,\tag{F.4}$$

whereas the electronic motion is described by

$$\vec{a}_e^R + \vec{a}_{ion} = -\frac{1}{c} (\vec{v}_e^R + \vec{v}_{ion}) \times \vec{B}(\vec{r}_e) - \frac{Z}{|\underbrace{\vec{r}_e^R - \vec{r}_{ion}^R}_{=0}|^3} (\underbrace{\vec{r}_e^R}_{=0} - \underbrace{\vec{r}_{ion}^R}_{=0}).\tag{F.5}$$

Correspondingly, the equations of motion for the electron-ion system in R finally read

$$\begin{aligned}m_{ion} \vec{a}_{ion}^R &= 0 \\ \vec{a}_e^R &= -\frac{1}{c} \vec{v}_e^R \times \underbrace{\vec{B}(\vec{r}_e)}_{\vec{B}^R} - \frac{Z}{|\vec{r}_e^R|^3} \vec{r}_e^R - \underbrace{\frac{1}{c} \vec{v}_{ion} \times \vec{B}(\vec{r}_e) - \vec{a}_{ion}}_{-\vec{E}^R}\end{aligned}\tag{F.6}$$

with the transformed electric and magnetic field components

$$\vec{E}^R(\vec{r}^R, t) = \frac{1}{c} \vec{v}_{ion}(t) \times \vec{B}(\vec{r}, t) + \vec{a}_{ion}(t) \quad (F.7)$$

$$\vec{B}^R(\vec{r}^R, t) = \vec{B}(\vec{r}, t) = \begin{pmatrix} -B(\vec{r}, t) \sin \phi(t) \\ B(\vec{r}, t) \cos \phi(t) \\ B_{dipole}(\vec{r}, t) \end{pmatrix}. \quad (F.8)$$

The electric and magnetic field strengths are time dependent in R due to their position dependency in the lab frame.

Finally we note that under the assumption that the ion can be regarded as infinitely heavy, *i.e.* not being accelerated at all by the Coulomb and magnetic fields and hence moving with a constant velocity $\vec{v}_{ion} = v_{ion} \hat{e}_y$ throughout the merging section, the above described method simply yields Eqs. (4.5) for the electric and magnetic fields. In this case the Galilei transformation, since relativistic effects are ignored,

$$\begin{aligned} \vec{v}_{frame}(t) &= \vec{v}_{ion} = \text{const} \\ \vec{r}_{frame}(t) &= \vec{v}_{ion} t \end{aligned} \quad (F.9)$$

transforms to the rest frame of the ion, an inertial frame (denoted by the superscript CV), where the relations

$$\begin{aligned} \vec{a} &= \vec{a}^{CV} \\ \vec{v} &= \vec{v}^{CV} + \vec{v}_{ion} \\ \vec{r} &= \vec{r}^{CV} + \vec{v}_{ion} t \end{aligned} \quad (F.10)$$

connect the lab frame and CV motions. The equations of motion for the electron then become

$$\vec{a}_e^{CV} = -\frac{1}{c} \vec{v}_e^{CV} \times \underbrace{\vec{B}(\vec{r}_e)}_{\vec{B}^{CV}} - \frac{Z}{|\vec{r}_e^{CV}|^3} \vec{r}_e^{CV} - \underbrace{\frac{1}{c} \vec{v}_{ion} \times \vec{B}(\vec{r}_e)}_{-\vec{E}^{CV}} \quad (F.11)$$

with the fields

$$\vec{E}^{CV}(\vec{r}^{CV}, t) = \frac{1}{c} \vec{v}_{ion} \times \vec{B}(\vec{r}, t) = \begin{pmatrix} 1/c B_{dipole}(\vec{r}, t) v_{ion} \\ 0 \\ 1/c B(\vec{r}, t) \sin \phi(t) v_{ion} \end{pmatrix} \quad (F.12)$$

$$\vec{B}^{CV}(\vec{r}^{CV}, t) = \vec{B}(\vec{r}, t) = \vec{B}^R(\vec{r}^R, t) \quad (F.13)$$

being identical to Eqs. (4.5).

Appendix G

Radiative Transition Probabilities

The probability for a transition of an atom from a state n, l, m to a state n', l', m' with the emission of a photon is given in the electric dipole approximation by [7]

$$W(n, l, m \rightarrow n', l', m') = \frac{4\omega^3}{3c^3} |\vec{r}_{nlm \rightarrow n'l'm'}|^2, \quad (\text{G.1})$$

where $\vec{r}_{nlm \rightarrow n'l'm'}$ is the dipole matrix element

$$\vec{r}_{nlm \rightarrow n'l'm'} = \int \psi_{n'l'm'}^* \vec{r} \psi_{nlm} d^3r \quad (\text{G.2})$$

with the principal, orbital and magnetic quantum numbers n, l and m of the hydrogenic wavefunction separated in spherical polar coordinates, $\psi_{nlm} = R_{nl}Y_{lm}$ (R_{nl} : radial wavefunction, Y_{lm} : spherical harmonic). ψ_{nlm} and $\psi_{n'l'm'}$ represent the initial and final wavefunctions respectively. Moreover, in Eq. (G.1) ω denotes the energy difference between the initial and final state

$$\omega = E_n - E_{n'} = -\frac{Z^2}{2n^2} + \frac{Z^2}{2n'^2} \quad (\text{G.3})$$

for an atom or ion of charge Z and c the velocity of light. The radiative decay rate of a given initial state into low-lying final states is obtained by summing Eq. (G.1) over all the corresponding final states, *i.e.*

$$W(n, l, m) = \sum_{n' l' m'} W(n, l, m \rightarrow n', l', m'). \quad (\text{G.4})$$

Using the dipole selection rules

$$\Delta l = l' - l = \pm 1 \quad \Delta m = m' - m = \pm 1, 0 \quad (\text{G.5})$$

the sum over m' can be evaluated for the two cases $l' = l+1$ and $l' = l-1$ separately,

$$\sum_{m'} |\vec{r}_{nlm \rightarrow n'l+1m'}|^2 = \frac{l+1}{2l+1} \left(R_{nl}^{n'l+1} \right)^2, \quad (\text{G.6})$$

$$\sum_{m'} |\vec{r}_{nlm \rightarrow n'l-1m'}|^2 = \frac{l}{2l+1} \left(R_{nl}^{n'l-1} \right)^2 \quad (\text{G.7})$$

with the integral over the radial wavefunctions given by

$$R_{nl}^{n'l'} = \int_0^\infty R_{nl} R_{n'l'} r^3 dr. \quad (\text{G.8})$$

In combined form Eqs. (G.6) and (G.7) read

$$\sum_{m'} |\vec{r}_{nlm \rightarrow n'l'm'}|^2 = \frac{\max(l, l')}{2l+1} \left(R_{nl}^{n'l'} \right)^2. \quad (\text{G.9})$$

This expression is independent of m . As an immediate corollary the life time of the initial state is independent of its magnetic quantum number and depends only on n and l . Therefore, an average transition rate for an electron in the initial n, l state is defined by averaging over the $2l+1$ possible values of m as

$$W(n, l) = \frac{1}{2l+1} \sum_m W(n, l, m). \quad (\text{G.10})$$

Taking into account Eqs. (G.1), (G.4), (G.5) and (G.9) this radiative decay rate is determined as

$$W(n, l) = \sum_{n'} \sum_{l'=l-1}^{l+1} \frac{4}{3} \frac{\omega^3}{c^3} \frac{\max(l, l')}{2l+1} \left(R_{nl}^{n'l'} \right)^2, \quad (\text{G.11})$$

whereas the transition probability for an individual state to state transition $n, l \rightarrow n', l' = l \pm 1$ (after averaging over m and summing over m') becomes

$$W(n, l \rightarrow n', l' = l \pm 1) = \frac{4}{3} \frac{\omega^3}{c^3} \frac{\max(l, l')}{2l+1} \left(R_{nl}^{n'l \pm 1} \right)^2. \quad (\text{G.12})$$

Appendix H

Continuity of the Transition Probability Across Threshold

First the equivalence of the probability for radiative stabilization evaluated on the n scale (Eq. (4.27))

$$P_s^{(1)}(\tau_c) = \tau_c \sum_{n > n_{max}} \bar{P}(n) \sum_{n'=1}^{n_{max}} \frac{2\omega^2}{c^3} \frac{2^5}{3\sqrt{3}\pi} \left(\frac{1}{n'^2} - \frac{1}{n^2} \right)^{-3} \frac{1}{n'^3 n^5}. \quad (\text{H.1})$$

and the corresponding probability evaluated on the energy scale (Eq. (4.40))

$$P_s^{(2)}(\tau_c) = \tau_c \gamma_E 4\sqrt{2} \sum_{n'=1}^{n_{max}} \frac{1}{Zn'} \int_{E < 0} \bar{P}(E) (-E)^{5/2} dE \quad (\text{H.2})$$

should be checked. For the initially high lying Rydberg states with $n \gg n'$ we may approximate $\omega = E_n - E_{n'} \approx -E_{n'} = Z^2/(2n'^2)$ and $(1/n'^2 - 1/n^2)^{-3} \approx n'^6$ in Eq. (H.1) and hence obtain with $\gamma_E = 16/(3\sqrt{3}\pi c^3)$

$$P_s^{(1)}(\tau_c) \approx \tau_c \gamma_E \sum_{n > n_{max}} \bar{P}(n) \sum_{n'=1}^{n_{max}} \frac{Z^4}{n' n^5}. \quad (\text{H.3})$$

On the other hand, Eq. (H.2) becomes with $(-E)^{5/2} = Z^5/(4\sqrt{2}n^5)$

$$P_s^{(2)}(\tau_c) = \tau_c \gamma_E \sum_{n'=1}^{n_{max}} \frac{1}{n'} \int_{E < 0} \bar{P}(E) \frac{Z^4}{n^5} dE \quad (\text{H.4})$$

thus having adopted the same form as Eq. (H.3).

Secondly, we want to verify the continuity of the radiative transition probabilities across the ionization limit, *i. e.*

$$\lim_{n \rightarrow \infty} D_{Ryd}(n) W(n \rightarrow n') = \lim_{E \rightarrow 0} D_{free}(E) W(E \rightarrow n'), \quad (\text{H.5})$$

where $D_{Ryd}(n)$ and $D_{free}(E)$ denote the density of states below and above threshold, respectively. $D_{Ryd}(n)$ is the density of Rydberg states for a given quantum number n Eq. (4.38) or in terms of n it is given by

$$D_{Ryd}(n) = \frac{n^5}{Z^2}, \quad (\text{H.6})$$

and $D_{free}(E)$ specifies the density of free electrons Eq. (4.33). $W(n \rightarrow n')$ and $W(E \rightarrow n')$ are the corresponding transition probabilities per unit time. The transition probability according to Eq. (H.1)

$$W(n \rightarrow n') = \frac{2\omega^2}{c^3} \frac{2^5}{3\sqrt{3}\pi} \left(\frac{1}{n'^2} - \frac{1}{n^2} \right)^{-3} \frac{1}{n'^3 n^5} \quad (\text{H.7})$$

reduces in the limit $n \rightarrow \infty$ (see also above) to

$$\lim_{n \rightarrow \infty} W(n \rightarrow n') = \gamma_E \frac{Z^4}{n'^5}. \quad (\text{H.8})$$

Accordingly, the left hand side of the continuity relation Eq. (H.5) becomes

$$\lim_{n \rightarrow \infty} D_{Ryd}(n) W(n \rightarrow n') = \gamma_E \frac{Z^2}{n'}. \quad (\text{H.9})$$

For the continuous spectrum we use the transition probability according to Eq. (4.39)

$$W(E \rightarrow n') = \gamma_E \frac{\sqrt{2}\pi^2}{V} \frac{Z^2}{n'} \frac{1}{\sqrt{E}}. \quad (\text{H.10})$$

With the density of states $D_{free}(E)$ of Eq. (4.33) the continuum state limit of Eq. (H.5) is determined as

$$\lim_{E \rightarrow 0} D_{free}(E) W(E \rightarrow n') = \gamma_E \frac{Z^2}{n'}, \quad (\text{H.11})$$

which precisely agrees with the bound state limit of Eq. (H.9) thus proving the continuity across the ionization threshold.

Bibliography

- [1] W. H. Tucker, *Radiation Processes in Astrophysics*, Cambridge, MIT Univ. Press (1975).
- [2] H. P. Summers and W. J. Dickson, *Application of Recombination (NATO ASI Series B, Physics)*, New York, Plenum (1992).
- [3] M. Amoretti, C. Amsler, G. Bonomi, A. Bouchta, P. Bowe, C. Carraro, C. L. Cesar, M. Charlton, M. J. T. Collier, M. Doser, V. Filippini, K. S. Fine, A. Fontana, M. C. Fujiwara, R. Funakoshi, P. Genova, J. S. Hangst, R. S. Hayano, M. H. Holzscheiter, L. V. Jergensen, V. Lagomarsino, R. Landua, D. Lindelöf, E. Lodi Rizzini, M. Macri, N. Madsen, G. Manuzio, M. Marchesotti, P. Montagna, H. Pruys, C. Regenfus, P. Riedler, J. Rochet, A. Rotondi, G. Rouleau, G. Testera, A. Variola, T. L. Watson and D. P. van der Werf, *Nature* **419**, 456 (2002).
- [4] G. Gabrielse, N. S. Bowden, P. Oxley, A. Speck, C. H. Storry, J. N. Tan, M. Wessels, D. Grzonka, W. Oelert, G. Schepers, T. Sefzick, J. Walz, H. Pittner, T. W. Hänsch and E. A. Hessels, *Phys. Rev. Lett.* **89**, 213401 (2002).
- [5] M. Stobbe, *Ann. Phys. (Leipzig)* **7**, 661 (1930).
- [6] H. A. Kramers, *Philos. Mag.* **46**, 836 (1923).
- [7] H. Bethe and E. Salpeter, *Quantum Mechanics of One- and Two-Electron Systems*, Springer, Berlin (1957).
- [8] H. Gao, D. R. DeWitt, R. Schuch, W. Zong, S. Asp and M. Pajek, *Phys. Rev. Lett.* **75**, 4381 (1995).
- [9] H. Gao, R. Schuch, W. Zong, E. Justiniano, D. R. DeWitt, H. Lebius and W. Spies, *J. Phys. B: At. Mol. Opt. Phys.* **30**, L499 (1997).
- [10] G. Gwinner, A. Hoffknecht, T. Bartsch, M. Beutelspacher, N. Eklöw, P. Glans, M. Grieser, S. Krohn, E. Lindroth, A. Müller, A. A. Saghir, S. Schippers, U.

- Schramm, D. Schwalm, M. Tokman, G. Wissler and A. Wolf, Phys. Rev. Lett. **84**, 4822 (2000).
- [11] A. Hoffknecht, C. Brandau, T. Bartsch, C. Böhme, H. Knopp, S. Schippers, A. Müller, C. Kozhuharov, K. Beckert, F. Bosch, B. Franzke, A. Krämer, P. H. Mokler, F. Nolden, M. Steck, Th. Stöhlker and Z. Stachura, Phys. Rev. A **63**, 012702 (2001).
- [12] W. Shi, S. Böhm, C. Böhme, C. Brandau, A. Hoffknecht, S. Kieslich, S. Schippers, A. Müller, C. Kozhuharov, F. Bosch, B. Franzke, P. H. Mokler, M. Steck, Th. Stöhlker and Z. Stachura, Eur. Phys. J. D **15**, 145 (2001).
- [13] C. Heerlein, G. Zwicknagel and C. Toepffer, Phys. Rev. Lett. **89**, 83202 (2002).
- [14] M. Hörndl, S. Yoshida, K. Tökési and J. Burgdörfer, Phys. Rev. Lett. **93**, 209301 (2004).
- [15] C. Heerlein, G. Zwicknagel and C. Toepffer, Phys. Rev. Lett. **93**, 209901(E) (2004).
- [16] C. Heerlein, G. Zwicknagel and C. Toepffer, Phys. Rev. Lett. **93**, 209302 (2004).
- [17] M. Hörndl, S. Yoshida, K. Tökési and J. Burgdörfer, in *Photonic, Electronic and Atomic Collisions*, edited by J. Burgdörfer, J. S. Cohen, S. Datz and C. R. Vane, Rinton Press, Princeton, 2002, p. 324.
- [18] M. Hörndl, S. Yoshida, K. Tökési and J. Burgdörfer, Hyperf. Interact. **146/147**, 13 (2003).
- [19] M. Hörndl, S. Yoshida, K. Tökési and J. Burgdörfer, Nucl. Instrum. Methods Phys. Res. Sect. B (2005) in press.
- [20] M. Hörndl, S. Yoshida, A. Wolf, G. Gwinner and J. Burgdörfer, submitted to Phys. Rev. Lett.
- [21] A. Hoffknecht, O. Uwira, S. Schennach, A. Frank, J. Haselbauer, W. Spies, N. Angert, P. H. Mokler, R. Becker, M. Kleinod, S. Schippers and A. Müller, J. Phys. B: At. Mol. Opt. Phys. **31**, 2415 (1998).
- [22] O. Uwira, A. Müller, W. Spies, A. Frank, J. Linkemann, C. Brandau, T. Cramer, C. Kozhuharov, J. Klabunde, N. Angert, P. H. Mokler, R. Becker, M. Kleinod and N. R. Badnell, Hyperf. Interact. **108**, 167 (1997).
- [23] H. Danared, Nucl. Instrum. Methods Phys. Res. Sect. A **335**, 397 (1993).

- [24] H. Danared, G. Andler, L. Bagge, C. J. Herrlander, J. Hilke, J. Jeansson, A. Källberg, A. Nilsson, A. Paal, K.-G. Rensfelt, U. Rosengard, J. Starker and M. af Ugglas Phys. Rev. Lett. **72**, 3775 (1994).
- [25] S. Pastuszka, U. Schramm, M. Grieser, C. Broude, R. Grimm, D. Habs, J. Kenntner, H.-J. Miesner, T. Schüßler, D. Schwalm and A. Wolf, Nucl. Instrum. Methods Phys. Res. Sect. A **369**, 11 (1996).
- [26] G. I. Budker, Sov. J. Atom. Energy **22**, 438 (1967).
- [27] G. Kilgus, D. Habs, D. Schwalm, A. Wolf, N. R. Badnell and A. Müller, Phys. Rev. A **46**, 5730 (1992).
- [28] A. Hoffknecht, *Rekombination hochgeladener Ionen mit freien Elektronen bei niedrigen Energien*, Dissertation, Shaker Verlag, Aachen (1999).
- [29] C. Brandau, *Messungen zur Photorekombination hochgeladener lithiumähnlicher Ionen*, Dissertation (2000).
- [30] L. H. Andersen and J. Bolko, Phys. Rev. A **42**, 1184 (1990).
- [31] E. Zerrad and Y. Hahn, J. Quant. Spectrosc. Radiat. Transfer **59**, 637 (1998).
- [32] D. J. McLaughlin and Y. Hahn, Phys. Rev. A **43**, 1313 (1991).
- [33] H. Danared, Nucl. Instrum. Methods Phys. Res. Sect. A **391**, 24 (1997).
- [34] A. Müller, S. Schennach, M. Wagner, J. Haselbauer, O. Uwira, W. Spies, E. Jennewein, R. Becker, M. Kleinod, U. Pröbstel, N. Angert, J. Klabunde, P. H. Mokler, P. Spädtke and B. Wolf, Phys. Scr. T **37**, 62 (1991).
- [35] L. H. Andersen, J. Bolko and P. Kvistgaard, Phys. Rev. Lett. **64**, 729 (1990).
- [36] H. Gao, S. Asp, C. Biedermann, D. R. DeWitt, R. Schuch, W. Zong and H. Danared, Hyperf. Interact. **99**, 301 (1996).
- [37] A. Hoffknecht, S. Schippers, A. Müller, G. Gwinner, D. Schwalm and A. Wolf, Phys. Scr. T **92**, 402 (2001).
- [38] O. Uwira, A. Müller, J. Linkemann, T. Bartsch, C. Brandau, M. Schmitt, A. Wolf, D. Schwalm, R. Schuch, W. Zong, H. Lebius, W. G. Graham, J. Doerfert and D. W. Savin, Hyperf. Interact. **108**, 149 (1997).
- [39] S. Baird, J. Bosser, C. Carli, M. Chanel, P. Lefvre, R. Ley, R. Maccaferri, S. Maury, I. Meshkov, D. Möhl, G. Molinari, F. Motsch, H. Mulder, G. Tranquille and F. Varenne, Phys. Lett. B **361**, 184 (1995).

- [40] G. F. Gribakin, A. A. Gribakina and V. V. Flambaum, *Aust. J. Phys.* **52**, 443 (1999).
- [41] A. Hoffknecht, T. Bartsch, S. Schippers, A. Müller, N. Eklöw, P. Glans, M. Beutelspacher, M. Grieser, G. Gwinner, A. A. Saghir and A. Wolf, *Phys. Scr. T* **80**, 298 (1999).
- [42] Q. Spreiter and C. Toepffer, *Hyperf. Interact.* **114**, 245 (1998).
- [43] Q. Spreiter and C. Toepffer, *J. Phys. B: At. Mol. Opt. Phys.* **33**, 2347 (2000).
- [44] Y. Hahn, *J. Phys. B: At. Mol. Opt. Phys.* **34**, L701 (2001).
- [45] G. Gwinner, D. Schwalm and A. Wolf, in *XXII International Conference on Photonic, Electronic and Atomic Collisions, Abstracts of Contributed Papers*, edited by S. Datz, M. E. Bannister, H. F. Krause, L. H. Saddiq, D. Schultz and C. R. Vane, Rinton Press, Princeton, 2001, p. 326.
- [46] J. Trost and J. Burgdörfer, *Verhandl. DPG (VI)* **34**, 257 (1999).
- [47] H. Goldstein, *Klassische Mechanik*, Akademische Verlagsgesellschaft, Wiesbaden (1978).
- [48] B. R. Johnson, J. O. Hirschfelder and K.-H. Yang, *Rev. Mod. Phys.* **55**, 109 (1983).
- [49] A. S. Dickinson and J. M. Patterson, *J. Phys. A: Math. Gen.* **19**, 1811 (1986).
- [50] W. H. Press, S. A. Teukolsky, W. T. Vetterling and B. P. Flannery, *Numerical Recipes in Fortran 77, The Art of Scientific Computing*, Second Edition, University Press, Cambridge (1992).
- [51] E. Forest and R. D. Ruth, *Physica D* **43**, 105 (1990).
- [52] H. Yoshida, *Phys. Lett. A* **150**, 262 (1990).
- [53] H. Friedrich and D. Wintgen, *Phys. Rep.* **183**, 37 (1989).
- [54] H. Hasegawa, S. Adachi and H. Harada, *J. Phys. A: Math. Gen.* **16**, L503 (1983).
- [55] C. Jung, *J. Phys. A: Math. Gen.* **19**, 1345 (1986).
- [56] H. Poincaré, *Les methods nouvelles de la mecanique celeste*, Gauthier-Villars, Paris (1892).

- [57] B. Eckhardt and C. Jung, J. Phys. A: Math. Gen. **19**, L829 (1986).
- [58] B. Eckhardt, Physica D **33**, 89 (1988).
- [59] B. Eckhardt, Europhys. Lett. **5**, 107 (1988).
- [60] C. Jung and H. J. Scholz, J. Phys. A: Math. Gen. **20**, 3607 (1987).
- [61] L. D. Landau and E. M. Lifshitz, *Course of Theoretical Physics, Volume 1, Mechanics*, Butterworth-Heinemann, Oxford (1976).
- [62] M. Pajek and R. Schuch, Phys. Rev. A **45**, 7894 (1992).
- [63] M. Abramowitz and I. E. Stegun, *Handbook of Mathematical Functions With Formulas, Graphs, and Mathematical Tables*, U. S. Department of Commerce, National Bureau of Standards, Applied Mathematics Series 55 (1972).
- [64] Private Communication with A. Wolf.
- [65] C. Wesdorp, F. Robicheaux and L. D. Noordam, Phys. Rev. Lett. **84**, 3799 (2000).
- [66] C. Wesdorp, F. Robicheaux and L. D. Noordam, Phys. Rev. A. **64**, 033414 (2001).
- [67] J. D. Jackson, *Classical Electrodynamics*, Third Edition, John Wiley & Sons Inc., New York (1999).
- [68] S. G. Kuzmin, T. M. O'Neil and M. E. Glinsky, Phys. Plasmas **11**, 2382 (2004).
- [69] S. G. Kuzmin and T. M. O'Neil, Phys. Rev. Lett. **92**, 243401 (2004).
- [70] H. Marxer and L. Spruch, Phys. Rev. A **43**, 1268 (1991).
- [71] H. Friedrich, *Theoretical Atomic Physics*, Second Edition, Springer, Berlin (1998).
- [72] E. P. Kanter, D. Schneider, Z. Vager, D. S. Gemmell, B. J. Zabransky, Gu Yuan-zhuang, P. Arcuni, P. M. Koch, D. R. Mariani and W. Van de Water, Phys. Rev. A **29**, 583 (1984).
- [73] A. Wolf, *Wechselwirkung zwischen hochgeladenen Ionen und freien Elektronen in einem Ionenspeicherring: dynamische Reibung und Rekombination*, Habilitation (1992).
- [74] Private Communication with G. Gwinner.

- [75] C. Heerlein, *Radiative Rekombination im Elektronenkühler, Numerische Analyse im Phasenraum*, Dissertation, Shaker Verlag, Aachen (2002).
- [76] C. Heerlein, G. Zwicknagel and C. Toepffer, Nucl. Instrum. Methods Phys. Res. Sect. B **205**, 395 (2003).
- [77] C. Heerlein and C. Toepffer, Hyperf. Interact. **146/147**, 19 (2003).
- [78] C. Heerlein and C. Toepffer, Comp. Phys. Commun. **147**, 494 (2002).
- [79] L. E. Ballentine, *Quantum Mechanics, A Modern Development*, World Scientific, Singapore (1998).
- [80] L. D. Landau and E. M. Lifshitz, *Lehrbuch der theoretischen Physik, Band 3, Quantenmechanik*, Akademie-Verlag, Berlin (1986).
- [81] J. Eichler, Y. Yoshihama and N. Tushima, Phys. Rev. A **65**, 033404 (2002).
- [82] R. Abrines and I. C. Percival, Proc. Phys. Soc. **88**, 861 (1966).

Acknowledgments

This thesis would not have been accomplished without a lot of help, support and motivation by other people. First of all, I would like to thank my PhD-advisor, *Joachim Burgdörfer*, who very much supported this work by innumerable discussions, helpful explanations and new ideas. His intuition for physics and ability to discern the overall interrelated picture behind a load of details have proven advantageous for the progress of this project frequently. Without his experience and advice this work would have never reached the form and results presented in this dissertation.

Secondly, I am highly indebted to *Shuhei Yoshida*, my great collaborator on this project, who never hesitated to discuss about physics with me. He was really patient in answering all my questions, helped me with various technical details of computing and numerics and, moreover, motivated me when I felt stuck in the project. In particular, I want to thank him for his big support before and during the ICPEAC (International Conference on Photonic, Electronic and Atomic Collisions) in 2001, where I was given the opportunity to present a “hot-topic” talk. Shuhei even continued to work on the computer program, after I had already traveled to the conference site in Santa Fe, and managed to obtain first results for the enhanced recombination rates just in time before my presentation.

My further gratitude goes to Prof. *Andreas Wolf* for his great interest in my research and stimulating discussions at various conferences, in particular, the important discussion at the HCI (Conference on the Physics of Highly Charged Ions) in Vilnius last autumn encouraging me to evaluate the radiative decay rates of the transiently formed Rydberg states inside the solenoid in detail. The obtained results are very promising hopefully leading to a joint paper in the near future. I appreciate his willingness to read and assess this thesis and, moreover, that he readily agreed to travel to Vienna to be co-examiner at the thesis defense.

In addition, I am indebted to *Gerald Gwinner*, who also greatly contributed to my present understanding of the rate enhancement phenomenon. I learned the idea of transient field-induced recombination during beam merging from his poster at the ICPEAC in Santa Fe and I benefited a lot from the discussions during this stay in Vienna in autumn 2001 and subsequent email communications.

Furthermore, I am very grateful to *Marek Seliger*, my boy-friend and also mem-

ber of Joachim's research group, for his overall support during my PhD-time. I benefited a great deal from his computing knowledge. He was helpful in preparing figures for conference presentations, some of these figures even appear in this thesis, and in installing my laptop. Besides the countless physics' discussions we definitely had during evening times I would, in particular, like to thank him for all his encouragement and motivation during times when I was desperate and did not feel any progress in my research.

I would like to acknowledge *Karoly Tókési* for his support during the first few months of my PhD, his invitation to the ATOMKI (Institute of Nuclear Research of the Hungarian Academy of Sciences) in Debrecen and his kind hospitality during my stay there. Many thanks also to *Nina Rohringer* for the pleasant time we spent together sharing one office and the numerous conversations on all sorts of topics. *Christoph Lemell* deserves special gratitude for the computer administration ensuring that all computers were ever working at the Institute. Finally, thank you to all the people of the research group for providing a very pleasant atmosphere, amusing coffee-breaks, interesting discussions and good chocolate.

I greatly acknowledge the financial support of the Austrian Science Fund FWF ("Fonds zur Förderung der wissenschaftlichen Forschung") provided by the grant number P15025 and the receipt of a research scholarship supplied by the Federal Ministry for Education, Research and Culture.

Last, but definitely not least, I want to thank my family, and all my friends at the Institute and outside for accompanying me during the last four and a half years - including all the ups and downs - with support and enjoyment.

Maria Hörndl

Institute for Theoretical Physics
Vienna University of Technology
Wiedner Hauptstrasse 8-10/136
A-1040 Vienna, Austria
phone: +43 1 58801-13633, fax: +43 1 58801-13699
maria@concord.itp.tuwien.ac.at
<http://dollywood.itp.tuwien.ac.at/~maria/>

PERSONAL DATA

Date and place of birth: October, 3rd 1976 in Waidhofen/Thaya, Lower Austria

Nationality: Austrian

Private address: Rienöblgasse 15/12, A-1040 Vienna, Austria

EDUCATION

10/2000 - 06/2005: PhD in physics at the Institute for Theoretical Physics at the Vienna University of Technology

Title: Classical Dynamics of Low Energy Electron-Ion Recombination in Storage Rings

Advisor: Dr. Joachim Burgdörfer

Co-Advisor: Dr. Shuhei Yoshida

06/2000: Master degree in physics, passed with distinction

10/1999 - 06/2000: Diploma thesis at the Atomic Institute of the Austrian Universities at the Vienna University of Technology

Title: Conserved Quantities and Equation of Motion in a Classical Soliton Model

Advisor: Dr. Manfred Faber

10/1995 - 06/2000: Study of physics at the Vienna University of Technology

07/1999 - 09/1999: Summer student at CERN, Geneva, Switzerland

09/1987 - 06/1995: Grammar school in Waidhofen/Thaya, Lower Austria, passed with distinction

09/1983 - 06/1987: Primary school in Windigsteig, Lower Austria

EMPLOYMENT, INTERNSHIPS AND TEACHING EXPERIENCE

10/2000 - 06/2005: PhD student in physics at the Vienna University of Technology supported by the Austrian Science Fund (FWF)

07/2000 - 08/2000: Internship at the NA-48 experiment at CERN, Geneva, Switzerland

10/1999 - 01/2000: Teaching assistant (tutor) at the Vienna University of Technology

02/1999 Internship at Siemens, Vienna, Austria

07/1998 - 08/1998: Internship at Siemens, Vienna, Austria

PUBLICATIONS

- M. Hörndl, S. Yoshida, A. Wolf, G. Gwinner and J. Burgdörfer, *Enhancement of Low Energy Electron-Ion Recombination in a Magnetic Field: Influence of Transient Field Effects*, to be submitted.
- M. Hörndl, S. Yoshida, K. Tökési and J. Burgdörfer, *Enhancement of Low Energy Electron-Ion Recombination in a Magnetic Field: Influence of Transient Field Effects*, Nucl. Instrum. Methods Phys. Res. Sect. B, in press (2005).
- M. Hörndl, S. Yoshida, K. Tökési and J. Burgdörfer, *Comment on "Radiative Recombination Enhancement of Bare Ions in Storage Rings with Electron Cooling"*, Phys. Rev. Lett **93**, 209301 (2004). (Comment on article C. Heerlein, G. Zwicknagel and C. Toepffer, Phys. Rev. Lett. **89**, 83202 (2002).)
- M. Hörndl, S. Yoshida, K. Tökési and J. Burgdörfer, *Enhancement of Low Energy Electron-Ion Recombination in a Magnetic Field*, Hyperf. Interact. **146-147**, 13 (2003).
- M. Hörndl, S. Yoshida, K. Tökési and J. Burgdörfer, *Low Energy Electron-Ion Recombination in a Magnetic Field: The Role of Chaotic Dynamics* in "Photonic, Electronic and Atomic Collisions" edited by J. Burgdörfer, J. S. Cohen, S. Datz and C. R. Vane, Rinton Press, Princeton, 2002, p. 324.
- M. Hörndl, S. Yoshida, K. Tökési and J. Burgdörfer, *Low Energy Electron-Ion Recombination in a Magnetic Field: The Role of Chaotic Dynamics*, Tagungsband der 23. Tagung über Energiereiche Atomare Stöße (EAS), 2002.
- M. Hörndl and G. Dissertori, *CERN Summer Student Project: ALPHA++*, Aleph Internal Note 99-097 (1999).

CONFERENCE PARTICIPATION, POSTERS AND TALKS

- 09/2004: Poster at the 12th International Conference on the Physics of Highly Charged Ions (HCI), Vilnius, Lithuania.
- 06/2004: Participation at 3rd Joint Collaboration Meeting of HITRAP, NIPNET and ION CATCHER, Krakow, Poland.
- 01/2004: Seminar talk at the Institute of Nuclear Research of the Hungarian Academy of Sciences (ATOMKI), Debrecen, Hungary.
- 11/2003: Participation at the Austrian - Hungarian Workshop on Charged Particle Transport through Nanostructures and Solids, Debrecen, Hungary.
- 07/2003: Poster at the XXIII International Conference on Photonic, Electronic and Atomic Collisions (ICPEAC), Stockholm, Sweden.
- 08/2002: Poster at the XVIII International Conference on Atomic Physics (ICAP), Cambridge, USA.
- 12/2001: Talk at the Workshop on Atomic Physics and X-Ray Free Electron Laser Related Dynamics, Dresden, Germany.
- 09/2001: Poster at the Annual Meeting of the Austrian Physical Society (ÖPG), Vienna, Austria.
- 09/2001: Invited talk at the 3rd Euroconference on Atomic Physics at Accelerators (APAC), Aarhus, Denmark.
- 07/2001: Selected hot topic talk and poster at the XXII International Conference on Photonic, Electronic and Atomic Collisions (ICPEAC), Santa Fe, USA.
- 04/2001: Talk at the Spring Meeting of the German Physical Society (DPG), Berlin, Germany.

LANGUAGES

German (native speaker), English (fluently)

SCHOLARSHIPS/ AWARDS

2003 - 2004: *Research scholarship* of the Vienna University of Technology, two times

2003: *Furtherance scholarship* of the Vienna University of Technology

2002: *TOP scholarship* of the province of Lower Austria

1997 - 2000: *Achievement scholarship* of the Vienna University of Technology, four times

COMPUTATIONAL SKILLS

Programming languages: C, C++, Fortran, Pascal, Visual Basic

Operating systems: Linux, Unix, Windows

Software: Mathematica, Microsoft Office, LaTeX, Gnuplot, HTML etc.

PERSONAL INTERESTS AND HOBBIES

Hiking, cycling, skiing and traveling